# Imaging Hemi-Thoracic Radiation Induced Lung Toxicity in Mice

---

*A thesis submitted for the degree of Doctor of Philosophy at the University of Oxford*

*Cynthia L. Eccles*

*CRUK/MRC Oxford Institute for Radiation Oncology and Biology and Wolfson College*

# ***Abstract***: *Imaging Hemi-Thoracic Radiation Induced Lung Toxicity in Mice*

*A thesis submitted for the degree of Doctor of Philosophy at the University of Oxford, Cynthia L. Eccles, CRUK/MRC Oxford Institute for Radiation Oncology and Biology and Wolfson College*

Lung cancer is the second most frequently diagnosed cancer, and the leading cause of cancer deaths in the United Kingdom. Two thirds of patients present with advanced disease, which contributes significantly to the high mortality rate associated with this disease. Radiation therapy (RT) is used frequently in the treatment of lung cancer, however the delivery of tumouricidal doses is often limited by the risk of radiation induced lung toxicity (RILT). RILT occurs in an acute phase as pneumonitis followed by a later phase of fibrosis. Because the RILT symptoms are often similar to those of pulmonary infection or disease progression, diagnosis can be difficult.

Approaches to improving the outcome of RT for lung cancer include:

1. Detection of RILT at an early stage. This would allow for the timely introduction of treatment and, therefore, avoidance of severe episodes of RILT. Longitudinal imaging studies of patients undergoing lung RT, using ionizing radiation (IR) free imaging techniques, such as magnetic resonance imaging (MRI) may provide a means of early RILT detection.
2. Concurrent administration of targeted radiosensitizers. Several molecularly targeted agents have been explored in this context. For example, the PI3K inhibitors Nelfinavir, NVP-NBKM120, and NVP-BEZ235 cause radiosensitization in pre-clinical models of cancer. These agents are being

introduced into clinical practise and so it is important to investigate their effect on normal lung tissues.

This thesis reports the development of a high throughput, multi-modality imaging programme for the longitudinal investigation of normal tissue toxicity in a pre-clinical model. The aims of the research were:

1. To investigate novel, non-invasive imaging methods for the detection of RILT.
2. To compare the incidence and severity of RILT following radiation alone to that following radiation plus PI3K/AKT/mTOR inhibition.

Eight longitudinal imaging studies were undertaken in C57BL6 and CBA mice to detect the effects of single (right) lung irradiation with or without targeted radiosensitizers. Radiation was delivered in a single fraction (14, 18 or 20 Gy) using a Gulmay cabinet irradiator, or a small animal radiation research platform (SARRP) to deliver single (20 Gy) or fractionated (3 x 15 Gy) RT under image guidance. Plethysmography, computed tomography (CT) and magnetic resonance imaging (MRI) were undertaken in representative animals from each cohort at baseline and at pre-determined time points up to 20 weeks. Histological examination of lung tissue was undertaken for correlative studies. RILT was scored using a semi-quantitative system reflecting the percentage of the lung volume that was abnormal on imaging. CT densities, MRI signal intensities, and area under the curve (AUC) or initial area under the curve (iAUC) estimations, were used for t-tests and regression analyses to determine the statistical significance of lung changes. An exploratory analysis of dynamic contrast enhanced MRI (DCE-MRI) as a tool to detect early radiation pneumonitis was undertaken using model- and non-model-based analyses.

The acquisition of high quality cardiorespiratory gated spin echo (SEMS), DCE, and high resolution MR angiography (ANGIO) on 4.7 and 7 T magnets was achieved by continuous optimization of imaging parameters and gating techniques.

The main findings from the work presented in this thesis were:

1. The incidence of RILT following hemi-thoracic radiation was similar whether the detection method used was MRI, CT or histological examination.
2. Severe RILT can be detected using cardiorespiratory gated DCE-MRI. Preliminary data suggest DCE-MRI may also detect mild to moderate RILT but this requires further validation.
3. The incidence and severity of RILT following RT + PI3K inhibitors was not significantly different to the incidence and severity of RILT following RT alone.

## ACKNOWLEDGEMENTS

I am extremely grateful to my supervisors, Professor Gillies McKenna, and Professor Kate Vallis for providing the opportunity to undertake the research presented in this thesis, and for taking on such an unlikely DPhil candidate (and especially for humouring my rowing 'habit'). I am also grateful to Mrs. Lis Turner and the Department of Radiation Therapy at the Churchill Hospital for their support of my studentship.

This work has been a truly collaborative effort between many groups within our large Department of Oncology and certainly would not have been possible without the guidance of my thesis committee, Professor Thomas Brunner, and Professor Fergus Gleeson, as well as the many other advisors who have contributed including Professor Ruth Muschel and Dr. Geoff Higgins.

The pre-clinical imaging described in this thesis was possible in large part due to the Radiobiology Research Institute's Imaging Core, namely Dr. Sean Smart, Dr. Danny Allen, Dr. Veerle Kersemans and their colleagues. Dr. Sally Hill has provided much advice on the care and handling of the animals; radiation physics guidance and support has been provided by Dr. Mark Hill's team namely, Dr. James Thompson and Dr. Luke Bird; post-doctoral fellows in Dr. Julia Schnabel and Sir Professor Mike Brady's group, Dr. Bartek Papiez and Dr. Ben Irving have provided tools and assistance for image analysis; Dr. Christiana Kartsonaki has provided statistical analysis, and Professor Cheryl Scudamore of the MRC Harwell, has provided assistance with the interpretation of the pathology samples. Professor Boris Vojnovic and Mr. Rob Newman have provided the plethysmograph used in these studies and the engineering team at the Oxford Institute for Radiation Oncology have produced the custom collimator and animal holder for the SARRP studies. Invaluable

guidance with the laboratory work, and input in proofreading was provided by lab manager Sarah Able.

Last but not least, I would like to give thanks my family, as well colleagues and friends at PMH who encouraged me to (and in some cases discouraged me from) moving an ocean away to take on this challenge.

# Contents

Chapter 1: Introduction

Chapter 2: Materials and Methods

Chapter 3: Preliminary Studies

Chapter 4: PI3K/AKT Inhibition and Radiation

Chapter 5: PI3K/AKT Inhibition and Image Guided Radiation (IGRT)

Chapter 6: Discussion

Appendix 1: Dosimetric Characterization of Radiation Delivery Systems

Appendix 2: Publications and Presentations

Appendix 3: Plethysmography

# TABLE OF CONTENTS

*Abstract* ..... i

ACKNOWLEDGEMENTS ..... iv

TABLE OF CONTENTS ..... vii

LIST OF FIGURES ..... xi

LIST OF TABLES ..... xv

LIST OF ABBREVIATIONS ..... xvi

1 INTRODUCTION ..... 2

1.1 Lung Cancer ..... 2

1.2 Presentation and Diagnosis of Lung Cancer ..... 5

1.3 Treatment of Lung Cancer ..... 7

1.3.1 Surgery for Lung Cancer ..... 8

1.3.2 Chemotherapy for Lung Cancer ..... 8

1.3.3 Radiotherapy and Chemo-Radiotherapy for Lung Cancer ..... 9

1.3.4 Other Treatments for Lung Cancer ..... 10

1.4 Challenges using radiotherapy to treat lung cancer ..... 10

1.5 Radiation Induced lung Toxicity (RILT) ..... 12

1.6 Current Methods to Predict RILT ..... 14

1.7 Imaging Methods to Detect RILT ..... 15

1.7.1 Computed Tomography ..... 15

1.7.2 Magnetic Resonance Imaging ..... 18

1.8 Use of Pre-clinical Models in RILT Detection ..... 23

1.9 Current Status of Pre-clinical Models to Assess RILT ..... 26

1.10 Other Methods for Increasing the Efficacy of Radiation Therapy for Lung Cancer ..... 28
1.11 Molecularly Targeted Agents and Lung Cancer Therapy ..... 29
1.11.1 Molecularly Targeted Agents and Radiotherapy for Lung Cancer ..... 30
1.12 PI3 –Kinase Inhibitors and Lung Cancer ..... 30
1.13 PI3-Kinase Inhibitors Evaluated in this Thesis ..... 31
1.14 Aims of this thesis ..... 34
2 MATERIALS AND METHODS ..... 39
2.1 Animal Models ..... 39
2.2 Plethysmography and Physical Assessment of Mice ..... 40
2.3 Radiotherapy and Dosimetry ..... 42
2.3.1 Cabinet Irradiation ..... 42
2.3.2 Image Guided Radiation ..... 43
2.4 Drug Administration ..... 47
2.4.1 Nelfinavir ..... 47
2.4.2 Bleomycin ..... 47
2.4.3 BEZ and BKM ..... 47
2.5 Tissue Analysis ..... 48
2.5.1 Western Blot Analysis – Non-irradiated tissue ..... 48
2.5.2 Histopathology – Irradiated tissues ..... 49
2.6 Imaging ..... 50
2.6.1 Computed Tomography (CT) ..... 50
2.6.2 Magnetic Resonance Imaging (MRI) ..... 51
2.7 Image Analysis ..... 56
2.8 Statistical Analysis ..... 59

3 PRELIMINARY STUDIES ..... 61
3.1 Introduction ..... 61
3.2 Preliminary Studies - C57BL6 Mice ..... 62
3.2.1 Experiment RT ..... 62
3.2.2 Experiment NFV ..... 70
3.3 Preliminary Studies – CBA Mice ..... 76
3.3.1 Introduction ..... 76
3.3.2 Experiment RT2 ..... 77
3.3.3 Experiment BLM ..... 81
3.3.4 Experiment NFV2 ..... 87
3.4 Discussion ..... 92
4 PI3K/AKT INHIBITION AND RADIATION ..... 96
4.1 Introduction ..... 96
4.2 Quantification of changes in pAKT in normal tissues following PI3K inhibition ..... 97
4.2.1 Rationale ..... 97
4.2.2 Results ..... 97
4.2.3 Discussion ..... 99
4.3 RT + BKM vs RT + BEZ ..... 100
4.3.1 Rationale ..... 100
4.3.2 Results ..... 100
4.4 Discussion ..... 117
5 PI3K/AKT INHIBITION AND IGRT ..... 121
5.1 Introduction ..... 121
5.2 Single Fraction IGRT ..... 122

5.2.1 Rationale....122
5.2.2 Results....123
5.3 Fractionated IGRT +/- BKM....138
5.3.1 Rationale....138
5.3.2 Results....139
5.4 Intermodality Comparison of Single versus Fractionated Experiments....151
5.4.1 Rationale....151
5.4.2 Results....151
5.4.3 Discussion....156
5.5 Chapter Discussion....156
6 DISCUSSION....161
7 REFERENCES....172
A.1 Appendix 1 – Dosimetric Characterisation of Irradiation Systems....192
A.2 Appendix 2 – Publications and Presentations....208
A.3 Appendix 3 –Plethysmography....211

# LIST OF FIGURES

## Chapter One

1.1 Study Schema - General

## Chapter Two

2.1 Plethysmographic Setup

2.2 SARRP Dosimetry

2.3 SARRP Setup for IGRT

2.4 MRI Sled and Birdcage Coil

2.5 Sample Coronal and Axial Slices of SEMS MRI

2.6 DCE-MRI Model Fitting

## Chapter Three

3.1 RT Experimental Schema

3.2 Animal Weights for Study RT

3.3 Breathing Rates for Study RT

3.4 SEMS Image Quality

3.5 Image Segmentation in ITK-Snap

3.6 Alveolitis for Study RT

3.7 NFV Experimental Schema

3.8 Animal Weights for Study NFV

3.9 Breathing Rates for Study NFV

3.10 Respiratory Motion Artefact versus Pneumonitis on MRI

3.11 Alveolitis for Study NFV

3.12 RT2 Experimental Schema

3.13 Animal Weights for Study RT2

3.14 Breathing Rates for Study RT2

3.15 RILT at 16 weeks on CT

3.16 BLM Experimental Schema

3.17 Breathing Rates for Study BLM

3.18 Coronal DCE-MRI

3.19 DCE-MRI iAUC Plot

3.20 Alveolitis for Study BLM

3.21 Pneumonitis on H&E Stained Lung Section

3.22 NFV2 Study Schema

3.23 Breathing Rates for Study NFV2

3.24 Intermodality RILT Incidence and Severity

## Chapter Four

4.1 pAKT Study Schema

4.2 AKT-phosphorylation in Normal Tissue

4.3 Quantification of AKT and pAKT in Normal Tissues

4.4 BEZ-BKM Study Schema

4.5 Toxicity

4.6 Breathing Rates for Study BEZ-BKM

4.7 Multi-modality Images of RILT 20 weeks following RT + BEZ

4.8 Sagittal DCE-MRI

4.9 Modelled DCE-MRI Acquisition and Analysis

4.10 Pharmacokinetic DCE-MRI Analyses

4.11 CT Lung Densities versus Time and RILT

4.12 Alveolitis for Study BEZ-BKM

4.13 Oesophagitis

4.14 Intermodality RILT Incidence and Severity

4.15 Comparison of RILT on CT, MRI and Histopathology

## Chapter Five

5.1 IGRT Study Schema

5.2 Animal Weights for IGRT

5.3 Breathing Rates for Study IGRT

5.4 RILT Score on SEMS MRI

5.5 Signal versus Time and RILT

5.6 Scoring RILT on ANGIO

5.7 iAUC versus Time

5.8 IGRT Raw Signal versus Time Curves

5.9 Mild to Moderate RILT Signal versus Time Curves

5.10 Consolidated Lung on CT and MRI

5.11 Gross Pathology

5.12 Histopathology

5.13 Alveolitis for Study IGRT

5.14 IGRT Case Study

5.15 IGRTfx Study Schema

5.16 Animal Weights for IGRTfx

5.17 Breathing Rates for Study IGRTfx

5.18 IGRTfx Raw Signal versus Time

5.19 Mild to Moderate RILT Signal versus Time Curves

5.20 CT Density (HU) versus RILT for IGRTfx +/- BKM

5.21 IGRTfx Case Study

5.22 Alveolitis for Study IGRTfx

5.23 IGRTfx Histopathology

5.24 Fibrosis for Study IGRTfx

5.25 Multi-modality RILT

5.26 Summary of RILT on CT, MRI and Histopathology

# LIST OF TABLES

## Chapter One

1.1 Literature citing Hemi-thoracic Mouse Irradiation

1.2 Oncologic Mechanisms and their Anti-tumoural Targets

1.3 Table of Longitudinal Imaging Studies

## Chapter Three

3.1 Table of Animals Evaluated at each Time Point in Study RT

3.2 Population Mean (range) Weights of Animals in Study RT

## Chapter Four

4.1 Change in Phosphorylation of AKT Following BEZ or BKM Administration

4.2 Proportion of Mice Demonstrating RILT

## Chapter Five

5.1 MRI Acquisition in Study IGRT

5.2 Inter-study RT versus RT + BKM Comparisons

## LIST OF ABBREVIATIONS

| | |
|---|---|
| 3D | Three-dimensional |
| 4D | Four-dimensional |
| 3D-CRT | Three-dimensional conformal radiotherapy |
| 4DCT | Four-dimensional computed tomography |
| µL | microliters |
| AAPM | American association of physicists in medicine |
| AIF | Arterial input function |
| AKT | Protein kinase B |
| Ant | Anterior |
| ARR | Association for Radiobiology Research |
| ASTRO | American Society for Radiation Oncology |
| ATM | Ataxia telangiectasia mutated |
| ATR | Ataxia telangiectasia and Rad3-related |
| AU | Arbitrary units |
| AUC | Area under the curve |
| $B_1$ | Radiofrequency energy field applied perpendicular to the longitudinal axis ($B_0$) to perturb the magnetization |
| BEZ | NVP-BEZ235, Dactolisib |
| BKM | NVP-BKM120, Burparlisib |
| BL | Baseline |
| BLM | Bleomycin |
| BPM | Breaths per minute |
| CBCT | Cone beam computed tomography |
| CF | Cystic fibrosis |

| | |
|---|---|
| CHART | Continuous hyper-fractionated accelerated radiotherapy |
| CHARTWEL | Continuous hyper-fractionated accelerated radiotherapy weekend-less |
| CIRT | Cancer Imaging and Radiation Therapy |
| COPD | Congestive obstructive pulmonary disease |
| CT | Computed tomography |
| DCE | Dynamic contrast enhanced |
| Dpi | Dots per inch |
| EBUS | Endobronchial Ultrasound |
| ECG | Electrocardiogram |
| ECL | Enhanced chemoluminescence |
| EGFR | European organisation for research and therapy of cancer |
| ERK | Extracellular signal regulated kinases |
| ESTRO | European Society for Radiotherapy and Oncology |
| ETOH | Ethanol |
| FA | Flip angle |
| FaDu | Human epithelia cell line isolated from squamous cell carcinoma of the hypopharynx |
| Fatsat | Fat saturation |
| fMRI | Functional magnetic resonance imaging |
| FOV | Field of view |
| FWHM | Full width half maximum |
| GCPR | G-protein-coupled receptors |
| Gd-DTPA | Gadolinium (MRI contrast agent) |
| GRE | Gradient echo |
| g | Gram |

| | |
|---|---|
| GUI | Graphical user interface |
| Gy | Gray |
| H&E | Haematoxylin and eosin |
| HIF-1 | Hypoxia-inducible factor 1-alpha |
| HIV | Human immunodeficiency virus |
| HPI | HIV protease inhibitor |
| HR | Hazard ratio |
| HSP90 | Heat shock protein 90 |
| HU | Hounsfield units |
| Hyp-hyp | Hypnorm-hypnovel (anaesthetic given in combination of 1:1:6 with sterile water) |
| Hz | Hertz |
| iAUC | Initial area under the curve |
| IGRT | Image guided radiation therapy |
| IMRT | Intensity modulated radiation therapy |
| IL | Interleukin (IL-1, IL-6) |
| IP | Intra-peritoneal |
| IR | Irradiations (*normally used for ionizing radiation) |
| ITK-SNAP | Imaging tool kit – snap |
| Kep | Exchange rate constants |
| Kg | Kilogram |
| $K^{Trans}$ | Vascular transfer constant |
| kV | Kilo-voltage |
| L | Left |
| LHS | Left hand side |

| | |
|---|---|
| LKB | Lyman-Kutcher-Burman |
| LLP | Liverpool lung protocol |
| MAPK | Mitogen-activated protein kinase |
| mAs | milliampules |
| MEK | Mitogen-activated protein kinase |
| MIRO | Molecular imaging in radiation oncology |
| mg | Milligram |
| min | Minimum or minute |
| mL | Millilitres |
| MLD | Mean lung dose |
| MRI | Magnetic resonance imaging |
| msec | Millisecond |
| MTA | Molecularly targeted agent |
| mTOR | Mammalian target of rapamycin |
| MTT | Mean transit time |
| MV | Mega-voltage |
| NCRI | National cancer research institute |
| NFV | Nelfinavir |
| NPL | National physics laboratory |
| NSCLC | Non-small cell lung cancer |
| OEMRI | Oxygen enhanced magnetic resonance imaging |
| OIRO | Oxford institute for radiation oncology |
| pAKT | Phosphorylated protein kinase B |
| PBF | Pulmonary blood flow |
| PBMC | Peripheral blood mononuclear cell |

| | |
|---|---|
| PBS | Phosphate buffered saline |
| PBV | Pulmonary blood volume |
| PET | Positron emission tomography |
| PFA | Paraformaldehyde |
| PI3K | Phosphoinositide 3-kinase |
| PK | Pharmacokinetic |
| PO | Para orale (by mouth) |
| POP | Parallel opposed pair |
| Post | Posterior |
| pTEN | Phosphatase and tensin homolog |
| R | Right |
| RAS | Rat sarcoma |
| RAF | Rapidly accelerated fibrosarcoma |
| RGB | Red, green, blue |
| RF | Radiofrequency |
| RFA | Radiofrequency ablation |
| RHS | Right hand side |
| RILT | Radiation induced lung toxicity |
| RIPA | Radioimmunoprecipitation assay buffer |
| ROI | Region of interest |
| RT | Radiation/Radiation therapy |
| RTi3 | Radiation therapy (inspire, inquire, innovate) conference |
| RTOG | Radiation therapy and oncology group |
| SABR | Stereotactic ablative body radiotherapy |
| SARRP | Small animal radiation research platform |

| | |
|---|---|
| SCLC | Small cell lung cancer |
| SEMS | Spin echo multi-slice |
| SI | Signal Intensity |
| SPGR | Spoiled gradient recalled acquisition |
| SQ | Squamous cells |
| SSFP | Steady state, free precession |
| Sup | Superior |
| T1 | Also referred to as spin lattice relation time, is a basic MRI sequence that relies on the longitudinal relaxation of a tissue's net magnetization vector. It has a short time to echo and time to repetition |
| T2 | A basic MRI pulse sequence that relies on the transverse relaxation (spin-spin relaxation) of the net magnetization vector. It has a long time to echo and time to repetition |
| T2* | Refers to a time constant in MRI describing the exponential decay of signal due to spin-spin interactions |
| T24 | Human bladder carcinoma cell line |
| TBNA | Trans bronchial needle aspiration |
| TE | Echo time |
| TKI | Tyrosine-kinase inhibitor |
| TR | Repetition time |
| UTE | Ultra short time to echo |
| V20 | Volume of lung treated with 20 Gy |
| VATS | Video assisted thoracic surgery |
| VEGF | Vascular endothelial growth factor |
| VEGFR | Vascular endothelial growth factor receptor |
| Vep | Fractional extravascular extracellular volume |
| VNMRS | Varian nuclear magnetic resonance systems |

| | |
|---|---|
| Vp | Fractional plasma volume (perfusion) |
| WT1 | Solid Water |

# Chapter 1

## *Introduction*

# 1 INTRODUCTION

## 1.1 Lung Cancer

Lung cancer is the second most frequently diagnosed cancer and is a leading cause of cancer deaths in the United Kingdom. It is the fourth most common cancer in Europe after breast, bowel and prostate cancers, and the most common cancer diagnosed worldwide with over 1.8 million cases and 1.59 million deaths reported in 2012 alone. Two-thirds of patients are diagnosed at a late stage, and as a result, lung cancer has one of the lowest survival rates of all cancers. In the UK, nearly 50% of patients present with Stage IV non-small cell lung cancer (NSCLC) or small cell lung cancer (SCLC) extensive disease. Survival decreases as the stage at presentation increases. Approximately 73% of patients who present with Stage I disease survive one year following diagnosis and less than 6% who present with Stage III disease survive more than one year (1). In addition to improved screening programs to reduce the number of lung cancer related deaths, improved therapies at all stages of presentation are urgently needed.

Estimates of worldwide incidence, mortality and prevalence of 26 cancers in the year 2012, are available in the GLOBOCAN series of the International Agency for Research on Cancer (2-4). A summary of the results are presented by Parkin et al (4) and includes the geographic variation between 20 large “regions” of the world. Overall, there were 10.9 million new cases, 6.7 million deaths and 24.6 million persons alive with cancer (within 3 years of their diagnosis) in 2012. The most commonly diagnosed cancers were lung, breast and bowel; the most common causes of cancer death were lung, stomach and liver. Of the two main subcategories of primary lung cancer (NSCLC and SCLC), NSCLC accounts for approximately 80-85% of all cases (5).

The detection of lung cancer at an early stage may result in improved outcomes. However, there are currently no lung cancer screening programs in the UK. According to Cancer Research UK (CRUK), lung cancer screening is currently not recommended because there is a lack of sensitive assays, only a small number of cancers would be detected and the tests involved in such screening programs carry significant cost and risk (1). It is suggested that for screening to be effective a simple, quick, inexpensive and risk-free test would be required. Tests such as X-rays do not usually detect early lung cancers, and expose patients to ionizing radiation. A recent study by the UK Health Technology Assessment programme evaluated the discrimination of the Liverpool Lung Project (LLP) risk model and demonstrated its predicted benefit of stratifying patients for CT screening by using data from three independent studies from Europe and North America (6). However, prospective studies are required to further validate the performance of this model and determine the optimal population risk thresholds for initiating lung cancer screening (for example, people who smoke, or have chronic obstructive pulmonary disease) (7). In Canada and the USA, researchers are using clinical trials to study the usefulness of chest X-ray and low dose CT scans to screen for lung cancer (8-10). The risks associated with exposure to radiation from CT versus X-rays are also currently being evaluated (11, 12).

Lung cancer is most common in people over the age of 60, and linked to lifestyle factors (smoking, occupational exposures, radiation) in approximately 89% of cases diagnosed in the UK. Although lung cancer mortality rates have more than halved for men in the UK since the 1970's, it has increased by 60% for women over the same period. This largely reflects the change in smoking behaviour in men and women over the last 30 to 40 years (1). Currently it is believed that the increase in risk of developing lung cancer for smokers compared to non-smokers is 20-25 times higher in males and 10-12 times higher in females in most age groups worldwide (13). Worldwide age-specific lung cancer incidence rates are

1.5-2.3% higher in developed countries, primarily reflecting the longer life expectancy and differences in age distribution between more and less developed countries. There are some key epidemiological differences in lung cancer incidence with the incidence of lung cancer on the decline in more developed countries for males, but at a plateau for females. Again, this is reflective of the trends in smoking status in these countries. In less developed countries the rates of lung cancer is predicted to increase with the endemic use of tobacco.

Among women, lung cancer mortality rates are increasing in countries such as Australia, China, Germany, Hungary, the Netherlands, Poland and Sweden. In China, Israel and Romania, lung cancer is on the rise for both sexes. However, overall incidence is on the decline in Hong Kong, Japan, Russia, Singapore and the UK, due in part to increased awareness of the effects of smoking. Lung cancer remains the most prominent cause of premature mortality among males and females in North America at 6.7% and 6.8% respectively. Lung cancer mortality remains lowest in African countries due to a lower prevalence of smoking and lower life expectancy due to infectious diseases (13).

Of the two main subtypes of primary lung cancer, SCLC accounts for approximately 15% of all lung cancer presentations, and > 95% of patients diagnosed are smokers. Because it is systemic in nature, SCLC is treated primarily with chemotherapy (14). NSCLC, the most predominant subtypes of which are squamous cell carcinoma (SCC) and adenocarcinoma (Adeno), is much more common, and can be treated with surgery, chemotherapy, radiation therapy or a combination of two or more treatment modalities. SCC is predominantly related to smoking manifesting as large, centrally located tumours, whereas adenocarcinomas are more commonly found peripherally. In most countries, SCC is more common in men, accounting for roughly 40-45% of all cases, whereas adenocarcinomas are more common in women, accounting for approximately 30% of all lung cancer in women.

Radiotherapy can be used to treat early stage NSCLC when surgery is not advised or declined. It can also be used with or without chemotherapy in more advanced disease, when surgery is not feasible. Other indications for radiotherapy are following surgery to sterilise the tumour bed, before surgery (with chemotherapy) to reduce the tumour burden with the aim of rendering the tumour resectable and in very advanced cancers to palliate symptoms such as pain, bleeding, or cough.

## 1.2 Presentation and Diagnosis of Lung Cancer

In the UK, patients are usually referred by their general practitioner for diagnostic tests if there is a high suspicion of lung cancer. Patients present with symptoms that include persistent cough with or without haemoptysis, chest and/or shoulder pain, fatigue or energy loss, weight loss, shortness of breath, hoarseness, or finger clubbing (a change in the shape of the end of the fingers). Patients with advanced cancers may present with similar but more severe symptoms, or symptoms specific to the location and stage of their disease. These can include, lung infections (e.g., pneumonia) that do not resolve with antibiotics, pleural effusions causing shortness of breath, pain, weakness or paraesthesia in the arm and shoulder (resulting from tumours in the apex of the lung causing brachial plexopathy), or facial oedema caused by pressure on the superior vena cava. For lung cancers that have spread beyond the lungs, symptoms such as bone pain or swelling can occur in the regions to which the cancer has spread such as the brain or liver.

A chest X-ray is usually the first test performed, however this can only confirm lung changes or abnormalities and is usually followed up with a computed tomography scan (CT). Depending on the suspected stage of the cancer determined, further investigations will be carried out following the National Institute for Health and Care Excellence (NICE) guidelines. If early stage cancer is suspected, a positron emission tomography-CT (PET-CT)

will be performed to demonstrate areas of active cancer, in particular whether or not there is lymph node involvement. Whenever feasible, a biopsy is performed to determine the histological type of cancer present, which will influence the choice of additional investigations. These may include bronchoscopy, endobronchial ultrasound-guided transbronchial needle aspiration (EBUS-TBNA) or magnetic resonance imaging (MRI) which are used to stage the tumour.

Staging describes the extent of cancer has growth and spread. The TNM staging system is the guide used most frequently to stage and describe cancers. It is maintained by the American Joint Committee on Cancer (AJCC) and the Union for International Cancer Control (UICC). The TNM guide rates the extent of the primary tumour (T), any nodal disease (N) and any metastases (M) found on diagnostic tests (15-21). For lung cancer, Stage I indicates localised disease, that is small and limited to a single area of the lung, Stage II and III are locally advanced cancers, with a tumour larger than 5 cm and/or extending to more than one lobe and /or spread to the lymph nodes, chest wall, diaphragm, mediastinal pleura, parietal pericardium, heart, trachea, oesophagus, or the laryngeal nerve. Stage IV lung cancer indicates the cancer is either in both lungs, has spread to another part of the body (e.g., liver or bones), or has caused a malignant pleural or pericardial effusion (19, 22). A full diagnostic work-up includes contrast-enhanced CT to demonstrate tumour anatomy, location and volume for staging (23) and PET-CT or mediastinal sampling to evaluate mediastinal lymph node involvement (24). A brain scan (CT or MRI) is usually performed in patients with SCLC to detect occult disease (24).

Additional diagnosis and staging exams may also include autofluorescence bronchoscopy and narrow band imaging (to detect early and pre-invasive lesions), mediastinoscopy (to complete staging of the mediastinum prior to thoracotomy) and systematic nodal dissection. Video-assisted thoracoscopy (VATS) is sometimes used to

obtain biopsies from the tumour mass, and for direct ascertainment of tumour invasion into the central mediastinal structures. VATS allows access to the hilar, aorto-pulmonary window, para-oesophageal and inferior pulmonary ligament stations (24).

## 1.3 Treatment of Lung Cancer

To determine the most appropriate treatment strategy, the intent of treatment must be defined as radical, given with the intent of substantial survival improvement which may or may not amount to a cure, or palliative, given with the intention of improving quality of life and the extension of life duration as a secondary benefit. The intent of treatment will depend on diagnosis, stage and comorbidities.

Treatment of lung cancers can be with a single modality, such as surgery, chemotherapy, radiofrequency ablation (RFA), radiotherapy, molecularly targeted agents, or a combination of two or more treatment modalities. According to a guideline on the radical management of patients with lung cancer (24), a document published in 2010 by the British Thoracic Society, definitive surgical resection is the treatment of choice whenever feasible. When not feasible, treatment with radical radiotherapy or chemo-radiotherapy should be considered but still requires a pre-treatment diagnosis. The assessment of lung function is required in the preoperative assessment of risk of operative mortality, the assessment of potential post-resection dyspnoea, as well as to determine whether or not a patient is at increased risk of radiation morbidity, especially as it relates to pre-existing conditions. A large number of studies have been published that address the contribution of lung function to operative mortality risk, most citing an optimum cut-off of postoperative predicted forced expiratory volume in one second (FEV1) of 40% (25).

Patients with poor lung function may encounter difficulties with radiotherapy, as they may not easily tolerate lying flat for ten to thirty minutes while treatment is administered

(26-29). Safe lower limits of respiratory function for radical radiotherapy are not definitively established (28, 30-36). However, knowledge of the risks of radiotherapy can be used to guide treatment planning. For example, in an effort to avoid irradiating normal lung, beam path-lengths may be placed through areas of radiologically abnormal lung (37). Radiotherapy planning parameters such as mean lung dose and V20 (the volume of the lung expressed as a percentage of total lung volume minus the tumour volume, receiving $\geq 20$ Gy), are currently the most effective tools for predicting radiation pneumonitis (26, 27, 38, 39), in both NSCLC and SCLC (40). These parameters are estimated on the basis of the sensitivity of a population of patients, meaning their predictive value for individual patients is limited (41). This emphasizes the need to be able to better predict, mitigate or detect radiation induced lung toxicities for patients undergoing radical radiotherapy.

### 1.3.1 Surgery for Lung Cancer

Surgery for lung cancer may involve the removal of a single lobe of the lung (lobectomy), a sleeve resection (which involves the removal of the affected section of a bronchus and any surrounding cancer within the lobe), or the removal of an entire lung (pneumonectomy) if the tumour is in the central area of the lung and involves two left or three right lung lobes. Alternatively, a wedge resection may be performed that removes a section of one or more lobes of the lung. This surgery is used in very early stage cancers that involve only a small region of lung tissue (42). Video-assisted thoracoscopic surgery (VATS) has the advantage that it is less invasive and so reduces the intensity and duration of post-operative recovery.

### 1.3.2 Chemotherapy for Lung Cancer

Preoperative (neoadjuvant/induction) chemotherapy is used to downstage the tumour in preparation for surgery, or to control micrometastatic disease. For Stage II and III NSCLC,

there is a strong body of evidence supporting the use of postoperative adjuvant chemotherapy with a hazard ratio (HR) of overall survival ranging from 0.74 to 0.89 (43-48). Currently, the most widely adopted post-operative chemotherapy regimen in the UK is the cisplatin-vinorelbine combination.

Other treatment modalities that are currently used in the treatment of lung cancer include molecularly targeted agents such as epidermal growth factor receptor (EGFR) inhibitors (e.g. erlotinib and gefitinib) and anaplastic lymphoma kinase-positive (ALK) inhibitors (e.g. crizotinib).

### 1.3.3 **Radiotherapy and Chemo-Radiotherapy for Lung Cancer**

As discussed above in Section 1.3, radiotherapy plays a role in the treatment of lung cancer in both radical and palliative settings. Several published systematic reviews have reported superior survival for patients treated with chemotherapy plus radiation compared to radiation therapy alone (49). A meta-analysis of six concurrent chemo-radiotherapy trials reported that increasing radiation dose (as opposed to increasing chemotherapy) improved both local control and overall survival; however the optimization of radiotherapy dose-fractionation regimens continues (50).

The NSCLC Collaborative Group reported on 22 trials (3033 patients) and showed a 13% reduction in risk of death, equivalent to an absolute benefit of 5% at 5 years, when cisplatin-based chemotherapy was combined with radiation therapy compared to radiation therapy alone (44, 49, 51). Patients for whom chemotherapy is contraindicated or who are of poor performance status are offered radical radiotherapy alone. For locally advanced (Stage II or III) lung cancers, conventional radiotherapy with doses of 60 Gy delivered in 2 Gy fractions is associated with 50-60% local control, median survival rates of approximately 15-17 months and five year survival rates of 13-16% (52).

### 1.3.4 Other Treatments for Lung Cancer

Radiofrequency ablation can be used for patients with primary tumours that are less than 3-3.5 cm as it is a minimally invasive procedure suitable for both radical and palliative cases. Medium-to-long-term follow up of patients who have undergone RFA have shown that survival is similar to other non-surgical treatments (53-55). Promising results for RFA have recently been reported: the survival rate for Stage I NSCLC was 78% at 1 year, 57% at 2 years, 36% at 3 years, 27% at 4 years and 27% at 5 years (53).

Recent advances in the field of radiation therapy with hypo-fractionated high-dose proton beam therapy show competitive survival results (56), and this is also the case with stereotactic radiosurgery (57). A combination of RFA and conventional radiotherapy has already shown better local control and survival rates than radiotherapy alone, with cumulative survival rates of 50% and 39% at the end of 2 years and 5 years, respectively (58).

## 1.4 Challenges using radiotherapy to treat lung cancer

Regardless of the intent of treatment with radiotherapy, radiation induced normal tissue toxicity (RILT), and lung tumour radioresistance pose serious limitations to the effectiveness of radiotherapy for lung cancer (59). Doses in excess of 100 Gy biologically equivalent dose (BED) are needed to achieve total control in 90% of NSCLC (60). Although some studies have demonstrated the effectiveness of dose escalation in the treatment of lung cancer, a recent Radiation Therapy Oncology Group (RTOG) study (RTOG0167) reported disappointing results, as 74 Gy in 37 fractions showed no additional benefit over 60 Gy in 30 fractions. Critics of the RTOG0167 (60) have posited that the high dose arm failed because of the protracted overall treatment time. It has also been pointed out that larger than necessary planning target volumes (PTV) were used, leading to increased normal tissue

toxicity, as well as suboptimal target volume delineation when FDG-PET was not incorporated (60, 61). In short the dose may have been escalated but the treatment itself was sub-optimal.

A major challenge in radiotherapy for lung cancer is respiratory lung motion, which requires the use of large treatment volumes to ensure coverage of the tumour throughout the respiratory cycle. However, over the last few decades several advances have been made in the planning and delivery of radiotherapy that make it feasible to direct high doses of highly conformal radiotherapy to lung targets. Some of these technical advances include the introduction of FDG-PET for more accurate target delineation, the use of 3D conformal radiotherapy (3D-CRT), 4-dimensional CT (4DCT) imaging, image guided radiotherapy systems that can perform real time imaging at the treatment unit in 2-, 3- or even 4-D (e.g., electronic portal image devices (EPID), cone beam CT (CBCT), respiratory correlated cone beam CT (RC-CBCT)), and intensity modulated radiotherapy (IMRT). Other advances include the use of hyper- or hypo-fractionated dose schedules e.g., stereotactic ablative body radiotherapy (SABR) (62-75). The rationale for hyper-fractionation is that the shorter time interval between treatment deliveries reduces the time for tumour cell repopulation or repair. In contrast, hypo-fractionated schedules facilitate the delivery of ablative doses in a limited number of fractions with an extended break in between allowing for normal tissue repair (76-82).

Using advanced radiotherapy techniques, dose escalation has been possible in early phase studies of Stage I-III NSCLC that indicate dose is a significant predictor of local control and survival (83-85). Although dose escalation studies investigating doses greater than 60 Gy have not established the optimal radiotherapy dose that achieves a balance between local control and side effects (84, 86, 87), the use of hypo-fractionated stereotactic radiotherapy in patients with Stage I or II disease is associated with local control rates of 80-

98% and overall survival of 52-83% at 2-5 years (88-97). The largest series to date reported a 5-year overall survival of 71% and local control rate of 84% (96, 97). A variety of doses and fractionations have been used, ranging from 30 Gy in two fractions to 75 Gy in 22 fractions (88-91, 93-97) .

A problem that improved radiotherapy technique may not be able to overcome is inherent tumour radioresistance. Radioresistant clones may be able to survive radiotherapy, and cause local recurrence of NSCLC (5, 98). In a review published by Le Pechoux et al, it has been suggested that while many recent advances in functional imaging and radiation therapy technology account for improved outcomes, strategies for overcoming radioresistance-related treatment failure in NSCLC are also needed (99). One proposal is that the concurrent use of molecularly targeted agents may reduce radioresistance (100, 101).

## 1.5 Radiation Induced Lung Toxicity (RILT)

The corollary of dose escalation is that in clinical trials, escalating radiation dose has resulted in dose limiting RILT (84). RILT consists of two phenomena: early acute pneumonitis and latent chronic fibrosis. Radiation pneumonitis is an early inflammatory reaction involving alveolar cell depletion and inflammatory cell accumulation in the interstitial space occurring within 12 weeks of lung radiotherapy (102). Histopathological findings of radiation pneumonitis are described as diffuse alveolar damage including oedema of the alveolar walls due to increased vascular permeability and exudation of proteins in the alveolar spaces (102, 103). Within a few weeks, pneumonitis may be followed by chronic fibrosis. Radiation induced lung fibrosis is characterised by the accumulation of fibroblasts, myofibroblasts, inflammatory cells and extracellular matrix proteins such as collagen (104, 105). The work presented in this thesis is concerned primarily with the early detection of radiation pneumonitis.

RILT is assessed clinically according to the RTOG/EORTC criteria, classified from Grade 0 to 5, depending on symptoms at presentation which may include cough, dyspnoea, fever, chest pain, infiltrative changes on x-ray or radiographic changes alone. Radiographically, radiation pneumonitis presents as diffuse opacities or nodular patterns on chest X-ray, and as regions of increased density, possibly associated with pleural, interlobar or pericardial effusions on CT (106-111).

The exact incidence of radiation pneumonitis varies widely between reports and depends on radiation technique, awareness, methods of reporting, and the evaluation of symptoms themselves (102). It is possible that because it is difficult to assess, the development of radiation pneumonitis is sometimes over-looked. Some authors report the incidence of moderate to severe radiation pneumonitis as low as 10-20% following irradiation or chemoradiation (28). Moreno et al (112), suggest the incidence of pneumonitis of RTOG Grade 3 or greater following 3D-CRT ranges from 2 to 31% (113-115), and is even higher following combined modality treatments (116-118). Between 50 and 90% of radiation therapy patients develop radiographic and pulmonary test abnormalities suggestive of radiation pneumonitis (107, 119).

Symptoms of radiation pneumonitis can appear similar to, or can be masked by, chronic obstructive pulmonary disease (COPD), infection, or pneumonia (27, 120-122). Acute pneumonitis can be life-threatening. Treatment of pneumonitis is aimed primarily at reducing inflammation with steroids (such as prednisone), which are given until the inflammation subsides and are then decreased. If identified early and treated promptly, most patients do well (123-126). If untreated, acute pneumonitis can progress to permanent fibrosis (106). RILT increases in frequency with increased radiation dose (26, 127, 128), increased volume of the lung irradiated (115), some combinations of chemotherapy and

radiation (28, 33, 125, 126, 129, 130), previous irradiation (125) and steroid withdrawal (131, 132).

## 1.6 Current Methods to Predict RILT

At present accurate models for RILT prediction are lacking and current risk assessment typically relies on physical dosimetric parameters such as mean lung dose (MLD) and percentage of lung volumes that exceed a threshold (such as V20) (27, 41, 116). As these parameters are based on population data, their predictive accuracy for individual patients is limited. It has been suggested that the MLD does not adequately take into account the effects of high doses (hot spots) within the irradiated volumes and a dosimetric alternative to MLD has been proposed for the prediction of radiation pneumonitis risk (133). Tucker et al recommended using the effective dose computed from the Llyman-Kutcher-Burman (LKB) model to account for small regions of high dose to better predict for Grade III or greater pneumonitis (134). The risk of ≥ Grade III pneumonitis increases steeply as a function of MLD in radiotherapy treatments using two or three beams only, however, in cases of more complex beam arrangements and heterogeneous dose distributions, the correlation between incidence of radiation pneumonitis and MLD becomes less convincing. Therefore the need for improved models to predict for moderate to severe radiation pneumonitis following modern radiotherapy is evident. Additionally, there may be clinically assessed trade-offs to be considered when planning and accepting a radiotherapy prescription. As such, improved patient specific methods of early detection and mitigation are required.

A known patient-specific risk factor for developing RILT following definitive radiation or chemo-radiation is cardiac comorbidity. In a retrospective analysis of 259 patients with locoregional lung cancer, 44% of the 75 patients who presented with cardiac comorbidities prior to radiotherapy or chemo-radiotherapy developed RILT. This is equivalent to an odds

ratio of developing RILT of 2.58 ($P < 0.01$) (135). Because patients with cardiac comorbidities are often ineligible for surgical treatments, the impetus to minimize and/or detect RILT early is very important in this patient population.

At the cellular level, radiation pneumonitis is characterized by lympholytic alveolitis resulting from inflammatory infiltrates of mononuclear cells (macrophages, monocytes and lymphocytes) arising from the vascular compartment into the pulmonary interstitium and alveolar spaces of the lung (136). The immediate cellular response to RILT involves the expression of inflammatory cytokines such as TNF-α, IL-1, and IL-6 which are produced locally and bind to receptors or stimulate cells distant from the field of injury by entering the circulation. These observations have prompted investigators to look to circulating biomarkers as predictors of RILT (136-138).

Several candidate biomarkers have shown potential in clinical and pre-clinical trials. In early studies, patients that developed RILT were more likely to have had elevated levels of TGF-β1. However, further investigations by Evans et al, have suggested that TGF-β1 is not predictive of RILT, but is associated with a higher incidence of the condition (139). Other circulating markers that have shown promising (or mixed) results in clinical studies are the interleukins IL-1 and IL-6 (140-142), and KL-6 (138, 143, 144). Although the use of cytokines as predictive biomarkers of RILT is not yet validated, it is possible that with complementary information from imaging and clinical assessments a more complete model for predicting RILT may be developed.

## 1.7 Imaging Methods to Detect RILT

### 1.7.1 Computed Tomography

Currently available imaging modalities can be used to assess regional lung damage, reduced lung function and potentially predict clinically relevant outcomes. The radiologic

appearance of radiation pneumonitis is variable inflammation or contraction and pleural thickening and is generally associated with increased lung density on high resolution CT imaging (145). The use of CT imaging to detect lung changes following radiotherapy was introduced in 1983 by Van Dyk et al at the Princess Margaret Hospital in Toronto (118). The investigators proposed that CT imaging could be used as a prognostic indicator of RILT by performing serial CT imaging in a single patient. The scans suggested an increase in lung density 73 days following hemi-body irradiation. However due to the difficulties in performing serial CT imaging on palliative patients these investigators performed further investigations using pre-clinical CT imaging, comparing control animals to others irradiated to 11 or 14 Gy and followed them for 14 and 24 weeks. An increase in lung density of 10% to 15% was observed in the irradiated mice (118). However in their concluding statements Van Dyk and collaborators suggested that because the most significant findings occurred in mice only weeks before death due to RILT, it may be that measurable changes on CT do not occur early enough to be useful as a prognostic indicator of radiation pneumonitis.

In 1987 Mah and Van Dyk (119), undertook a clinical study of 54 patients who underwent CT imaging before and after radiotherapy. It was shown that CT imaging has potential as a quantitative measure of lung damage. By assessing the lung density of irradiated and non-irradiated lung regions, they found 36 of 54 patients showed lung damage on CT with a mean relative increase in lung density of $0.20 \pm 0.10$ in the irradiated areas, compared to mean density changes of $0.02 \pm 0.09$ in the non-irradiated lung regions. The magnitude of the increase in lung density showed good correlation with CT findings observable on visual inspection. Eighteen patients without visible lung damage also had increases in lung density on CT imaging of $0.00 \pm 9\%$ and $-5\% \pm 7\%$ in the irradiated and non-irradiated regions respectively. Based on this study, Mah and Van Dyk concluded that

an increase in average lung density of ≥ 5% is associated with the visible detection of radiation induced lung damage (119).

Further work is needed to define the value of CT for early prediction of radiation damage to the lungs, before it is adopted into routine clinical practise. To date the use of CT imaging to predict RILT has not been adopted in clinical practise. Several reasons may explain this, including uncertainty about the optimal timing of image acquisition, concerns over the administration of 'unnecessary' ionizing radiation to patients, and the variability in the appearance of radiation pneumonitis on CT.

The development of radiation pneumonitis varies widely amongst patients and is not always accompanied by clinical symptoms in its early stages, so that it is difficult to optimize the timing of CT imaging to predict RILT. According to Robbins et al, 50 to 100% of patients undergoing lung radiotherapy demonstrate acute lung injury on imaging, however only 5 to 35% of these patients present with symptoms (145). Longitudinal imaging has been used to detect radiation induced lung changes following, for example, dose escalation studies and treatments using stereotactic radiotherapy (146). However, this has been challenged by De Ruysscher et al (146), who have commented that in serial CT imaging studies variations in lung density may result from 'noise' or non-radiation related technical issues including respiration, individual patient changes unrelated to radiotherapy, or patient positioning. De Ruysscher et al studied 91 patients treated with radiation or chemo-radiation, who underwent CT at baseline and three months following treatment, aiming to distinguish between radiation induced lung density changes (determined using Hounsfield Units (HU)), and changes related to 'noise'. The results of this study showed that variations in lung densities were unrelated to radiation if the change in CT density was ≤ 0.5 HU/Gy. That is for a patient receiving 70 Gy, only alterations in lung density greater than 35 HU would be considered to be a result of radiation changes.

Another consideration when using CT to detect and predict RILT is the radiation dose from lung CT imaging which varies according to patient size and the technique used, but is in the range of 1.5-7 mSv (or 0.15 to 0.7 cGy absorbed dose) per scan. It is important to consider this additional radiation exposure when monitoring patients or undertaking studies to determine the best time point at which to assess and intervene in patients at greater risk of developing acute or late onset lung toxicity.

Alternative imaging modalities used to detect RILT clinically and pre-clinically have included hyper-polarized $^{129}$Xe MRI (147), $^{99}$mTc-DTPA lung scintigraphy (148, 149), hyper-polarized 13C-pyruvate MRSI (150, 151), and hyper-polarized $^{3}$He MRI (152). Recently MR imaging requiring no specialised equipment or gases has proven useful in the imaging of interstitial lung disease and in particular for imaging of inflammatory responses (153, 154). As radiation pneumonitis presents as an inflammatory response it stands to reason these imaging techniques may be useful in the diagnosis or early detection of radiation pneumonitis.

### 1.7.2 Magnetic Resonance Imaging

Until the development of modern MR imaging protocols that include features such as short echo times (TE), short acquisition times, the use of parallel imaging, and cardio-respiratory gating, lung MRI has been particularly challenging. Significant obstacles to the use of MRI to investigate lung pathology are the low-density of lung tissues resulting in poor signal, and cardiorespiratory motion. Also problematic are magnetic susceptibility artefacts at air-tissue interfaces which are distortions of the image that result- from microscopic variations in the magnetic field strength occurring near interfaces of substances of varying magnetic susceptibility. To overcome low signal to noise ratio (SNR), methods such as signal averaging or increasing voxel size to increase SNR can be used. The trade-offs of

using these solutions include significant increases in imaging time (to the extent it becomes clinically impractical) and the lack of ability to detect small lesions (such as new metastatic disease).

In patients, the issue of respiratory motion can often be overcome by using breath-hold sequences. Sequences must be designed to be short enough that patients can tolerate single or repeated breath-holds, usually of a maximum duration of 20 seconds. An important consideration when using breath-hold MRI is whether or not lung inflation affects signal intensity. In general signal intensity is higher at expiration as the relative density of protons in a voxel is increased and the bulk volume magnetic susceptibility difference is reduced as air is expelled. For images requiring a high contrast to noise ratio (CNR) between pulmonary vessels or nodules, full expiration is most suitable as this can provide a darker background (155). When breath-held sequences are not possible (e.g. in patients unable to tolerate breath-holding for 20-30 seconds) respiratory or spirometric triggering or gating can be used. This involves the synchronization of the image acquisition to the subjects' respiratory cycle, and the acquisition of a signal proportional to the respiratory state of the lung. This can be achieved using the MRI signal or external hardware such as respiratory bellows or active breathing control systems.

Three basic sequences have proven useful in overcoming some of the challenges of lung MRI, and are considered as platforms from which to develop specific MRI protocols. These three sequences are 1) spoiled gradient echo (SPGR or spoiled-GRE), 2) balanced steady state free precession (SSFP), and 3) fast spin echo (FSE) sequences, and have formed the foundation for MRI methodological development in this thesis. A spoiled gradient echo sequence is conceptually the simplest of these three pulse sequences. It is inherently T2* weighted and has multiple applications, with acquisitions available in both two and three dimensions, it can be acquired with or without fat saturation (fatsat). T2* relaxation refers

to the decay of transverse magnetization caused by a combination of spin-spin relaxation and magnetic field inhomogeneity. It is the main determinant of GRE sequence contrast which forms the basis of susceptibility-weighted (SW) imaging, perfusion imaging and functional MRI (fMRI). A heavily weighted T1 3D spoiled gradient echo image (SPGR) with a short TR and high flip angle (FA) will provide a starting point for any contrast enhanced structural imaging of the lung. The balanced steady state free precession (SSFP) sequence is structurally similar to the SPGR but refocuses the transverse magnetization at each end of the TR interval instead of spoiling it, to make more efficient use of the available magnetization. Using multi-slice or 3D SSFP sequences are a quick and contrast-free way to perform a pulmonary angiogram (a high resolution imaging sequence used to detect pulmonary embolism or arteriovenous malformations). The third imaging sequence, a fast spin echo (FSE) sequence uses spin echoes (the reappearance of the MR signal following free induction decay resulting from the rephrasing of the dephasing spins) instead of gradient echoes (an echo signal generated from a free induction decay produced by reversing the direction of the magnetic field gradient or applying balanced pulse before and after a refocusing RT pulse). To make this type of sequence suitable for rapid imaging requires breath-held or gated imaging, and a long echo train. The echo train (a series of 180° rephrasing pulses and their corresponding echoes) is generated by repeating the refocusing of the first spin so all lines in k-space are acquired in a single echo train. This lends itself to lung imaging because the train of 180 degree pulses refocuses any field inhomogeneities, so that all images become T2-weighted (in which fat appears dark and water appears bright) (155). At the Oxford Institute for Radiation Oncology, basic MRI sequence development, which included anatomical and functional sequences for comparison with CT and histopathology, began prior to and continued throughout the experiments described in this thesis.

#### 1.4.1.1 *Spin Echo Multi-slice Imaging*

A spin echo multi-slice (SEMS) sequence was developed with the view to optimising cardio-respiratory gating which involved, among other things, the development of user competence and consistency as well as the selection of the appropriate bandwidth for parenchymal imaging. In MRI, bandwidth defines how many frequencies will be encompassed in each image. An increased bandwidth can be used to image blood flow. However a decreased bandwidth helps to eliminate flow and motion artefact, which is more desirable for parenchymal imaging. As such, initial development experiments included repeat imaging to determine the optimal bandwidth for cardio-respiratory noise-reduction.

#### 1.4.1.2 *Dynamic Contrast Enhanced MRI (DCE-MRI)*

Dynamic contrast enhanced (DCE) MRI using Gd-DPTA (or similar) in a heavily T1-weighted 3D GRE sequence can provide a fully quantitative map of pulmonary blood volume (PBV), blood flow (PBF) and transit time (MTT), if a deconvolution with arterial input function (AIF) measured in the larger arteries is known (155). These basic pulse sequences can be further sensitized to physiological processes as signal can be modulated by respiration, blood flow, or inhalation of O2 to give functional information. Dynamic contrast-enhanced (DCE) perfusion imaging is considered the most robust MR technology for obstructive airway disease (153, 154). It reflects the effect of hypoxic pulmonary vasoconstriction, meaning that lung perfusion images may be regarded as a surrogate for lung ventilation. In this project, locally developed DCE-MRI sequences were introduced to describe parenchymal perfusion and optimized over the course of the experiments with the optimization of robust gating methods providing the greatest gains in image quality.

The interpretation of DCE-MRI can be undertaken using modelled or non-modelled methodologies. Non-model based analysis can be undertaken using area under the curve

(AUC) pharmacokinetics, where the AUC represents signal enhancement over time. Assuming linear pharmacokinetics with an elimination rate constant of 'K', one can show that AUC is proportional to the presence of contrast within a volume of tissue over time. In the case of lung inflammation (or alveolitis), an enhanced or sustained increase in signal might be associated with inflammatory response (156). In MRI imaging the iAUC (initial area under the curve) is a mixed parameter that can display correlations with the vascular transfer constant ($K^{Trans}$), fractional extravascular extracellular volume ($V_{ep}$), fractional plasma volume (perfusion: $V_p$), and ultimately an intractable relationship with all three. iAUC can also provide semi-quantitative measurement such as peak enhancement and information about initial wash-in gradients. Evelhoch et al (157, 158) suggested that iAUC relates to blood flow, vascular permeability and fractional interstitial space. Rukart et al and Walker-Samuel et al have attempted to characterise the relationship between iAUC and model-based parameters (159, 160).

Models selected for testing were based on work by Naish et al (161) who described the benefits of several models, including the classic Kety model which describes contrast agent diffusion between tissue components; the Tofts model which improves upon the Kety model by approximating the role of accumulation and contrast wash-out in the fractional extravascular extracellular volume ($V_{ep}$), under the assumption that the contrast agent is well mixed within the vascular plasma space; and the extended Tofts model which is better suited to tissues such as the lung that have intrinsically high blood volumes by applying an automatically defined arterial input function (AIF) component.

#### 1.4.1.3 *Pulmonary MR Angiography (ANGIO)*

The development of pulmonary MRI angiography (MRA) has facilitated the ability to generate a physiological record of blood flow. It is primarily used as an alternative to

invasive catheter angiography or CT angiography, as it confers the advantages of being less invasive and ionizing radiation free when examining arteries (162-164). MRA typically uses gadolinium to shorten the T1 of blood so that it is shorter than that of other tissues. Short TR sequences can be developed to produce bright images of blood. MRA can be flow-dependent or flow-independent. Flow dependent MRA takes advantage of the fact that blood is flowing within vessels to distinguish the vessels from static tissues. Flow independent MRA requires no contrast enhancement, and is based on the differences of T1, T2 and the chemical shift of the different tissues of the voxel. This method can be particularly advantageous in regions of slow flow, as found in patients with vascular diseases. Because MRA typically requires short acquisition times using parallel imaging or time-resolved techniques, when acquired on a high-T magnet, the resultant images not only have increased SNR, but also excellent spatial resolution. In looking for a quick, high resolution image that is affected minimally by variations in respiratory patterns, an MRA sequence developed for work outside of the context of this thesis was introduced into the sequences acquired and evaluated for the detection of RILT in general and radiation pneumonitis specifically.

## 1.8 Use of Pre-clinical Models in RILT Detection

Unlike COPD or cystic fibrosis, RILT is a stochastic event that occurs after treatment and, at present, is predicted imperfectly (106). Small animal irradiation technology is available (165), which permits regional RILT models in murine strains which have been well-characterized and are quite predictable and reproducible (166-169). Thus, small animal models provide a cost-effective platform to develop novel imaging in the context of RILT, and include histologic confirmation and/or invasive monitoring of physiology that would be impossible in patients irradiated for lung cancer. Determining the best way to use novel

imaging protocols in a predictable pre-clinical model will minimize burden to cancer patients and should expedite clinical translation of novel imaging protocols (170).

Murine models of RILT have been used for nearly four decades, with the majority of the work undertaken in C57BL, CBA, and C3H mouse strains. Early investigations used whole body and whole thorax irradiations, which have proven useful in the development of methods of RILT detection, the ability to differentiate between early and late phases of RILT, and the identification of mouse models that develop RILT on timelines and at doses similar to patients.

All of these mouse strains have demonstrated RILT following whole-thorax irradiation in single fraction doses ranging from 10 to 15 Gy. CBA mice display two phases of response to whole-thorax irradiation, which was first described by Travis et al as an early phase of pneumonitis and a later phase of fibrosis (171). C3H strains show similar responses to the CBA mice (172, 173). C57 strains tend to be resistant to pneumonitis, but show clear development of fibrosis often accompanied by pleural effusions; with the exception of the sub-strain C57L/J mice, which demonstrate pneumonitis between three and six months following radiation (174). According to Down et al (175), CBA mice tend to develop RILT on a similar timescale to humans, with RILT evident on CT imaging at 14 weeks following a single dose of 20 Gy. C57BL6 mice show a high propensity to early pulmonary injury on receiving as little as 10 to 15 Gy irradiation to the whole thorax.

Until recently most pre-clinical investigations of RILT used whole thorax lung irradiations, not single or partial lung irradiations. Radiation volume effects appear to be more significant than dose effect in the irradiation of murine lungs (176), and limited information exists in the literature as to the most effective dose to use to induce radiation toxicity in a single lung (175, 177, 178).

Whole body plethysmography is a well-established method of detection of lung damage which was initially established by Travis et al in the 1970's. It has been used subsequently by several groups to assess whole body irradiation toxicity including Down (175), Liao (176), and Nicholas (179). A significant increase in breathing rate, not related to age, correlates with the loss of lung function following thoracic irradiation (179-182).

In the mid 1990's tools became available to further refine radiation techniques and preliminary investigations into hemi-thoracic and partial lung irradiations began to appear in the literature. Liao et al undertook to define volume effect and determine whether response to radiation was homogeneous (176). In two experiments, single doses of 12 to 20 Gy were delivered to 17 to 84% of lung volume, and the morbidity from radiation pneumonitis was evaluated using breathing rate, lethality, and histological evidence of pneumonitis. This work demonstrated that the slopes of the dose-response curves for irradiation of partial lung volumes were shallower than those for whole-lung irradiation, and that a heterogeneous response to radiation was observed that was dependent on the site irradiated. Namely, changes were greater for volumes irradiated in the apex than the base. An important observation was the fact that histological damage did not always produce observable morbidity, which is similar in patients who sometimes have radiologic lung changes without symptoms.

Recently, Saito et al (183) reported the detection of early radiation lung damage in mice receiving a single dose of 20 Gy to one lung on CT (184). Van Dyk and Hill (118), found that post-irradiation density changes in mice followed a similar pattern to breathing rate changes observed by Travis et al (168). Limited changes were observed prior to 15 weeks post radiation, with earlier onset observed in animals receiving higher doses.

## 1.9 Current Status of Pre-clinical Models to Assess RILT

Until recently, increased breathing rates on plethysmograpy and histological confirmation using H&E and Masson's trichrome staining, have been the 'gold standard' methods of pre-clinical detection of RILT. However, histological confirmation is not only invasive, but also limits longitudinal and serial imaging studies. Additionally, as Travis et al have reported, plethysmography may not be as sensitive to RILT induced by single or partial lung irradiation compared to bilateral lung irradiation.

Recent advances that can facilitate improved pre-clinical modelling of the clinical situation include the use of micro-CT imaging to detect and quantify RILT in murine models, hemi-thoracic irradiation instead of whole-thorax RT (175, 177, 178), conformal and stereotactic radiation using micro-irradiators with image-guidance, and the establishment of animal models that display spontaneous growth of lung lesions as opposed to using orthotopic models to investigate tumour-normal tissue interactions and assessments (185-190).

The mouse models selected for this thesis were initially chosen based on literature reports of studies in which single or partial lung irradiation was administered. Table 1.1 summarises the publications that describe radiation pneumonitis following single or partial lung irradiation that were available when the experiments undertaken in this thesis were designed. Most of these studies described the biphasic phenomenon of RILT including an acute phase (pneumonitis or alveolitis) followed by a chronic phase (fibrosis).

| Author, year | Strain | Dose (Gy) | Time to Respiratory Change |
|---|---|---|---|
| Lissner, 1966 | C57BL/6 | 12.5 and 22.5 Gy | Phase I 7-70 days<br>Phase II 70-210 days |
| Travis, 1980 | CBA | 8-20 Gy (right or both lungs) | 26 weeks (pneumonitis)<br>>36 weeks (fibrosis) |
| Lockhart, 1986 | CBA | 14, 18 | 14-22 weeks<br>Peak at 16 weeks |
| Down, 1986 | CBA/C57Bl<br>$CBBF_1$ | 15, 17.5, 20, 25, 30<br>15, 20 | 4 - 28 weeks (peak @ 16)<br>Peak at 26-28 weeks |
| Cappuccini, 2011 | C57Bl/6 | 15 | 16 weeks |
| Eldh, 2012 | C57Bl/6J | 12.5 or 22.5 | 7-70 days (1-10 weeks) |

**Table 1.1 Literature citing hemi-thoracic irradiation in mice.** The shaded rows indicate citations that became available after the current project commenced.

Micro-CT has been established as a method to detect both early and late lung toxicity in mice and has been shown to correspond to both pathology and plethysmography (175, 179, 181, 191, 192). Normal mouse lungs have a CT density of -200 to -500 HU, with the higher number more closely related to lungs gated on the exhale phase of respiration and the lower number more closely related to fully inflated lungs (191). As lungs become inflamed (pneumonitic) or consolidated (fibrotic) it is possible to visualise differences in lung densities between irradiated and non-irradiated lungs on CT, as well as define regional lung damage. However, concerns about repeated radiation exposures in patients, have resulted in few longitudinal imaging studies to determine the appropriate time at which to detect lung changes prior to physiologic symptoms. This reinforces the notion that an ionizing radiation free imaging method, such as MRI, would be helpful in the context of RILT detection.

Micro-MRI systems exist with high field strengths (e.g., 4.7 and 7 Tesla) and the ability to develop and acquire sophisticated sequences, including cardio-respiratory triggering and functional imaging. These modern systems enable the pre-clinical development of novel imaging protocols that are easily translated to observational clinical studies. Development of robust protocols would allow patients undergoing radiation or chemo-radiation for lung

cancer to be screened with MRI at key time-points to detect and mitigate radiation toxicity prior to the manifestation of clinical symptoms.

## 1.10 Other Methods for Increasing the Efficacy of Radiation Therapy for Lung Cancer

An alternative to detecting and managing RILT is to improve methods of delivering radiotherapy that increase doses to the target while minimizing the amount of radiation delivered to normal tissue. Recently, it has been determined that the therapeutic efficacy of RT can be enhanced by the addition of pharmacological compounds that target specific pathways involved in cell survival (193). The use of drugs with low toxicity that act as radiosensitizers could minimise normal tissue toxicity by enabling radiation dosage to be reduced while achieving similar therapeutic efficacy.

Several candidate radiosensitization pathways are currently under investigation, including DNA repair pathways and angiogenesis. A wide range of potential therapeutic agents do appear to modulate tissue radiosensitivity; including systemic chemotherapy agents that enhance RT efficacy and novel radiosensitizing agents (192, 194, 195). Some of the most promising molecular targets for radiosensitization are summarized below in Table 1.2 adapted from Palacios et al (196), and though identified for the purposes of treating prostate cancers, may prove useful in other solid tumour sites including lung cancer.

An optimal radiosensitizer would reach the tumour in adequate concentrations to manifest a predictable response in combination with irradiation and selectively kill the tumour but not the surrounding normal tissues (197). It would also directly enhance DNA damage, alter cell biochemical and molecular responses to radiation, decrease tumour cell repair of DNA damage and enhance cell death by apoptosis (197). Targeted radiosensitizers fall into three major categories: hypoxic cell sensitizers, bioreductive drugs and molecular

radiosensitizers (198). Hypoxic drugs are classical radiosensitizers that target hypoxic cells to make them more susceptible to RT. First and second generation nitroimidazoles were used as hypoxic cell sensitizers in combination with radiotherapy in the late 1970's and early 1980's, but proved to be neurotoxic (199, 200). Later drugs such as the 5-nitromidazoles proved to be less neurotoxic and useful in tumour sites such as squamous cell carcinomas of the head and neck (201, 202). Bioreductive agents are metabolically reduced to cytotoxins, which show greater toxicity towards hypoxic tumour cells than oxygenated cells. They include three classes of drugs: 1) quinones, 2) benzotrianzine di-N-oxides and 3) alkylamino-anthraquinone N-oxides. Finally, molecular radiosensitizers can be divided into two major categories, signal transduction inhibitors and DNA signalling modulators.

**Table 1.2 Oncologic Mechanisms and their Anti-tumoural Targets**

| Mechanism | Target |
|---|---|
| **Angiogenesis** | VEGF |
| **Apoptosis/cellular proliferation** | AKT, PTEN |
| **Cell Cycle** | p21 |
| **Cell growth, differentiation, survival** | Cox-2, RAS |
| **DNA Repair** | p53, ATM |
| **Invasive Growth** | c-MET |

The development of molecularly targeted agents is the focus of many current translation and clinical studies.

## 1.11 Molecularly Targeted Agents and Lung Cancer Therapy

The signal transduction pathways that underlie oncogenesis, cancer cell survival, metastatic disease development and drug resistance are complex (203). Cancer cells harbour abnormalities in multiple signal pathways and rely on redundant signalling pathways for survival when one pathway is blocked (204, 205). Constitutive activation of the molecular pathways responsible for cancer survival is sustained by different mechanisms, and therefore combination treatment that aims to inhibit multiple targets or redundant pathways simultaneously may be the most effective way to improve therapeutic efficacy.

### 1.11.1 Molecularly Targeted Agents and Radiotherapy for Lung Cancer

Improved understanding of the biology of cancer has led to the development of effective therapeutic oncologic interventions such as trastuzumab (Herceptin), imatinib (Gleevec), and bevacizumab (Avastin) (206). For example therapies targeted at EGFR and VEGF have established a role in the treatment of advanced NSCLC. In NSCLC in particular, the introduction of treatment with the EGFR inhibitor gefitinib in patients with mutations in the EGFR gene has demonstrated a significant therapeutic benefit (207).

Radiation induces tumour death by damaging cell membranes, DNA, and microvascular endothelial cells. Antiangiogenic agents reduce vascular density but improve tumour oxygenation. Use of VEGFR inhibitors enhances the therapeutic efficacy of irradiation in human NSCLC by hindering the repair of sub-lethal radiation damage. Trials combining erlotinib and bevacizumab with thoracic radiation are ongoing. New strategies must be developed for the integration of this triple-combination treatment. As radiation therapy enhances HSP90 chaperone function, leading to the emergence of radio-resistant lung cancer cells, therapeutic agents that block this pathway are likely candidates for decreasing radio-resistance by suppressing HIF-1alpha and VEGF expression and thus inhibiting the survival and angiogenic potential of lung cancer cells. Aurora kinase inhibitors in combination with radiation therapy seem to have an additive effect in pre-clinical models in NSCLC (5).

## 1.12 PI3 –Kinase Inhibitors and Lung Cancer

In NSCLC, phosphatidylinositol-3-kinase (PI3K)/protein kinase B (AKT)/mTOR (PI3K/AKT/mTOR) signalling is frequently deregulated due to mutations affecting an upstream regulator, EGFR. The PI3K/AKT/mTOR pathway impacts many aspects of cell growth and survival. PI3K mediates AKT activation which in turn activates cellular proteins involved in protein synthesis including ribosomal protein S6-kinases and 4E-binding

protein. The inhibition of PI3K/AKT/mTOR signalling through pharmacologic and genetic approaches induces anti-proliferative effects on certain NSCLC cell lines and in lung cancer mouse models.

The PI3K/AKT pathway is associated with all three major radiation resistance mechanisms: intrinsic radiosensitivity, tumour cell proliferation, and hypoxia. Activation of this pathway can be the result of stimulation of receptor tyrosine kinases such as EGFR or VEGFR, or from mutations or amplification of PI3K or AKT that are frequently found in NSCLC. Furthermore, several treatment modalities, including radiotherapy, can stimulate this survival pathway. Monitoring and manipulation of this pathway may have important implications for the management of NSCLC. Direct inhibition of PI3K/AKT may increase radiosensitivity by antagonizing the radiation induced cellular defence mechanisms, especially in tumours in which the PI3K/AKT cascade is constitutively activated (99, 208-210). Quantification of the activation status of the PI3K/AKT pathway is a potential parameter for predicting treatment outcome.

## 1.13 PI3-Kinase Inhibitors Evaluated in this Thesis

Several PI3K/AKT/mTOR inhibitors have demonstrated efficacy as anti-cancer agents and tumour radiosensitizers in vivo and in vitro, including Nelfinavir (NFV), NVP-BKM-120 (BKM), and NVP-BEZ-235 (BEZ) (211-214). Nelfinavir is a PI3K/AKT inhibitor that was first used as an anti-retroviral in HIV patients. The first report of anti-tumoural activity using an HIV protease inhibitor (HPI) was published in a case report by Niehues et al (215). In 2003 Sgadari et al reviewed the literature on widely used protease inhibitors including nelfinavir and concluded that these inhibitors can affect important cellular and tissue processes such as angiogenesis, tumour growth and invasion, inflammation, cell survival and remodelling (216).

Because activation of the PI3K/AKT signalling pathway is common in human cancers, it was hypothesized that HPIs could inhibit AKT activity resulting in increased tumour cell sensitivity to ionizing radiation-induced cell death. Work published by Pore using xenografts in nude mice showed the combination of nelfinavir and radiation increased the time to regrowth compared to radiation or nelfinavir alone (217). As the radiosensitizing effect in vivo was greater than predicted by in vitro clonogenic survival assays, the authors hypothesized that nelfinavir had an effect on tumour oxygenation. Using the hypoxia marker EF5, they confirmed that that use of nelfinavir resulted in increased oxygenation in the xenografts. Further pre-clinical validation of the effects of nelfinavir on tumour radiosensitization was undertaken by this group and others before early clinical trials were undertaken in patients with liposarcomas (218), locally advanced rectal cancer (219), glioblastoma multiforme (220), and locally advanced pancreatic carcinoma (170). In each of these trials nelfinavir was relatively well tolerated by the patients and limited radiation toxicity was reported, which suggests nelfinavir does not enhance or accelerate normal tissue toxicity in combination with radiotherapy.

However, because of its known oxygenation effects on tumours, and a case study reporting fatal haemoptysis during radiation for lung cancer in a HIV-positive patient taking nelfinavir (221), the effects of molecularly targeted agents in combination with radiation must be carefully evaluated in normal tissues (not just tumours and tumour cells) prior to the introduction of radiation dose escalation studies in patients.

BKM is a selective PI3K inhibitor that radiosensitizes tumour cells by inhibiting tumour cell growth and survival. In pre-clinical work by Liu et al, BKM was assessed as a radiosensitizer for hepatocellular carcinoma. It was observed that treatment of Balb/c mice bearing ectopic xenografts with BKM prior to administering radiation led to inhibition of radiation-induced AKT phosphorylation and enhanced radiation-induced tumour cell

apoptosis (222). BKM has been used in combination with chemotherapy and other molecularly targeted agents (MTAs) in early clinical trials in patients with solid tumours including lung cancers. Chang et al found BKM enhanced radiosensitivity in radioresistant prostate cancer cells (224), although the effect was greater when using the dual PI3K/mTOR inhibitor BEZ.

BEZ inhibits PI3K and mTOR kinase activities by affecting tumour cell apoptosis and growth inhibition in PI3K/mTOR-overexpressing tumour cells. Fokas et al, using T24 bladder and FaDu hypopharyngeal cancer cells, demonstrated that BEZ can improve tumour oxygenation and vascular structure over a prolonged period and that in combination with radiation can enhance the delay of tumour growth without changing tumour oxygenation (225). These results suggested that targeting the PI3K/mTOR pathway can modulate the tumour microenvironment to induce a prolonged normalization of blood vessels resulting in a substantial therapeutic gain with potential implications for cancer therapy. Further work by this group has confirmed that BEZ enhances radiation-induced killing in tumour and endothelial cells (225). The results of this work are supported by others investigating tumour specific radiosensitization in prostate cancer cells (214, 224, 226, 227), glioma (228), and glioblastoma cells (229). Kim et al investigated the potential of BEZ to enhance radiosensitization of cisplatin-resistant NSCLC cells by disabling autophagy as a mechanism of self-preservation in in vitro and in vivo experiments (230). Their results were similar to those reported by Fokas et al in that the combination of BEZ and radiation showed a dramatic tumour growth delay in a mouse xenograft model and that cell proliferation was reduced by 88%.

Ataxia-telangiectasia mutated (ATM) is one of the major kinases that responds to ionizing radiation induced DNA double-strand breaks (DBSs), and is commonly mutated and inactivated in NSCLC. Engleman (231) and Konstantinidou (232) have shown BEZ is

an effective radiosensitizer in murine lung cancers. Mukherjee et al (233) have shown the BEZ is potent ATM inhibitor that confers an extreme degree of radiosensitization in human glioblastoma (GBM) cell lines. These investigators showed that BEZ produced a greater degree of radiosensitization than ATM inhibitors alone, likely because of the combined effects of ATM and AKT inhibition on DSB repair, cell cycle checkpoints and cell survival.

Little has been published concerning the effect of these agents on normal tissue radiosensitivity. Prior to clinical testing, it is important to confirm that PI3K/AKT/mTOR targeted drugs do not enhance radiosensitivity in normal tissues.

The three drugs selected for this project are the subject of clinical interest and preliminary investigations of principal investigators at the CRUK/MRC Oxford Institute for Radiation Oncology. In this thesis the effects of the targeted radiosensitizers NFV, BEZ and BKM on normal lung tissue in a murine model is reported. Physiologic, pathologic and imaging endpoints were used to investigate the effect of adding PI3K inhibition to radiotherapy

## . Aims of this thesis

The aims of the research reported in this thesis were:

1. To develop a high throughput, multi-modality imaging program for longitudinal investigation of normal tissue toxicity in a pre-clinical model.
2. To investigate novel, ionising radiation-free, non-invasive imaging methods for the detection of RILT in a pre-clinical model.
3. To compare the incidence and severity of RILT in animals treated with radiation alone to that in animals treated with radiation plus PI3K/AKT/mTOR inhibitors in a pre-clinical model.

The research to address these aims was undertaken in a series of longitudinal imaging studies in two mouse models. Table 1.3 summarizes the experiments undertaken in this thesis.

| | Study | Mice | No. mice | Intervention | Last follow-up |
|---|---|---|---|---|---|
| Preliminary Studies (Chapter Three) | RT | C57 | 30 | 18 Gy RT vs. Sham RT | 16 weeks |
| | NFV | C57 | 30 | 18 Gy RT + NFV vs NFV<br>NFV 1 mg/mL @ 20 mg/Kg | 16 weeks |
| | RT2 | CBA | 24 | 18 Gy RT vs. Sham RT | 20 weeks |
| | BLM | CBA | 21 | 14 Gy RT + BLM vs 18 Gy RT<br>BLM – single IP injection 80ml/kg | 14 weeks & 20 weeks |
| | NFV2 | CBA | 30 | 20 Gy RT + NFV vs 20 Gy RT<br>(NFV 1 mg/mL @ 20 mg/Kg) | 20 weeks |
| PI3K/AKT-inhibitors +/- RT (Chapter Four) | pAKT | CBA | 12 | PO BEZ or BKM<br>Daily by gavage for 3 days:<br>BKM - 20 mg/kg (6 mg/mL), BEZ - 30 mg/kg (4 mg/mL) | Immediate |
| | BEZ-BKM | CBA | 32 | 20 Gy RT + BEZ vs 20 Gy RT +BKM<br>Daily by gavage for 3 days:<br>BKM - 20 mg/kg (6 mg/mL), BEZ - 30 mg/kg (4 mg/mL) | 20 weeks |
| IGRT +/- BKM (Chapter Five) | IGRT | CBA | 26 | 20 Gy IGRT vs 20 Gy IGRT + BKM<br>BKM - daily by gavage for 3 days 20 mg/kg (6 mg/mL) | 20 weeks |
| | IGRTfx | CBA | 26 | 45 Gy/3 Fx IGRT vs 45 Gy/3 Fx IGRT + BKM<br>BKM daily by gavage for 3 days 20 mg/kg (6 mg/mL) | 20 weeks |

**Table 1.3 Summary of Longitudinal Imaging Studies**

For all studies, animals were weighed, imaged and underwent plethysmography prior to the administration of radiation to the right thorax in a single (14, 18 or 20 Gy) or multiple fractions of radiotherapy (3 x 15 Gy) with or without targeted radiosensitizers (NFV, BKM, BEZ) in three daily administrations (IP or PO), or chemotherapeutic agents (BLM). Following the interventions, animals underwent imaging (CT and MRI), plethysmography and histopathological examination at pre-determined or clinically necessary time points generally following the pattern of 8, 12, 16 or 20 weeks following irradiation with studies terminating at 16 or 20 weeks and additional evaluations at 6, 10, 14 or 18 weeks in some experiments. Below is a generalised schema of the longitudinal experiments undertaken in this thesis.

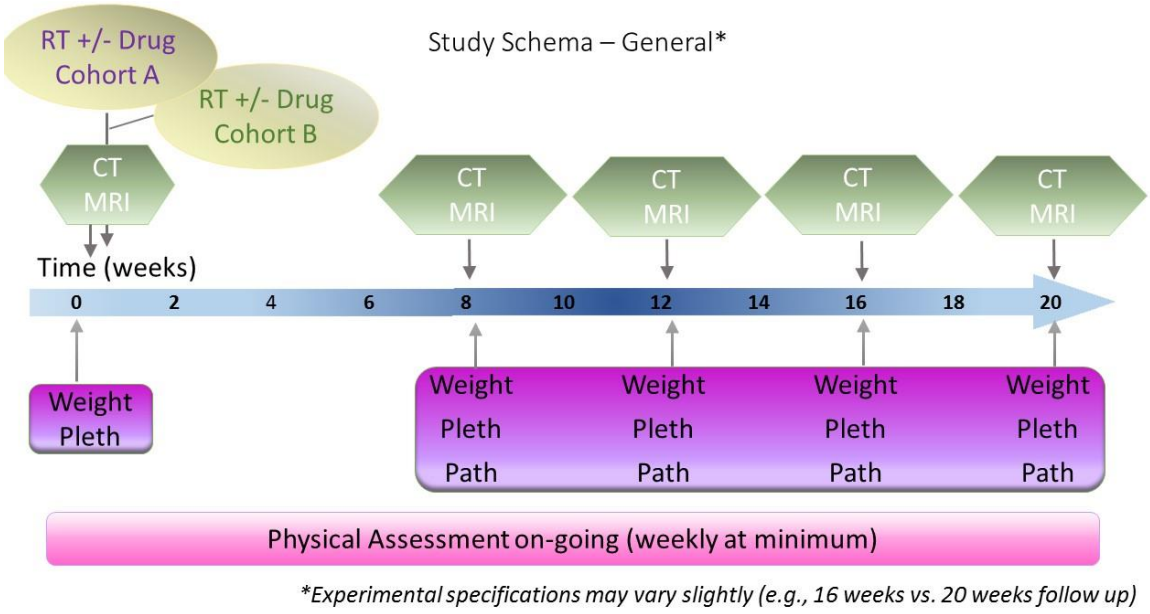



**Figure 1.1 Study Schema - General**

# Chapter 2

*Materials and Methods*

# 2 MATERIALS AND METHODS

Nine experiments were undertaken using two different mouse strains to detect the effects of radiation with or without targeted radiosensitizers or known lung irritants on normal lung tissue. With the exception of one study (pAKT), all animals had weights and breathing rates measured at baseline. Groups of animals in each study cohort underwent CT and MR imaging at baseline. Subsequently groups of representative animals were assessed by plethysmography, CT, MRI and pathology at pre-determined time-points. Additional plethysmography, CT, MRI and/or pathology were conducted as deemed necessary based on toxicity assessments. The general well-being of the animals was monitored weekly (or more frequently) by visual observation and recording weights. Though assessed weekly; animal weights were reported only at scheduled time points, or if animals demonstrated a failure to thrive.

## 2.1 Animal Models

The murine models investigated were C57BL6 and CBA mice, which are two of the most commonly used mouse strains for lung toxicity studies. Both C57BL6 and CBA mice exhibit predictable patterns of RILT following radiation exposures with temporal onsets similar to humans (174). Using the limited literature available at the time the study was developed and to satisfy local ethics constraints, the initial radiation doses to be studied were selected as they had been shown to cause radiation response in whole thoracic irradiation.

All animal procedures were carried out in accordance with the UK Animals (Scientific Procedures) Act 1986 and with local ethical committee approval. Ten to twelve week old female C57BL6 or CBA mice were chosen for the experiments in this thesis. All animals were housed according to local procedures in groups of 4 to 6 mice per cage in up to 12

cages, with food and water available ad libitum. Animals were maintained and monitored to a maximum of 20 weeks following irradiation.

## 2.2 Plethysmography and Physical Assessment of Mice

Animal weights, respiratory rate and amplitude were measured at baseline, at planned time-points (e.g., 8, 12, 16, 20 weeks post irradiation) and more frequently as needed.

Plethysmography of 2-6 mice was performed using a small rodent whole body plethysmograph developed in-house by Professor Boris Vojnovic and Mr Rob Newman, as described in the user manual which is included with permission in its entirety as Appendix 3. Briefly, this system consists of a sealed Perspex chamber into which a single mouse is placed. The instrument monitors pressure changes within the chamber by means of a small electret-type microphone capsule that is used as a pressure sensor. Variations in pressure within the chamber are processed and recorded using a graphical user interface (GUI) on a lap-top computer. The system has four such chambers connected to the laptop and can record data for four animals simultaneously, providing a read-out as shown in Figure 2.1.

To assess respiratory rates, awake, free-breathing animals were placed in the chamber and allowed to settle for 30-60 seconds (60 seconds for animals not familiar with the system). The respiratory rate recording was commenced immediately after the chamber was closed, but the first 30-60 seconds was removed from the reported data as it is likely that any measurements taken during this period would be more reflective of animal motion than respiration (169, 171). The mean respiratory rates were determined for a period of three minutes, similar to the method reported by Travis et al (169). Animals that demonstrated greater than 15% increase in breathing rate over baseline, were monitored more frequently (daily or alternate daily) and those with more than 35% increase were imaged (if feasible)

and then euthanized. Pooled data for each cohort from each time point was compared using t-tests and linear regression.



**Figure 2.1 Plethysmographic Setup**. Four animal chambers and laptop feedback and recording system (top panel). Bottom left: respiratory readout where the red trace indicates respiratory amplitude (measured in arbitrary units that can be converted to Hertz) and the blue trace represents breathing rates measured every second and recorded as breaths per minute. Close up of a mouse in the chamber during plethysmographic assessment (bottom right).

Animals experiencing weight loss greater than 20%, increased breathing rates of greater than 35%, unresolved moist desquamation for 24 hours or other adverse events causing discomfort, were euthanized. Animals that approached these limits at any scheduled time point were euthanized at that time point and used for tissue sampling and pathological evaluation but not reported as having undergone unscheduled euthanasia. Mice were euthanized by intravenous (IV) or intraperitoneal (IP) injection of pentobarbital (IP was used when IV was not possible for technical reasons).

## 2.3 Radiotherapy and Dosimetry

### 2.3.1 Cabinet Irradiation

For studies RT, NFV, RT2, NFV2, BLM and BEZ-BKM, animals were irradiated using a Gulmay cabinet irradiator (Xstrahl, Camberly UK), with 320 kV and 10 mAs delivered at a rate of approximately 1.8 Gy/min. Dosimetric confirmation of the system was undertaken and is reported in Appendix 1.

Animals were anaesthetised using an intraperitoneal (IP) injection of 0.3 µL Hypnoval and Hypnorm (hyp-hyp) delivered in sterile water using a 1:1:6 ratio. Before losing consciousness, animals were coaxed into Perspex holders head first with their forelegs extended superiorly and supported at the axilla using adjustable built-in supports. Using gross anatomical landmarks the animal position was adjusted such that only the thorax was exposed. Lead shielding (0.3 cm) was placed manually from midline and extended laterally to ensure only the right thorax would be exposed to radiation. Animals were monitored by camera throughout the procedure. Following the procedure, all animals were recovered in a heated recovery box and then transferred to their cages once fully awake and alert.

Initially animals were treated in a prone position with a single beam to the posterior chest wall (experiments RT and NFV). However in later experiments animals received half of the dose of radiation using a posterior beam and half using an anterior one (experiments RT2, NFV2, BLM, and BEZ-BKM).

Up to five mice were irradiated at one time, by positioning them side by side along the central axis of the beam, with a maximum distance 20 cm from the centre of the treatment field. For animals undergoing radiation plus a targeted agent, radiation was delivered two hours after dosing on the final day of drug administration.

Animals were irradiated with 14 Gy, 18 Gy or 20 Gy to the right lung using the above described techniques.

### 2.3.2 Image Guided Radiation

Image guided, single- (20 Gy) and multi- (3 x 15 Gy) fraction irradiations (experiments IGRT and IGRTfx) were performed using the Xstrahl SARRP irradiator, (234, 235) which consists of a constant-voltage, dual focus, 225 kVp X-ray source (Varian NDI-225-22) mounted on a rotating gantry, a robotic stage with four degrees of freedom ($x$, $y$, $z$, $\phi_Z$) on to which the mouse is mounted and a flat panel digital X-ray detector (PerkinElmer XRD 0829 AN14) for imaging. Dose rate measurements and spatial characterization was performed prior animal experimentation and is described in Appendix 1.

Using a representative mouse, cone-beam CT (CBCT) and the collimator dimensions, a parallel-opposed-pair irradiation plan was generated with the Xstrahl (Xstrahl Limited, Surrey, UK) planning software to determine the beam-on time required to deliver 15 Gy and 20 Gy using a parallel opposed pair, for the IGRTfx and IGRT experiments respectively.

Figure 2.2 shows the dose wash (in green) and associated scale, generated for a plan with a mid-plane prescription dose of 20 Gy (10 Gy from each of the two beams), including 'hotspots' in the ribs.

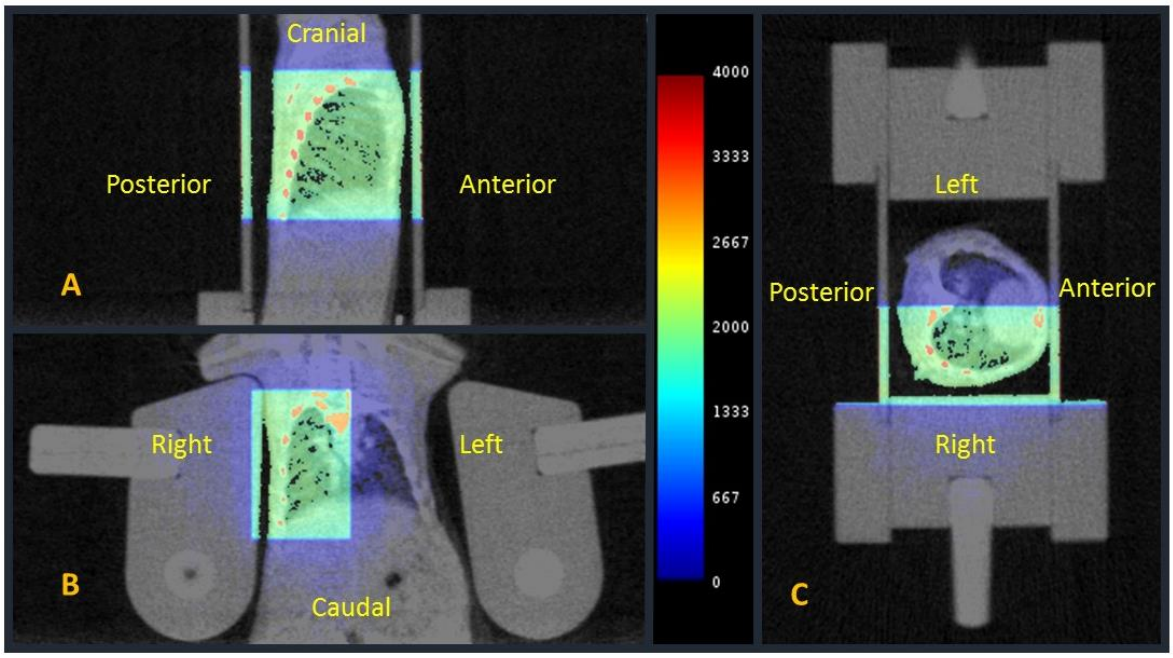



**Figure 2.2 SARRP Dosimetry:** Single fraction 20 Gy treatment plan using a custom collimator and parallel opposed fields with 50% weighting on each of the anterior and posterior beams , planned on a micro-CBCT of a representative mouse using density corrections available in the SARRP dose planning system (Xstrahl Ltd, Surrey UK). Dose colourwash shown on saggital (A), coronal (B) and axial (C) views.

Image-guided radiotherapy was performed using an in-house customized collimator (7 mm x 14 mm in size), and parallel-opposing-pair (POP) technique to deliver 20 Gy in a single fraction (10 Gy to the anterior and 10 Gy to the posterior fields) or 45 Gy in three fractions on alternate days (also using a parallel opposed pair).

Following anaesthetic induction, sedation was maintained using continuous isoflurane (2%). Animals were imaged and irradiated vertically in a custom made Perspex holder (Figure 2.3) with the gantry at $90^{O}$ to the vertical. The holder incorporates a compressible balloon located under the mouse to monitor breathing rate, a heating pad and a rectal temperature probe. Additionally the holder included thin polycarbonate windows (1 mm thick) front and back over the region of the chest to minimize X-ray attenuation within the treatment field. The main body of the collimator was constructed from brass with additional

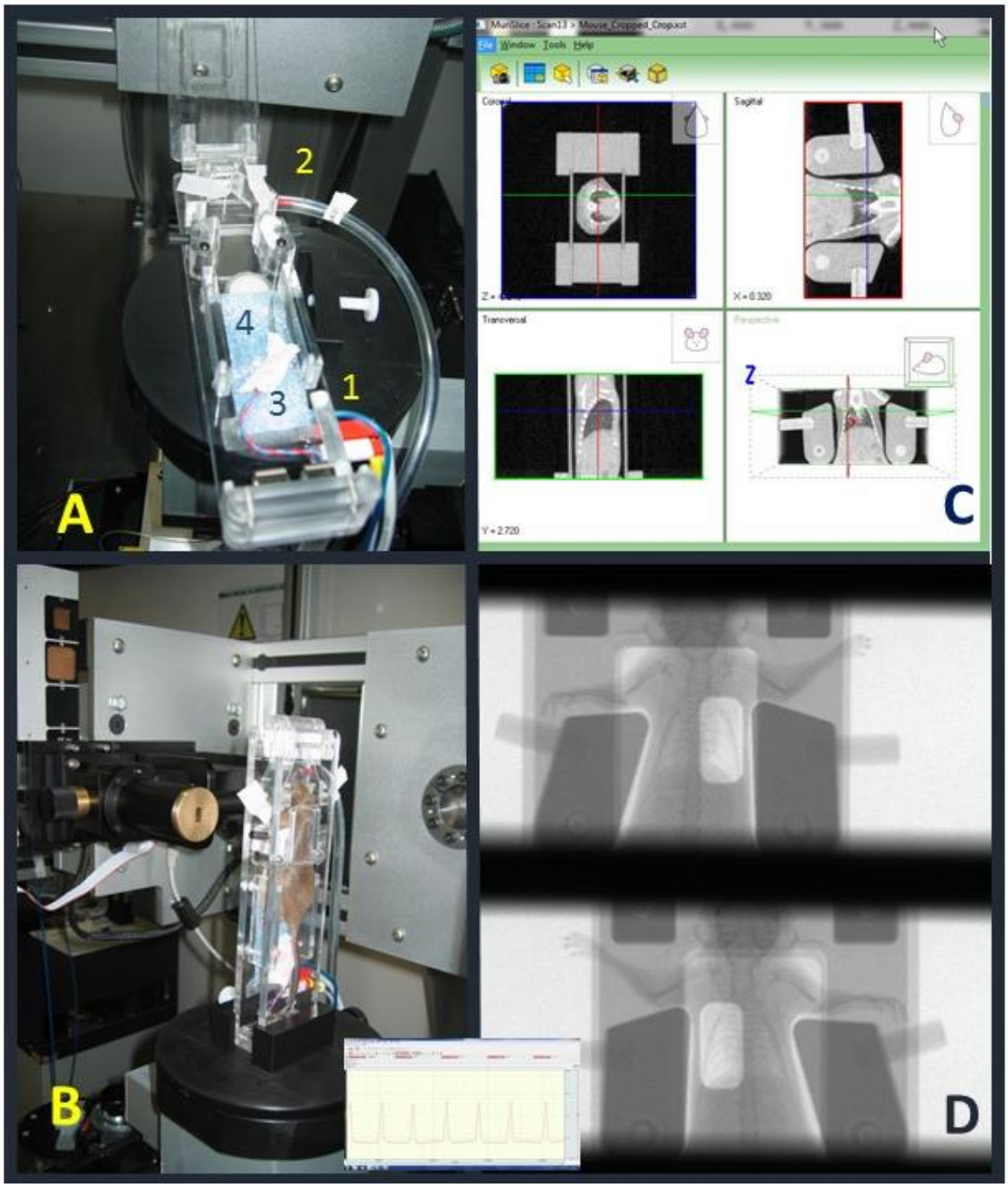
lead with an open aperture of 7 mm x 14 mm to define the irradiation field incident on the mouse enabling one lung to be irradiated while minimising dose to the other.

Imaging was performed in the absence of a collimator using 50 kVp X-rays (fine focus, 2 mA), while therapeutic exposures were performed using 220 kVp x-rays (broad focus, 13 mA, half-value-layer of 0.79 mm Cu) with a collimator in place to define the irradiation field.

With the chest of the mouse positioned approximately at the isocentre, a CT image was obtained by rotating the mouse through 360°. This image was then used to reposition the mouse to ensure that the required lung was irradiated while minimizing exposure to the other. To check alignment a single planar X-ray image of the mouse was acquired with and without the collimator in place and the two resulting images overlaid to identify the treatment field with respect to the mouse anatomy. If any further positional adjustments were made for a particular mouse then alignment was checked again using the same method. Following therapeutic irradiation from one side, the mouse was rotated through $180^{O}$ and the alignment was confirmed using planer X-ray images with and without the collimator (see Figure 2.3).

The lung was irradiated with parallel-opposed (POP) fields achieved by rotating the mouse through $180^{O}$ between exposures. Because the centre of the collimated field is aligned with the axis of rotation of the stage, the treatment fields were coincident at the isocentre for each exposure.

**Figure 2.3 SARRP Setup for IGRT:** (A) Perspex vertical mouse holder with feeds (1) to an integrated heating system (blue pad), flexible tubing for anaesthetic gases (2), rectal thermometer (3) and respiratory balloon (4); (B) Mouse in vertical position in Perspex holder on rotating stage with gantry positioned to deliver an anterior beam; (C) screen shot of CBCT on Murislice (Xstrahl Ltd, Surrey, UK), used for isocentre positioning; (D) Pre and post irradiation verification radiographs with custom collimator in place. Inset, respiratory readout used to monitor animals throughout radiation setup and delivery.



## 2.4 Drug Administration

### 2.4.1 Nelfinavir

Mice in experiments NFV, and NFV2 received nelfinavir (1 mg/mL @ 20 mg/Kg) administered by IP injection daily for three days either alone or followed by RT which was administered within two hours of the final nelfinavir injection. The nelfinavir (NFV) dose used was selected based on previous work at the Oxford Institute for Radiation Oncology (211, 236-238), personal correspondence with Dr. T. Brunner and limitations defined in the relevant Project License.

### 2.4.2 Bleomycin

Twelve CBA mice in experiment BLM received a single IP injection of Bleomycin (80 mg/Kg) followed by 14 Gy RT two hours following injection.

### 2.4.3 BEZ and BKM

BKM and BEZ were administered by oral gavage daily for three days at a dose of 20 mg/kg (6 mg/mL) and 30 mg/kg (4 mg/mL) respectively. Oral gavage was performed using a flexible cannula that was passed through the side of the mouth of an upright scruffed mouse, through the oesophagus and into the stomach. These dose schedules were selected in part based on personal correspondence with colleagues regarding effective, tolerable dosing schedules (personal correspondence Dr. E. Fokas, and Prof.T. Brunner, March and May 2012) as little existed in the literature prior to the undertaking of this project (225, 239, 240). Animals were euthanized for tissue sampling or went on to have radiation two hours following the final administration of drug.

## 2.5 Tissue Analysis

### 2.5.1 Western Blot Analysis – Non-irradiated tissue

AKT and pAKT levels in the lung and spleen of mice dosed with BEZ or BKM were determined using Western blot analysis.

Tissue samples were weighed and homogenised in approximately 10 x volume radioimmunoprecipitation assay (RIPA) buffer (Sigma-Aldrich, St Louis, MO) with a Complete Protease Inhibitor tablet added (Roche, Welwyn Garden City, Hertfordshire). The homogenates were incubated on ice for 30 mins and then centrifuged at 12,000 g for 15 min at 4 °C. The supernatants were harvested, and protein concentrations measured using the Pierce BCA Protein Assay Kit (Thermo Scientific). Protein lysates (6.5 µl at 1.5 mg/ml) were mixed with 2.5 µl NuPAGE LDS Sample Buffer (Life Technologies, Paisley UK) and 1 µl NuPAGE Reducing Agent (Life Technologies, Paisley UK), heated to 70 °C for 10 minutes and loaded onto a 4-12% Bis Tris gel (Life Technologies, Paisley UK).

Electrophoresis was conducted at 200V for 50 minutes in NuPAGE MOPS SDS Running Buffer (Life Technologies, Paisley UK). After electrophoresis, the proteins were transferred from the gel onto a nitrocellulose membrane (Bio-Rad, Hercules CA). Transfer was conducted at 100 V for one hour in a transfer tank containing NuPAGE Transfer Buffer (Life Technologies, Paisley UK) with 10% methanol. The membrane was blocked in 5% BSA in Tris Buffered Saline (TBS) with 0.1% Tween for 1 hr at room temperature. After blocking, membranes were incubated with primary antibodies (rabbit anti-AKT antibody, Cell Signalling, 1:1000 dilution in blocking buffer; or rabbit anti-pAKT antibody, Cell Signalling, 1:2000 dilution in blocking buffer) for 1 hr at room temperature. Washes (3 x 5 min) were carried out carried out at room temperature in TBS/0.1% Tween. Membranes were then incubated with secondary antibody (goat anti-rabbit IgG-HRP conjugate, Life

Technologies, 1:3000 dilution in blocking buffer) for one hour at room temperature. Washes (3 x 5 min) were carried out and chemiluminescent reagent (ECL reagent – Thermo Scientific) was applied to blots and incubated for 1 minute. Blots were applied to film (Super RX, Fujifilm) in a dark room and developed in an automated film developer.

### 2.5.2 **Histopathology – Irradiated tissues**

To correlate with imaging results and visualize histopathological damage at pre-determined time points or when euthanasia was required due to toxicity, Haematoxylin and eosin (H&E) and Masson's trichrome staining were performed on single lung sections from each animal euthanized. The left (non-irradiated) lungs were used as controls for comparison to the irradiated (right) lungs.

Following euthanasia (as described in section 2.2), lungs were inflated with phosphate buffered saline (PBS) via the trachea, fixed with 4% paraformaldehyde (PFA) and removed. Lungs were fixed for 24 - 48 hours in PFA and then transferred to 70% ethanol (ETOH) for storage in experiments RT, NFV, RT2, NFV2 and BLM. Following consultation with Professor C. Scudamore, who joined to assist in the interpretation of the histopathology results and as an advisor from experiment BEZ-BKM onwards, lungs were inflated with and stored in 4% PFA. Lung tissue was then routinely processed into paraffin blocks and single 5 µm sections were stained using H&E and Masson's trichrome to assess alveolar inflammation and fibrosis respectively.

For the purposes of this thesis, alveolar inflammation was defined as the accumulation of foamy macrophages and/or polymorphonuclear inflammatory cells within the lung parenchyma (within alveolar spaces and/or alveolar septae) and was scored as follows: 0, no macrophage or inflammatory cells present; 1, aggregates of macrophages or inflammatory cells within occasional alveoli; 2, increased small foci of macrophages and inflammatory

cells scattered across lung field; 3, macrophages and inflammatory cells in larger foci affecting approximately 30–50% of the lung field; 4, same as 3 but affecting more than 50% of the lung field; 5, all alveoli contain macrophages and/or inflammatory cells (modified from Ford et al 2001, (241)). Fibrosis was defined as the accumulation of fibrous tissue and scored as follows; 0, normal lung with no fibrosis, 1 minimal fibrosis affecting 5-10% of alveolar spaces in the lung field, 2 focal areas of fibrosis affecting up to 20% of the lung field, 3 larger areas of fibrosis affecting approximately 30-50% of the lung field, 4 more confluent areas of fibrosis with loss of structural features, 5 complete fibrosis of the lung field with obliteration of normal architecture (modified from Ashcroft 1988, (242)).

## 2.6 Imaging

CT and MRI were performed in a single imaging session whenever possible to minimise the number of anaesthetic procedures animals underwent.

### 2.6.1 Computed Tomography (CT)

Following induction of anaesthesia and MRI imaging, respiratory-gated CT images were immediately acquired using the CT component of the Inveon PET-CT system (Siemens Health Care).

Mice were positioned head-first, prone, on a heating pad, with a respiratory balloon positioned under their abdomen. Continuous flow 2% isoflurane was provided through a channel reaching under their nose to maintain anaesthesia and respiration to 30-40 breaths per minute (BPM). A small cone was placed over the animal's head to minimize the gas escaping the system. Respiratory signal was captured using the Biopack (Biopack Medical, Lausanne, Switzerland) feedback system to monitor respiration and gate image acquisition.

CTs were acquired using 65 kV and 500 µA with a 200 msec exposure time per projection over 180 projections. Images were reconstructed using a standard Feldkamp

algorithm for cone beam CT (CBCT) generating an image matrix of 768 x 768 x 512 with an isotropic voxel size of 102.4 µm. All images were scaled to report Hounsfield Unit. Imaging details are outlined below:

**Imaging System**: CT component of the Inveon PET/CT scanner (Siemens Health Care). Consisting of a standard x-ray source with a maximum power of 80 W, peak voltage range 40-80 kVp, and a tungsten anode spot size of 46 µm for 65 kVp and d500 µA.

**Animal Position**: Prone

**Physiologic Monitoring**: Respiratory Rate and Temperature

**Imaging Parameters**: Respiratory Gated CT imaging using 65 kV and 500 µA with 0.5 mm Aluminium additional tube filtration, 200 msec exposure time per projection, 180 projections 360º stepwise rotation without settling time, low magnification (source to centre 262.24 mm; source to detector 345.58 mm), fan beam angle of 17.0686º, binning factor of 4, trans-axial x axial matrix size of 3072 x 2048.

**Image Reconstruction**: performed using standard Feldkamp algorithm for cone beam CT reconstruction, with a Shepp-Logan filter with cut-off at the system Nyquists frequency, resulting in an image matrix of 768 x 768 x 512 with an isotropic voxel size of 102.4 µm. Images were scaled to report HU.

**Duration of Scan** (approx.): 15-20 mins

### 2.6.2 Magnetic Resonance Imaging (MRI)

MRI was performed on groups of 2-4 animals per cohort using a 4.7 T or 7.0 T Varian VNMRS Console (Varian Inc., Palo Alto) at baseline and again at pre-determined time points or at other times if the physical condition of the animal warranted increased monitoring.

Details of the imaging procedures and how they evolved over the course of the study are described below. In brief, cardiorespiratory gated spin echo multi-slice (SEMS), dynamic contrast enhanced (DCE), and in the later experiments high resolution MR angiography (ANGIO) images were acquired under anaesthetic (2% isoflurane following induction). An integrated heating pad was used to maintain a core temperature which was monitored using a rectal thermometer (Harvard Apparatus, Holliston, MA). Cardio-respiratory monitoring was conducted with electrocardiogram (ECG) leads and a respiratory balloon placed under the thorax, using the Biopack (Biopack Medical, Lausanne, Switzerland) feedback system. All images were respiratory or cardiorespiratory triggered.

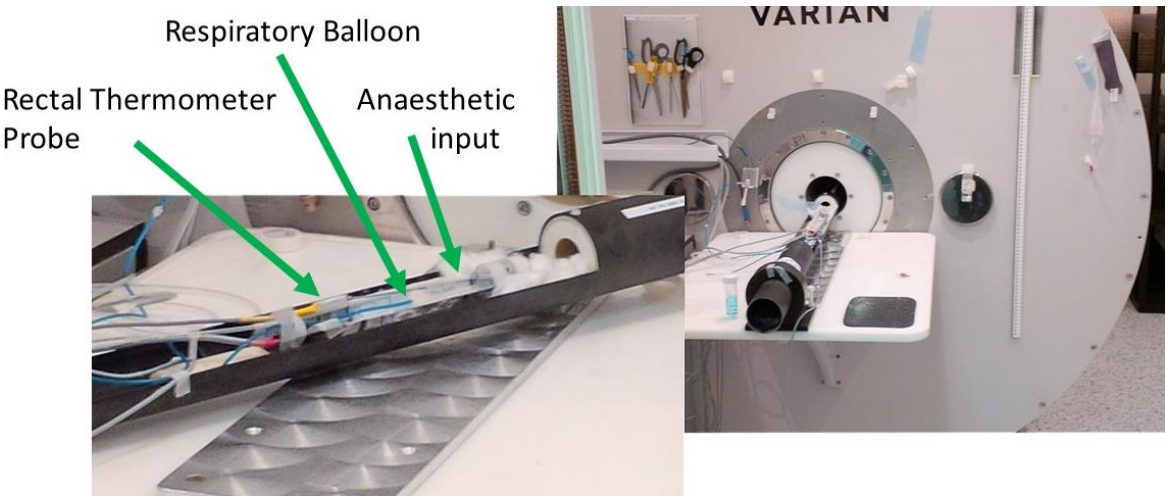



**Figure 2.4 MRI Sled and Birdcage Coil**. Inset: sled with physiological monitoring equipment. Background: Sled ready to enter magnet for imaging.

### 2.6.2.1 *Spin Echo Multi-Slice (SEMS) – Anatomic Imaging*

#### 2.6.2.1.1 *Basic Sequence Parameters*

**Magnet and Coil Used**: 4.7 T, 25 mm inner-diameter quadrature birdcage coil

**Animal Position**: Prone

**Physiologic Monitoring**: Respiration (respiratory balloon), Heart Rate ECG leads in scalp, Core Temperature via rectal thermometer. Heating Pad outside coil.

**Imaging Parameters**: Cardio-respiratory triggered, T1w spin echo multi-slice (SEMS) sequence with TE of 10 msec, effectively infinite TR as time required for number breaths required to complete the slice loop was longer than 5*T1, 0.5 mm slice thickness, FOV 2.7 cm and matrix of 128 x 128 pixels

**Duration of Scan** (approx.): Variable due to cardio-respiratory triggering, approx. 25 mins

**Duration of Imaging Session** (approx.): 1-1.5 hours

#### 2.6.2.1.2 *Variations for experiment BEZ-BKM*

**Imaging Parameters**: TE of 8.3 msec

**Duration of Scan** (approx.): Variable due to cardio-respiratory triggering, approx. 20 mins

**Duration of Imaging Session** (approx.): 0.75-1.0 hours

#### 2.6.2.1.3 *Variations for experiments IGRT and IGRTfx*

**Magnet and Coil Used**: 7.0 T, 25 mm-inner diameter quadrature birdcage coil (Rapid), with the exception of some baseline imaging that was done on the 4.7 T

**Animal Position**: Supine

**Physiologic Monitoring**: Respiration (respiratory balloon placed posteriorly), Heart Rate ECG leads in thorax

**Duration of Scan** (approx.): Variable due to cardio-respiratory triggering, approx. 10-15 mins

**Duration of Imaging Session** (approx.): 0.5-1.0 hours

### 2.6.2.2 *Dynamic Contrast Enhanced (DCE) MRI – Functional Imaging*

#### 2.6.2.2.1 *Basic Sequence Parameters*

**Magnet and Coil Used**: 4.7 T, 25 mm-inner diameter quadrature birdcage coil (Rapid),

**Animal Position**: Prone

**Physiologic Monitoring**: Respiration (respiratory balloon), Heart Rate ECG leads in scalp, Core Temperature via rectal thermometer. Heating outside coil.

**Notes**: Cardio-respiratory triggered, 3D gradient echo sequence modified over time with major improvements to C-R triggering, acquired using 10 dummy scans, followed by acquisitions at every heartbeat. Not truly T1 quantifiable.

**Imaging Parameters**: TE 0.6 - 0.7 msec, TR 1.1 – 2.006 msec, FOV 5.4 x 2.7 x2.7 cm, 48-64 phase encodes, 128 x128 matrix, slice thickness of 0.5 mm, 400 micron spatial resolution, and Flip Angle 5 °.

#### 2.6.2.2.2 *Variations for experiment BEZ-BKM*

**Physiologic Monitoring:** Heating pad under abdomen/thorax.

**Notes**: Development of fT1 quantification by $B_1$ field calibration using Flip Angle imaging. Other developments included the introduction of auto-syringe and time-stamping in later part of these experiments.

**DCE Imaging Parameters**: TE 0.59 msec.

**B1 Field Calibration**: Inter-leaved TR experiments using TR of 20 and 100 msec, TE of 0.363 msec, and variable flip angles to estimate T.

#### 2.6.2.2.3 *Variations for experiments IGRT and IGRTfx*

**Magnet and Coil Used**: 7.0 T, 25 mm inner-diameter quadrature birdcage coil (Rapid), with the exception of some baseline imaging that was done on the 4.7 T.

**Animal Position**: Supine

**Physiologic Monitoring**: Respiration (respiratory balloon placed posteriorly), Heart Rate ECG leads in thorax.

**Notes:** Cardio-respiratory triggered, 3D gradient echo sequence without T1 quantification by $B_1$ field calibration. Other developments included a modification in the gating control by

introducing dummy scans between heart beats to make the sequence more robust to motion. Auto-syringe injections and timestamps continued to be used.

**DCE Imaging Parameters**: TE 0.6 msec.

**$B_1$ Field Calibration**: Inter-leaved TR experiments using TR of 20 and 100 msec, TE of 0.363 msec, and variable flip angles to estimate T1.

#### 2.6.2.3 *High Resolution Pulmonary MR-Angiogram (ANGIO)*

##### 2.6.2.3.1 Basic Sequence Parameters (experiments BLM and NFV2 only)

**Magnet and Coil Used**: 4.7T, 25 mm inner-diameter quadrature birdcage coil (Rapid),

**Animal Position**: Prone

**Physiologic Monitoring**: Respiration (respiratory balloon), Heart Rate ECG leads in scalp, Core Temperature via rectal thermometer. Heating outside coil.

**Imaging Parameters**: TE 1.003 msec, TR 2.006 msec, FOV 5.4 x 2.7 x 2.7 cm, 128 x128 matrix, slice thickness of 0.5 mm, 200 micron spatial resolution, Flip Angle 5° (5° at centre, 0° at edge of coil)

**Notes:** Acquired post gadolinium (post DCE-MRI acquisition); acquisition run over two heart beats.

##### 2.6.2.3.2 *Variations for experiments BEZ-BKM*

**Imaging Parameters**: TE 2 x 0.59 msec, TR 2 x 1.1 msec, variable Flip Angle (5°, 15° or 45°).

**Notes:** Acquired post gadolinium (post DCE-MRI acquisition); acquisition of 32 data points over 4 consistently acceptable heart beats.

#### 2.6.2.3.3 Variations for experiments IGRT and IGRTfx

**Magnet and Coil Used**: 7.0T, 25 mm-inner diameter quadrature birdcage coil (Rapid), with the exception of some baseline imaging that was done on the 4.7 T

**Animal Position**: Supine

**Physiologic Monitoring**: Respiration (respiratory balloon placed posteriorly), Heart Rate ECG leads in thorax.

**Imaging Parameters**: variable Flip Angle (5° and 10°).

**Notes:** Developments included a modification in the gating control by introducing dummy scans between heart beats to make the sequence more robust to motion. Auto-syringe injections and timestamps continued to be used.

## 2.7 Image Analysis

Right and left lung contours were generated on CT and MRI independently in ITK-SNAP, an open-source medical image processing application (243). Images were contoured using the 'snake tool', that uses intensity regions or image edges (as selected by the user) for automated segmentation, and then manually modified to ensure consolidated lung tissue was not excluded from the segmentation and/or retract contours from chest wall/ribs. All images were segmented by a single observer with a contouring reproducibility rate of > 95%. Right and left lung segmentations were used to evaluate radiation changes in following ways:

a) A semi-quantitative assessment of RILT was reported separately for CT and each MRI sequence used, by determining the percent volume of the irradiated lung demonstrating changes on CT or MRI using a scoring system modified from the one proposed by Lee et al (244). In Lee's scoring system individual scores were awarded for each of ground glass attenuation, bronchiectasis, reticular opacity, consolidation

bronchial wall thickening and honeycombing. To facilitate intermodality image comparisons, as well as comparison with pathology findings, a single combined severity score was used to describe any or all of those features. The scoring system applied was as follows: 0, absence of a reaction; 1, involvement in less than 5% lung; 2, involvement in 5-25%; 3, involvement in 25-50%; 4, involvement in 50-75%; 5, involvement in 75-100%.

b) Using multiple t-tests and regression analysis, changes in mean lung volumes and CT densities over time were evaluated and compared to RILT.

c) For study BLM, using a DCE-MRI sequence that was under development, the AUC and iAUC were generated from the raw MRI signal (in arbitrary units). Both AUC and iAUC were calculated in MATLAB (The Mathworks Inc., Natick, Massachusetts, U.S.A) by Dr. Danny Allen using each voxels within the segmented lung and then the mean of those values taken. The iAUC was the area up to 90 seconds after injection; AUC was the total area up to the shortest experiment time, which was 182 seconds.

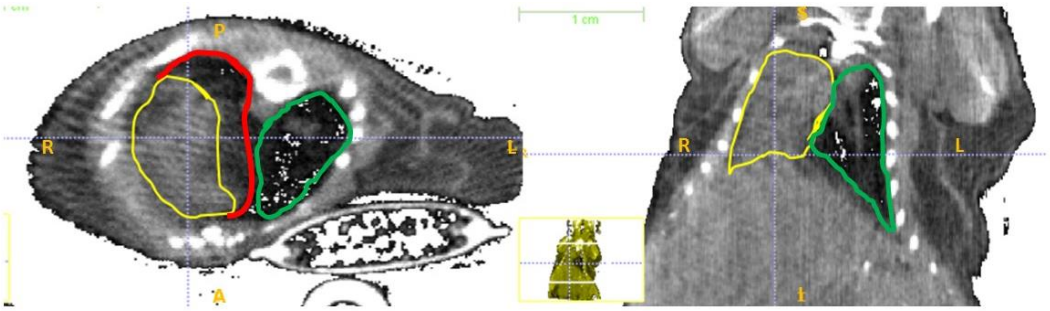



**Figure 2.5 Sample Coronal and Axial slices of SEMS MRI**. Right (red) and left (green) lung segmentations as well as the consolidated lung volume (yellow) representing RILT in the right lung.

From experiments NFV2 and BEZ-BKM, the fully quantifiable DCE-MRI sequence developed by Dr. Sean Smart and his team, was used for model-based and non-model based analyses. The non-model-based analysis was performed by determining iAUC and AUC values from the raw MRI signal with the assistance of Dr. Danny Allen.

For the model-based analysis, sample data from mice with and without known RILT was used to determine the model of best fit for sample data. After testing the classic Kety, Tofts, and extended Tofts models, the extended Tofts model was selected for analysis. Following validation of the model (see Figure 2.6), the extended-Tofts model was selected as it accounts for contrast concentration in blood plasma which makes up approximately 55% of the blood, whilst still assuming a well-mixed model. The fitting formula used was

$$C_t(t) = v_p C_p(t-\tau) + K^{trans} \int_0^{t-\tau} C_p\left(t-\tau\ -t'\right) \exp\left(-k_{ep}t'\right) dt' \quad (161).$$

Once the model was selected, $K^{Trans}$ , Kep, and Vp values were determined using PkView, a Viewer for 3D/4D data and Pk modelling developed by Dr. Ben Irving and Dr. Julia Schnabel (Post-doctoral researcher and Professor of the Institute of Biomedical Engineering, University of Oxford).

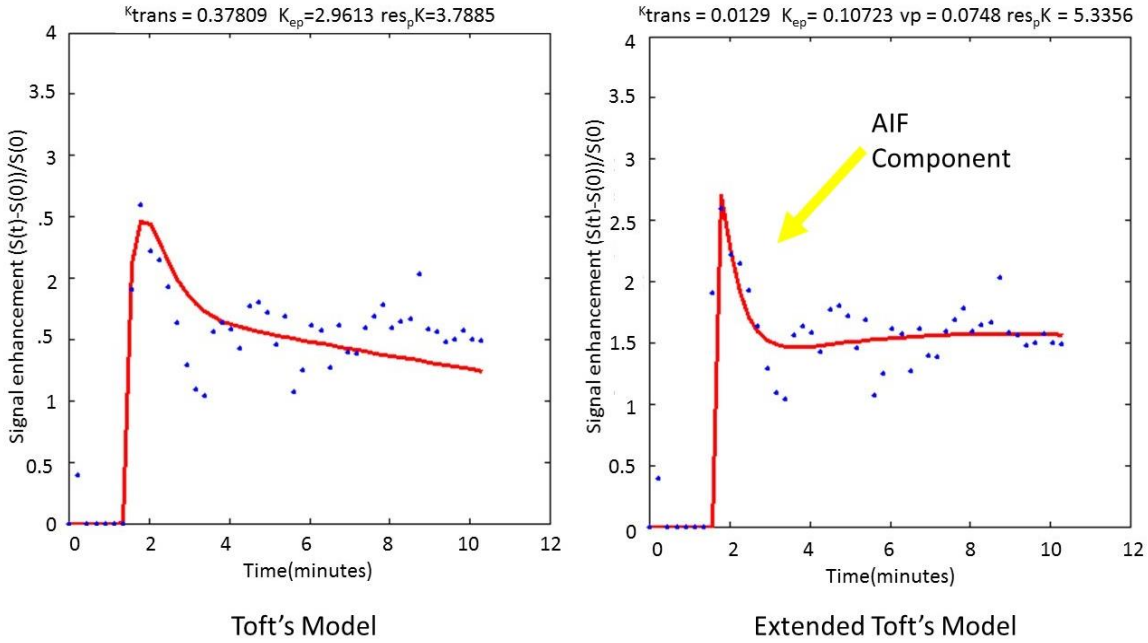



**Figure 2.6 DCE-MRI Model Fitting:** Plots demonstrating improved fit offered by the Extended-Tofts model by adding a arterial input factor (AIF) component when compared to the Toft's model. In this example signal enhancement is plotted against time to generate values of $K^{Trans}$, fractional plasma volume (vp), and Kep, which is a rate constant between the extravascular extracellular space (EES).

## 2.8 Statistical Analysis

Statistical analyses were performed by C. Kartsonaki (staff statistician) using R programming language (245) with plots generated in R and/or GraphPad Prism (version 6.00 for Windows, GraphPad Software, La Jolla, CA) and Microsoft Excel (Microsoft, Redmond WA). Due to the small number of animals sampled at each time point and the limited number of radiation reactions, inter- and intra- cohort and inter- and intra- modality comparisons using multiple t-tests (using pooled and discrete time-points), and linear regression models were determined to be the most suitable statistical methods of analysis. Regression models were fitted with the variable in question (e.g., breathing rate) as the response, with time and cohort as explanatory variables; using time first as a categorical variable (which allowed each time point to have its own estimated effect) and as a numeric variable. Additional models were used to include interactions for time and group, to demonstrate the effects of time for the control and experimental animals.

# Chapter 3

## *Preliminary Studies with C57BL6 and CBA Mice*

# 3 PRELIMINARY STUDIES

## 3.1 Introduction

The murine models investigated were C57BL6 and CBA mice, which are two of the most commonly used mouse strains for lung toxicity studies following thoracic and hemi-thoracic irradiation (175, 177, 178, 246). Both C57BL6 and CBA mice exhibit predictable patterns of RILT following radiation exposures with temporal onsets similar to humans (174).

This chapter describes the initial experiments undertaken locally to determine the appropriate protocol details required for such investigations. The aim of these experiments were to:

1) Establish a suitable mouse model locally for investigations of radiation pneumonitis
2) Establish a suitable radiation method and prescription dose to reliably produce radiation pneumonitis at 12 to 16 weeks following RT
3) Establish a MR imaging methodologies by which to detect radiation pneumonitis that are comparable to conventional methods of detecting radiation pneumonitis (e.g., pathology)
4) Compare RILT development in the presence and absence of a targeted radiosensitizer.

Central to this chapter was the establishment of reliable MRI imaging protocols for the comparison of normal and irradiated lungs. These imaging protocols included a spin echo multi-slice sequence (SEMS) for the detection of normal (and abnormal) anatomy, and a dynamic contrast enhanced (DCE) imaging method that has been reported as showing promise in assessing parenchymal perfusion in patients with other lung diseases such as COPD, emphysema and asthma (153, 247-250). Due to the inherent difficulties of MRI

acquisition in the lung, the ability to use these images qualitatively or quantitatively is primarily dependent on the ability to perform effective cardiorespiratory gating.

## 3.2 Preliminary Studies - C57BL6 Mice

Two experiments were undertaken using the C57BL6mice:

1. Experiment RT: Single fraction 18 Gy radiation (n = 15) vs. Sham irradiation (n = 15)
2. Experiment NFV: Three daily administrations of nelfinavir 1mg/mL @ 20 mg/Kg (n = 15) vs three daily administrations of Nelfinavir followed by a single fraction of 18 Gy radiation (n = 15)

### 3.2.1 Experiment RT

All irradiations were performed on the cabinet irradiator as described in Chapter 2 using a single posterior field delivered to the right thorax. Animals in this experiment were followed to a maximum of 16 weeks following radiation. Figure 3.1 is a schematic of the preliminary C57BL6 studies.

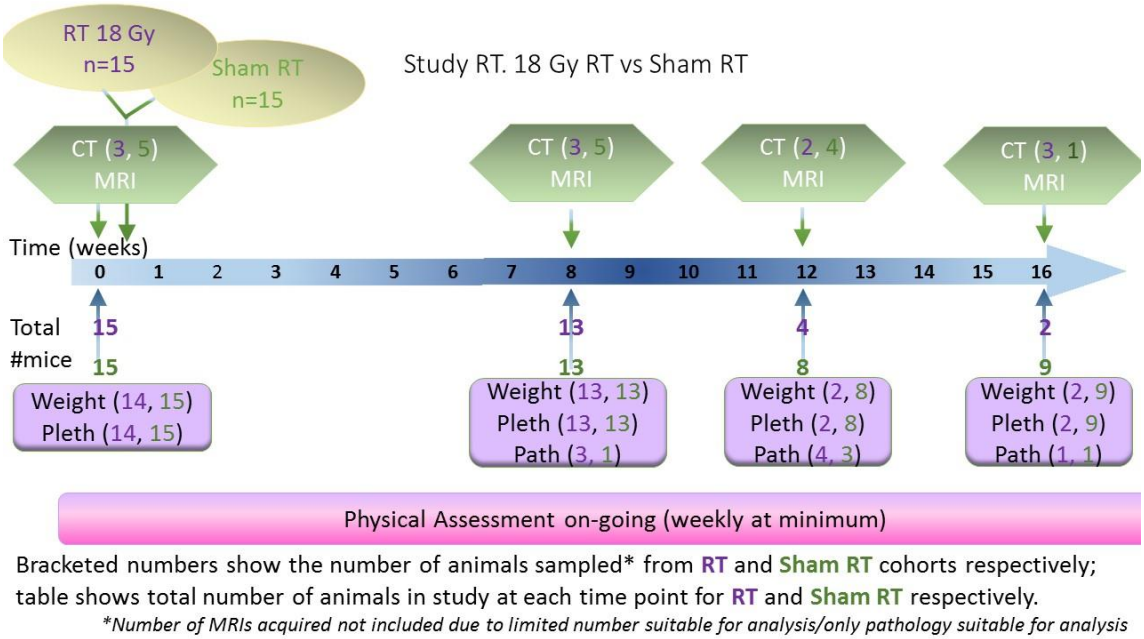



**Figure 3.1 RT Experimental Schema**

Baseline measurements were acquired for 30 female C57BL6 mice that underwent single fraction irradiations of 18 Gy (n = 15) or sham irradiation (n = 15) to the right lung. Animal mean weights at baseline were 20 g (range 18 – 23 g) and the mean respiratory rate was 364 BPM (range 326 – 403 BPM). Table 3.1 details the number of animals evaluated at each time point using plethysmography, imaging (MRI and CT) and pathology.

**Table 3.1 Table of Animals Evaluated at each Time Point in Study RT**

| | Baseline | Week 8 | Week 12 | Week 16 |
|---|---|---|---|---|
| **Weights** | All | 25 | 9 | 11 |
| **Plethysmography** | All | 26 | 10 | 11 |
| **MRI** | 3RT/6sham | 3RT/5Sham | 2RT/4Sham | 3RT/1Sham |
| **CT** | 3RT/6sham | 3RT/5Sham | 2RT/4Sham | 3RT/1Sham |
| **Pathology** | None | 4RT | 2RT | 1RT |

### 3.2.1.1 *Results*

#### 3.2.1.1.1 Physical Assessment and Plethysmography

Four of 30 mice required unscheduled anaesthesia due to moist desquamation or ulceration caused primarily by over-grooming following an initial dry desquamation in the irradiated area (n = 2), ulcerations of their feet (n = 1), and one animal developed a mass on her the shoulder, the origin of which remains uncertain. Otherwise animals in both the irradiated and control groups showed no adverse events over the course of the experiments, as judged by general appearance, activity and weights.

| Cohort | Baseline (mean; range) | 8 weeks (mean; range) | 12 weeks (mean; range) | 16 weeks (mean; range) |
|---|---|---|---|---|
| **Sham** | 19.7; 18.5-20.7 | 22.3; 21.5-23.7 | 24.0; 22.3-25.8 | 24.8; 23.0-28.1 |
| **Irradiated** | 19.4; 18.2-20.5 | 22.6; 22.5-22.6 | 21.4; 22.3-23.0 | 22.7; 21.3-24.0 |

**Table 3.2 Population Mean (range) Weights of Animals in grams for Study RT**

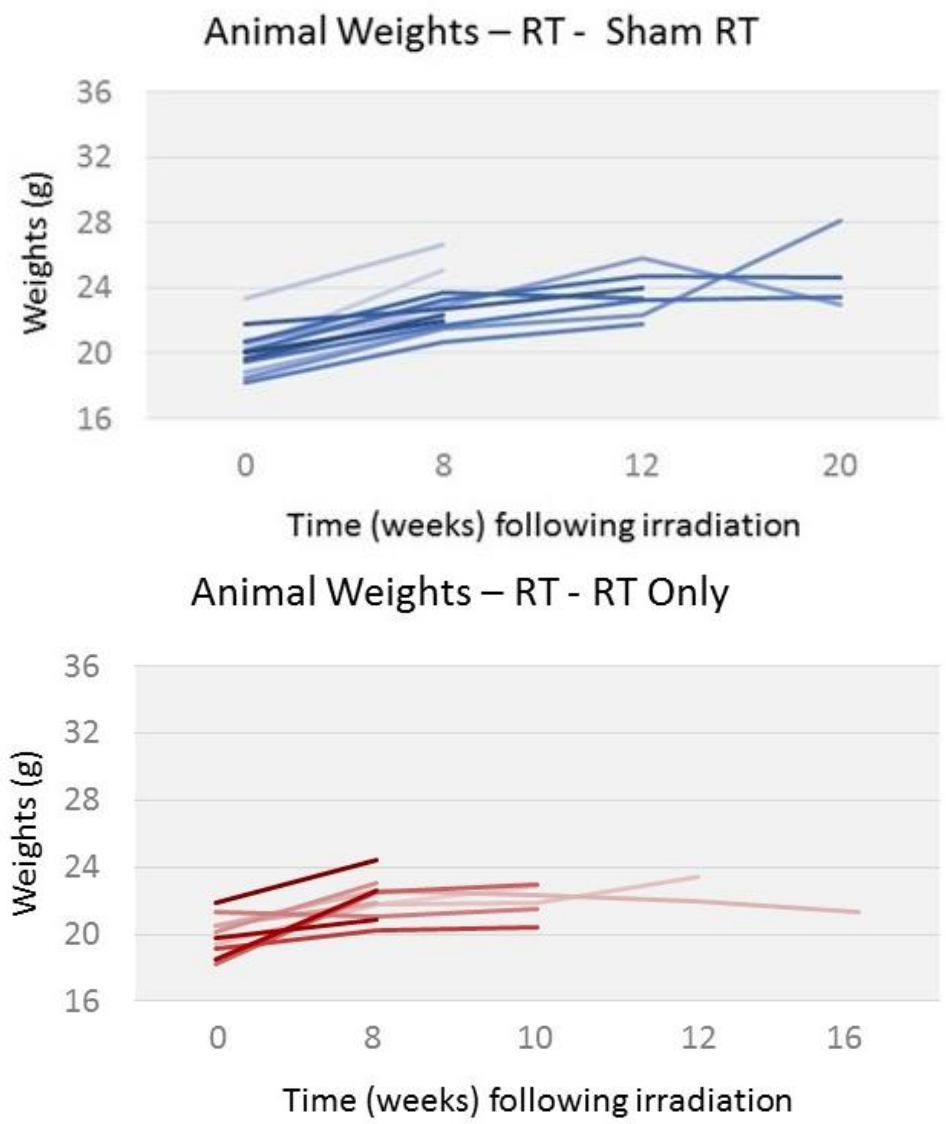



**Figure 3.2 Animal Weights for Study RT:** Plots of weights of animals on study from baseline to 16 weeks following irradiation for control animals (top) and animals receiving 18 Gy RT to the right lung.

One of the irradiated mice lost 6% of her maximum weight (22.6 g) at 8 weeks post-radiation, to the time of the end of study. This weight loss was enough to warrant an increase in the frequency of observation of this mouse, however not enough (≥ 15%) to warrant unscheduled euthanasia. Over all animals observed, this was the only animal receiving radiotherapy that experienced weight loss.

There was little change in breathing rate on plethysmography in either cohort which was not suggestive of RILT. Figure 3.3, plots individual and population mean breathing rates of all animals evaluated at each time point, which varied little between cohorts or over time (with the exception of the occasional outlier). Paired t-tests of the data, show there is no significant difference in the breathing rates of the animals treated with radiation or sham irradiation. However the statistical relevance may have been observed if there were more animals available at weeks 12 and 16.

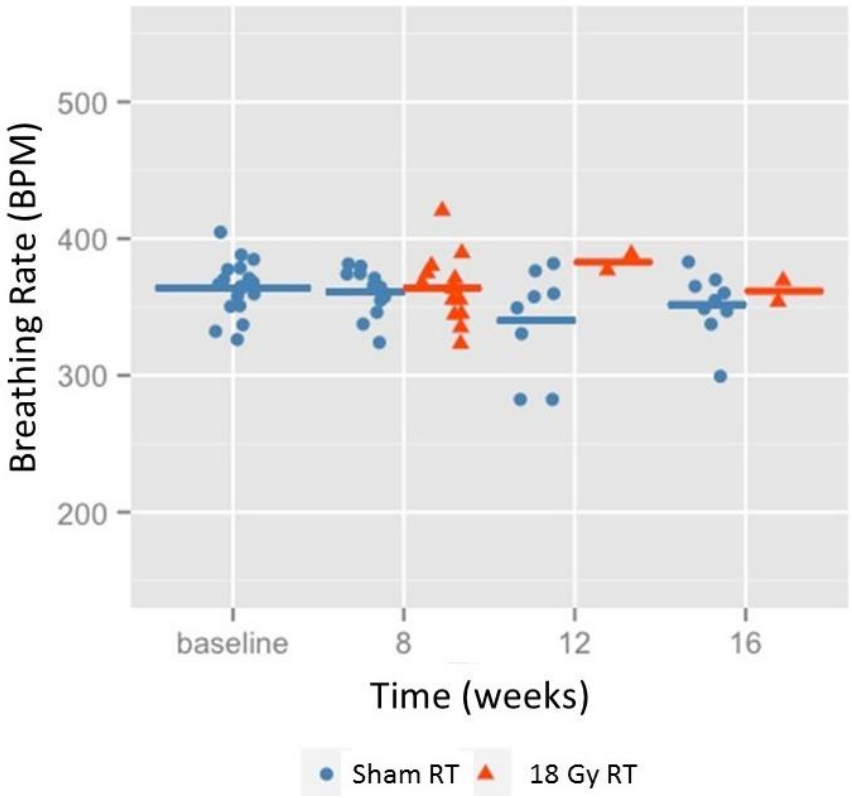



**Figure 3.3 Breathing Rates for Study RT:** Scatter plot of individual and population mean breathing rates for mice receiving sham RT or 18 Gy RT to the right lung.

Based on previous reports, an increase in breathing rate of > 35% was selected as the definitive threshold indicating radiation induced lung toxicity for the experiments in this thesis. The results presented here indicate a maximum population change in BPM of - 7% and + 6%. One outlier in the irradiated group demonstrated a 15% increase in BPM at week

8. This animal demonstrated no associated weight loss, with weights recorded as 19.1 g, 20.2 g, and 20.4 g at baseline week 8 and week 12 respectively.

#### 3.2.1.1.2 MRI

MRI was acquired in one to six animals at each time point, following baseline, however image analysis was not feasible due the challenges caused by difficulties optimising the cardio-respiratory gating and the fact that no animals experienced detectable radiation pneumonitis.

Below are examples of this variation in MRI quality. Figure 3.4 shows axial and coronal SEMS images of three animals imaged at 8 weeks following 18 Gy irradiation, none of which show radiation pneumonitis. The images on the left contain significant motion artefact (caused by insufficient gating), the images in the centre show poor signal, and the images on the right show an image acquisition with poor lung quality.

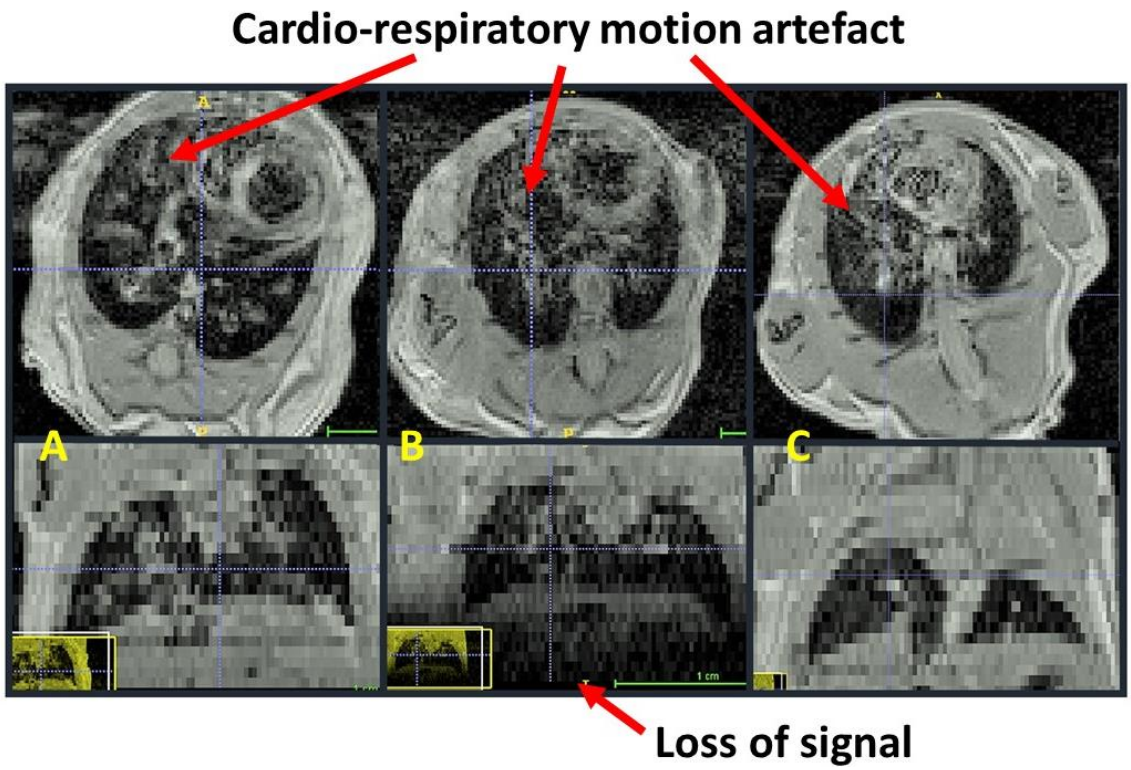



**Figure 3.4 SEMS Image Quality:** Corresponding axial and sagittal SEMS images demonstrating variability in image quality, and cardiorespiratory artefact. Examples from three mice (A, B, and C) at 8 weeks following RT.

#### 3.2.1.1.3 CT

Of a total planned 24 CT acquisitions, 19 were acquired and suitable for analysis; eight at baseline, four at eight weeks, three at twelve weeks, and four at 16 weeks following radiation respectively. Of the images suitable for analysis following baseline 4 were irradiated and 9 underwent sham irradiation.

For all evaluable images (n = 19), right and left lung segmentations were generated in ITK-Snap as seen in Figure 3.5 and assigned a RILT score as described in Chapter Two (section 2.7). All lungs in both cohorts were assigned a RILT score of 0 (no lung volume demonstrating radiological changes compared to baseline images).

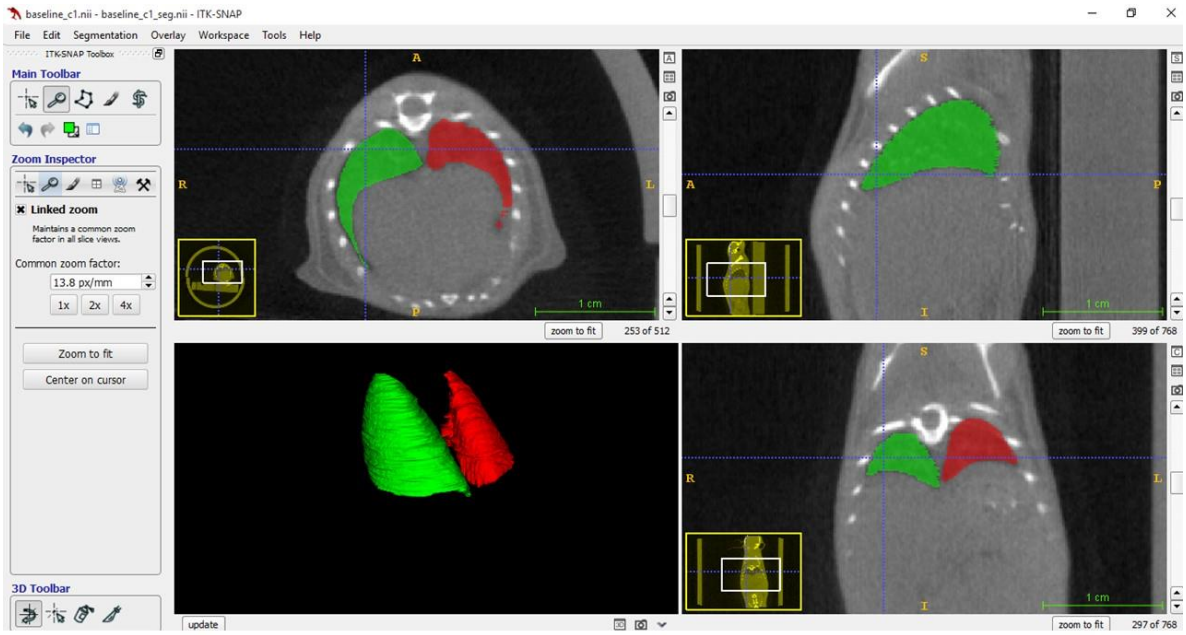



**Figure 3.5 Image Segmentation in ITK-Snap:** Screen capture of lung CT in ITK-Snap with right (red) and left (green) lungs contoured in the axial (top left), sagittal (top right) and coronal (bottom right) planes, and a 3-dimensional (3D) representation (bottom left).

Paired t-tests determined that the right lungs were significantly larger than the left lungs ($P = 2.044e^{-05}$), however both continued to increase in size as the mice aged. There was no difference in the size or rate of growth between the right lung volumes for the sham irradiated and irradiated animals at any time point

#### 3.2.1.1.4 Pathology

Single sections including both lungs were extracted from 8, 12, and 16 weeks following irradiation and stained with H&E. No samples were extracted from sham irradiated mice. Due to the sub-optimal staining quality (caused by storage in ethanol for transport as requested by the preliminary processing team), there was a low degree of confidence in the scores generated. The maximum severity scores reported were two out of five. This score was assigned to lung sections from two mice at 8 weeks post irradiation and two mice at 12 weeks post irradiation. No reactions were observed in the unirradiated (left) lungs. Figure 3.6 plots the number of animals sampled at each time point and their respective severity score.

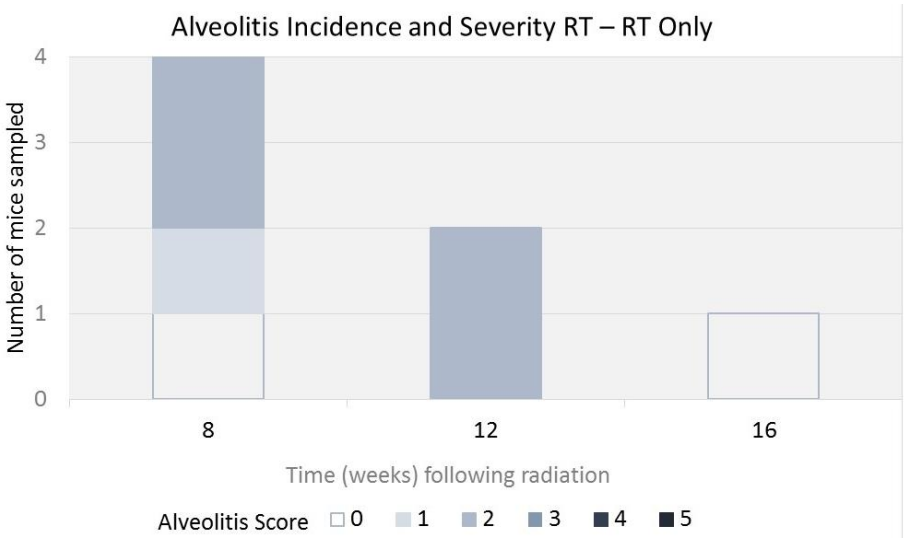



**Figure 3.6 Alveolitis for Study RT:** Bar plots of the incidence and severity scoring for alveolar inflammation in studies RT.

### 3.2.1.2 *Discussion*

Limited data was generated in experiment RT, and this was due to several factors. These include the acquisition of suboptimal MRI images that were the result of insufficient gating, user error (i.e., failing to remove the couch from the FOV during acquisition), and a ring artefact that resulted from a failure to calibrate the scanner following the installation of a new x-ray tube. Due to ethical limits on frequency and duration for which animals could be anesthetised, repeat imaging was not always permitted in the event that imaging data were of insufficient quality for analysis. However examination of the available data shows that radiation pneumonitis could not be detected using plethysmography, CT or MRI. The histopathological analysis cannot be reported with confidence, due to poor specimen quality and low specimen numbers examined.

### 3.2.2 Experiment NFV

#### 3.2.2.1 *Rationale*

Experiment NFV compared the effects of NFV alone to NFV plus radiation using plethysmography, histopathology, CT and MR imaging. All animals in this experiment received three daily doses of NFV as described in section 2.4.1. Half of the animals (n = 15) received a single dose of 18 Gy, delivered using the cabinet irradiator ass described in section 2.3.1. Animals were followed to a maximum of 16 weeks following irradiation.

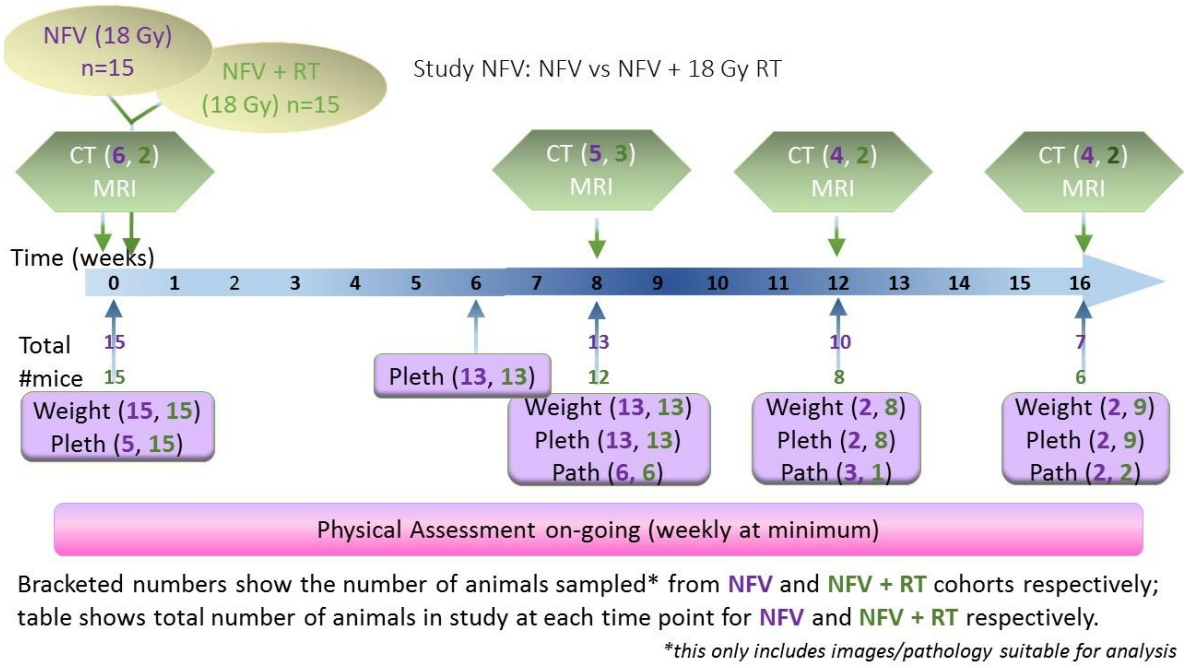



**Figure 3.7 NFV Experimental Schema**

#### 3.2.2.2 *Results*

##### 3.2.2.2.1 Physical Assessment and Plethysmography

Animals receiving NFV alone or radiation plus nelfinavir were observed up to 16 weeks following irradiation. Eleven animals required unscheduled euthanasia: two receiving NFV alone and nine undergoing radiation following three daily doses of NFV.

Nine animals experienced moist desquamation or ulceration caused by over-grooming following an initial period of dry desquamation in the irradiated area, and two animals experienced ulcerations of their tail thought to be caused by overheating of the heating pad in the MRI.

No animals required unscheduled euthanasia due to weight loss. Figure 3.8 shows that the majority of animals gained or maintained weight over the course of the experiment. The asterisks in Figure 3.8 below indicate two animals euthanized at 14 weeks following irradiation due to desquamation lasting 24 hours, and that had weights assessed prior to the euthanasia.

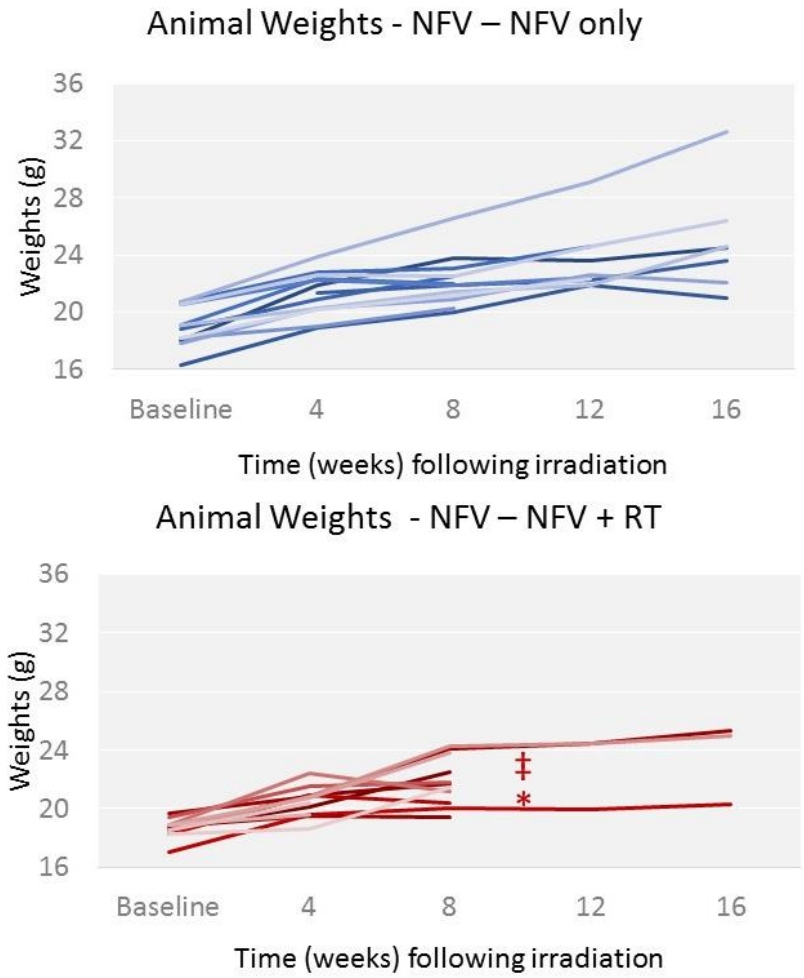



**Figure 3.8 Animal Weights for Study NFV:** Plots of weights of animals on study from baseline to 16 weeks following irradiation for animals receiving NFV (top) or NFV plus 18 Gy RT to the right lung.

Similar to the previous experiment, plethysmographic assessment did not indicate radiation induced lung damage. Figure 3.9 details these changes over time, demonstrating no significant difference in breathing rates between the study cohorts (P = 0.9934).

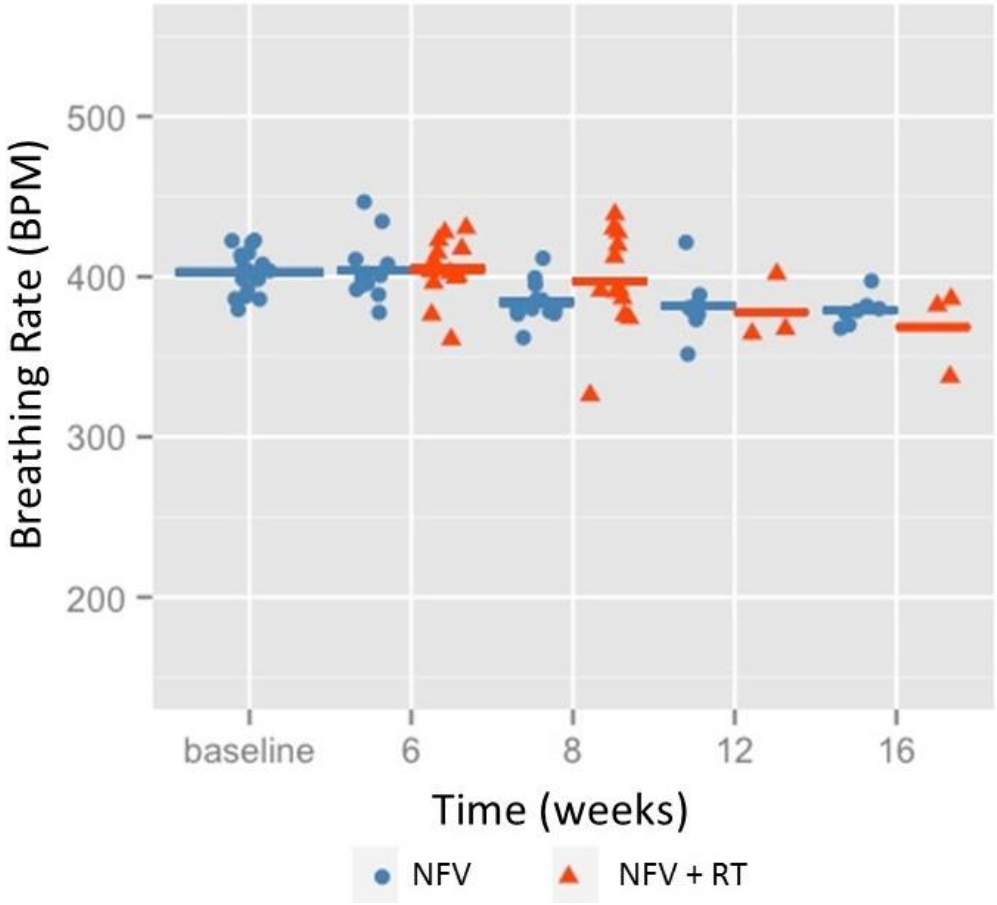



**Figure 3.9 Breathing Rates for Study NFV:** Scatter plot of individual and population mean respiratory rates for all animals evaluated at baseline, 6, 8, 12, and 16 weeks following RT for animals receiving NFV (blue) or NFV + 18 Gy RT (red).

#### 3.2.2.2.2 MRI

MRI acquisition and respiratory gating was very much under development throughout this experiment. A single animal demonstrated limited lung consolidation at 16 weeks following 18 Gy irradiation plus NFV as shown in Figure 3.10. In this series of axial images, yellow arrows indicate lung changes due to radiation and red arrows, highlight noise caused by respiratory-cardiac motion. If assessing these images using raw signal intensity (SI) or a

percent change in SI between irradiated and unirradiated lungs, the result would be obscured by the motion artefact.

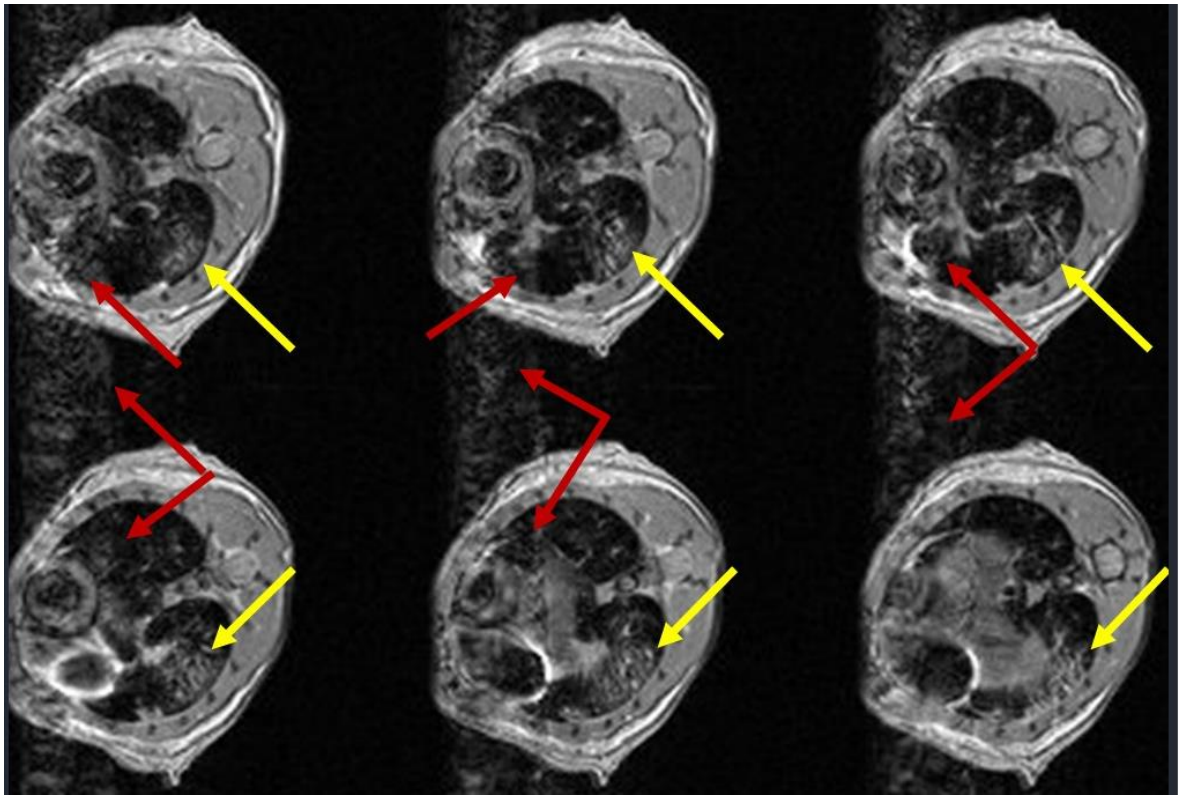


**Figure 3.10 Respiratory Motion Artefact versus Pneumonitis on MRI.** Serial axial images on SEMS MRI demonstrating motion artefact (red arrows) and radiation pneumonitis (yellow arrows) in a single mouse lung.

3.2.2.2.3 CT

Thirty-six CT acquisitions were made at baseline, 8, 12, or 16 weeks following irradiation. Image quality was sufficient for lung segmentation and scoring in a total of 24 CTs; 8, 5, 4, and 7 CTs acquired at baseline, 8, 12, and 16 weeks following irradiation respectively. As described in Chapter Two (section 2.7) the RILT scores were determined independently for CT and MRI. The maximum score assigned to any CT dataset was 1/ 5, in a single mouse imaged at 16 weeks following radiation plus NFV. This is the same animal as shown on the SEMS MR imaging in Figure 3.10, where the RILT score was two.

#### 3.2.2.2.4 Pathology

Alveolar inflammation and fibrosis scores were reported for 20 samples from study NFV1. Figure 3.11 summarizes the incidence and severity of alveolitis for both arms of the study.

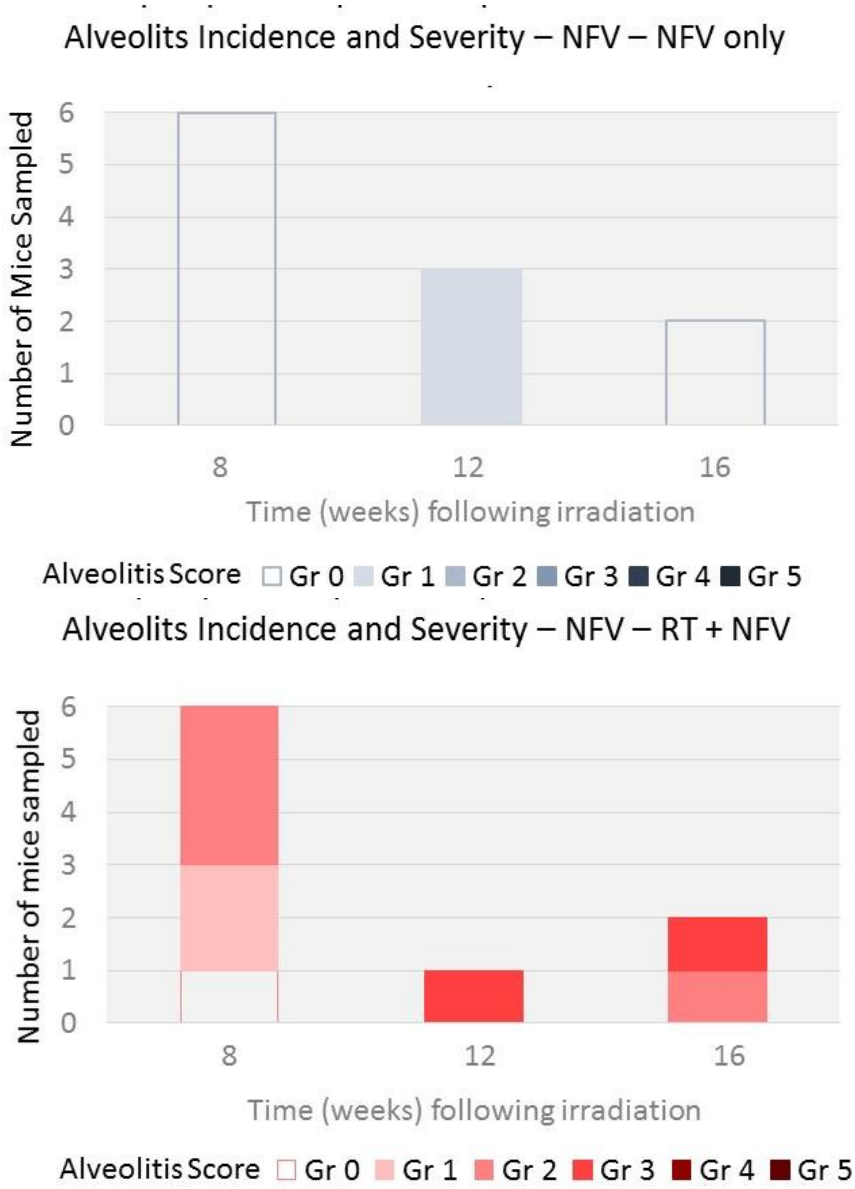



**Figure 3.11 Alveolitis for Study NFV:** Bar plots summarizing the incidence and severity of alveolitis scored on H&E stained lung sections for animals having received NFV (top) or NFV + RT.

Plots showing fibrosis are not shown as fibrosis was reported in only one mouse, at 16 weeks following irradiation. Early radiation changes greater than Grade 2 occurred in one

lung sampled at 12 weeks following radiation (RT + NFV) and one of two mice sampled at 16 weeks following radiation (RT + NFV). At both 8 and 16 weeks post treatment none of the samples from the NFV only group demonstrated alveolar inflammation or fibrosis.

#### 3.2.2.3 ***Discussion***

Despite dosimetric characterization of the Cabinet Irradiator (the results of which are described in Appendix 1), and confirmation of geometric accuracy of radiation delivery as confirmed by discolouration and loss of fur in the irradiated animals, the incidence of radiation damage (pneumonitis or fibrosis) was limited. As such modifications were made to experimental protocols in attempts to increase the frequency of RILT. These included

1) Using a parallel opposed pair (POP) technique to distribute the dose more evenly,
2) Increasing the length of observation following irradiation from 16 to 20 weeks, and
3) Selecting a new mouse model for further experimentation.

MRI quality continued to be hindered by the ability to ensure appropriate cardiorespiratory triggering. With the animals' respiratory rates reduced to 30-40 BPM, with approximately five heartbeats per breath, variable but very short TEs were required to achieve gating. Variations in respiratory or cardiac rhythms greatly affected the image quality. These variations could be caused by changes in animal temperature, coughing or sneezing. Additionally, the placement of cardiac leads (in the posterior head) and respiratory balloons could affect the magnitude of the signals received by the system. An important part of these early studies was to develop user expertise, and methods for ensuring greater consistency in CR gating.

## 3.3 Preliminary Studies – CBA Mice

### 3.3.1 Introduction

Based on the results of the preliminary studies using C57BL6 mice, and expanding the focus of the literature search from partial or single lung to whole thorax irradiation to determine which animals strains are radiation pneumonitis sensitive, (173, 175), it was decided to use CBA mice in the next set of experiments.

Experiments RT and NFV were essentially repeated in the CBA mice with a few minor changes to imaging technique, and longer follow-up to a maximum of 20 weeks. A third experiment with a view to producing a positive control using Bleomycin in combination with radiation was undertaken. Bleomycin (BLM), is an anti-tumour antibiotic isolated from Streptomyces verticillus (251) that is used as a chemotherapeutic agent, primarily in the treatment of germ cell tumours. A major therapeutic limitation of BLM is that it is induces lung fibrosis (fibrosing alveolitis) in up to 10% of patients receiving the drug (252, 253). Bleomycin, also causes pulmonary toxicity in mice, (254-257) the time course of which has been studied in C57BL6 and CBA mice, and is the reason this drug was selected as a positive control in combination with radiation. Because the observation of radiation pneumonitis (as opposed to fibrosis) was the main objective, a conservative dose of BLM was selected.

The preliminary experiments undertaken in CBA mice were:

1. Experiment RT2: Single fraction 18 Gy radiation (n = 13) vs. Sham irradiation (n = 13) followed to 20 weeks post radiation
2. Experiment BLM: Single IP injection of Bleomycin (80 mg/Kg) followed two hours later by a single fraction of 14 Gy (n = 12) or a single fraction of 18 Gy radiation (n = 9) followed to 14 and 20 weeks post radiation respectively

3. Experiment NFV2: Mice receiving 20 Gy RT (n = 14) alone vs. 20 Gy RT + NFV (n = 12) followed to 20 weeks post radiation

As above, all irradiations were performed on the Cabinet Irradiator as described in section 2.3.1. Animals in this experiment were followed until 14 (BLM cohort) or 20 (RT only cohort) weeks following radiation.

### 3.3.2 **Experiment RT2**

#### 3.3.2.1 ***Rationale***

The preliminary RT versus Sham RT experiment was repeated in the newly selected mouse model with a view to capturing radiation pneumonitis on MRI, and providing a platform for RT toxicity experiments involving PI3K/AKT inhibitors. Figure 3.12 is a schematic of Experiment RT2.

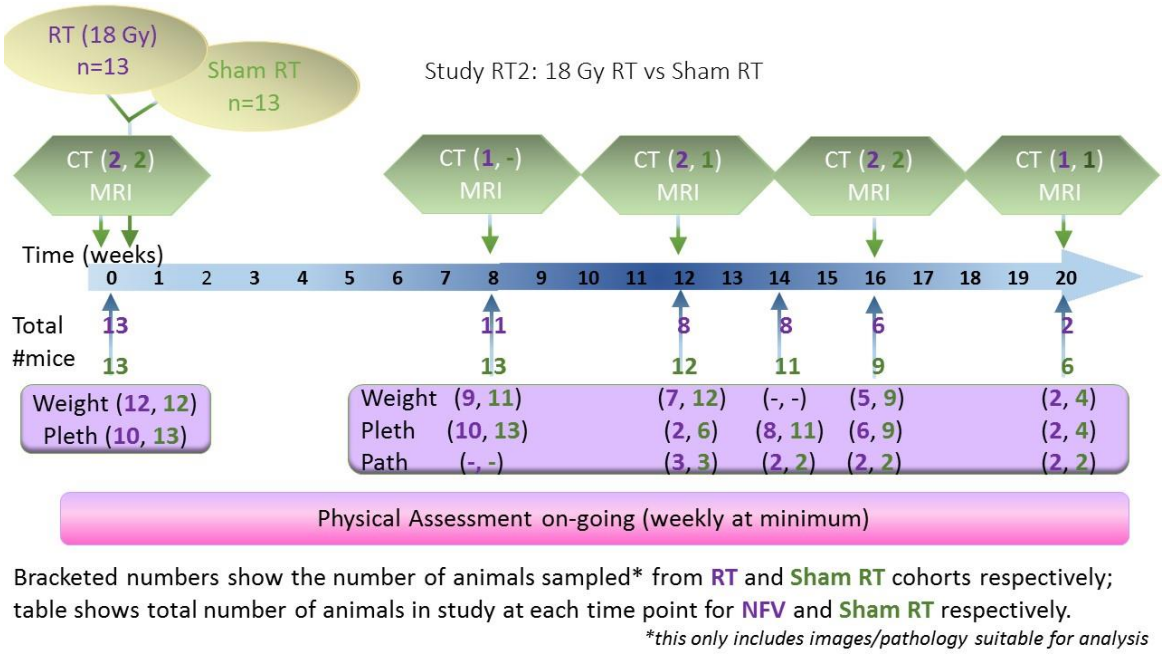



**Figure 3.12 RT2 Experimental Schema**

### 3.3.2.2 *Results*

#### 3.3.2.2.1 Physical Assessment and Plethysmography

Twenty-six 10 to 12 week old, female CBA mice underwent right lung irradiation (n = 13) or sham irradiation (n = 13). Based on the skin reactions observed in the previous experiments half of the dose was delivered from the anterior and half from the posterior.

No mice were identified as failing to thrive based on weight loss, however there was a marked difference in the weight gain of the mice treated with radiation vs those treated with sham irradiation as demonstrated in Figure 3.13.

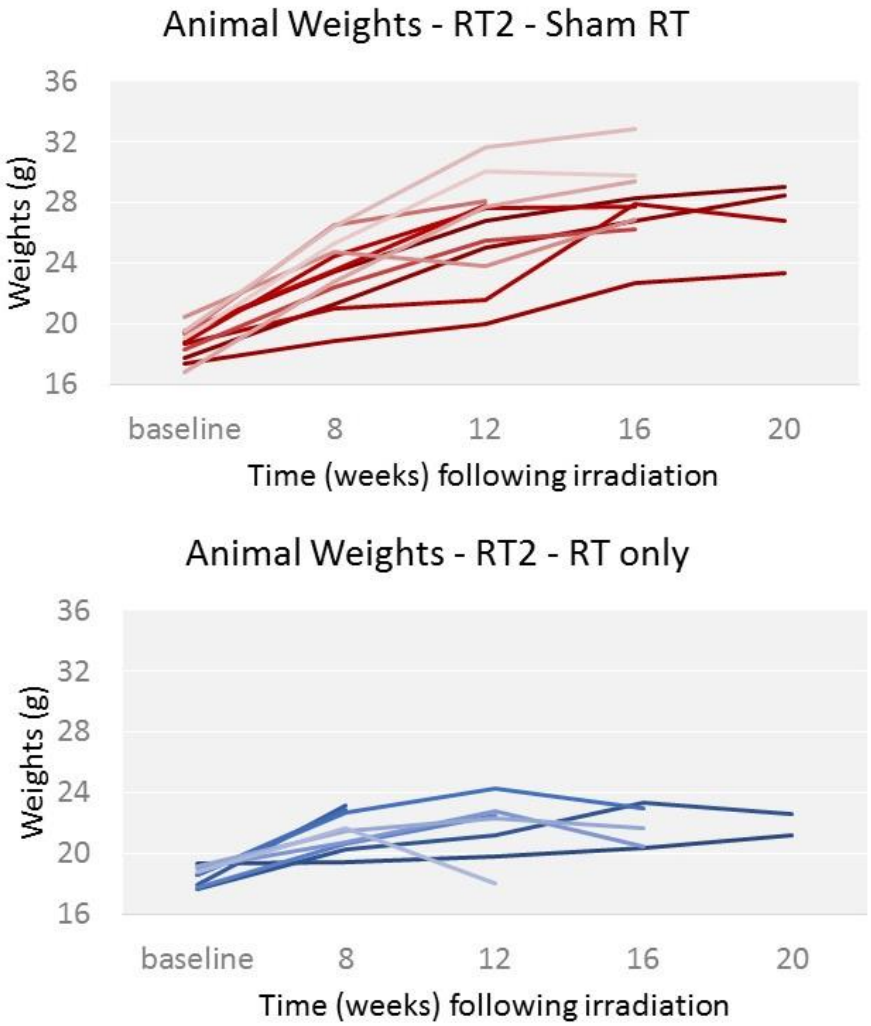



**Figure 3.13 Animal Weights for RT2:** Plots of animal weights for mice on study from baseline to 20 weeks following irradiation for control animals (top) and animals receiving 18 Gy RT to the right lung.

There was very little difference in the plethysmographic results between the irradiated and non-irradiated animals with the only notable difference being at 12 weeks where the mean respiratory rate of the irradiated animals increased from 389 BPM at baseline to 423 BPM (+10%) and 392 BPM (+0.7%) in the unirradiated animals. There was no significant difference between cohorts at this time point ($p = 0.712$) or over the experiment as a whole ($p = 0.2092$), using a two-tailed non-paired t-test and an interactive linear regression with group and time respectively. Figure 3.14 plots the plethysmographic results for irradiated and unirradiated cohorts.

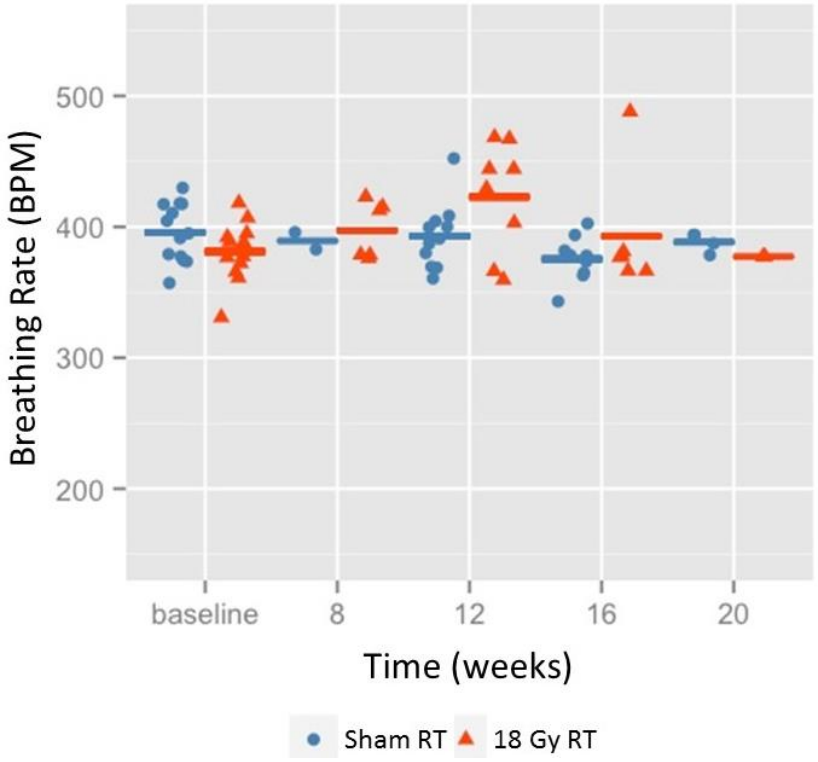



**Figure 3.14 Breathing Rates for Study RT2:** Scatter plot of individual and population mean animal weights for control animals (blue) and animals receiving 18 Gy to the right lung (red).

#### 3.3.2.2.2 CT

Fourteen of 20 CT scans acquired from baseline to week 20 were suitable for segmentation and evaluation. Figure 3.15 is a representative image of the only mouse to

demonstrate radiographic changes. The right lung on this CT was given a score of five of five, at 16 weeks post irradiation. All other images assessed following radiation were scored as 0 (no lung volume demonstrating radiologic changes). The animal in image 3.15 had the second highest breathing rate at this same time point, and a 7% weight loss between weeks 8 and 12. The largest weight-loss observed was a 10% loss between weeks 12 and 16 in another mouse in the same cohort.

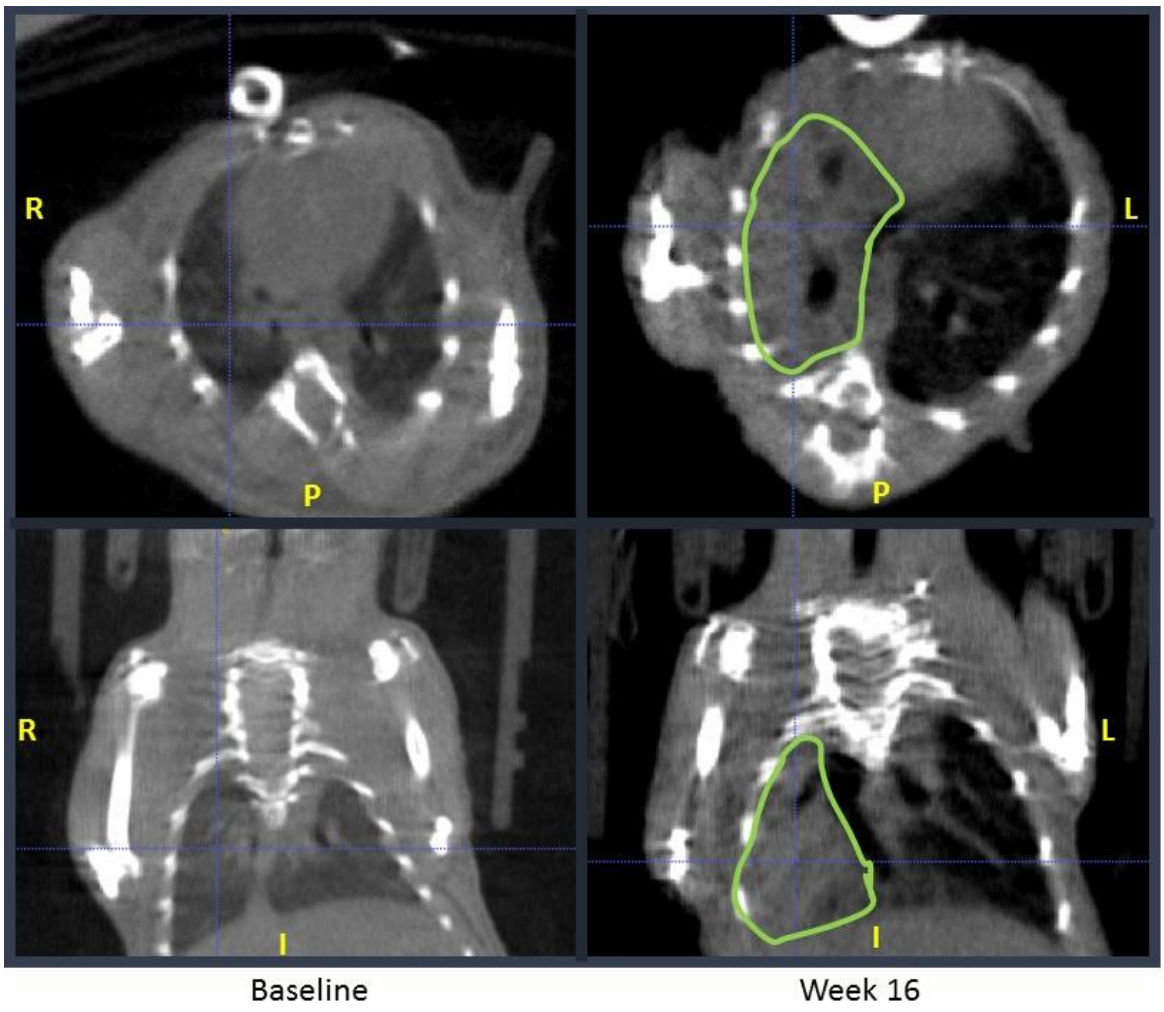



**Figure 3.15 RILT at 16 Weeks Compared to Baseline on CT:** Axial (top) and coronal (bottom) CT slices for a single mouse at baseline (left) and 16 weeks (right) post irradiation showing near complete lung consolidation at 16 weeks, segmented in green.

#### 3.3.2.2.3 Pathology

The earliest signs of alveolitis were observed on pathology at 16 weeks following irradiation. Grade Two alveolitis was observed in both irradiated and non-irradiated animals, therefore only scores greater than Grade Two were interpreted as radiation pneumonitis. This was observed in a single irradiated animal at week 16.

### 3.3.3 **Experiment BLM**

#### 3.3.3.1 ***Rationale***

Bleomycin (BLM), is an anti-tumour antibiotic isolated from Streptomyces verticillus (251) that is used as a chemotherapeutic agent, primarily in the treatment of germ cell tumours. Bleomycin, causes pulmonary toxicity in mice, the time course of which has been studied in a number of mouse strains including C57BL6 and CBA mice, and is the reason this drug was selected as a positive control in combination with radiation in this thesis.

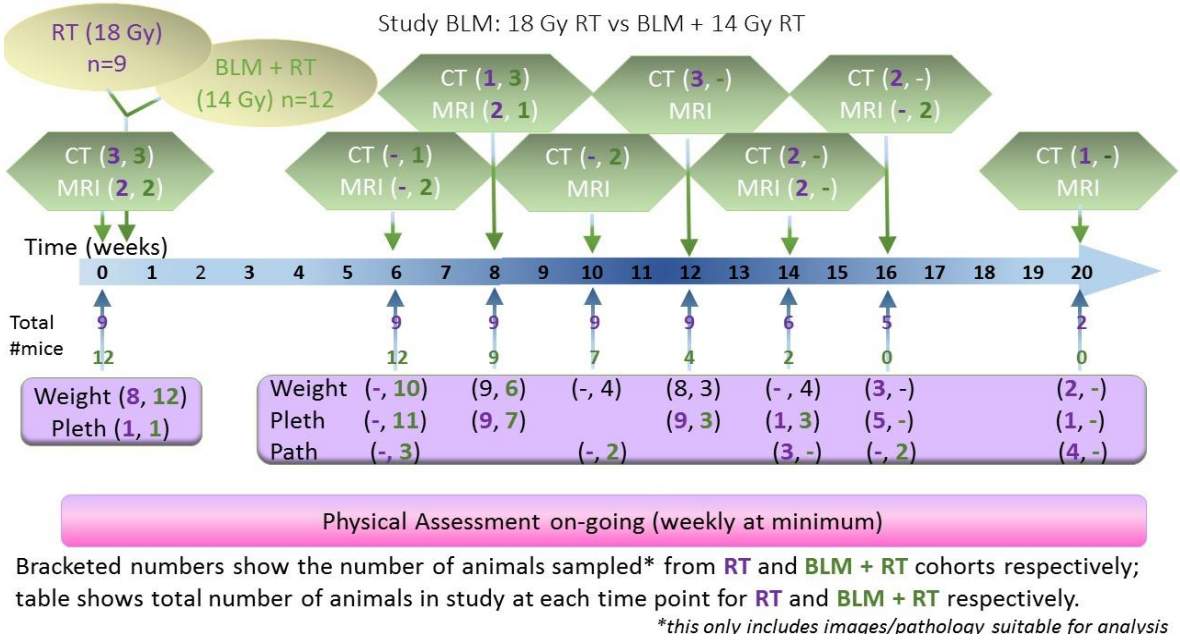



**Figure 3.16 BLM Experimental Schema**

### 3.3.3.2 *Results*

#### 3.3.3.2.1 Physical Assessment and Plethysmography

It was anticipated animals receiving Bleomycin and radiation would suffer adverse effects and therefore, no animals in this cohort were maintained past 14 weeks. Animals receiving RT alone, were followed to 20 weeks. Notable weight losses were observed only in two animals receiving RT alone

Figure 3.17 shows little variability in breathing rate in animals undergoing RT + BLM. The animals irradiated with 18 Gy alone showed increased breathing rates at all time points following baseline, with significant changes at weeks 12 (21% increase) and 16 (17% increase ) weeks following irradiation. Two outliers showed decreases of 13% and 7% at weeks 14 and 16 respectively.

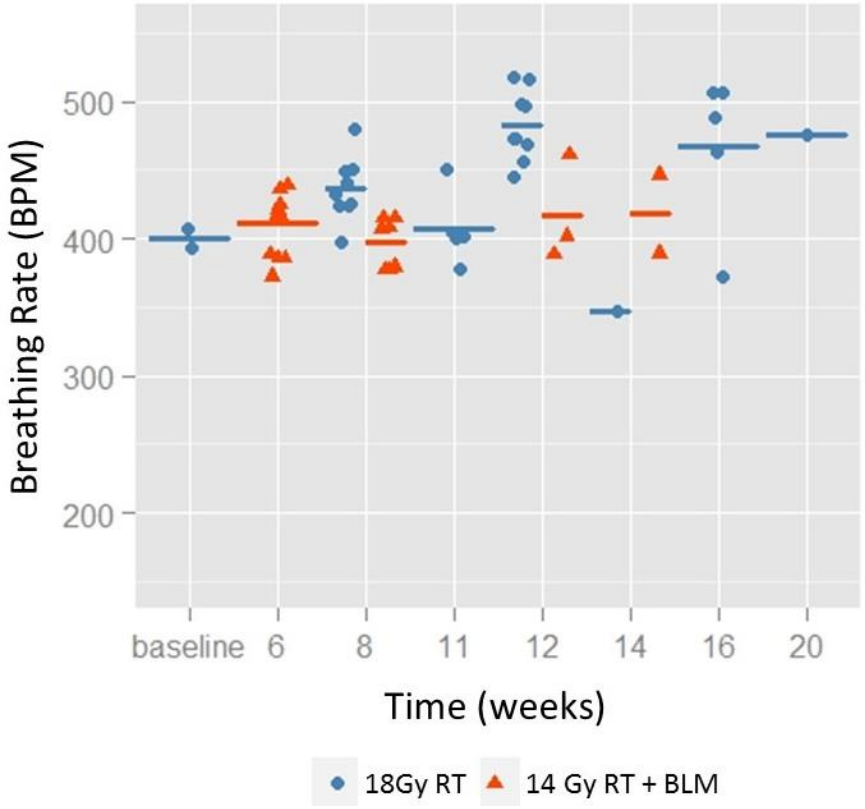



**Figure 3.17 Breathing Rates for Study BLM:** Scatter plot of individual and population mean respiratory rates of mice receiving 18 Gy to the right lung (blue) or 14 Gy to the right lung plus BLM (red).

#### 3.3.3.2.2 MRI

In addition to SEMS images, the development of a dynamic contrast enhanced (DCE-MRI) imaging protocol was undertaken, with the assistance of Dr. Sean Smart. In brief, a 3D, cardiorespiratory gated gradient echo sequence with a TE of 0.6 msec, TR of 1.1 msec, 64 x 64 Phase Encodes (PE) and an acquisition Field of View (FOV) of 5.4 x 2.7 x 2.7 cm was used. A bolus of 0.3 µL Gadolinium (Omniscan, GE Healthcare) was injected following 10 'dummy' scans (or repeats). DCE-MRI was attempted at each imaging session (n = 49) and 11 images were suitable for analysis; four at baseline, two at week six, three at week 8, and one from each of weeks 14 and 16 (Figure 3.18).

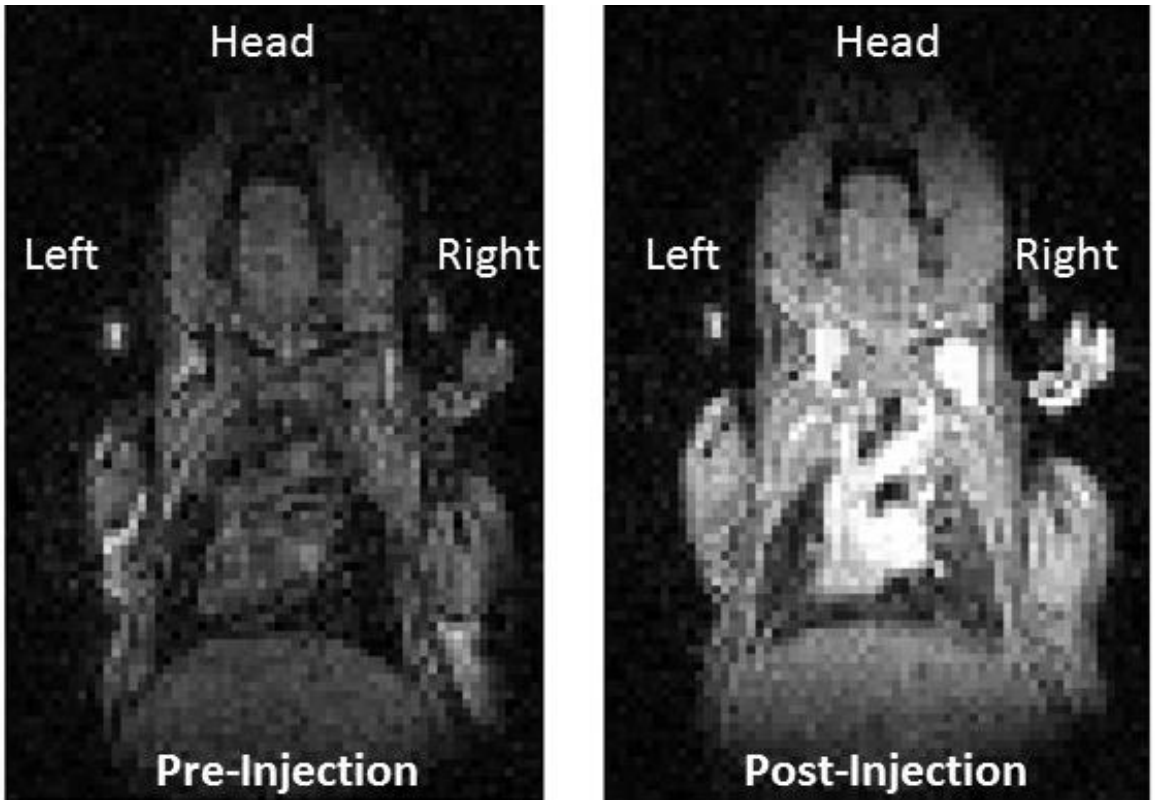



**Figure 3.18 Coronal DCE-MRI:** Coronal DCE-MRI slices prior to (left) and post (right) Gd- DTPA injection in mouse showing no RILT 12 weeks following irradiation.

Images were unsuitable for analysis primarily due to insufficient gating or an absence of contrast uptake (likely due to poor vascular access). The sequence relied heavily on robust

cardiorespiratory gating as it attempted to acquire data on every heartbeat, as such insufficient cardiac signal, or irregular heartbeats greatly affected the success of this image acquisition.

Figure 3.19 plots the changes in initial area under the curve (iAUC) in the right and left lungs plotted against time. Insufficient images were available to comment on the usefulness of this imaging method in the detection of radiation pneumonitis. Based on these results the sequence was further modified for subsequent experiments.

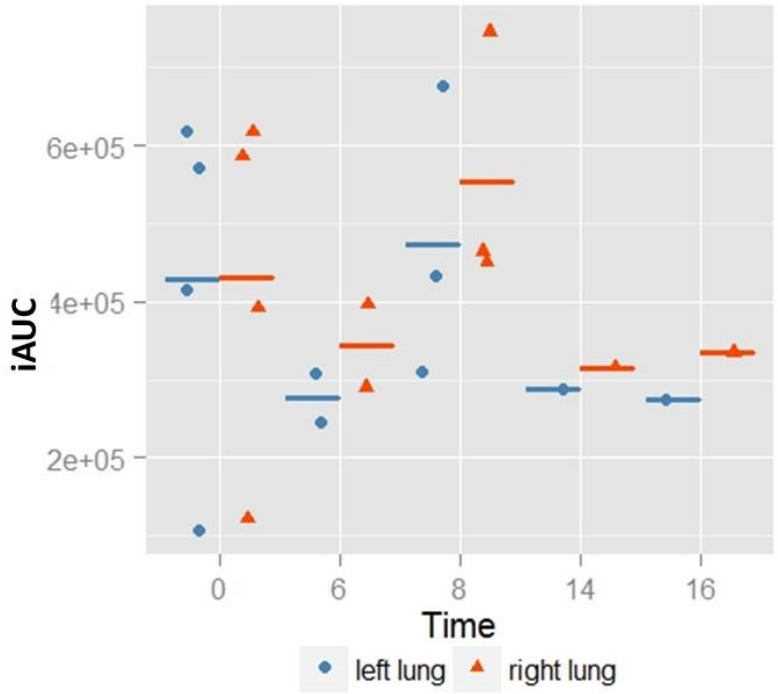



**Figure 3.19 DCE-MRI iAUC Plot**: Scatter plot of individual and population mean iAUC for the right (irradiated, red symbols) and left (unirradiated, blue symbols) lungs plotted against time for 11 mice. Only the mouse imaged at week 14 had RILT (Grade 3) reported from CT.

3.3.3.2.3 CT

No animals receiving RT + BLM imaged on CT demonstrated pathological changes at any time point following irradiation. Three animals receiving radiation (18 Gy) alone imaged on CT, showed Grade 2 (n = 2) or Grade 3 (n = 1) radiation changes at 14 (n = 1) and 16 (n = 2) weeks following radiation.

#### 3.3.3.2.4 Pathology

Lung sections were available at weeks 6 and 11 weeks following treatment for CBA mice receiving radiation (14 Gy) plus BLM, and at 12, 14 and 16 weeks for mice receiving radiation (18 Gy) alone. Figure 3.20 plots the incidence and severity of alveolitis in all mice sampled.

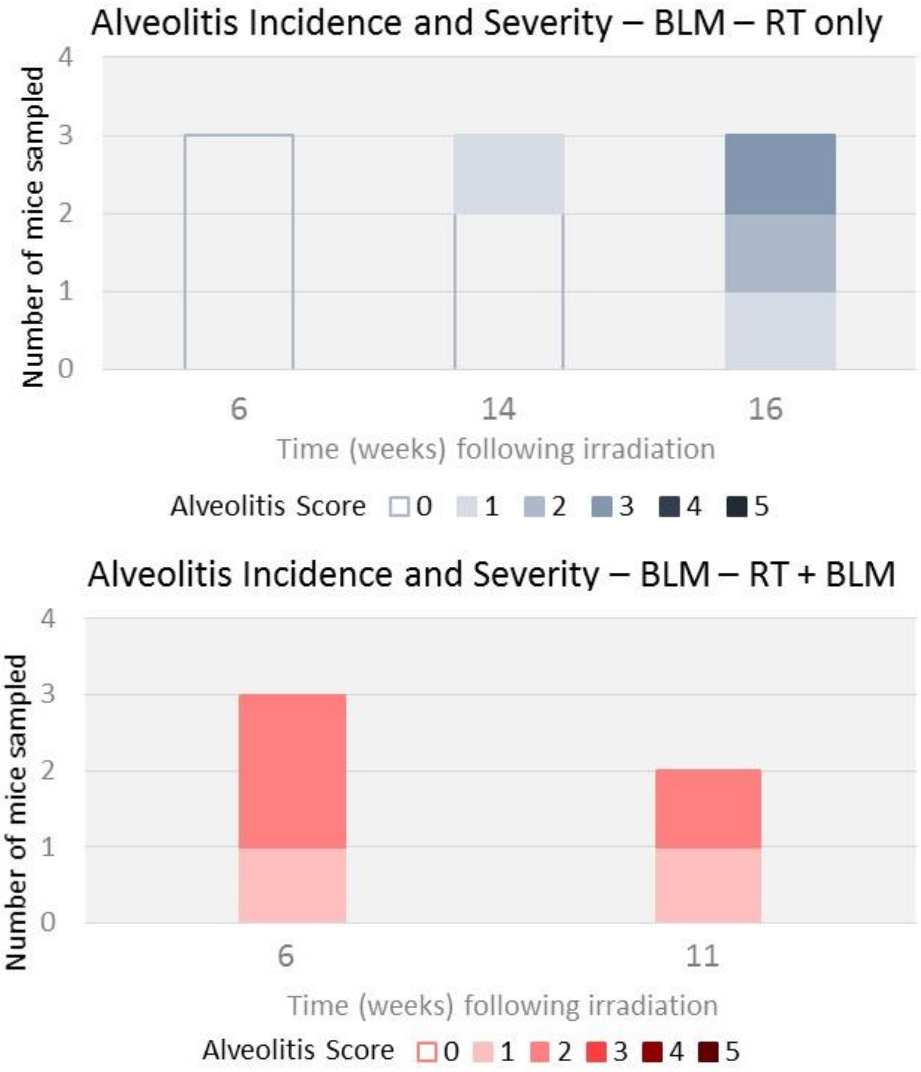



**Figure 3.20 Alveolitis for Study BLM:** Bar plots of Incidence and severity of alveolitis on H&E stained lung sections for animals which received 18 Gy to the right lung (top) and 14 Gy to the right lung plus BLM (bottom)

All mice demonstrating alveolar inflammation, did so in both lungs. However, severity scores in the left lung were generally lower than in the right (irradiated) lungs. Fibrosis was seen in all mice sampled at 16 weeks following treatment with scores ranging from 1 to 3.

Figure 3.21 is a representative lung section of mouse undergoing 18 Gy RT to the right lung only, 16 weeks following irradiation, stained with H&E. This section had alveolitis and fibrosis scores of 2 of 5. Red arrows highlight alveolar inflammation and hyaline material (both indicators of radiation pneumonitis).

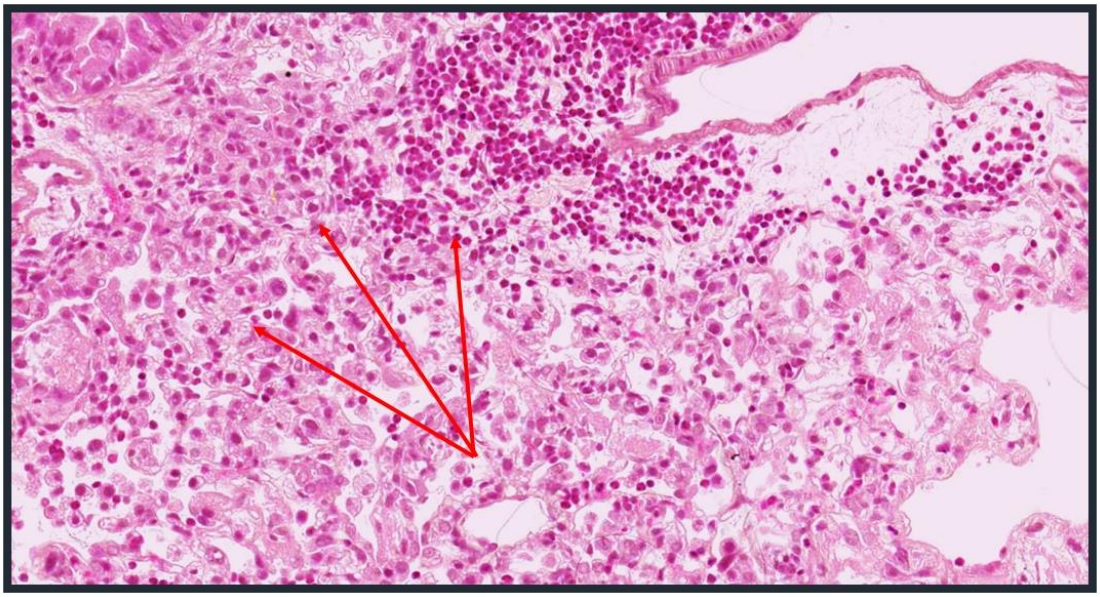


**Figure 3.21 Pneumonitis on H&E Stained Lung Section:** H&E stained section of right lung 16 weeks following 18 Gy irradiation with red arrows highlighting aspects of radiaton pneumonitis.

#### 3.3.3.2.5 Discussion

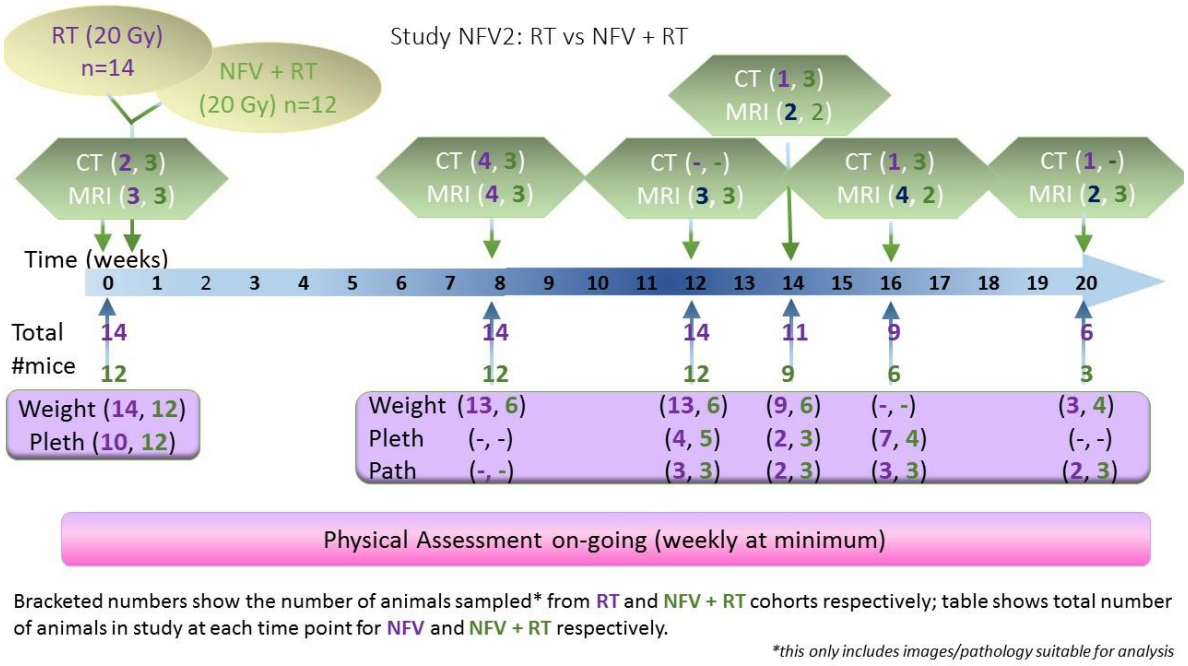
Although limited in number, mild to moderate RILT events were observed on imaging and pathology that are consistent with the development of radiation pneumonitis in this mouse model. On histopathology, bilateral lung toxicity would be expected in the BLM + RT arm of the study as BLM is a known lung irritant. However it was also observed in the RT only arm. This has been reported previously by groups observing the spread of radiation

pneumonitis into the shielded lungs of C57BL6 mice and rats irradiated receiving hemi-thoracic radiation (177, 258). This has also been observed in patients undergoing radiotherapy. Eldh has suggested that the invasion of inflammatory cells into the alveolar septae is accompanied by an increased expression of pro-inflammatory cytokines in the lung tissue. These soluble mediators may be involved in spreading lung inflammation to untreated areas which is expressed as oedema that is less pronounced than that in the irradiated lung (259-261).

### 3.3.4 Experiment NFV2

#### 3.3.4.1 *Rationale*

Experiment NFV2 was a near repeat of experiment NFV, with the exception that mice underwent radiation plus NFV or radiation alone. Figure 3.22 is a schema of experiment NFV2.




Bracketed numbers show the number of animals sampled* from RT and NFV + RT cohorts respectively; table shows total number of animals in study at each time point for NFV and NFV + RT respectively.

*this only includes images/pathology suitable for analysis

**Figure 3.22 NFV2 Study Schema**

#### 3.3.4.2 ***Results***

##### 3.3.4.2.1 Physical Assessment and Plethysmography

Twenty-six mice underwent 20 Gy radiation alone (n = 14) or following NFV administration (n = 12). During this twenty week experiment, three animals did not survive the MRI session, one incurred a foot injury and another incurred a tail injury (both possibly from the heating pad on MRI). Two animals in the RT only group experienced 12% and 15% weight loss at 14 weeks. The greatest weight loss (> 20%) occurred in a single mouse in the RT + NFV group, at 18 weeks following irradiation.

Using a Welch two sample t-test to compare breathing rates between cohorts over time there was no statistically significant difference between the groups ($p = 0.9795$). The maximal increases in breathing rate were seen in single outliers in the RT + NFV group at weeks 12, 15, and 16; the increases were 17%, 21%, and 19% respectively (Figure 3.23). The increase in breathing rate of the mouse from the RT+NFV cohort demonstrating an increase in breathing at 15 weeks, correlated with Grade 2 alveolitis score on pathology and Grade 3 CT score at week 16.

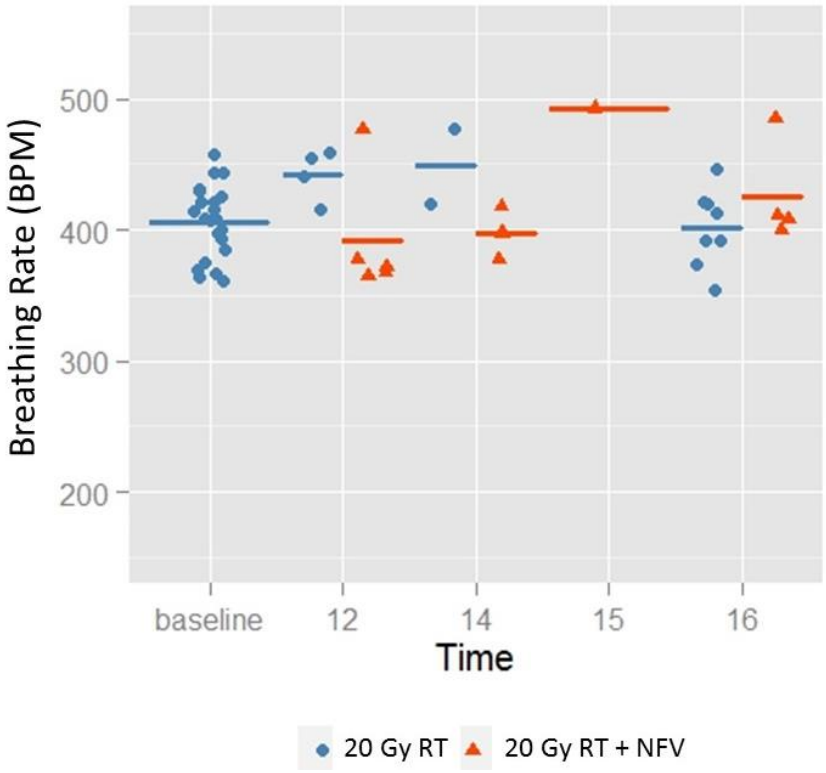



**Figure 3.23 Breathing Rates for Study NFV2:** Scatter plot of individual and population mean respiratory rates of mice receiving 20 Gy to the right lung (blue) or 20 Gy to the right lung plus NFV.

#### 3.3.4.2.2 MRI

MRI acquisitions were made on 35 occasions at baseline and following radiation, and resulted in the successful acquisition of 29 SEMS and 23 DCE-MRI images. The proportion of useable MRI was more successful in this experiment compared to the previous ones, and was primarily due to more reliable cardio-respiratory gating.

The largest challenge in image analysis remained the limited number of animals demonstrating radiation pneumonitis. Of all animals imaged, a single mouse from the RT + NFV arm demonstrated lung consolidation due to radiation at 16 weeks following radiation.

With so few RILT events, it is difficult to draw any conclusions other than a reliable DCE-MRI sequence has been developed, for pre-clinical imaging that shows potential in the detection of RILT.

#### 3.3.4.2.3 CT

CT was unavailable due to technical issues requiring intervention from external engineers during weeks 12 and 14 of this experiment, limiting the number of usable datasets generated (n = 6), following baseline. Two mice showed radiation responses on CT, with Grade Three and One toxicity scores at weeks 16 and 20 respectively. This corresponded to a 33% radiation response rate at each of these time points.

#### 3.3.4.2.4 Pathology

Of all the pathology samples read from animals undergoing RT alone (n = 10) or RT + NFV (n = 12), only two animals in the RT + NFV cohort demonstrated alveolitis, and a single animal in the RT only cohort demonstrated perivascular inflammation. The reactions were observed at weeks 16 and 20. Again the poor quality of the staining (due to storage in ethanol), and limited number of radiation reactions makes the interpretation of the results difficult.

#### 3.3.4.2.5 Intermodality Comparisons

Figure 3.24 plots the number of mice sampled at each 12, 14, 16 and 20 weeks post irradiation demonstrating radiation reactions (i.e., having radiation pneumonitis scores $\geq 1$) as assessed by pathology, CT and MRI for animals in both study cohorts (RT and RT + NFV

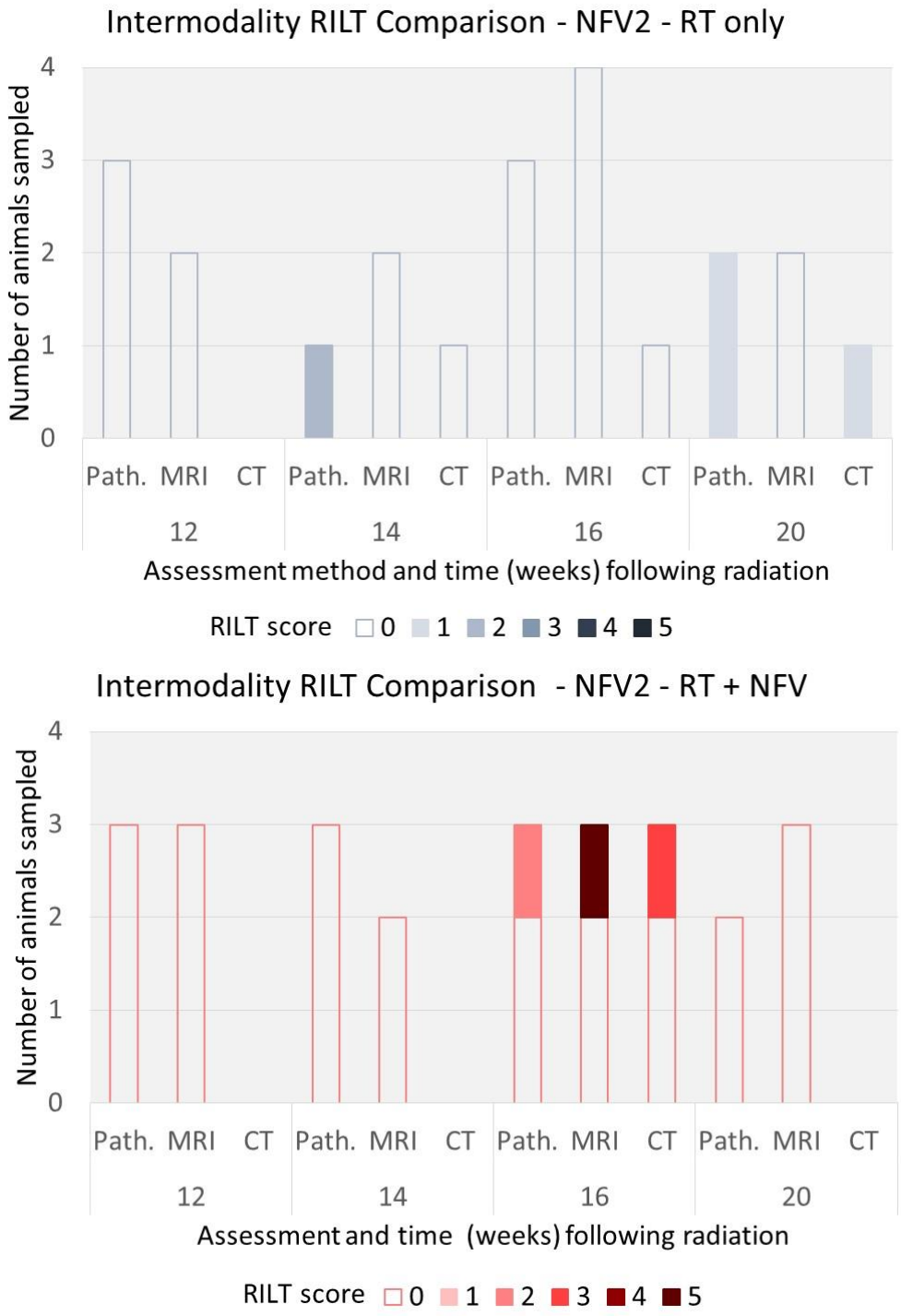



**Figure 3.24 Intermodality RILT Incidence and Severity**: Bar plots of the incidence and severity of RILT seen on CT, MRI and histopathology for animals having undergone 18 Gy RT to the right lung (top) or 18 Gy RT to the right lung plus NFV (bottom).

Analyses to examine the correlation between the methods used to determine RILT (CT, MRI, pathology), were limited due to small the numbers of animals evaluated and few animals demonstrating radiation response. Additionally, the number of animals undergoing multiple assessments at any given time point was limited. As such, any intermodality correlations would report primarily on animals displaying normal lung tissue, and any statistical significance could be due to chance.

## 3.4 **Discussion**

Five longitudinal radiation and imaging studies were undertaken in two mouse strains that were useful in determining the appropriate mouse model and radiation dose to use in subsequent studies. Imaging methodologies were tested and refined for the investigation of new imaging methods by which to detect radiation pneumonitis in normal lung tissue, following radiation with or without PI3K-inhibtiors.

Fur loss on the right thorax of irradiated animals indicated that radiation was delivered to the intended area, however a limited number of definitive radiation reactions were observed on CT, MRI or histopathology. It is possible that using shielding placed close to the animals (as opposed to closer to the source of radiation), created a region of build-up depositing more dose near the incident surface than anticipated, resulting in a superficial reaction with limited lung toxicity. This prompted the implementation of parallel opposing pair (POP) radiation technique to distribute the dose more evenly throughout the right thorax for subsequent experiments.

Collis et al reported that mice given single IP doses of BLM of 120 mg/kg with 13.7 Gy thoracic radiation had increased respiratory rate in a ratio of 1.4:1 when compared with un-treated mice four weeks following RT (256). No mice receiving 13.7 Gy with 120 mg/kg BLM survived past 12 weeks following RT. Using this information and following

discussion with Dr. Sally Hill, lead in the Biomedical Services, Oxford Institute for Radiation Oncology, it was decided to use a similar dose of radiation (14 Gy in a single dose), and a more conservative dose of BLM (80 mg/kg), so that mice would survive to be observed at 12 weeks or more. However, because most literature on radiation plus BLM toxicity studies used whole thorax RT, where the volume effect of radiation would have been greater than that for hemi-thoracic RT, it would seem the doses selected in this thesis were somewhat conservative, as again limited expression of RILT was observed.

In the BLM experiment, increases in breathing rate of ≥ 15% were seen in 27%, 76%, 45%, and 33% of animals treated with RT alone at 8, 12, and 16 and 20 weeks respectively; 12% of animals had increased breathing rates ≥ 35%, at 12 weeks following irradiation. For the animals treated with RT + BLM, 33% and 50% had increased breathing rates of ≥ 15% at 12 and 14 weeks respectively. Liao et al (176) have observed that as lesser volumes of lung are irradiated, the change in breathing rate begins later and peaks at a lower level than when animals receive whole thorax irradiations. Although limited, longitudinal observations in the preliminary experiments presented in this chapter were encouraging as several animals showed signs of breathing rate increases of ≥ 15% (the local threshold requiring increased monitoring of breathing rate and weight). However, a greater number of observations would be required to enhance the statistical significance of these reactions.

Confirmation of RILT using imaging was limited in these early experiments, due in part to limited radiation reactions but also by the fact that imaging methods had not yet fully matured. The number of CT images available for analysis in studies RT2, NFV2 and BLM was limited in part due to challenges with insufficient respiratory gating, user error (e.g., failure to remove the couch from the imaging FOV), and ring artefacts which were the result of error the omission of an appropriate calibration of the imager following intervention by

external engineers. These issues lead to the development of an automated calibration and improved gating methodologies.

Where CT was suitable for analysis, a consistent (but not statistically significant) trend in increasing lung density over time in the irradiated lungs when compared to baseline and/or the unirradiated lungs was observed.

MRI methodologies, in particular the development of reliable CR-gating under development throughout the experiments reported in this chapter. A high quality anatomical SEMS sequence was refined, and DCE-MRI sequence was developed. MRI images were acquired most successfully in experiment NFV2. However RILT was only evident in one animal at 16 weeks following irradiation. This finding did have 100% correlation with histopathology and CT imaging.

Overall the experiments in this chapter used 133 mice, undertook 135 CT images, 70% of which were suitable for analysis, and 5% of which demonstrated RILT. MR imaging was most successful in experiment NFV2 with 85% acquisitions suitable for analysis, and RILT was seen on one occasion. Radiation pneumonitis was observed on pathology as early as eight weeks following RT, and was most severe at 16 weeks following RT with Grade 3 and 4 RILT scores. Correlations of RILT incidence and severity were attempted (section 3.3.4.2.5), however were limited due to the limited number of RILT observations on imaging. Based on the findings in these preliminary experiments, further experiments were developed using CBA mice, POP radiation, an increased dose of 20 Gy, and longitudinal observations to a maximum of 20 weeks following irradiation.

# Chapter 4

*PI3K/AKT inhibition and radiation*

# 4 PI3K/AKT INHIBITION AND RADIATION

## 4.1 Introduction

In addition to the continued development of robust MRI lung imaging protocols, a major aim of the experiments in this chapter was to confirm there is no increased radiosensitivity caused by PI3K inhibitors in normal lung tissue compared to radiation alone.

Pure and combined PI3K inhibitors have demonstrated efficacy as anti-cancer agents and tumour radiosensitizers in vivo and in vitro (211-214). However little has been published concerning the effect of these agents on normal tissue radiosensitivity. In this chapter the effects of the targeted radiosensitizers BEZ235 (BEZ) and BKM120 (BKM) on normal lung tissue in a murine model is reported. Physiologic, pathologic and imaging endpoints were used to investigate the effect of adding PI3K inhibition to radiotherapy.

This chapter reports the results for Experiment pAKT, an analysis of the effect of BEZ and BKM on AKT phosphorylation in normal lung tissue, and Experiment BEZ-BKM, which was designed to explore the effects of 20 Gy radiation to the right lung with or without the targeted radiosensitizers BKM and BEZ. Additionally, MR imaging methods were further developed to include a full $B_1$ quantification of the DCE-MRI to allow for model-based analysis pharmacokinetic evaluations. This chapter covers the results of two studies:

1. pAKT: CBA mice receiving only BKM (n = 4), BEZ (n = 4) or vehicle (n = 4) to compare AKT phosphorylation in normal tissues
2. BEZ-BKM: CBA mice receiving 20 Gy RT + BEZ (n = 15) vs mice receiving 20 Gy RT + BKM (n = 15)*

*NB again in an attempt to minimize the number of animals used, the RT only animals from Experiment RT2 were used as controls Experiment BEZ-BKM.

## 4.2 Quantification of changes in pAKT in normal tissues following PI3K inhibition

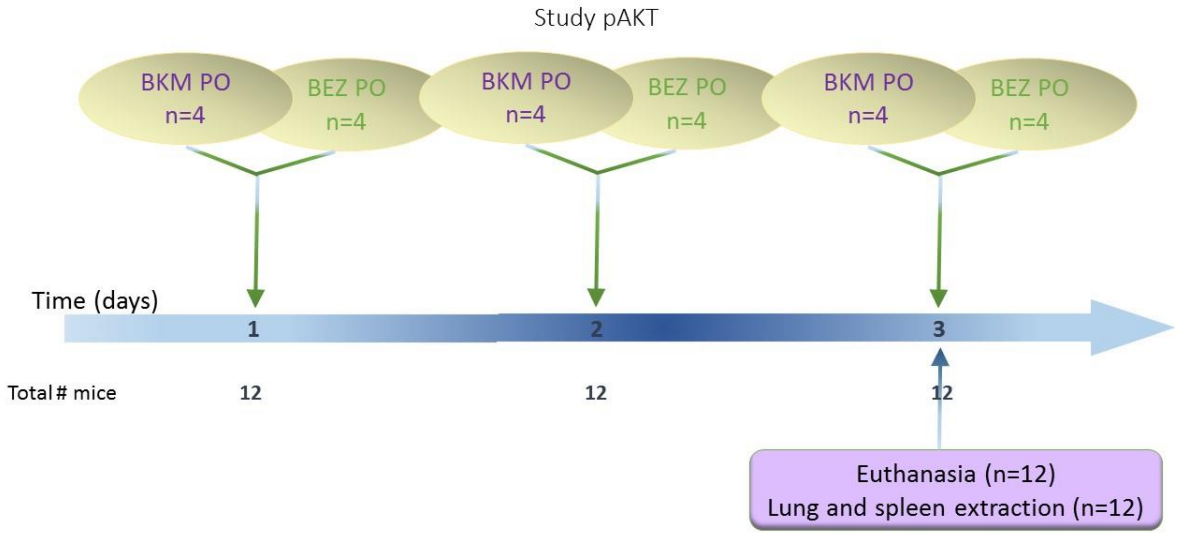



**Figure 4.1 pAKT Study Schema**

### 4.2.1 Rationale

The aim of this study was to investigate the effects of PI3K/AKT inhibitors on AKT phosphorylation in non-irradiated lung tissue. If inhibition of AKT could not be detected, then it could be hypothesized that these drugs are unlikely radiosensitizers in normal lung tissue.

### 4.2.2 Results

Fresh lung and spleen samples from 12 mice were evaluated; four control animals, four animals irradiated with three oral doses of BKM at 6mg/mL (20 mg/kg) and four animals with three oral doses of BEZ at 4 mg/ml (30 mg/kg).

Western Blot analyses showed a reduction in pAKT levels in animals receiving BEZ or BKM when compared to untreated mice. In the lung, pAKT was reduced in the majority of animals given BKM or BEZ. In the spleen, pAKT was reduced in all animals treated with

BKM. Figure 4.2 shows a representative Western Blot for AKT (left, top panel) and pAKT (right, top panel) in animals treated with vehicle, BEZ or BKM.

In this example AKT levels are consistent across the treatment groups and pAKT is decreased in the BEZ treated lung, with no change in the BKM treated lung. pAKT shows a slight decrease in BEZ treated spleen and larger decrease in BKM treated spleen.

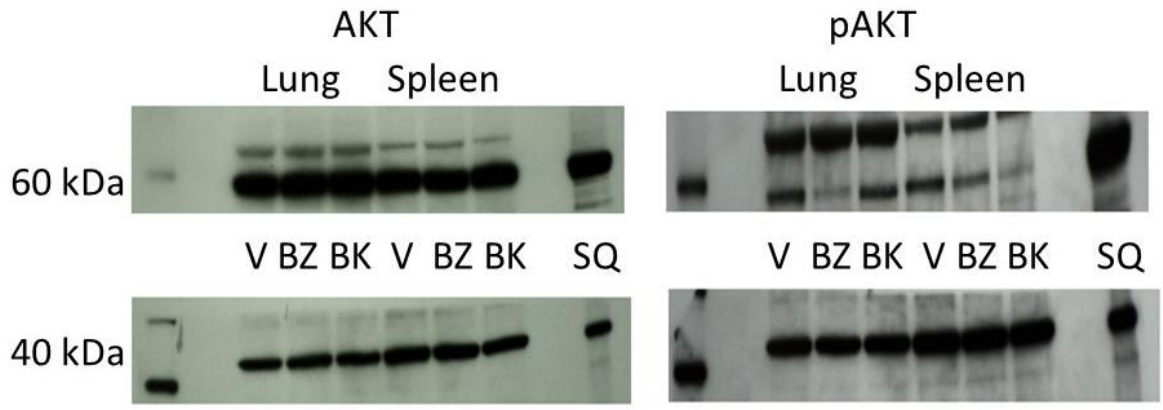



**Figure 4.2 AKT-phosphorylation in Normal Tissue:** Western Blots measuring changes AKT and pAKT in lung and spleen of mice treated with vehicle (V), BEZ (BZ) or BKM (BK). Lysate from SQ20B human head and neck cancer cells was used as a positive control for AKT and pAKT expression (SQ). Bottom panels show beta actin loading controls.

The population mean results quantified in ImageJ, (262-264) showed that the expression of pAKT in the spleen was reduced in all animals treated with BKM compared to the vehicle treated animals. Changes in pAKT in the spleen of animals treated with BEZ were too variable to be conclusive. Only minor changes in AKT expression were observed in lung and spleen in both treated and untreated animals. Table 4.1 and Figure 4.3 summarize the mean population differences in AKT and pAKT in the lung and spleen of BEZ and BKM treated animals.

**Table 4.1 Change in Phosphorylation of AKT Following BEZ or BKM Administration**

| | | LUNG | | SPLEEN | |
|---|---|---|---|---|---|
| | | % Change | Range | %Change | Range |
| **AKT** | BEZ | -1.5% | -5.0% +1.3% | +3.3% | -0.5% +5.5% |
| | BKM | +0.5% | -3.5% +4.5% | +2.7% | -2.5% +7.8% |
| **pAKT** | BEZ | -17.0% | -29.8% -3.8% | -2.6% | -8.9% +4.2% |
| | BKM | -14.1% | -27.7% -1.4% | -6.4% | -11.2% -1.5% |

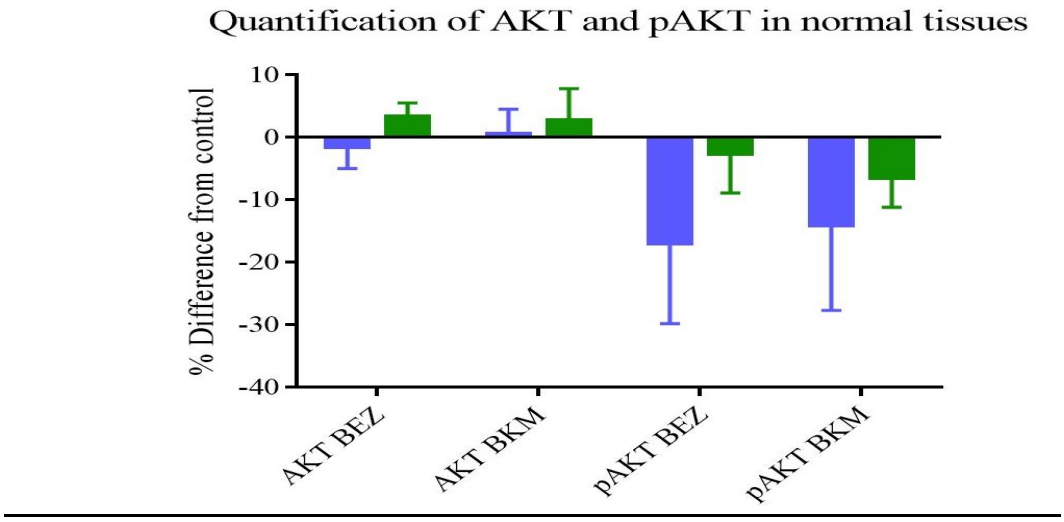



**Figure 4.3 Quantification of AKT and pAKT in Normal Tissues:** Absolute mean population percent change in phosphorylation of AKT following administration of BEZ or BKM in the lung (blue) and spleen (green)

### 4.2.3 **Discussion**

Using Image-J to assess the band intensity from the Western Blot analyses, decreases in pAKT expression of 17% and 14% were observed in animals receiving BEZ and BKM respectively. No significant changes in AKT were observed in either lung or spleen following administration of either drug. Because there were decreases in pAKT following drug administration there is potential for these drugs to sensitize normal tissue to radiation. Further experiments investigating these effects in vivo are warranted to confirm the safety of translation to early clinical trials.

## 4.3 RT + BKM vs RT + BEZ

### 4.3.1 Rationale

To evaluate the effects of RT plus PI3K/AKT inhibitors on normal lung tissue, and further refine imaging techniques for radiation pneumonitis detection with a view to translation to clinic.

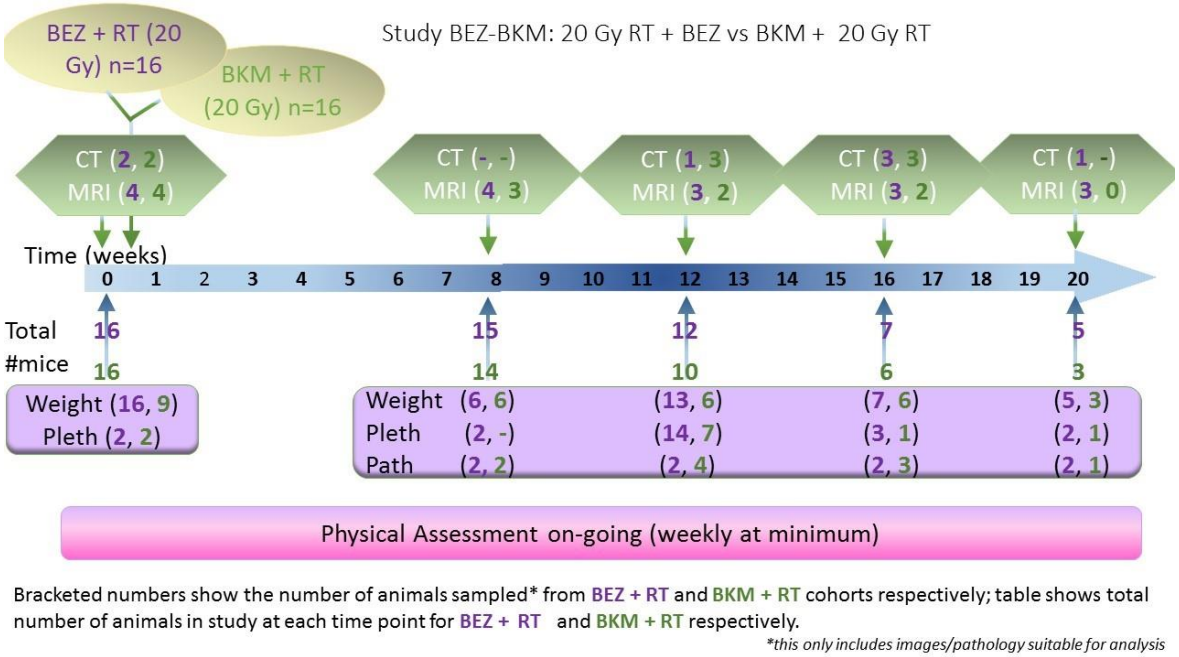



**Figure 4.4 BEZ-BKM Study Schema**

### 4.3.2 Results

#### 4.3.2.1 *Physical Assessment and Plethysmography*

Thirty-two mice underwent 20 Gy right lung irradiation following the administration of BEZ (n = 16) or BKM (n = 16) and were followed to a maximum of 20 weeks following radiation. Six mice (2 in the BKM study arm and 4 in the BEZ study arm) experienced failure to thrive, defined by greater than 10% weight loss and/or a hunched appearance (Figure 4.5). Two mice in the BEZ arm were euthanized at 8 weeks following RT due to weight loss. Four others (2 BEZ and 2 BKM) were euthanized earlier than planned: the two

mice in in the BKM study arm experienced 10% weight loss at 10 days following irradiation, one mouse in the BEZ arm showed a significant reduction in breathing rate (Figure 4.6), and the other BEZ treated mouse experienced weight loss later in the study.

In mice without respiratory distress, imaging and/or dissection showed bowel obstruction of unknown cause. The onset of symptoms varied from weight loss roughly one week following radiation (n = 2), a gradual reduction in respiratory rate starting approximately four weeks following radiation (n = 1), or weight loss with hunched appearance at 8 and 12 weeks following radiation (n = 3).

**Figure 4.5 Toxicity:** Mouse at 8 weeks following IR+BEZ showing hunched appearance (left), and bowel obstruction in a mouse which was euthanized following euthanasia at 12 weeks following RT+BEZ, due to progressive weight loss.



Figure 4.6 plots individual and population respiratory rates at each time point for each cohort. One mouse also underwent plethysmography at both four and four and a half weeks following irradiation, time points which are not included in the plot. This mouse was euthanized at four and a half weeks following radiation due to progressive weight loss, a hunched appearance and a rapid onset of reduced respiratory rate (> 35% decrease from baseline). This mouse was in the RT + BEZ cohort of the study. Additionally, a mouse in the RT + BEZ study arm, showed progressive weight loss and a hunched appearance, and is represented by the point on the plot at 17 weeks. Due to the weight loss observed, this mouse

was weighed on alternate days and had weekly plethysmography until it recovered. The animal showed little clear evidence of RILT on imaging and pathology.

With the exception of the 19% increase in breathing rate observed in the BKM arm at 16 weeks and excluding the two outliers, there was little change in the respiratory rates of the mice, regardless of radiation response seen on imaging and pathology.

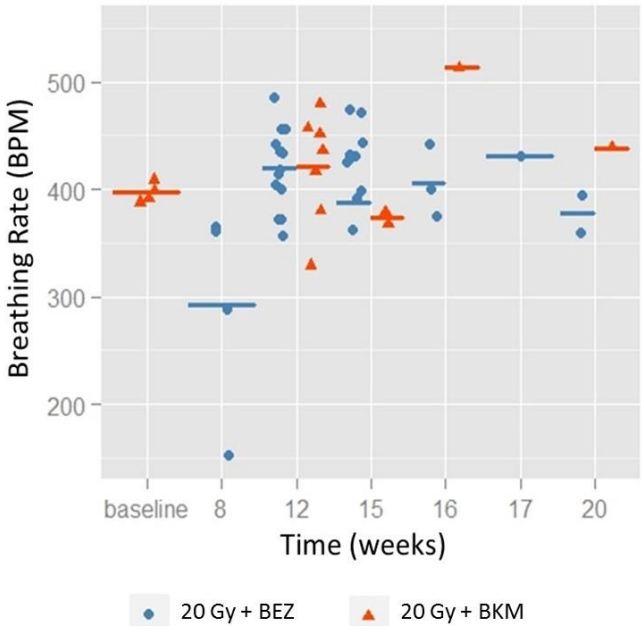



**Figure 4.6 Breathing Rates for Study BEZ-BKM:** Scatter plot of individual and population mean respiratory rates of mice receiving 20 Gy to the right lung plus BEZ (blue) or 20 Gy to the right lung plus BKM (red).

#### 4.3.2.2 ***MRI***

Successful SEMS and DCE-MRI images were acquired on 20 occasions following baseline. Mice demonstrated RILT on SEMS MRI on five of 20 occasions. Four animals demonstrating RILT were from the RT + BEZ arm at 16 (n = 2) and 20 (n = 2) weeks following radiation respectively. The fifth animal was from the RT + BKM group and showed RILT at 14 weeks following radiation. Figure 4.7 shows representative CT and MR images for a single animal imaged at baseline and 20 weeks following RT with severe (Grade 4) lung consolidation and inflammation represented by the increased lung density on CT and increased signal on MRI.

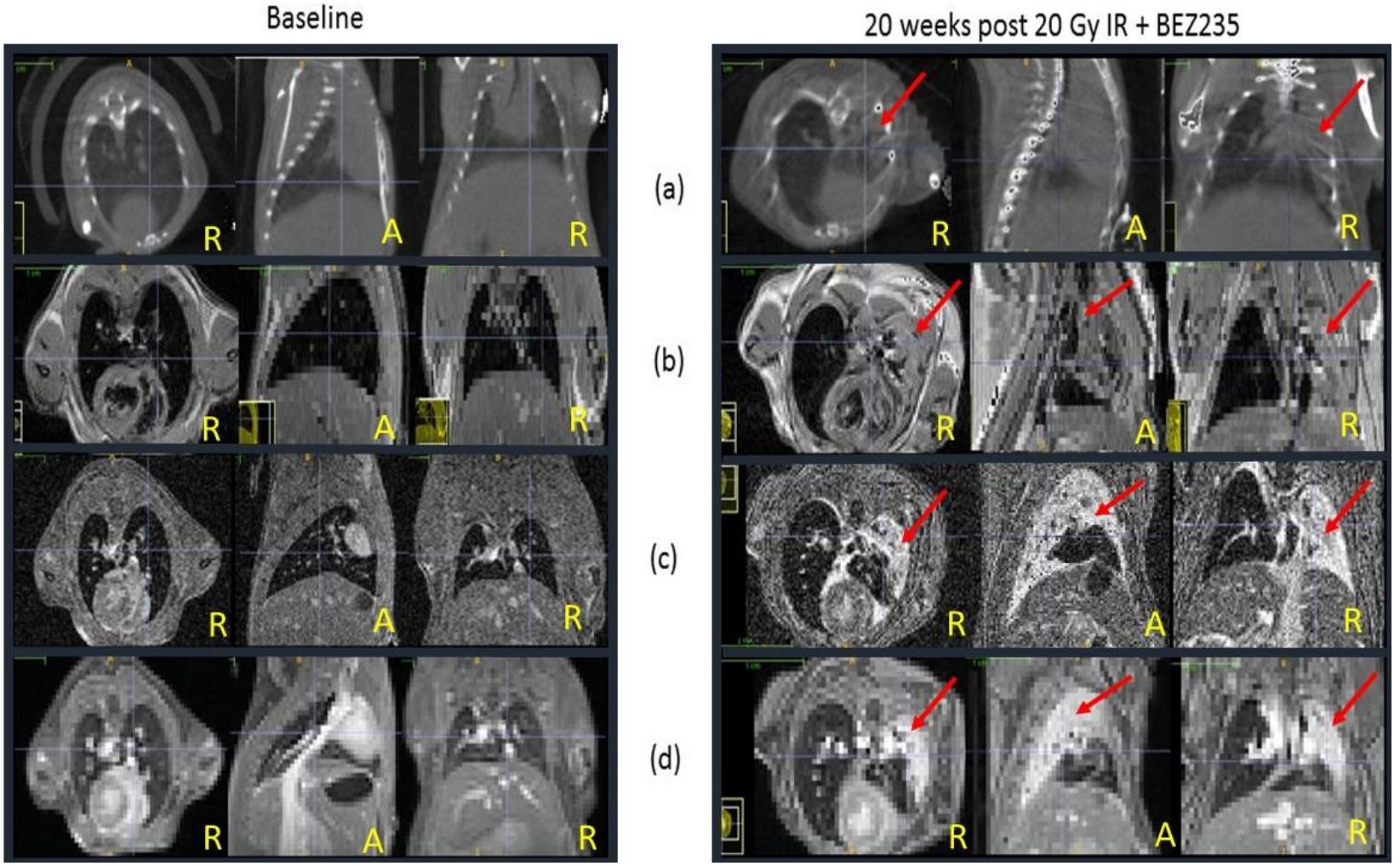



**Figure 4.7 Multi-modality Images of RILT 20 weeks following RT + BEZ:** Axial (left), sagittal (centre) and coronal (right) images of a CBA mouse at baseline and 20 weeks following 20 Gy RT + BEZ to the right lung on CT (a), SEMS MRI (b), high resolution pulmonary angiography (c), and DCE-MRI imaging (d). Image orientation indicated by anterior (A) and right (R). Arrows indicate RILT.

The work of this chapter focused on the development of DCE analysis using model-based and non-model-based analysis methods. Figure 4.8 below is a representative DCE image of a mouse immediately prior to, during and immediately following a bolus injection of 0.3 µL Gadolinium.

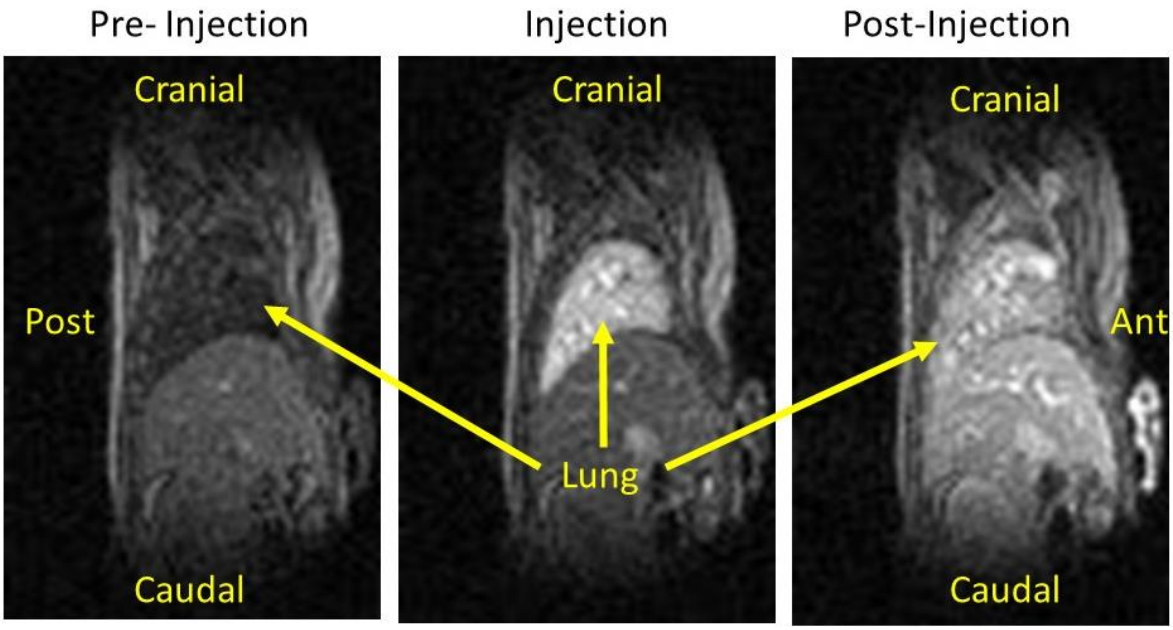



**Figure 4.8 Sagittal DCE-MRI:** Representative mouse MRI, showing slices acquired immediately prior to a bolus injection of 0.3 µL Gadolinium, at the time of injection showing early uptake in the lung only, and immediately following injection showing uptake in other tissues and the start of wash-out in the lung.

To generate and analyse DCE-MRI, a calibration scan was acquired followed by a series of repeat images using the sequence described in section 2.6.2.2.2. Ten repeats were acquired prior to contrast injection, and up to 30 were acquired after. The average time for each acquisition was variable as it was dependent on cardio-respiratory gating, but on average was approximately 11 seconds (range 6 - 19 seconds). The raw images were then used to generate a 'mean DCE' image that was for lung segmentation. Using an overlay tool in the PKViewer, a signal intensity map was generated on a voxel-by-voxel basis. By applying the appropriate model, pharmacokinetic maps (e.g., for $K^{Trans}$, Vep, Kep) could be created and presented as a curve of signal enhancement over time with detailed

pharmacokinetic values for evaluation potential in the detection of RILT. Further investigations are required to determine if a modelled-fit pharmacokinetic analysis is more informative than a non-modelled fit analysis.

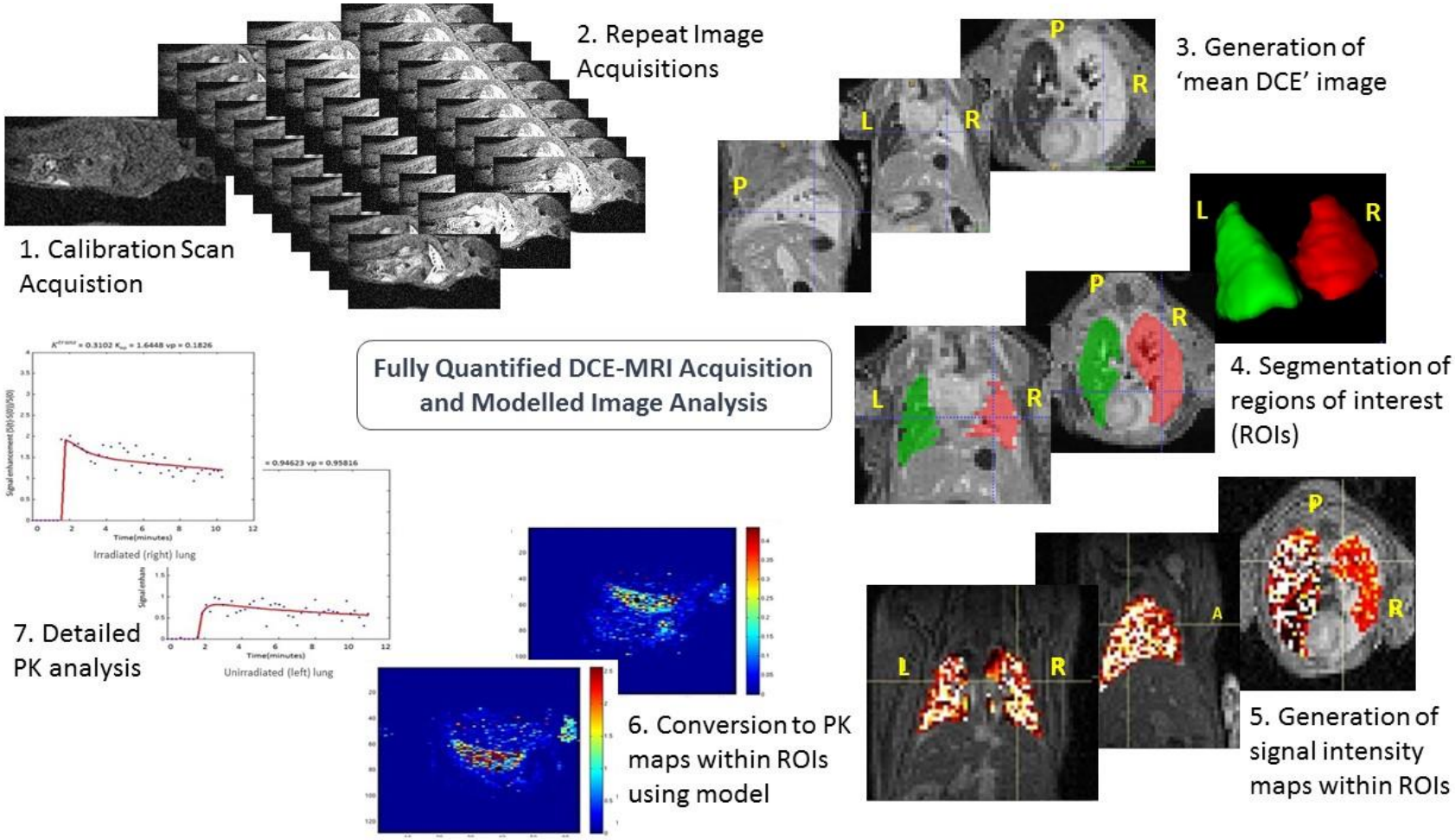



**Figure 4.9 Modelled DCE-MRI Acquisition and Analysis:** Following the acquisition of a calibration scan (1) used for B1 quantification, 10 'dummy scans are acquired, before a bolus injection of 0.3 µL gadolinium. Repeat images (2). An average image is then developed using all repeats (3), and used for lung segmentation (4). Images and segments are imported into PKViewer to create SI maps (5), to which the chosen model is applied to create PK maps (6) that can be used for a detailed image analysis (7).

Figure 4.10 presents the results of the modelled data presented as a series of plots for the BEZ + RT arm of study BEZ-BKM. With a limited number of RILT events, it is difficult to draw conclusions from this analysis. The goal of these preliminary evaluations was to correlate changes in the pharmacokinetic metrics with incidence of RILT.

The non-modelled data was analysed using paired t-tests of iAUC and AUC for mice receiving BEZ + RT, and suggested a statistically significant difference between the right (irradiated) and left (unirradiated) lungs with P values of 0.04611 and 0.03559 respectively. This was not true of cohorts demonstrating no RILT. Linear regression models applied to the data confirmed a trend of decreasing values over time in both iAUC and AUC respectively with the only significant change occurring at week 16 following irradiation. This is corresponded to the time point with the highest population mean RILT score of 2.7/5 for the three animals imaged.

To determine which analysis (modelled-fit vs non-modelled fit) is most suitable would require analysis of a larger cohort of animals demonstrating a progression of mild to severe RILT development.

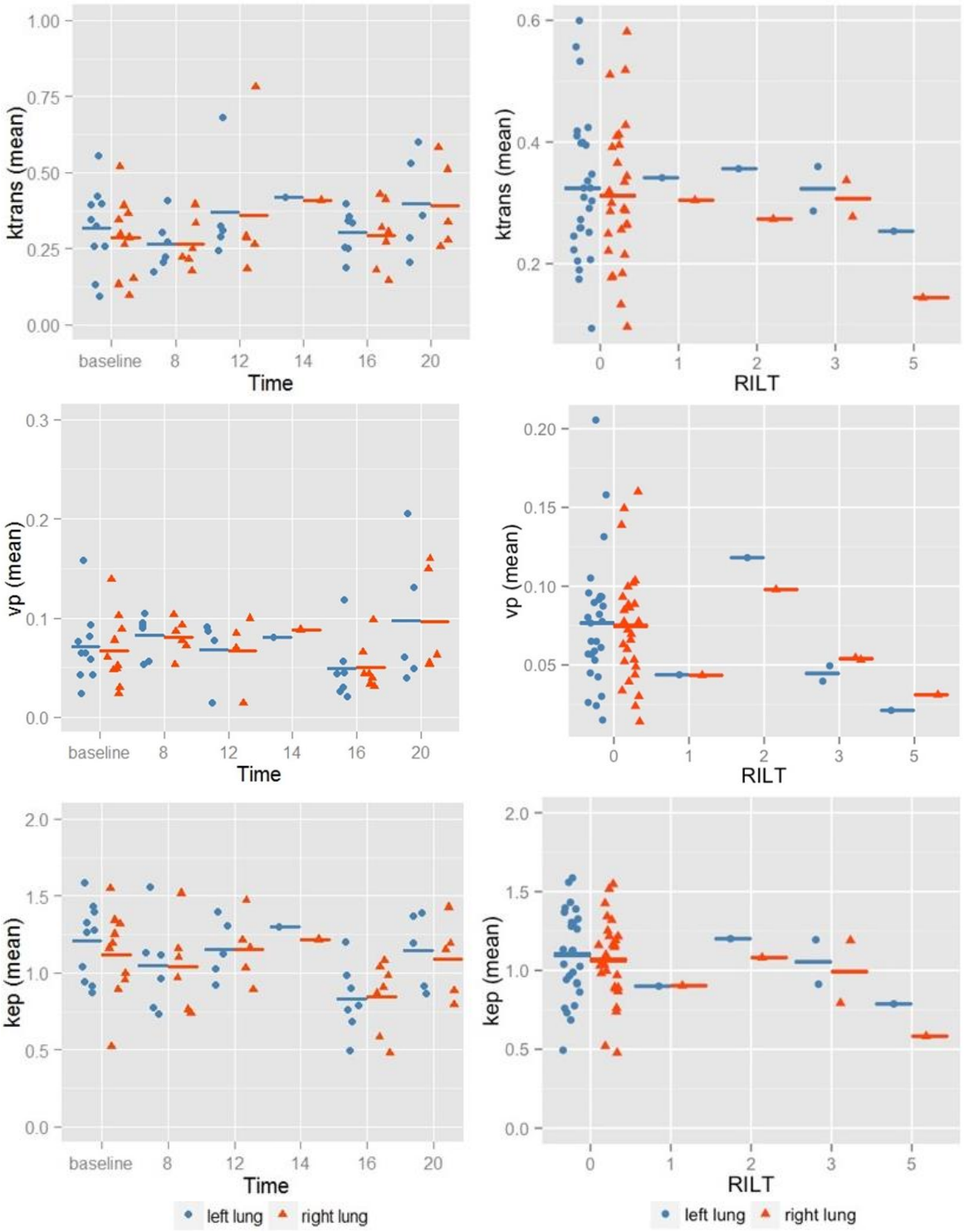



**Figure 4.10 Pharmacokinetic DCE-MRI Analyses:** Scatter plots of individual and population mean left (blue) and right (red) lung changes using the parameters $K^{Trans}$, $V_p$ and $K_{ep}$ plotted against time (left plots) and RILT (right plots) for mice that received BEZ plus 20 Gy RT to the right lung.

#### 4.3.2.3 *CT*

Twenty-one CT data sets were available for this analysis, 17 following baseline. CT was unavailable due to technical issues requiring intervention from external engineers during week 8 of the experiment. Useable CTs for all other time points were contoured for image analysis.

Mice in the RT + BEZ study arm demonstrated RILT with the highest frequency on CT. RILT was reported in two out of three mice imaged at 14 weeks, two out of three mice imaged at 16 weeks and two out of three mice imaged at 20 weeks following irradiation.

The maximum RILT score of 5 was seen in two mice at 14 weeks, one from each study arm. Table 4. 2 summarizes the proportion of animals showing RILT on CT at each time point and the population mean RILT score.

| | RT + BKM | | RT + BEZ | |
|---|---|---|---|---|
| **Week** | **#** | **Mean** | **#** | **Mean** |
| **8** | - | - | - | - |
| **12** | 0/3 | 0 | 0/1 | 0 |
| **14** | 1/2 | 2.5 | 2/3 | 2 |
| **16** | 0/3 | 0 | 2/3 | 2.3 |
| **20** | - | - | 2/3 | 2.3 |

**Table 4.2 Proportion of Mice Demonstrating RILT:** Proportion of mice (#) demonstrating RILT at each imaging time point for all cohorts in studies NFV2 and BEZ/BKM, and associated population mean RILT score (mean = sum of all scores/number of mice imaged).

Eight animals showed an increase in CT density (mean HU) in the right lung ≥ 15% when compared to the population mean at baseline. Fifty percent of all animals (from both arms) with increased lung densities, had radiological changes that were observable by eye resulting in toxicity scores ≥ 1 reported.

The population mean change in HU at 14 weeks following RT for animals receiving BEZ + RT was + 35% (range 28% to 56%) with a mean RILT of 2 (range 0-5). Figure 4.11 plots individual and population mean CT density changes against time (left) and RILT score (right) for animals receiving RT + BEZ (top) and RT + BKM (bottom).

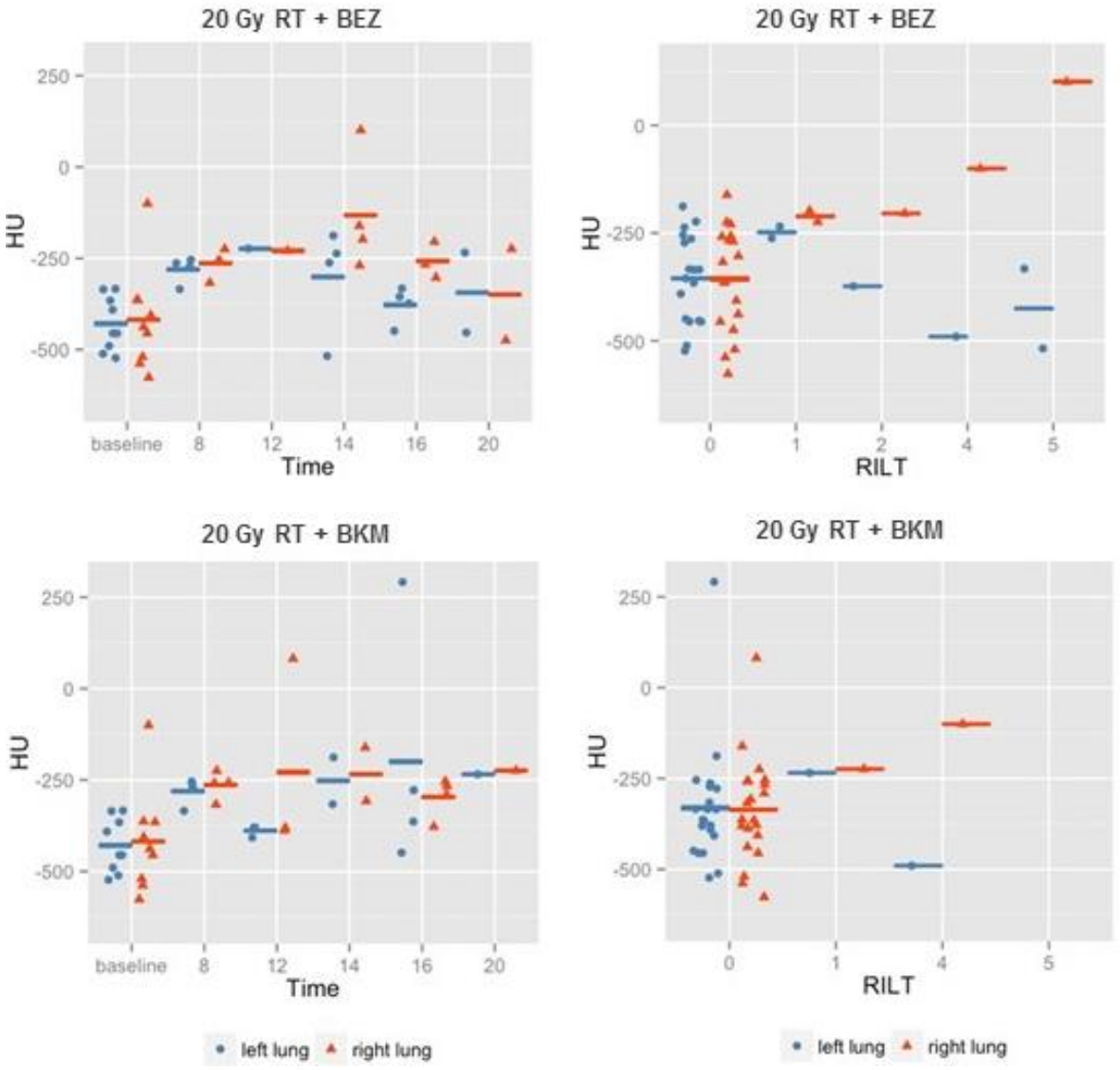



**Figure 4.11 CT Lung Densities versus Time and RILT:** Scatter plots of individual and population mean CT lung densities (HU) plotted against time (left) and RILT score (right) for animals receiving 20 Gy RT + BEZ (top plots) or 20 Gy RT + BKM (bottom plots).

The incidence of RILT observed on CT in animals undergoing RT + BKM and RT + BEZ was compared to the incidence of RILT observed on CT in animals undergoing RT alone (from study NFV2) using regression analysis and paired t-tests. The paired t-tests showed no significant differences in incidence of RILT between 20 Gy RT alone and 20 Gy RT + BEZ ($P = 0.2084$) or 20 Gy RT alone and 20 Gy RT + BKM ($P = 0.6557$).

#### 4.3.2.4 ***Pathology***

Alveolitis was the dominant pathology, and was first seen in a single animal at 8 weeks following irradiation plus BEZ, with a pneumonitis score of 2/5 in the irradiated lung. Overall, pathological evidence of radiation pneumonitis was infrequent. Of the animals sampled 29% and 40% demonstrated alveolitis in the BEZ and BKM groups respectively. Fibrosis was reported in the lungs of one animal in the BKM group at 16 weeks following irradiation.

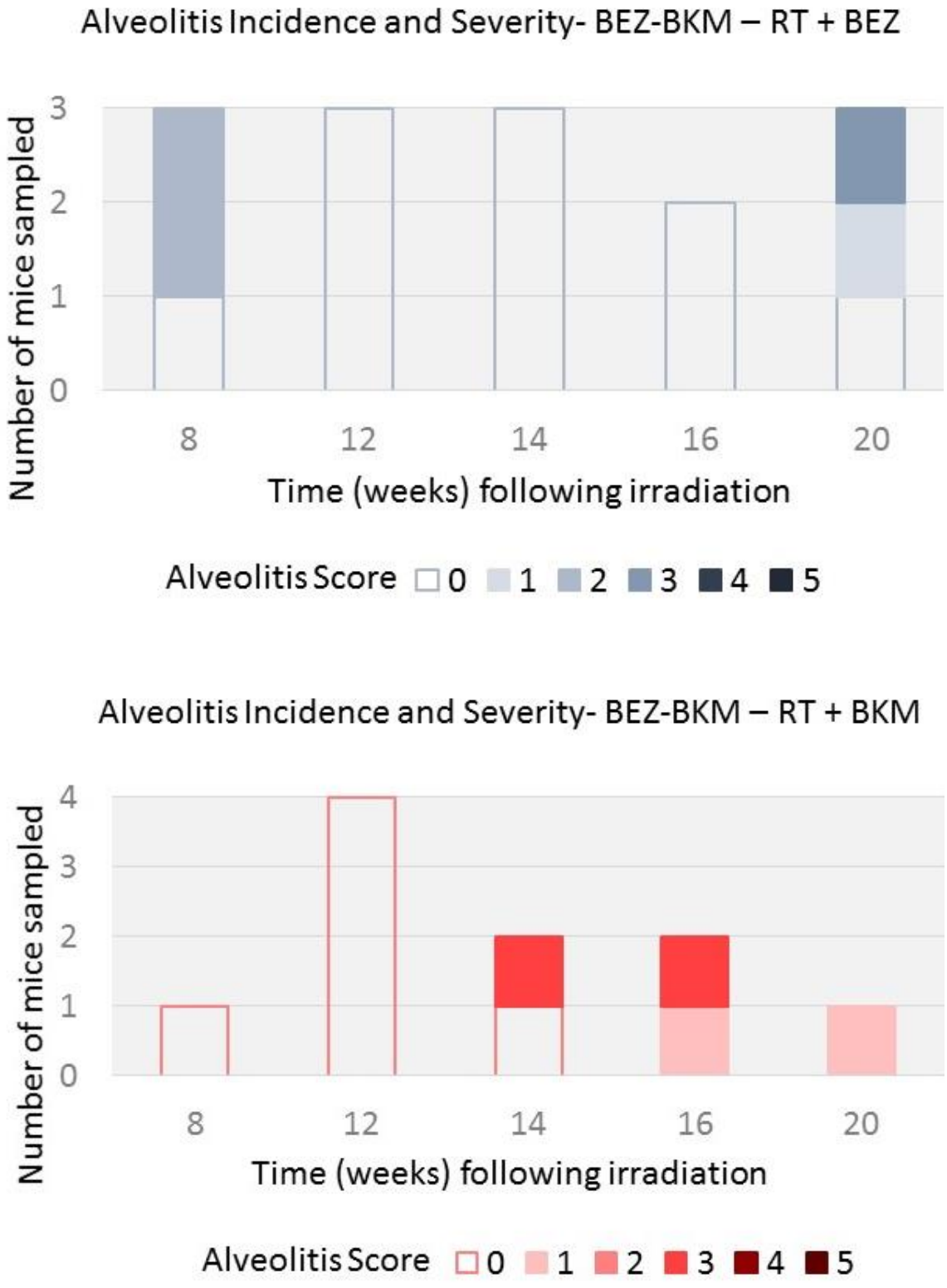



**Figure 4.12 Alveolitis for Study BEZ-BKM:** Bar plots of the incidence and severity scoring for alveolar inflammation in studies RT.

There was a single incidence of a finding of Grade 3/5 oesophagitis (reported as oesophageal wall inflammation and oesophageal ulceration) at 8 weeks following RT + BEZ (Figure 4.13), with a score of 3/5 for both oesophageal wall inflammation and oesophagitis. This mouse showed no evidence of RILT, however did show rapid weight loss and observable signs of distress prior to being euthanized at this time-point.

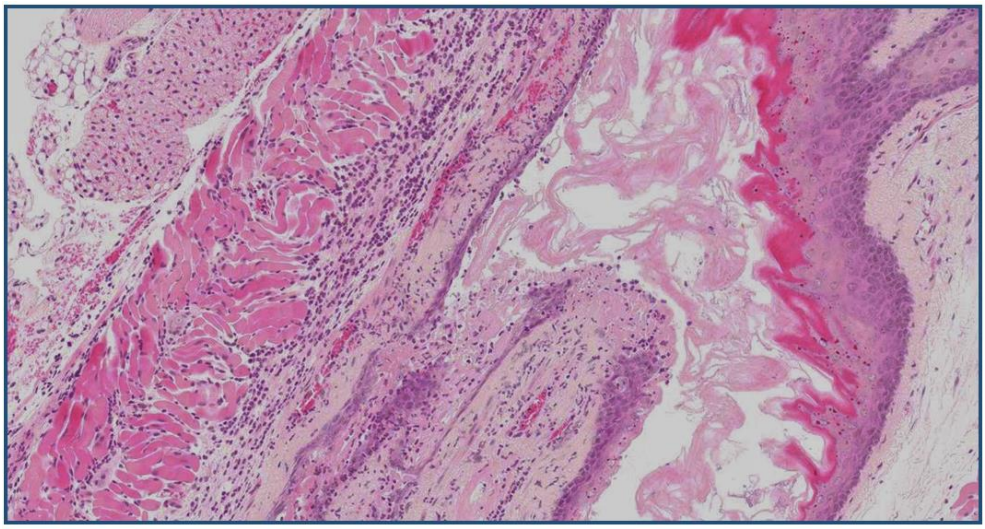


**Figure 4.13 Oesophagitis:** Haematoxylin-eosin stained section showing oesophagitis in a mouse 8 weeks following 20 Gy irradiation to the right lung, showing oesophageal wall inflammation and ulceration.

#### 4.3.2.5 *Intermodality Correlations*

For the mice that did display evidence of RILT a weak trend towards increased lung density in the irradiated lung was seen at 14 and 16 weeks post RT on regression analysis. This corresponded with a minor increase in breathing rate and an average pneumonitis score of three out of five on H&E staining. Additionally using a linear regression to analyse pharmacokinetic metrics from the DCE-MRI, the only significant changes were seen at 16 weeks in the RT + BEZ cohort, which demonstrated the most severe RILT at this time point.

Figure 4.14 compares the RILT scores recorded at each time point determined using imaging and pathology. In the BKM group, radiation response was observed more frequently in pathology studies compared to imaging. In the BEZ group, all animals underwent all assessments. For the two animals with radiation response, CT and MRI suggested more

severe toxicity than pathology. At the other time points, animals sacrificed for pathology were not necessarily those imaged at the corresponding time point.

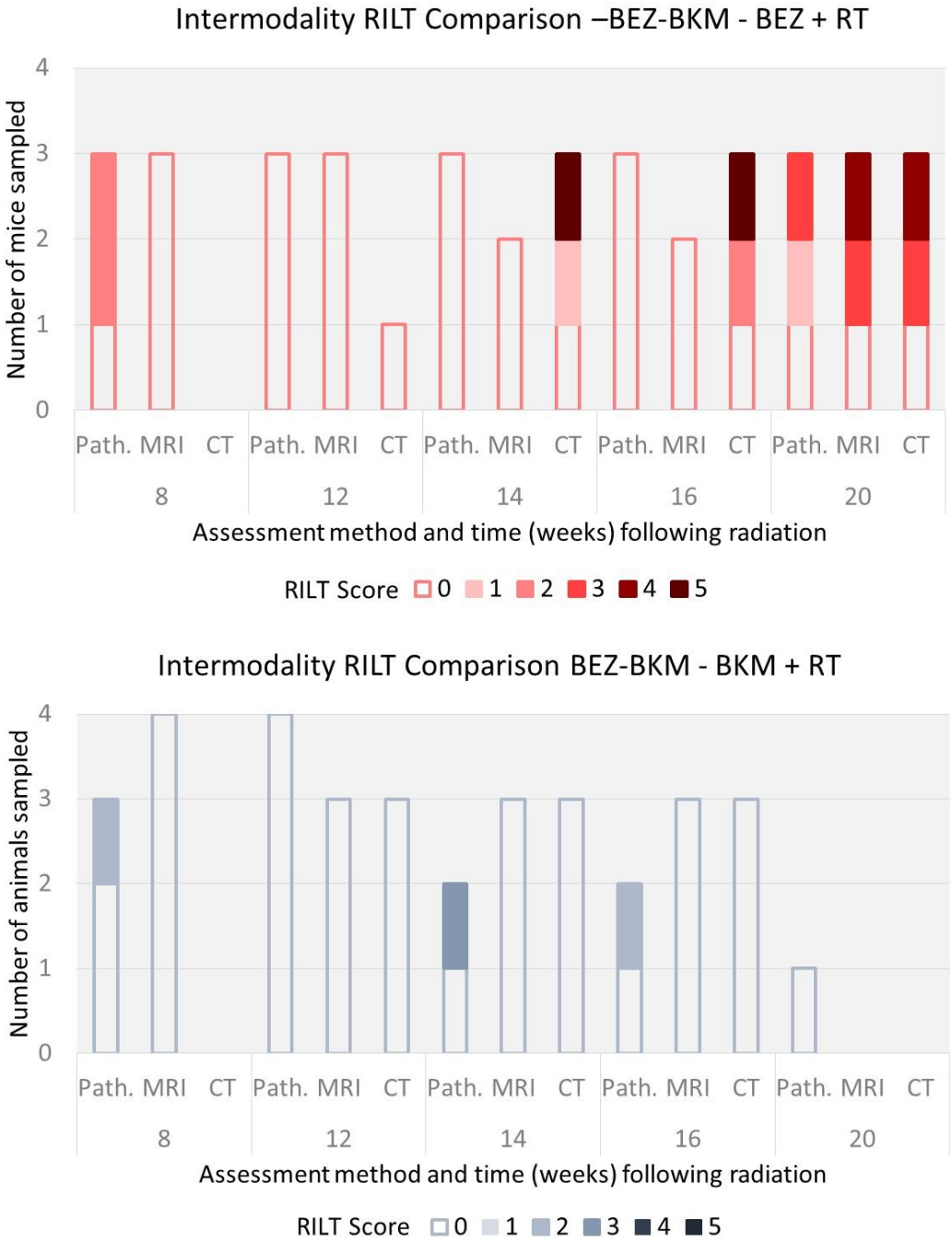



**Figure 4.14 Intermodality RILT Incidence and Severity:** Bar plots of the incidence and severity of RILT seen on CT, MRI and histopathology for animals having undergone 20 Gy RT plus BEZ (top) or 20 Gy RT plus BKM (bottom).

Intermodality correlations were determined using the proportion of animals sampled from each cohort that showed RILT. Figure 4.15 shows CT, MRI, and pathology of a single

mouse at week 20 in the BEZ group and its associated RILT scores. This animal also experienced peak increase in breathing rate of + 28 % at 16 weeks following RT and recovered to a breathing rate 10% greater than baseline by 20 weeks. No significant weight loss was observed in this animal.

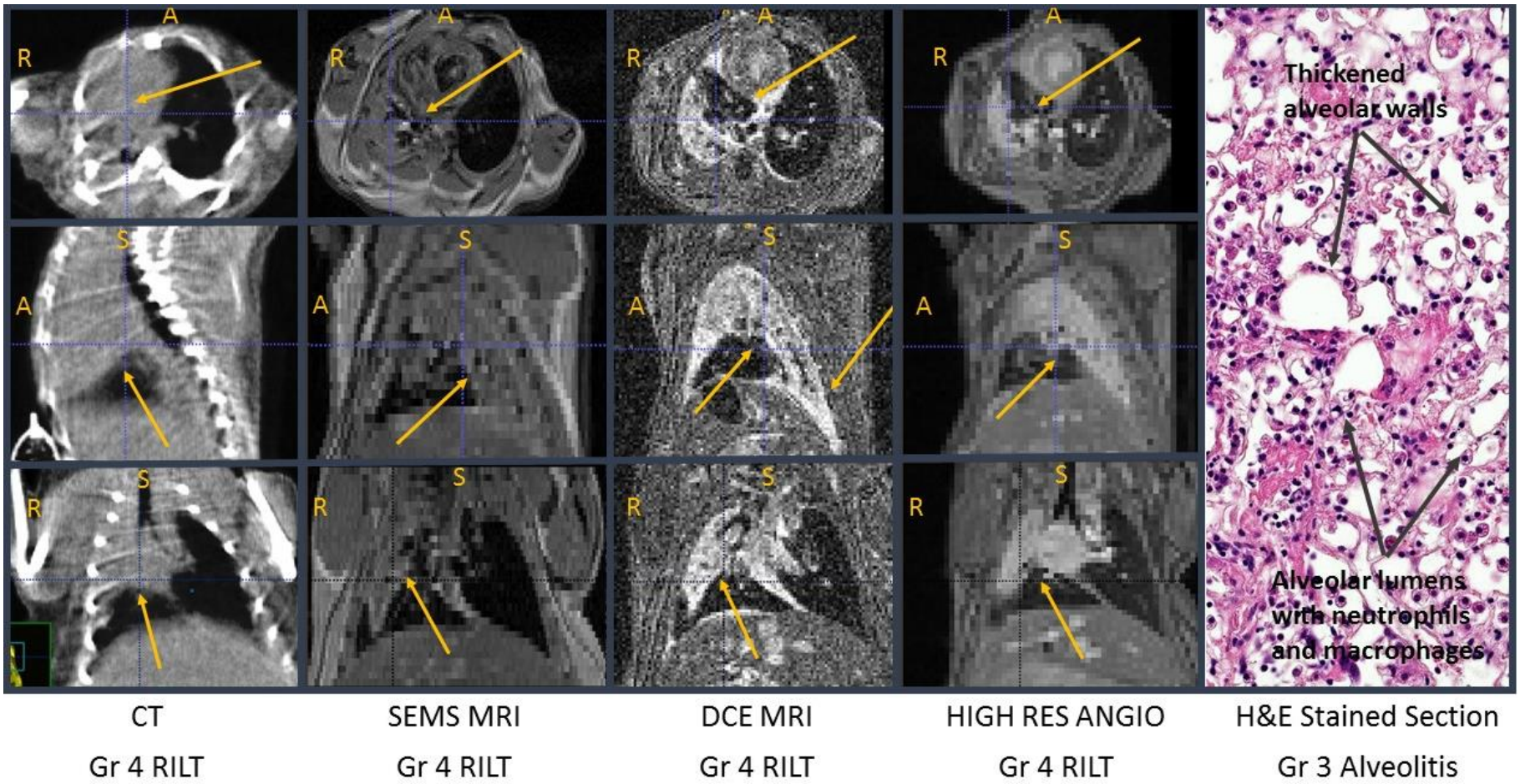



**Figure 4.15 Comparison of RILT on CT, MRI and Histopathology:** CT and MRI images of a single mouse at 20 weeks following 20 Gy RT + BEZ and associated H&E stained lung section demonstrating Grade 4 RILT (50-75% lung inflammation/consolidation) and Grade 3 alveolitis. R = right, A = anterior, S = superior. Arrows on images represent lung changes from normal/baseline.

## 4.4 **Discussion**

The initial experiment in this chapter (pAKT) measured the levels of pAKT in lung and spleen tissues from CBA mice treated with BKM or BEZ, and compared the data with tissues from vehicle treated animals. The results presented in this chapter showed a decrease in pAKT in the lungs of animals treated with PI3K/AKT inhibitors, indicating that PI3K inhibitors affect normal tissues.

Experiment BEZ-BKM investigated the effect of the PI3K/AKT inhibitors on breathing rates, CT and MRI imaging, and histopathology in CBA mice. Changes in breathing rates were more frequently observed in these experiments than those described in Chapter Three, and appeared most often between weeks 12 and 16. These findings were similar in time scale to those reported by Jackson, who showed that CBA mice experienced respiratory rate increases at 12-15 weeks following 15 Gy and at 10-12 weeks following 12.5 Gy to the whole thorax (173).

As in the previous experiments, limited RILT events were observed, despite the fact that all irradiated animals showed fur loss followed by a regrowth of white fur in the irradiated volumes, and the cabinet dosimetry confirmed that dosage was accurate.

It is possible the imaging interval of 4 weeks may have not have been frequent enough to observe transient changes in the lung, therefore it was decided to add an additional time point at 14 weeks to further studies. Additionally, mice that were chosen for euthanasia at the predetermined time points were those animals showing early signs of radiation responses (weight loss, increase in breathing rate). Sacrificing mice at the time at which a RILT response was developing reduces the chances of detecting this response using imaging methods.

MR imaging as performed in this project, does appear to be a suitable method of detection of RILT and has the advantage that it is non-invasive and avoids exposure to ionizing radiation. Given the dose and volumes irradiated in these mice, the expectation was that there would be more mice with radiation induced toxicity. Cappuccini et al have had success using 15 Gy single fraction hemi-thoracic irradiation in C57BL6 mice to induce RILT, although fibrosis was only observed after 22.5 Gy (177). However Lockhart (265) and Down (175), observed RILT in CBA mice following hemi-thoracic irradiation doses as low as 15 Gy with peak reactions observed at 16 weeks.

Based on CT imaging BEZ treated animals demonstrated a greater incidence of RILT when compared to BKM treated animals; with four animals in the BEZ treatment group demonstrating RILT compared to only one in the BKM treatment group. Similarly on MRI, all four of the twenty animals imaged following baseline that showed RILT were from the BEZ + RT arm. On histopathology 3/12 BEZ and 3/11 BKM samples showed alveolitis. On imaging, BEZ has demonstrated a greater radiosensitizing effect on normal tissue than BKM, and using the data from study RT2, BEZ also showed a greater radiosensitizing effect than both RT + NFV and RT alone. Given BEZ is also an ATM-inhibitor and has demonstrated greater radiosensitivity than ATM inhibitors alone, it would serve to reason that this combined inhibitor would induce a greater effect than pure AKT inhibitors. However, the differences observed in this experiment were not statistically significant and studies in which all animals undergo each of the assessment methodologies at each time point would be required to validate this hypothesis. It was not always possible to image animals on both CT and MRI due to limitations on the local project licence as to the duration of anaesthesia the animals were allowed to undergo.

In pre-clinical models Schnell et al (266) used DCE-MRI in rats bearing orthotopic tumour models following treatment with BEZ and showed a reduction in $K^{Trans}$ that was

associated with a reduction in tumour vasculature permeability. Despite the limited number of RILT events in this work, preliminary and novel investigations performed using model-based and non-model-based analyses of DCE-MRI detection of RILT, using sequences developed by the Imaging Core (under the guidance of Dr. Sean Smart) were encouraging. Animals demonstrating RILT on other assessment modalities demonstrated increased (and sustained) gadolinium uptake on DCE-MRI which likely represents an inflammatory response (i.e., pneumonitis).

# Chapter 5

*PI3K/AKT inhibition and image guide radiation (IGRT)*

# 5 PI3K/AKT INHIBITION AND IGRT

## 5.1 Introduction

Based on the results of the previous chapters, the increase in radiation dose from 18 to 20 Gy resulted in the ability to detect RILT in approximately 50% of the mice sampled at 14 and 16 weeks post-irradiation using pathology and CT imaging respectively. Additionally, reliable anatomical and functional MRI protocols had been developed, which were predominantly motion artefact-free, with sequences clearly able to detect RILT in the irradiated mice. The radiation delivery method however, remained somewhat crude.

Clinical radiotherapy involves radiation conformed tightly to the targeted area, in up to four-dimensions (4-D) and uses on-treatment image guidance to accurately deliver radiation in multiple fractions. At the time of the inception of this thesis, few authors had published on single or partial lung irradiation and normal tissue toxicity in mice (171, 175, 181, 246, 258). Details on animals having undergone conformal irradiations were sparse. Only recently have technological advances made it possible for authors to report on small field or conformal lung irradiation in mouse models (177, 178, 267, 268). These new tools, such as the SARRP system, can be used to design small animal radiation experiments that better reflect clinical radiotherapy, either in terms of improved targeting (image guidance) or dose/fractionation.

With the acquisition and commissioning of a SARRP system at the CRUK/MRC Oxford Institute for Radiation Oncology, it became feasible to investigate pre-clinical image guided radiation (IGRT) in single and multi-fractionated experiments with and without the administration of a targeted radiosensitizer selected from the previous studies.

For the experiments described in this chapter, the single agent BKM was selected, due to interest in introducing this agent clinically in patients undergoing palliative radiotherapy for ≥ Grade III lung cancers.

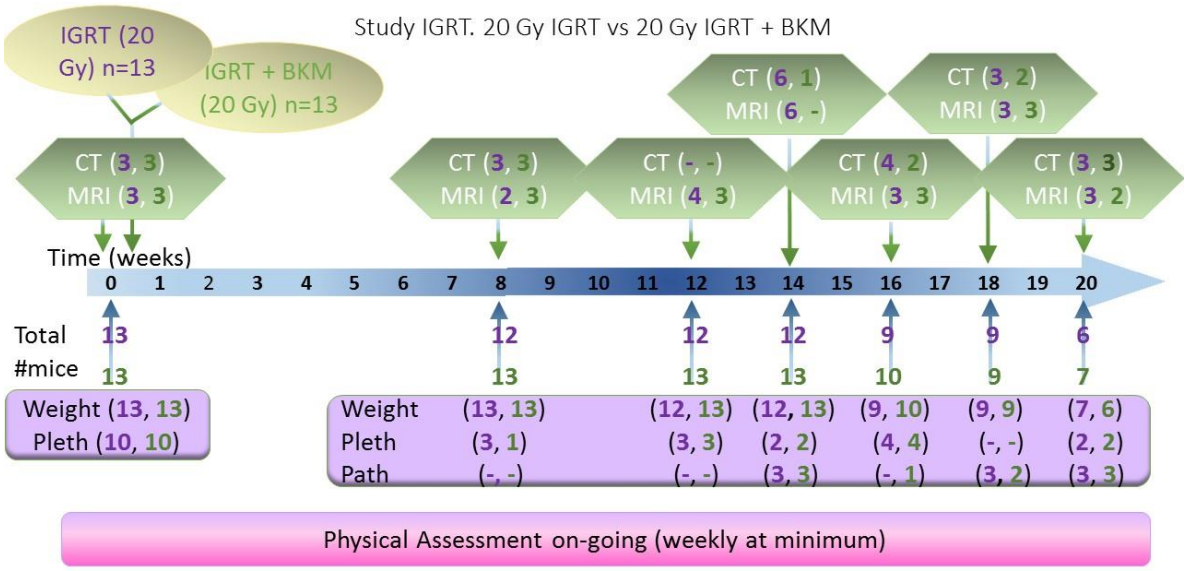
Following dosimetric confirmation of the SARRP system and planned radiations (Appendix 1), single- and multi- fraction RT experiments were undertaken, to investigate the response to radiation alone versus radiation plus the targeted radiosensitizer BKM (Figure 5.1). In brief the experiments were:

1. IGRT: Single 20 Gy fraction of radiation, targeting the right lung, with (n = 13) or without (n = 13) BKM.
2. IGRTfx: Three 15 Gy fractions of radiation delivered on alternate days to the right lung, with (n = 13) or without (n = 13) BKM.

## 5.2 Single Fraction IGRT

### 5.2.1 Rationale

The aim of this experiment was to evaluate the effects of image guided radiation plus the PI3K inhibitor BKM, a drug that holds interest for our group clinically, on the incidence of RILT in normal lung tissue. As the radiation dose and targeted agent were consistent with those used in the previous experiment (BEZ-BKM), it was possible to compare the effects of image guided radiation to that administered using the cabinet irradiator.




Bracketed numbers show the number of mice sampled* from IGRT and IGRT + BKM cohorts respectively; table shows total number of mice in study at each time point for IGRT and IGRT + BKM respectively.

**this only includes images/pathology suitable for analysis*

**Figure 5.1 IGRT Study Schema**

### 5.2.2 Results

#### 5.2.2.1 *Physical Assessment and Plethysmography*

Of the 26 mice in the study, three experienced progressive weight loss between weeks 12 and 16 following irradiation that required increased monitoring and, in one case, euthanization. Net weight losses in the range of 14% to 20% occurred in two animals that received RT + BKM and one that received RT alone, with the maximum weight lost (and euthanization) occuring in the animal in the RT alone cohort. Two animals demonstrated an initial weight loss of 8% but went on to regain 4% and 9% respectively.

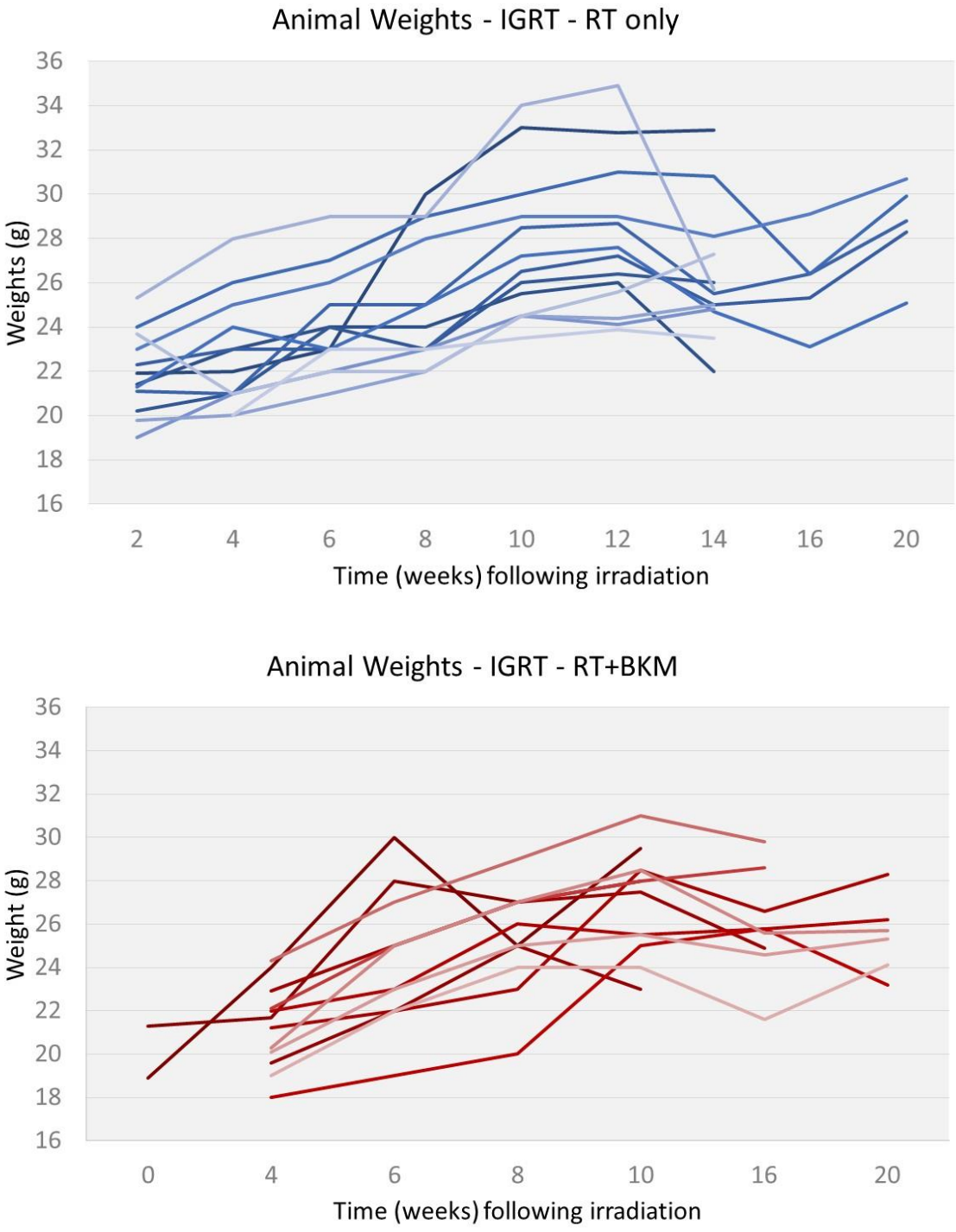



**Figure 5.2 Animal Weights for IGRT:** Plots of animal weights for mice on study from baseline to a maximum of 20 weeks following irradiation for animals receiving 20 Gy RT to the right lung (top) and animals receiving 20 Gy RT to the right lung plus BKM (bottom).

**NB – at baseline animal weights were recorded as cage averages, with the exception of animals undergoing baseline imaging, as such individual weights are only available from weeks 2, 3 or 4.*

Welch two sample t-tests confirmed there was no statistically significant difference in the breathing rates of animals receiving IGRT + BKM or RT alone ($p = 0.5432$) over all time points. In both treatment groups, breathing rate was observed to reach a peak at week 14, which was followed by a significant decline at week 16, as shown in Figure 5.3.

In both arms of the IGRT study ≥ 33% mice evaluated at 12 and 14 weeks following irradiation had an increase in breathing rate of ≥ 15% over baseline. This prompted more frequent monitoring of animal status, but none of the animals breached the toxicity thresholds stated on the project license (> 35% increase in breathing rate). At 14 weeks one mouse in the IGRT + BKM arm had an increase of 25%. Figure 5.3 plots the details of individual and population mean respiratory rates for both cohorts.

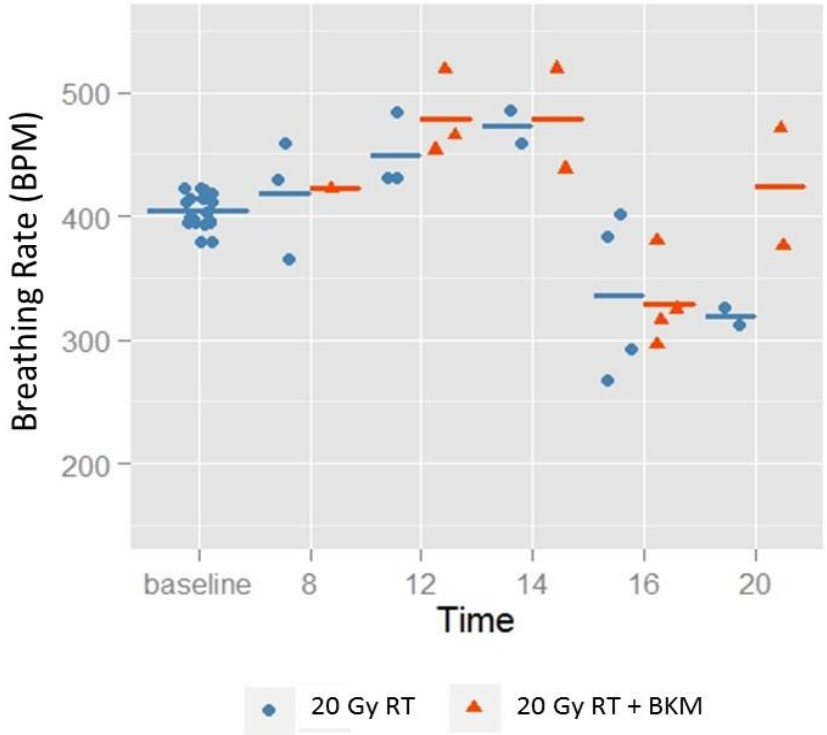



**Figure 5.3 Breathing Rates for Study IGRT**: Scatter plots of individual and population mean respiratory rates (BPM) of mice undergoing IGRT +/- BKM in a single fraction of 20 Gy

#### 5.2.2.2 *MRI*

Following radiation, 32 MRI datasets were available and assigned a RILT score. This was the most complete experiment to date with the total number of datasets available at each time point shown in Table 5.1.

**Table 5.1 MRI Acquisition in Study IGRT**

| | 20Gy | 20 Gy + BKM |
|---|---|---|
| Baseline | 3 | 3 |
| 8 weeks | 3 | 3 |
| 12 weeks | 4 | 3 |
| 14 weeks | 6 | - |
| 16 weeks | 3 | 3 |
| 18 weeks | 3 | 3 |
| 20 weeks | 3 | 3 |

Using the fully developed anatomical and functional MRI sequences, and the most complete data sets of any of the chapters in this thesis, it was possible to compare independently assigned toxicity scores between SEMS, DCE-MRI, and ANGIO images, which showed complete correlation. For each sequence, 5 instances were scored at 0, 5 instances were scored at 2, 10 instances were scored at 3, 7 instances were scored at 4, and 5 instances were scored at 5. There was no difference in the frequency of RILT between animals undergoing radiation plus BKM or radiation alone ($P = 0.5229$)

Continued MRI methodological development (i.e., implementing the changes detailed in section 2.6.2) resulted in improved imaging with reliable gating methods that facilitated noise-free image acquisition, that was not available in the experiments described in the previous chapters. The use of a supine animal position in the experiments in this chapter, allowed cardiac leads to be placed closer to the animal's heart, and facilitated the detection of every heart beat which improved the ECG signal and enabled steady state maintenance

between heart beats during the high resolution flip angle imaging. The corollary of this was that image registration between CT and MRI was not possible due the difference in animal positioning.

Figure 5.4 plots the RILT scores assigned on MRI. The frequency of RILT was greatest in the RT arm, with 86% percent of all animals imaged given RILT scores of 2-5. Of the animals imaged in the RT + BKM arm, 53% were assigned RILT scores of 2-5.

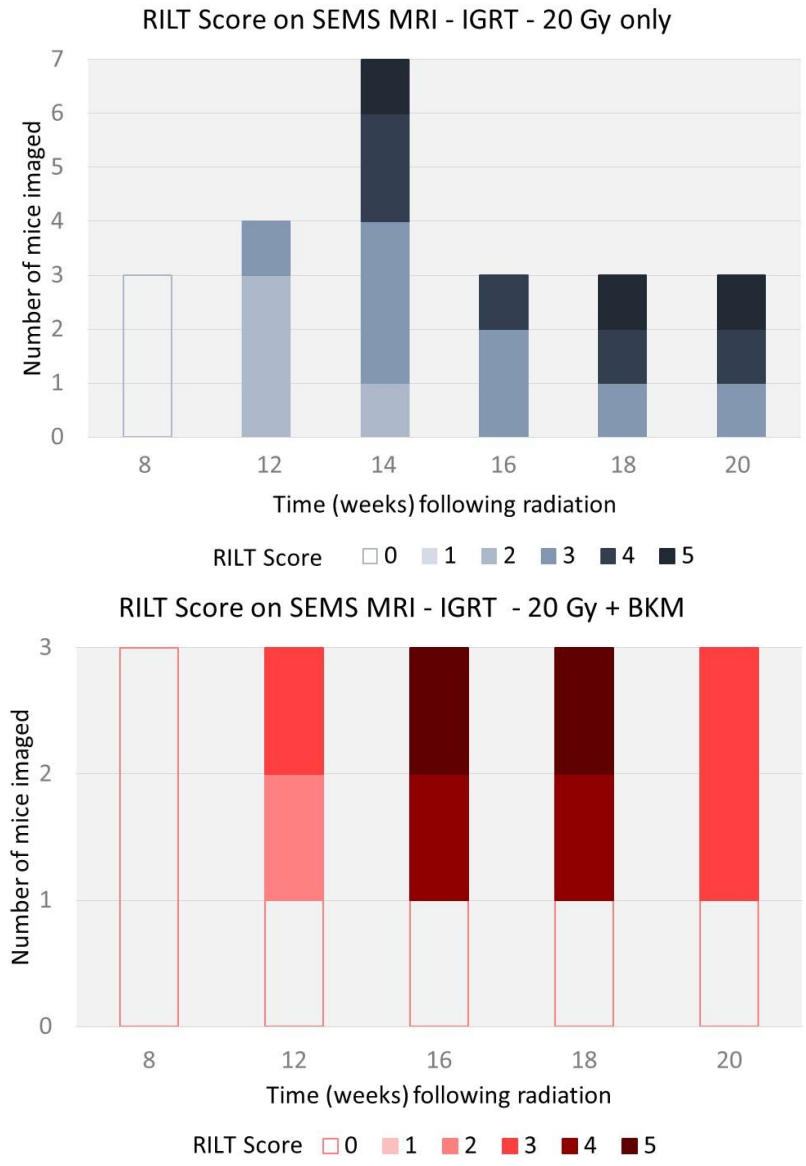



**Figure 5.4 RILT Score on SEMS MRI:** Bar plots of incidence and RILT scores as determined on SEMS MRI for animals undergoing 20 Gy RT (top) or 20 Gy RT +BKM (bottom) to the right lung.

Using SEMS images, the mean signal intensity from the right and left lungs was determined in each mouse imaged at each imaging time-point and plotted against RILT score (Figure 5.5). Paired t-tests confirmed the signal intensity was significantly different in the right and left lungs with P-values <0.001.

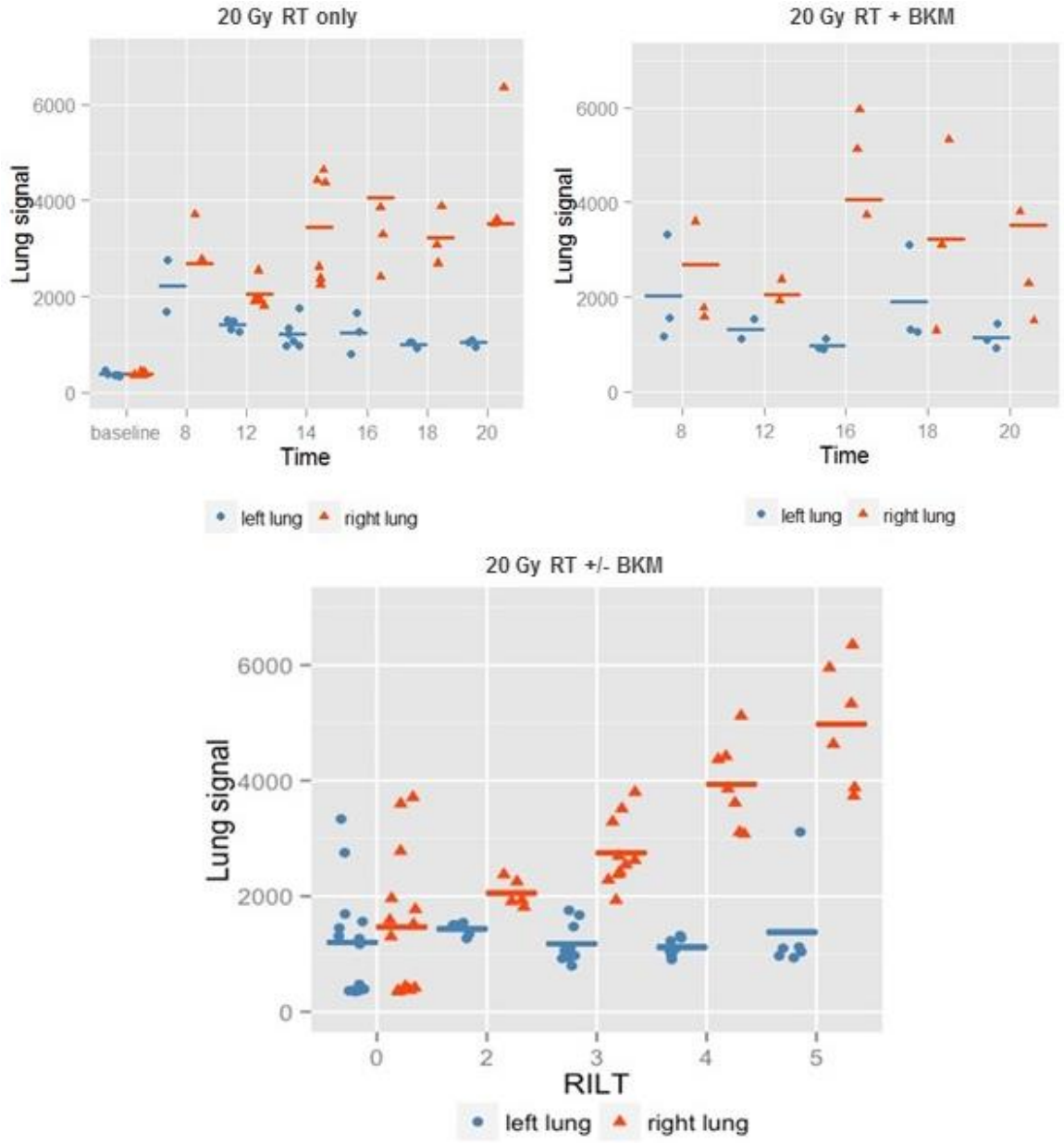



**Figure 5.5 Signal versus Time and RILT:** Scatter plots of individual and population mean MR Signal Intensity of the right and left lung against time (top) and RILT (bottom). Top: SI vs. time or animals receiving 20 Gy (left) or 20 Gy + BKM (right). The increased signal in the right lungs correspond with maximum RILT scores. Bottom: SI for right and left lungs for both cohorts versus RILT. Note the increasing lung signal in the right (irradiated) lungs with increasing RILT score.

To illustrate these RILT scores on the ANGIO imaging sequence, Figure 5.6 shows representative axial, sagittal and coronal images assigned RILT scores of 0 (lung demonstrating no radiation changes), 3 (25%-50% of the lung volume affected by radiation changes), and 5 (75%-100% of the lung affected by radiation changes). These images highlight the significantly improved image quality compared to those acquired in earlier experiments.

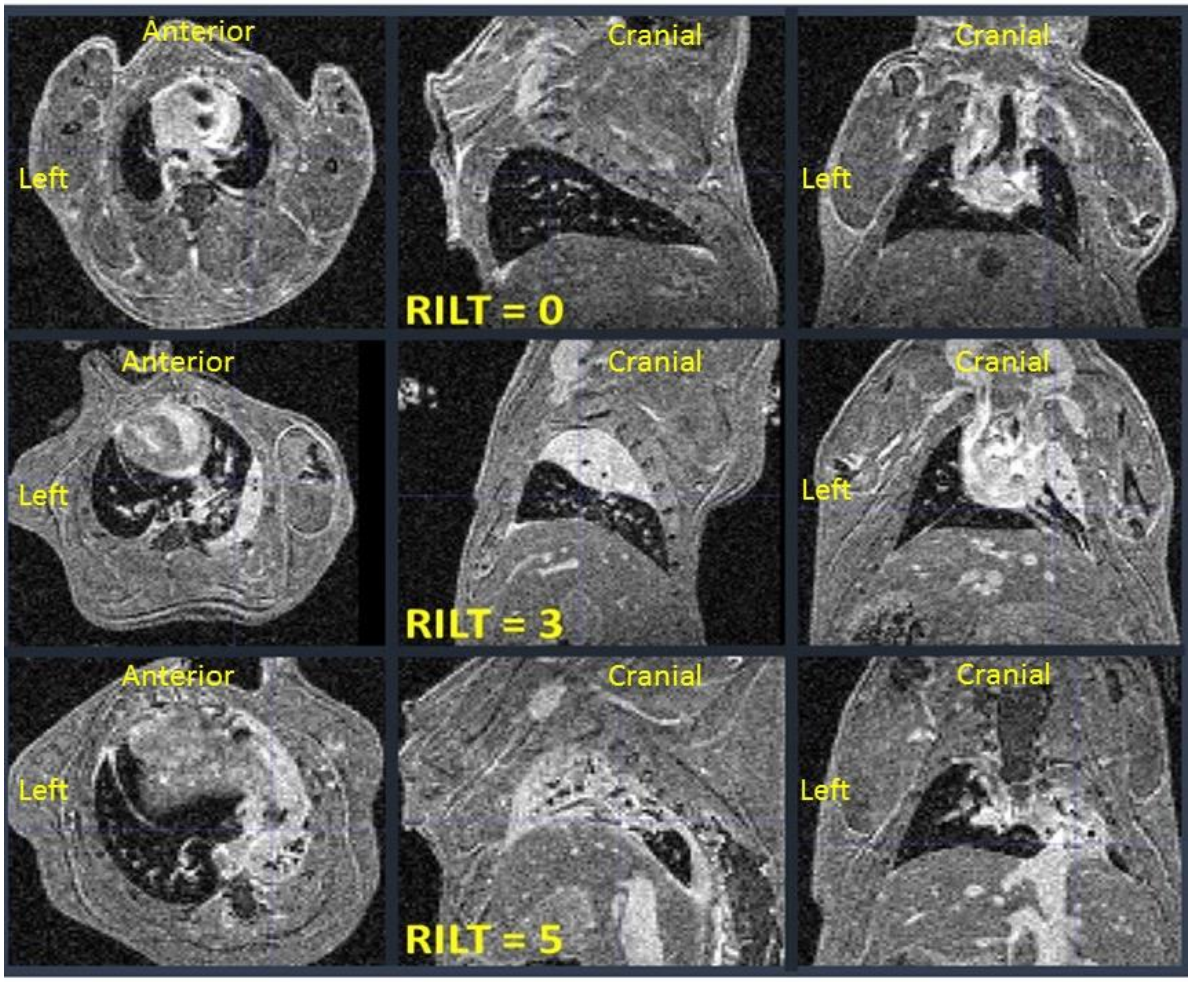



**Figure 5.6 Scoring RILT on ANGIO:** High resolution flip angle images (ANGIO) of mice from study IGRTfx showing mice with no RILT, a RILT score of 3 (middle) and a RILT score of 5 (bottom).

On DCE-MRI, the initial area under the curve (iAUC) was observed to increase with increasing RILT in the right (irradiated) lung while demonstrating relatively little change in

the left (unirradiated) lung (Figure 5.7). A comparison of iAUC between right lungs with and without RILT was statistically significant (P-value = 0.0002238).

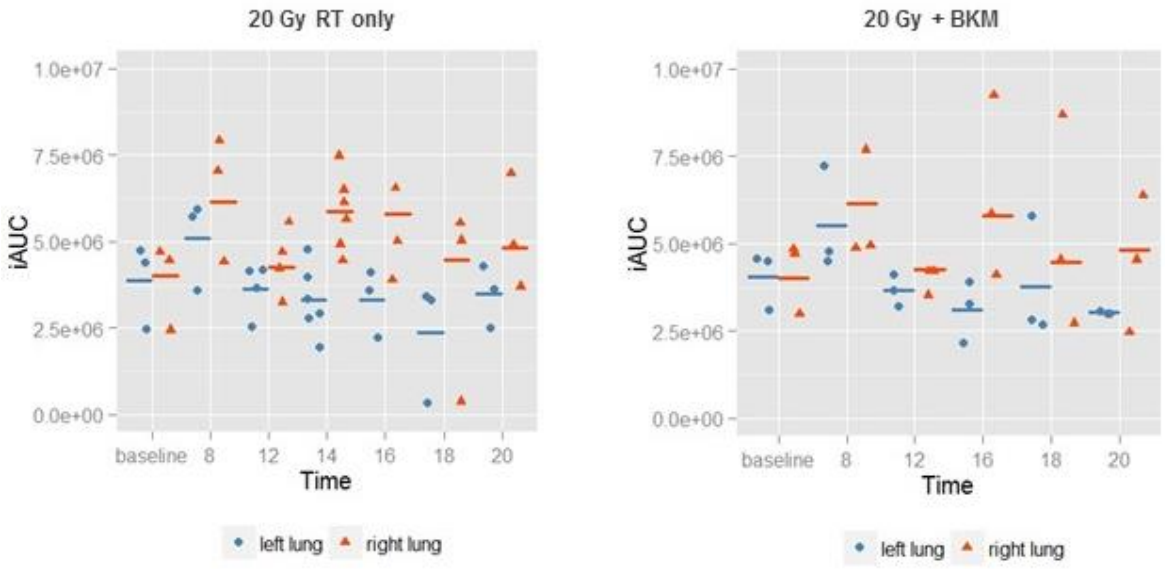



**Figure 5.7 iAUC versus Time**: Scatter plots of individual and population mean iAUC for the right and left lungs of mice irradiated in single fraction 20 Gy alone (left) or 20 Gy + BKM (right) against time seen on MRI imaging.

.

Individual graphs of signal intensity (SI) v time were generated from the DCE raw data of the right lungs (Figure 5.8). In general, the curves of the animals with the most severe toxicity scores (4 and 5) reach a higher peak of signal intensity than the curves of animals which did not experience radiation toxicity (score of 0). This increased signal intensity represents an increase in gadolinium uptake, most likely due to an inflammatory response (alveolitis or pneumonitis) within the irradiated lung. However there is significant overlap in the SI curves for animals with Grade 0, 2 and 3 toxicity scores.

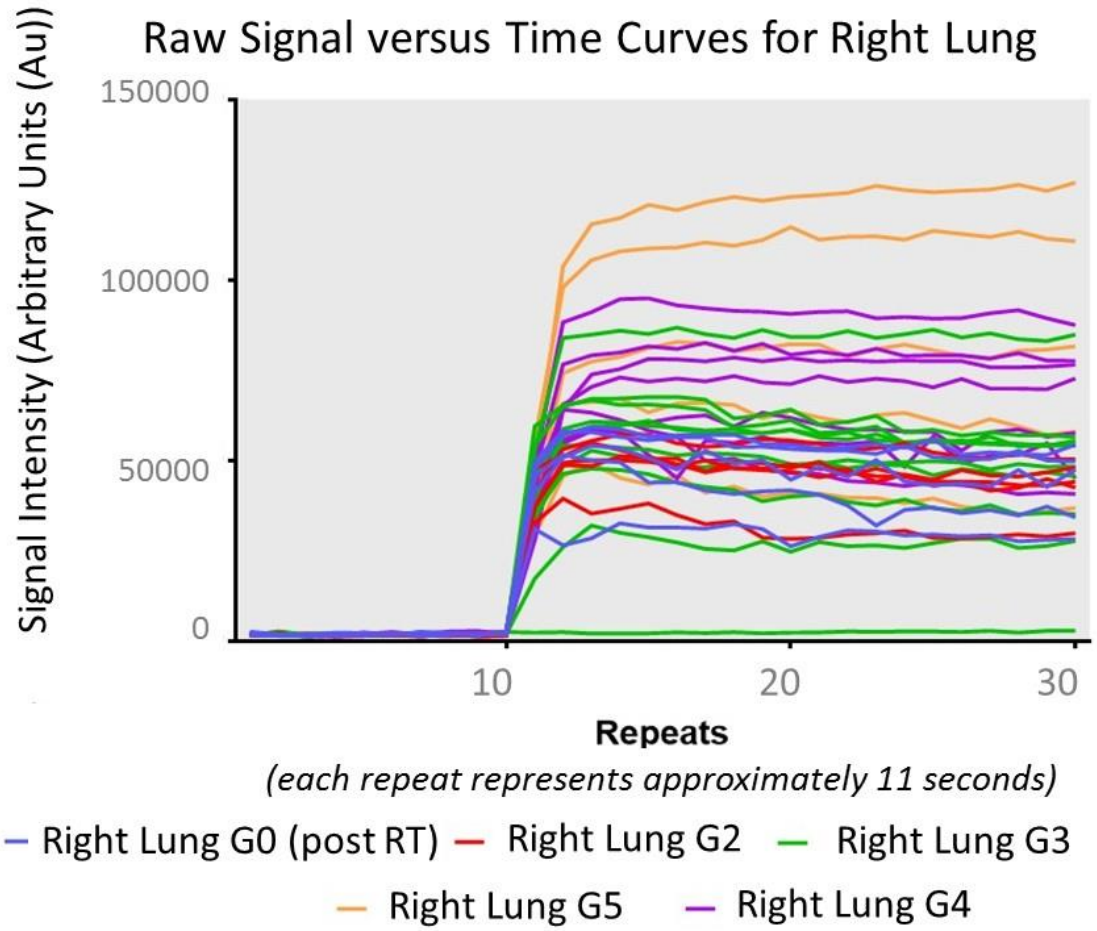



**Figure 5.8 IGRT Raw Signal versus Time Curves:** Individual plots of raw signal intensity versus time (represented by repeat image acquisitions) for the right lungs of animals treated with 20 Gy RT +/- BKM.

Mean and standard error (SEM) SI vs time curves have been plotted for mice with RILT scores of 0, 2 and 3 (Figure 5.9). There was a small increase in mean peak SI for the Grade 3 mice compared to Grades 2 and 0. However, there was greater variability in SI between individual animals experiencing Grade 3 toxicity; as evidenced by the large error bars. Evidence of contrast washout, which manifests as a gradual decline in the slope of the curve following peak intensity, was similar in mice with Grades 3, 2 and 0 toxicity scores.

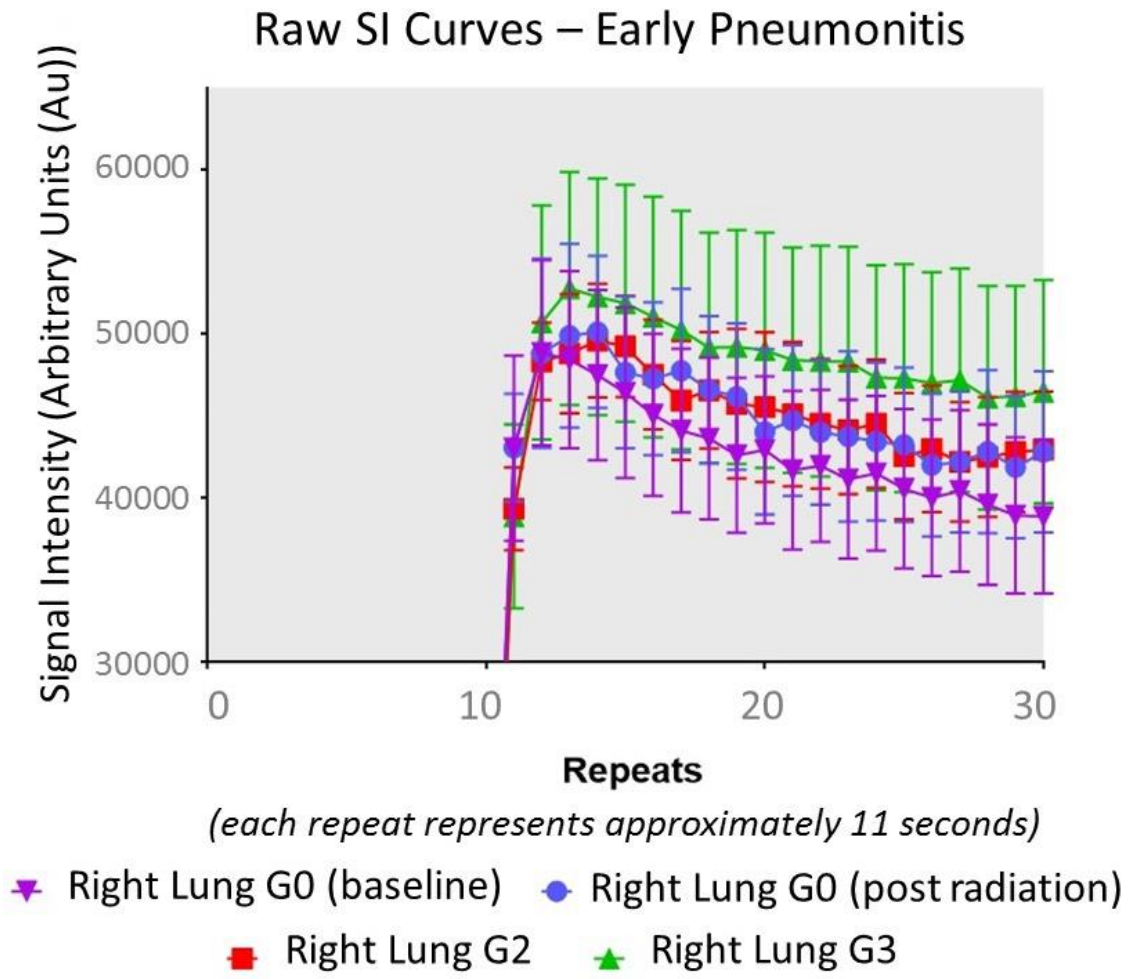



**Figure 5.9 Mild to Moderate RILT Signal versus Time Curves:** Individual raw signal versus time (represented as repeat image acquisitions) for animals following RT +/- BKM demonstrating RILT scores of 0, 2, or 3.

#### 5.2.2.3 *CT*

Twenty-seven CT images were suitable for analysis following irradiation. In approximately 20% of CTs, complete lung consolidation made segmentation very challenging despite the availability of automated segmentation tools (i.e., using boundary and/or CT density methods). These images were entirely manually segmented. Figure 5.10 is an example of a mouse with near complete lung consolidation assigned a RILT score of 5 on CT and 4 on SEMS MRI. This figure highlights one of the challenges of CT segmentation, which is that tissue interfaces (e.g., between the consolidated lung and the chest wall or liver) are difficult to distinguish by eye or segmentation software, due to lack

of a discernible boundary or distinguishable difference in signal intensity (HU). In these cases, CT-MRI co-registration of the images could facilitate lung delineation.

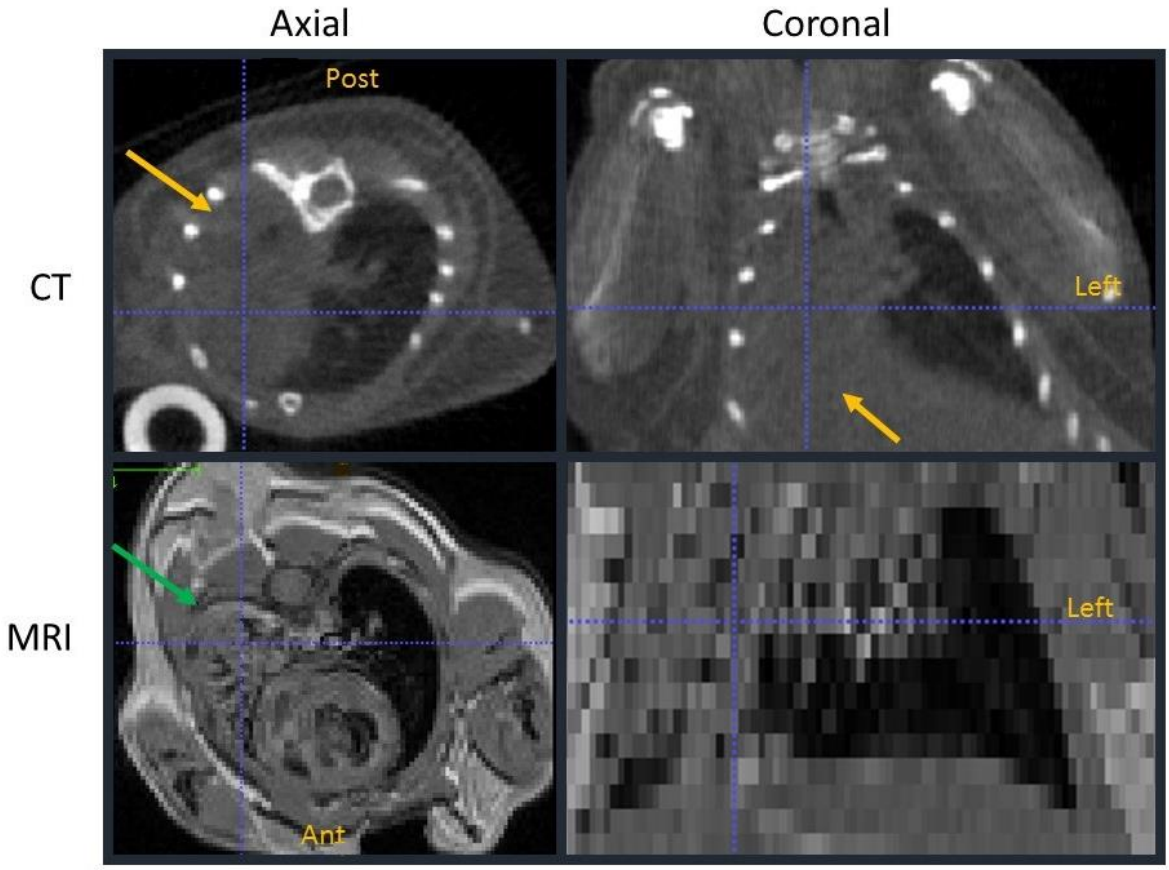



**Figure 5.10 Consolidated Lung on CT and MRI:** Axial and coronal images of a mouse imaged near complete lung consolidation as seen on CT and SEMS MRI, highlighting some of the challenges of lung segmentation on CT (yellow arrows), when compared to MRI (green arrow).

Hill and Van Dyk (118, 119) proposed an HU increase of 10-15% was indicative of RILT. In study IGRT, 12/13 mice demonstrating 15% increase in lung density on CT from baseline were assigned a RILT score ≥ 1. One mouse had a RILT score of 0. The work presented here corresponds to a 92% sensitivity rate for this metric.

#### 5.2.2.4 *MRI-CT Comparisons*

On 17 occasions following baseline there were paired CT-MRI scored datasets. Twenty-nine percent of the pairs had the same RILT score assigned to both CT and MRI images, and

in 42% of cases, the RILT scores varied by only 1 scoring point. The majority of cases in which differences in RILT scores between the two modalities were observed occurred in animals with scores of 3 or 4 (25-50% or 50-75% of the lung volume demonstrating radiation changes). In these cases the effects of contouring accuracy and reproducibility of animal positioning between imaging modalities could have a significant effect on scoring a lung as having more or less than 50% involvement. Using a paired t-test the scores assigned to CT were not significantly different to those assigned to MRI ($P = 0.0583$). In 75% of the cases with variability between imaging modalities, MR images were assigned the greater score.

#### 5.2.2.5 *Pathology*

Because limited toxicity was observed at weeks 8 and 12 on pathology in the previous experiments, it was decided that euthanasia for lung extraction at 8 or 12 weeks would only be performed should there be indications of toxicity on imaging or plethysmography.

Radiation changes in the lung were first observed at 14 weeks post intervention in both RT alone and RT + BKM study arms. The most severe RILT occurred at 16 weeks in an RT + BKM mouse that was assigned alveolar inflammation and fibrosis scores of 4 and 3 respectively. Figures 5.11 and 5.12 are representative images of gross pathology and histopathology from animals with RILT following IGRT + BKM.

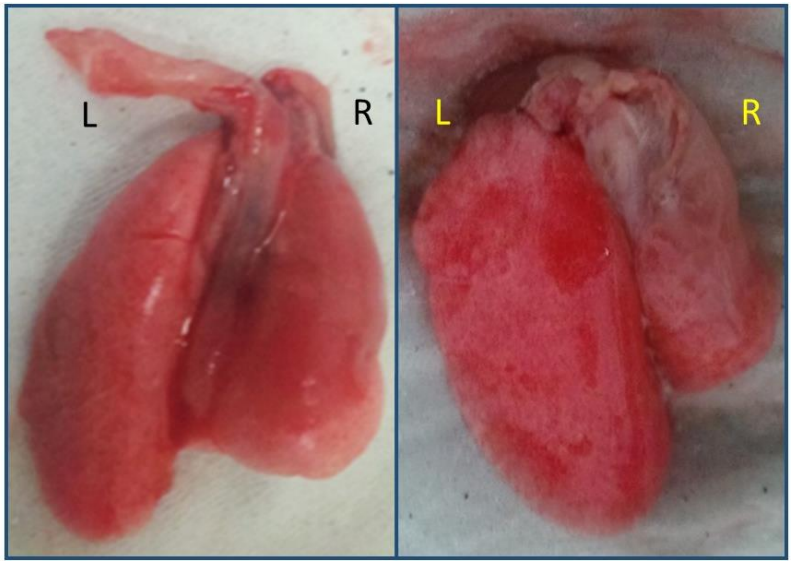



**Figure 5.11 Gross Pathology:** Right and left lungs extracted at 16 weeks following 20 Gy RT to right lung plus BKM, demonstrating size reduction and discolouration of right lung.

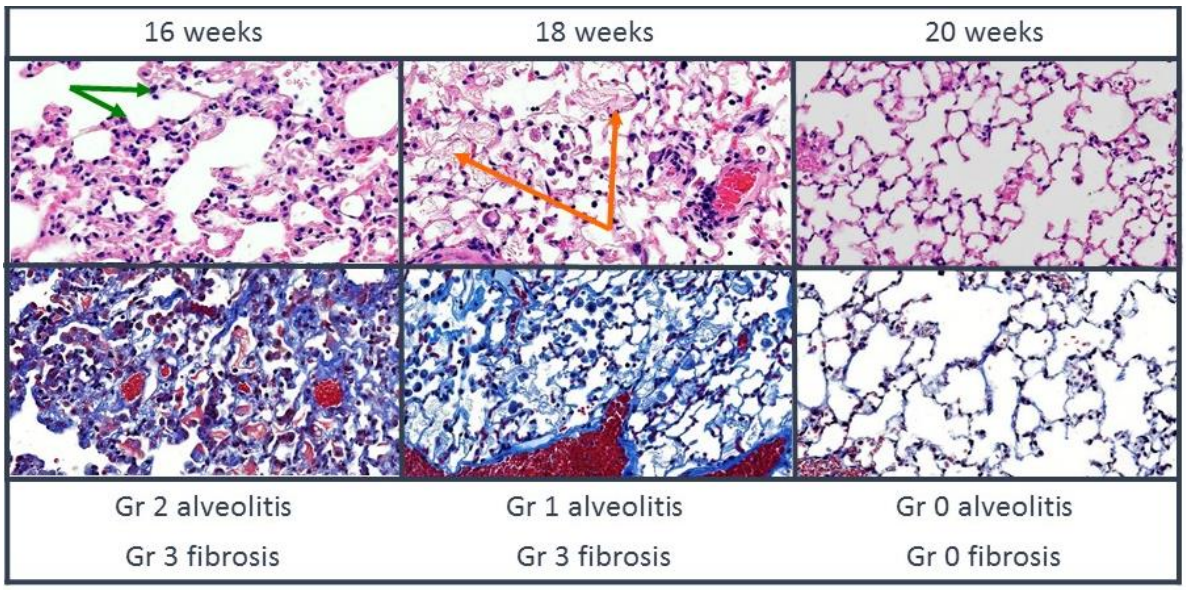



**Figure 5.12 Histopathology:** Hematoxylin-eosin (top) and Masson's trichrome (bottom) stained lung sections from mice treated with IGRT + BKM at 16, 18 and 20 weeks following radiation. Arrows indicate inflammatory cells (green) and hyaline material (orange). Alveolitis was scored on a scale of 0-5, with 0 indicating no alveolitis and 5 indicating complete tissue consolidation. Masson's trichrome staining was used to visualise collagen deposition.

Figure 5.13 shows the alveolitis incidence and severity scores for the mice in both treatment groups. The results presented in this chapter are concerned primarily with the pathological findings on the right (irradiated lungs). However, it should be noted that in the IGRT+BKM arm, alveolitis was observed in the unirradiated left lung in 1/3 mice at week

14, 1/1 mice at week 16 and one out of two mice at week 18. Alveolitis scores in the unirradiated lungs were lower than in the irradiated lungs.

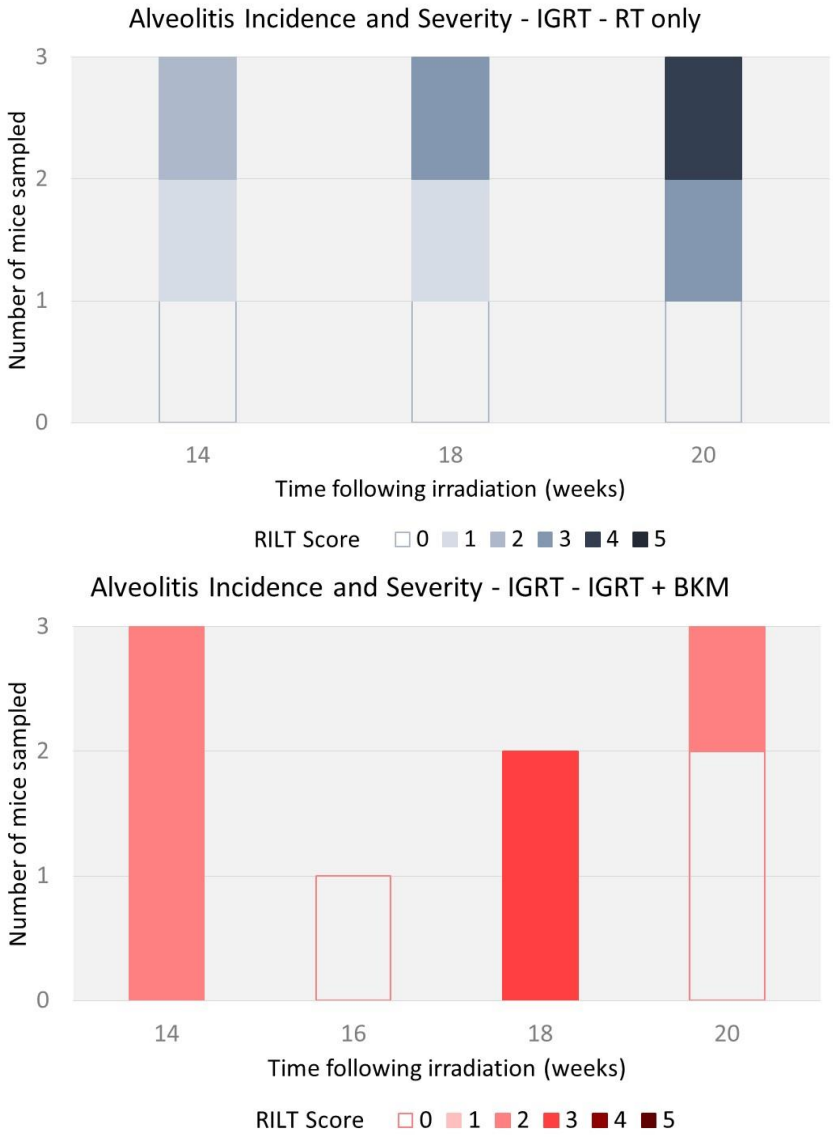



**Figure 5.13 Alveolitis for Study IGRT:** Bar plots of the incidence and severity scoring for alveolar inflammation in irradiated lungs from experiment IGRT.

Fibrosis was observed in 5 of 9 RT only animals, in the right lung only, at weeks 14 (n = 1, score 2), 16 (n = 2, scores 1 & 3), and 18 (n = 2, scores 2 & 3). In the IGRT + BKM arm, two animals demonstrated fibrosis at weeks 16 and 18. Because of the pathologies observed in the unirradiated lungs, and limited number of samples available it is important to interpret the pathology results with caution.

5.2.2.6 *Case Study*

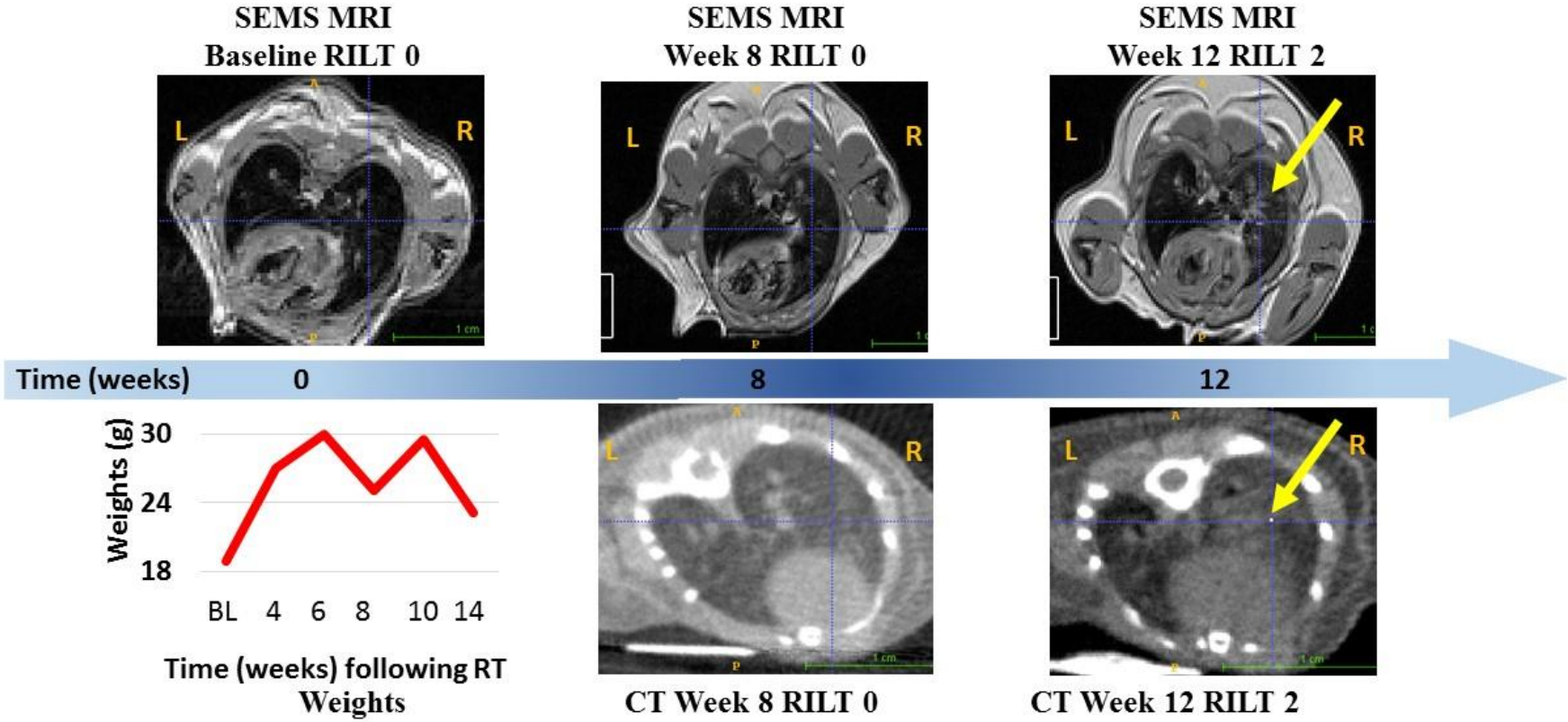



**Figure 5.14 IGRT Case Study:** Single mouse that underwent serial imaging following 20 Gy IGRT to the right lung. CT images at 8 and 12 weeks following radiation demonstrated grade 0 and 2 RILT respectively. SEMS MRI at baseline, weeks 8, and 12 were scored as grade 0, 0, and 2 respectively. This animal demonstrated a weight loss of 16% between weeks 6 and 8 but then recovered by week 10. Only to have a 21% drop in weight by week 14 at which point it was sacrificed. The alveolitis and fibrosis scores on H&E and Masson's stained lung sections were both 2.

## 5.3 Fractionated IGRT +/- BKM

### 5.3.1 Rationale

In the clinical situation, a single dose of 20 Gy is rarely used to treat a patient with lung cancer. A popular dose/fractionation for small, peripheral tumours treated using stereotactic body radiotherapy is 45 Gy delivered in 3 x 15 Gy fractions on alternate days (269-271). For this reason, and to investigate the effects of higher radiation doses on normal lung tissue, the experiment was repeated in 26 mice with (n = 13) and without (n = 13) BKM followed by 3 fractions of 15 Gy delivered Monday, Wednesday, Friday for a total dose of 45 Gy delivered over 5 days. The results are reported below and compared to the single fraction experiment.

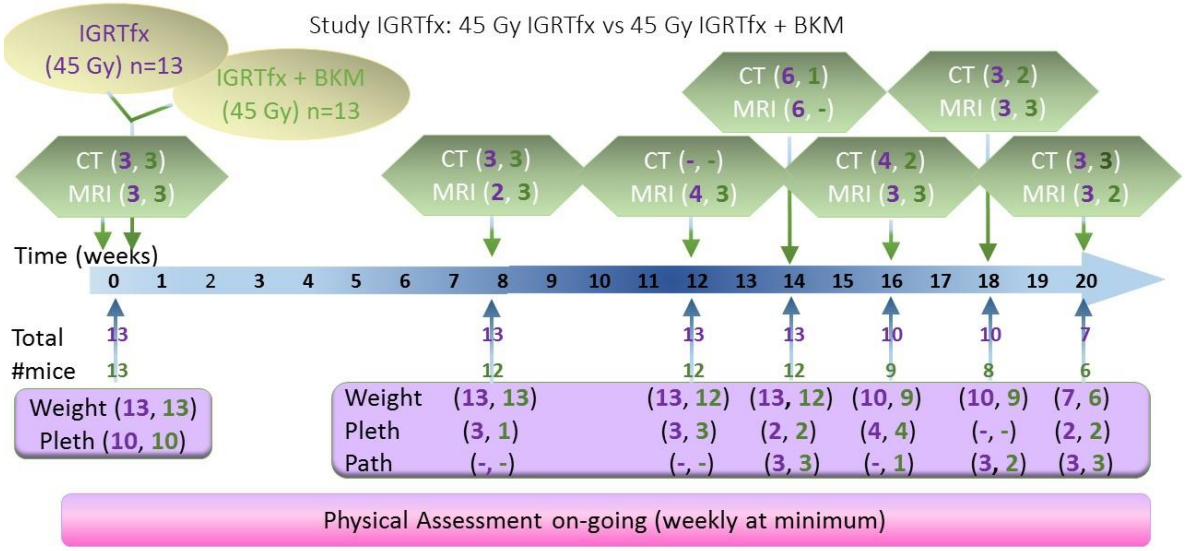



**Figure 5.15 IGRTfx Study Schema**

### 5.3.2 **Results**

#### 5.3.2.1 ***Physical Assessment and Plethysmography***

Twenty-six 10-12 week old CBA mice underwent fractionated radiotherapy to the right lung with (n = 13) or without (n = 13) BKM. Three mice experienced weight loss requiring euthanasia at 12 (n = 2), and 14 (n = 1) weeks following irradiation in the RT only (n = 2) and RT + BKM (n = 1) cohorts respectively (Figure 5.16).

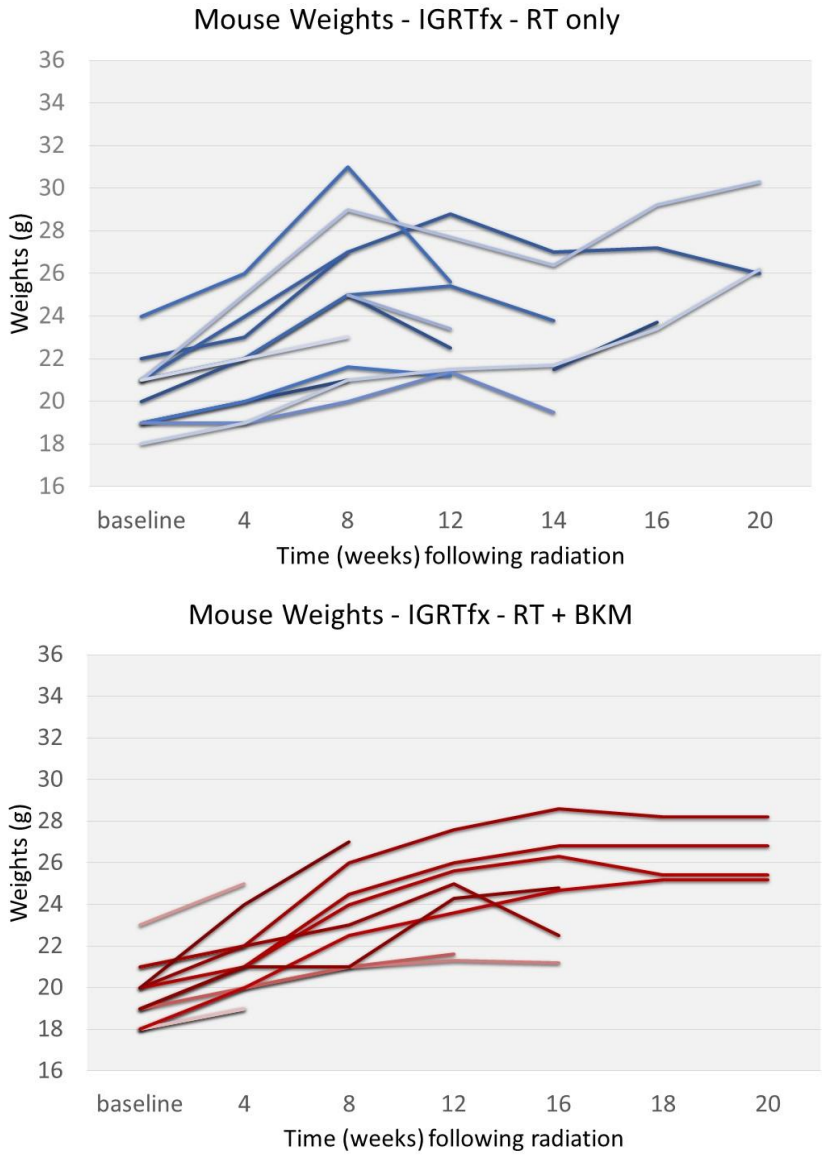



**Figure 5.16 Animal Weights for IGRTfx**: Plots of weights of animals on study from baseline to a maximum of 20 weeks following fractionated IGRT alone (top) or with BKM (bottom).

Figure 5.17 shows the breathing rates of the mice in study IGRTfx. Welch two sample t-tests determined no statistically significant difference in breathing rates over time between animals receiving RT only and those receiving RT + BKM (P = 0.8007). Breathing rate appeared to peak in both cohorts at week 12 followed by a decline at week 14. The mouse in the RT only group which demonstrated the lowest breathing rate at week 14 (Figure 5.17) was the animal which experienced a 20% weight loss that required euthanasia.

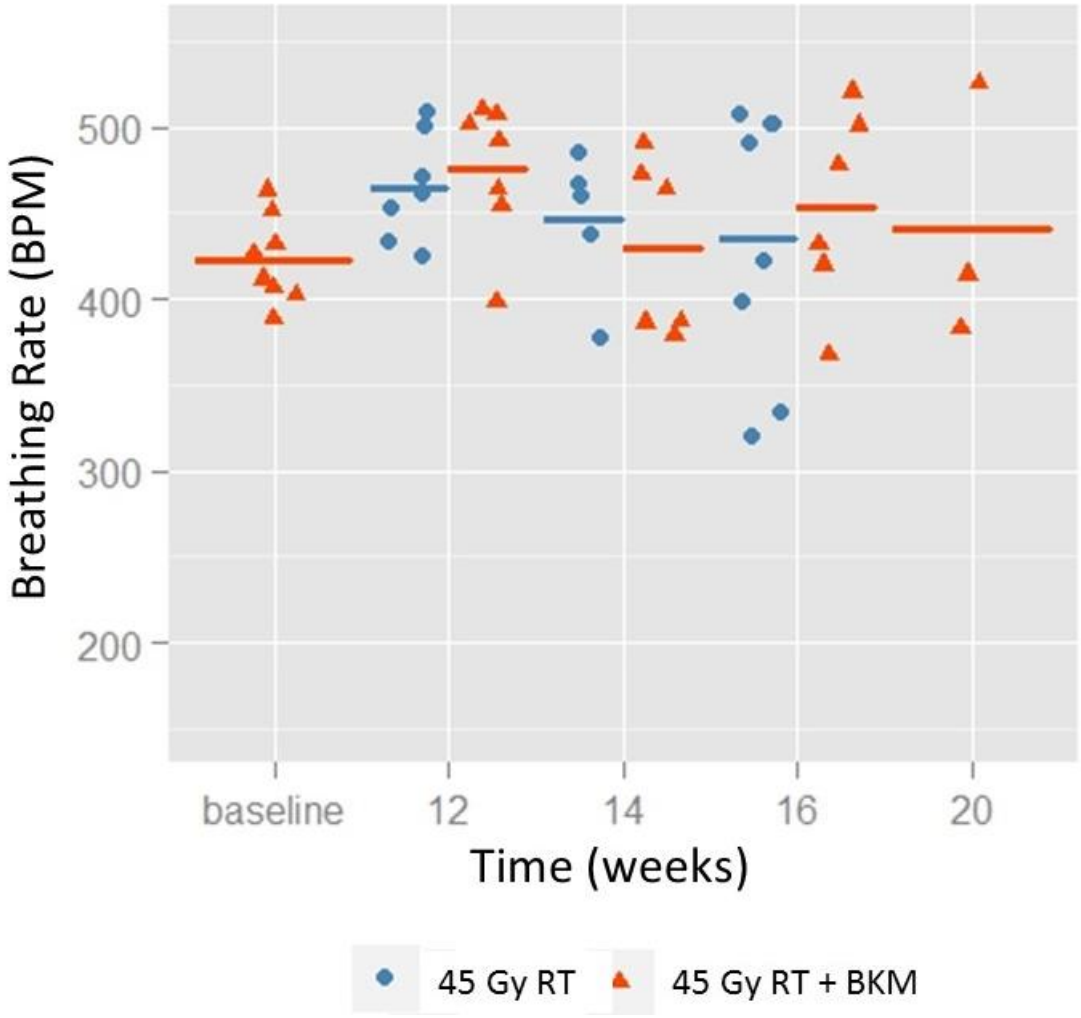



**Figure 5.17 Breathing Rates for Study IGRTfx:** Scatter plot of individual and population mean respiratory rates of mice receiving 3 x 15 Gy to the right lung (blue) or 3 x 15 Gy to the right lung plus BKM.

An increase in breathing rate of ≥ 15% was observed on at least one time point following radiotherapy in > 25% of animals across both treatment groups. The increase in

plethysmographic changes in this experiment appears to be correlated with the increased frequency and severity of radiation pneumonitis observed

#### 5.3.2.2 ***MRI***

Twenty-seven SEMS and DCE MRI data sets were suitable for evaluation, and toxicity scores showed full correlation between the two methods. The earliest time point at which ≥ Grade 3 toxicity was observed was 12 weeks following irradiation. Toxicity ≥ Grade 3 was detected on MRI in 82% and 58% of the RT only and RT + BKM cohorts respectively. However it should be noted that due an error, no mice from the RT + BKM cohort were imaged at 16 weeks. With this time point removed, the RT only cohort showed ≥ Grade 3 toxicity in 64% of the animals evaluated.

Using the data with matched time points only, a student paired t-test indicates there is no significant difference in the frequency of radiation reaction in animals in both cohorts (P = 0.9376). An F-test comparing variances (P = 0.5073) suggested there was no significant differences between the two arms of the experiment, even though variability within individual mice toxicity scores did exist.

##### *5.3.2.2.1.1 Exploratory DCE-MRI Analysis*

Figure 5.18 shows the population mean right (irradiated) and left (unirradiated) lung signal intensity vs time curves for mice with RILT scores of zero and 5. Significantly higher peak signal intensity was observed in the irradiated lungs with Grade 5 toxicity. This suggests an increased contrast uptake which is likely to be related to an inflammatory response (pneumonitis/alveolitis). In addition, the washout in the Grade 0 lungs is much more marked and represented by a decrease in slope on the plot following the peak SI.

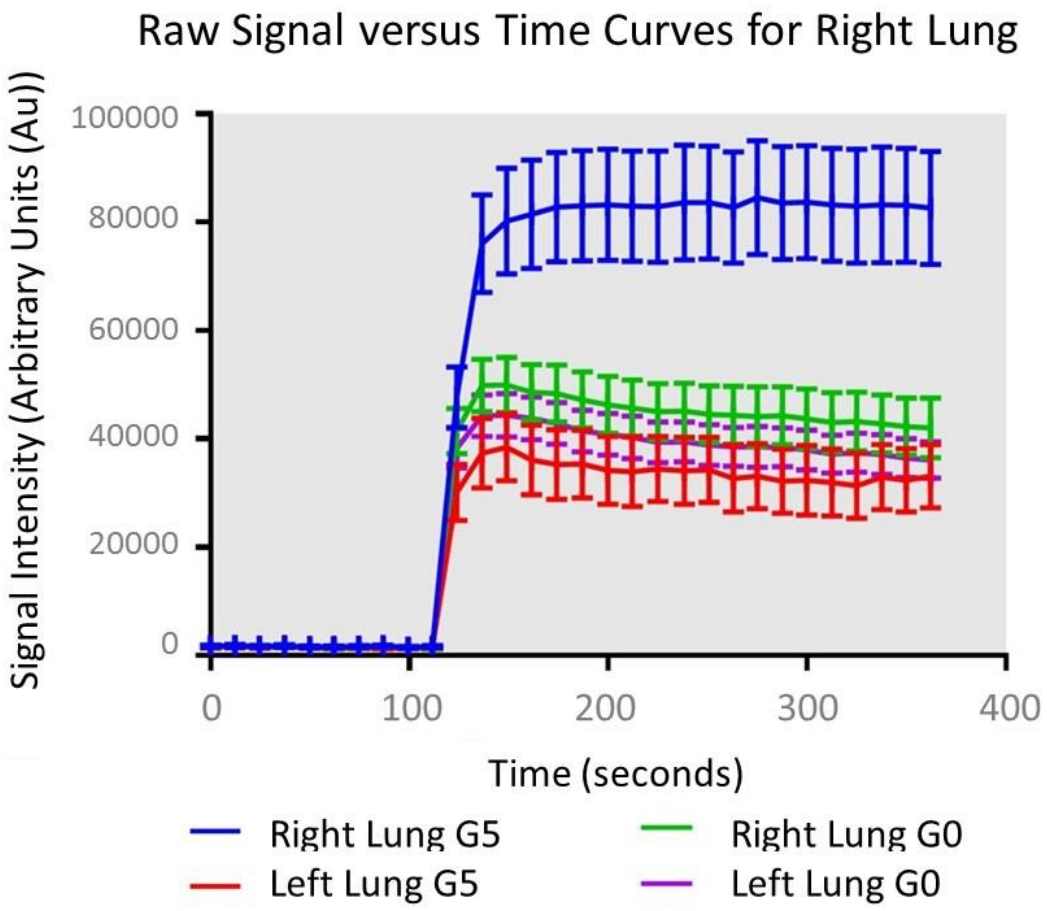



**Figure 5.18 IGRTfx Raw Signal versus Time:** Population mean and SEM signal intensity versus time plots of the right and left lungs of animals following 45 Gy +/- BKM with RILT scores of 5 and 0 in the irradiated (right) lung.

Multiple t-tests confirmed there was no significant difference between the left lungs in the animals with right lung toxicity scores of 5 and 0, or between the right and left lungs of the animals with no RILT (P = 0.3868 and 0.4720). There were however significant inter-animal differences in the mice with Grade 5 toxicity (P = 0.0001, $R^2$ = 0.2285), and differences when the right lungs were compared from the two groups (P = 0.0041, $R^2$ = 0.1332). The results were similar, but less significant for animals with toxicity scores of 3 and 4. There were not enough instances of Grade 1 and 2 toxicity to report any statistical details.

There is a clear difference in the SI between lungs with obvious radiation changes and those with no changes, however the goal would be to identify radiation pneumonitis early in its development. Early radiation pneumonitis is likely represented by the animals with Grade 1, 2, and 3 RILT scores. A limited number of animals demonstrated Grade 3 (n = 6) and 2 (n = 1) toxicities. The raw signal intensity curves for these seven mice are plotted in Figure 5.19. The single animal with Grade 2 RILT showed a peak SI of 55000 AU, which was similar to the five animals reported with Grade 2 RILT in the previous chapter. The population mean peak SI from experiment IGRT was 49585 AU and four of five animals had a peak SI $\geq$ 50000. The peak SI of the grade 2 animal is lower than the peak SI of the grade 3 animals, and higher than that of most of the Grade 0 rated lungs.

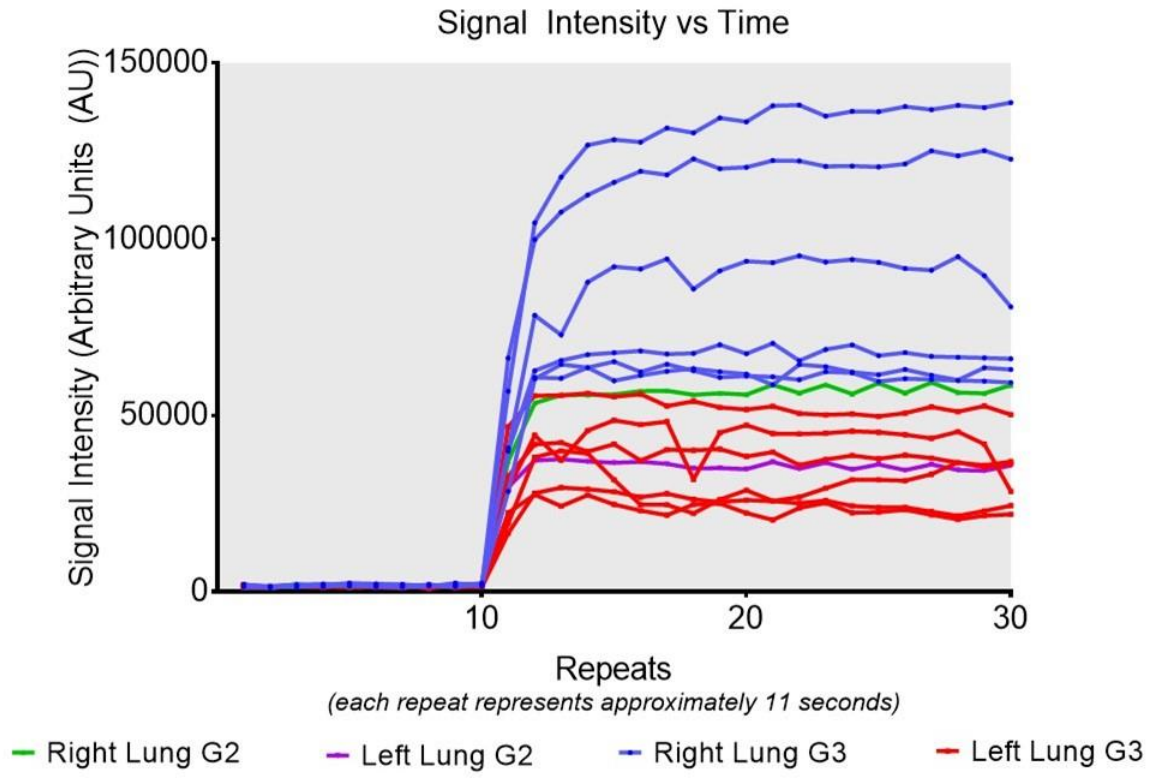



**Figure 5.19 Mild to Moderate RILT Signal versus Time Curves:** Individual raw signal versus time (represented as repeat image acquisitions) plots of the right and left lungs of animals following 45 Gy +/- BKM with RILT scores of 2 and 3 in the irradiated (right) lung.

In animals with no radiation change, a mean reduction of 15% signal intensity was observed three minutes following peak SI. This trend was not observed in animals demonstrating Grade 4 or 5 RILT. Further validation is required, but it could be hypothesized that animals showing SI peaks of 45000 – 55000 AU with sustained SI (i.e. ≤ 15% decrease over three minutes following peak intensity) in an irradiated lung may be identified as at risk for radiation pneumonitis and observed with greater frequency.

#### 5.3.2.3 *CT*

Twenty-five CTs were available and suitable for scoring following baseline and irradiation. The earliest RILT was observed at 8 weeks following irradiation in three mice, all with a RILT score of one. There was a marked increase in RILT observed on CT at week 12, with three of the four animals on the RT only arm demonstrating Grade 4 toxicity (with the 4$^{th}$ animal scored as Grade 3). Figure 5.20 plots CT densities of the right lung of animals treated with IGRT or IGRT + BKM against assigned RILT values for each mouse imaged at each time point with the population mean shown as a solid line. Regression analysis confirmed there was no statistically significant difference between the animals receiving IGRT with or without BKM ($P = 2.937e^{-08}$). However there was a definite trend towards increased HU in animals with higher RILT scores.

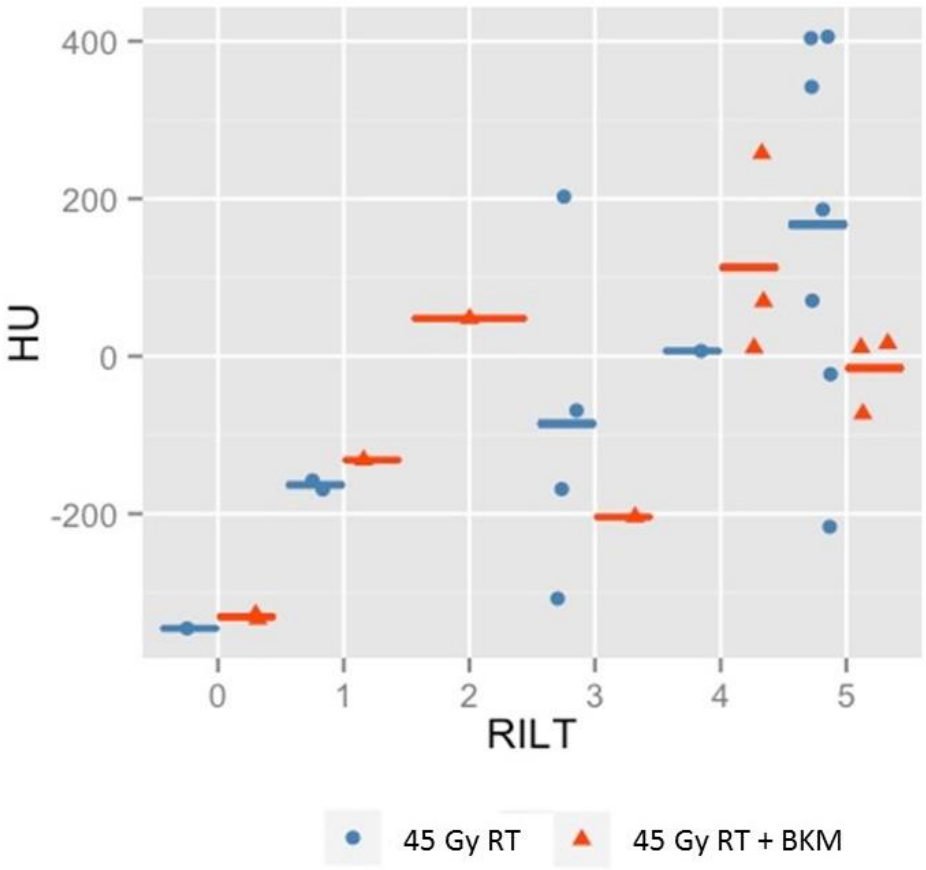



**Figure 5.20 CT Density (HU) versus RILT for IGRTfx +/- BKM:** Individual and population mean lung densities (HU) for the right (irradiated) lungs plotted against RILT.

#### 5.3.2.4 *CT-MRI Comparison*

Twenty MRIs had matched CT images that were also suitable for analysis (i.e., the same mouse underwent successful CT and MRI on the same day). RILT scores of 0 to 5 were assigned to the MRI and CT images independently and compared. Thirty-five percent of the paired images were in 100% agreement, 40% had scores that varied by ± 1 grade, and 10 % had greater variation between MRI and CT scores assigned. In 10 of 13 cases where the CT score varied from the MRI score, the CT score was higher. Due to the image quality of the CT compared to the SEMS and ANGIO MRIs, and the use of the simplified scoring system, it is more likely that CT overestimated the severity of lung toxicity and not that the MRI underestimated the toxicity.

Despite the variation in absolute scores on CT and MRI, an unpaired t-test of all animals scored showed no significant differences between the toxicities recorded using either modality ($P = 0.2503$, $R^2 = 0.0346$), and an F-test to compare the variances also showed no significant difference ($P = 0.9247$). Figure 5.21 is a case study of a single mouse at weeks 8, 12 and 16 respectively.

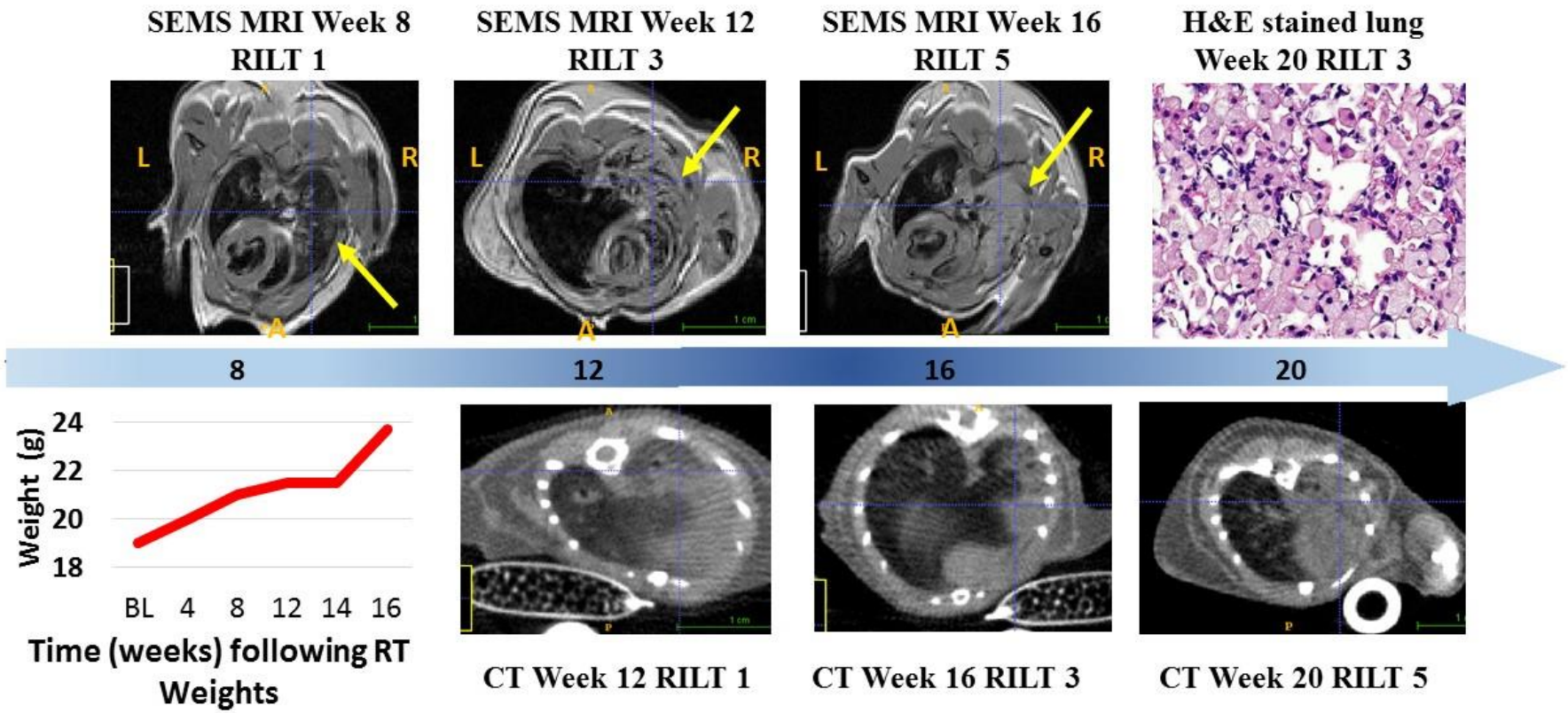



**Figure 5.21 IGRTfx** Case Study: Single mouse that underwent serial imaging following 3 x 15 Gy IGRT to the right lung. CT images at 8 and 12 weeks following radiation demonstrated grade 1 and 5 RILT respectively. SEMS MRI at weeks 8, 12, and 16 were scored as grade 1, 3, and 5 respectively. H&E stained lung sections taken at 20 weeks following IGRT show grade 3 pneumonitis. This animal's weight did not prove to be an indicator of poor lung health as seen in the plot on the timeline.

### 5.3.2.5 *Pathology*

As in experiment IGRT, if mice did not show indications of lung toxicity on imaging or plethysmography, the first euthanasia for organ retrieval occurred at 12 weeks following irradiation. At 12 weeks post radiation, all mice sampled in the radiation plus drug arm (n = 3) showed poor lung inflation, but no inflammatory response (i.e., alveolitis), and all mice in the RT alone arm (n = 3) showed pneumonitis and perivascular inflammation in one or both lungs. Figure 5.22 plots the incidence and severity of alveolitis in the irradiated lungs of all mice sampled and Figure 5.23 shows images of representative samples from animals.

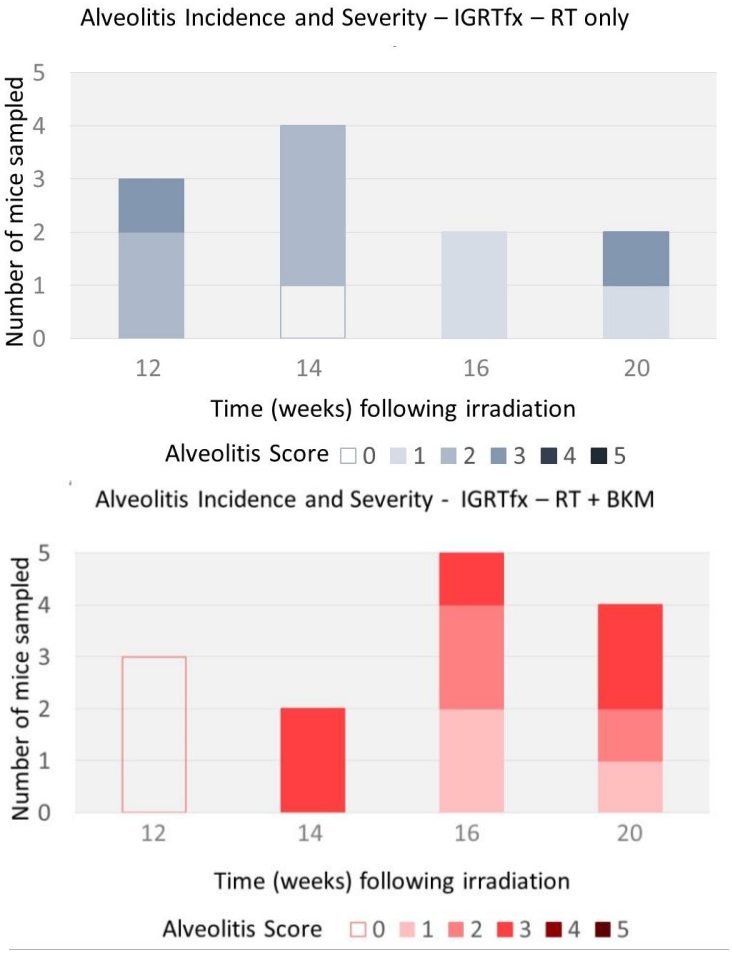
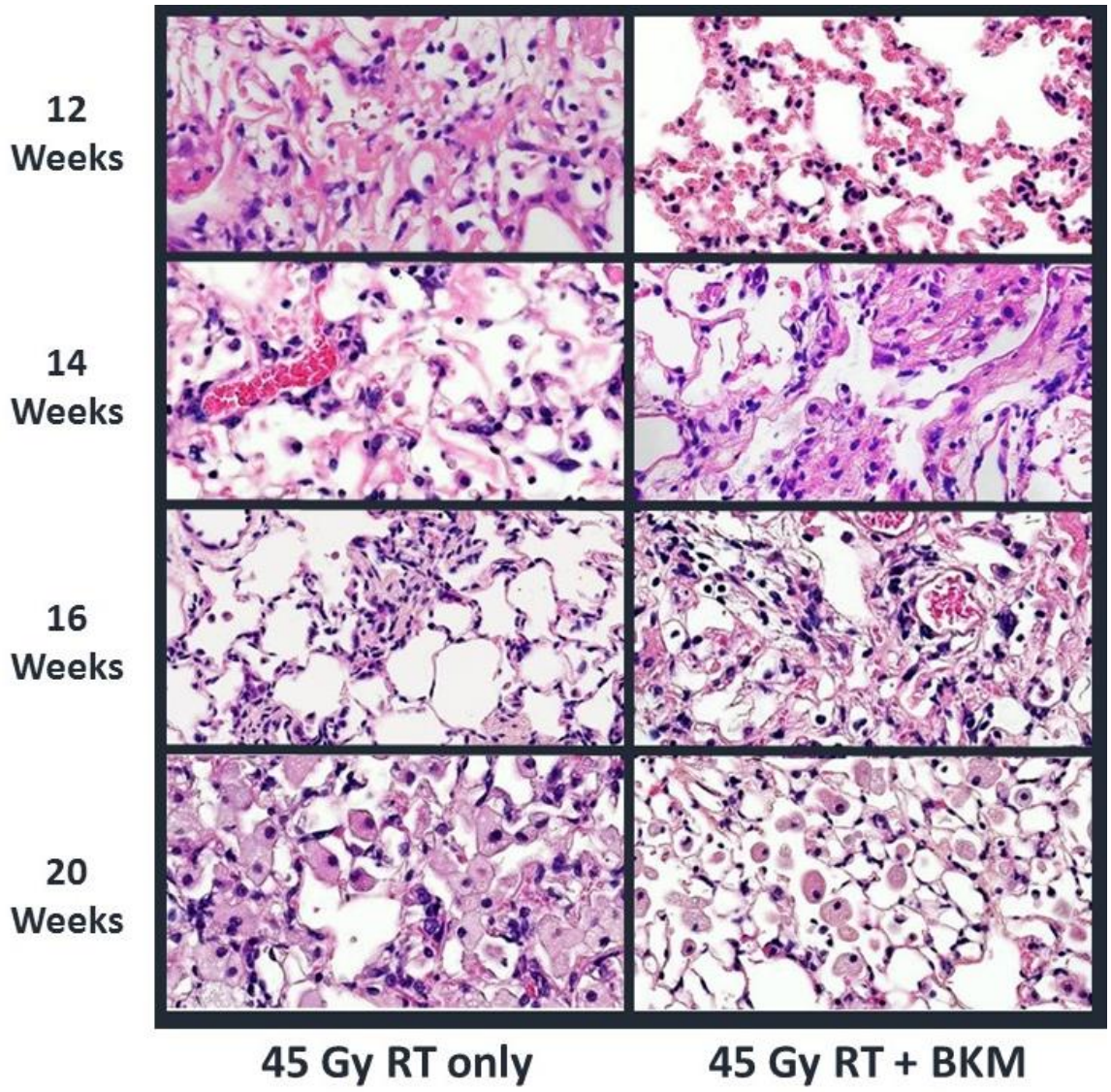


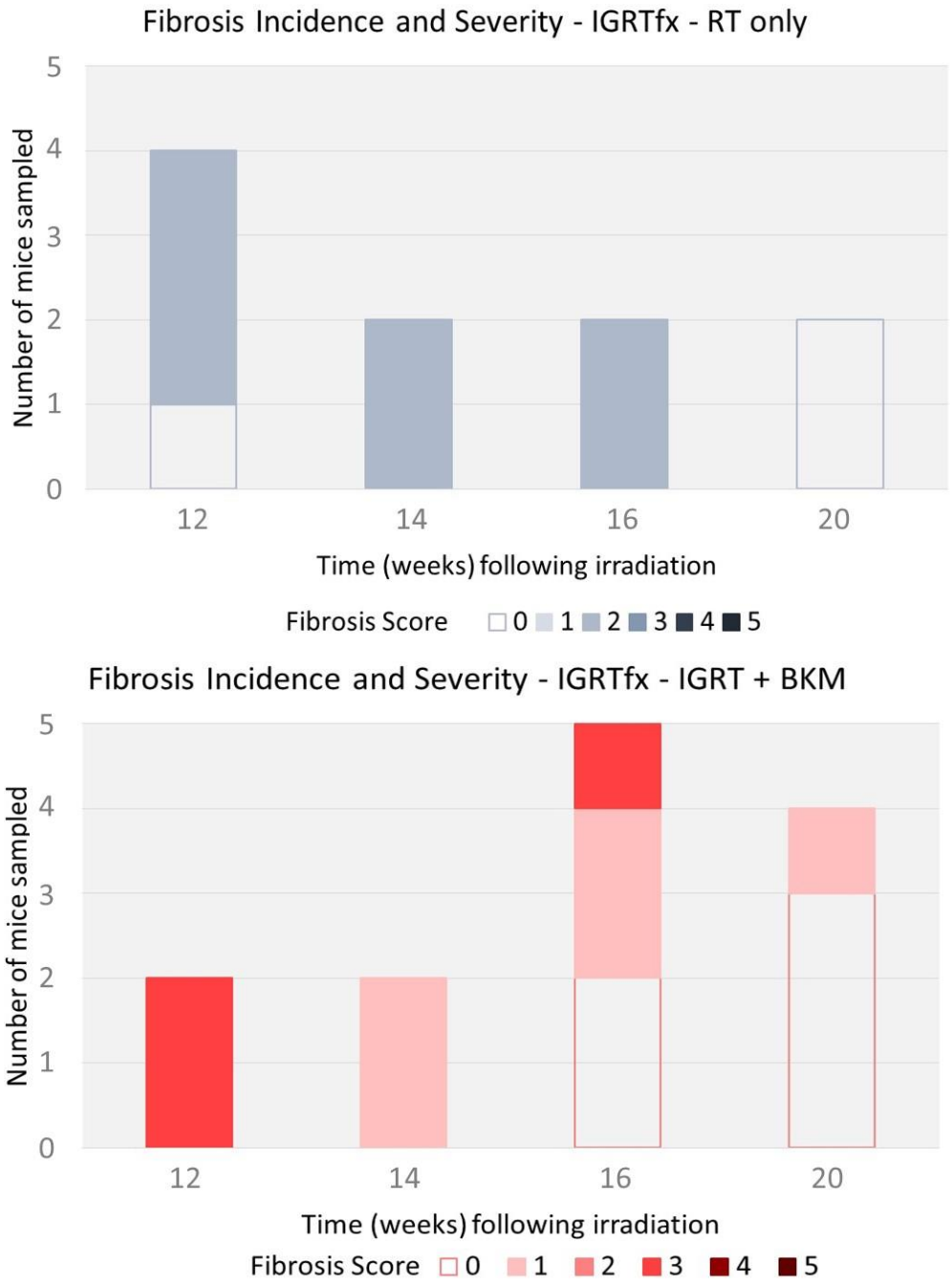

**Figure 5.22 Alveolitis for Study IGRTfx**: Bar plots of the incidence and severity scoring for alveolar inflammation in study IGRTfx for animals undergoing fractionated IGRT alone (top) or with BKM (bottom).

**Figure 5.23 IGRTfx Histopathology**: Histopathological sections representative of alveolar inflammation in H&E stained lung sections (red arrows) at 12, 14, 16, or 20 weeks following IGRTfx +/- BKM




The results presented in this chapter are concerned primarily with the pathological findings on the right (irradiated lungs). However is should be noted that in 16% of all samples reported, pathological findings were observed in the unirradiated left lung (compared to 39% in the irradiated right lung). This study also had the greatest incidence of fibrosis scored on Masson's trichrome stained histopathology in the irradiated lungs.

**Figure 5.24 Fibrosis for Study IGRTfx:** Incidence and severity of radiation induced fibrosis as determined on histopathology for animals sampled following fractionated IGRT alone (top) or with BKM (bottom) in the irradiated lungs.



## 5.4 Intermodality Comparison of Single versus Fractionated Experiments

### 5.4.1 Rationale

The experiments in this chapter had more complete data sets than the earlier experiments, and it was therefore possible to perform an exploratory analysis of the correlation between the methods used to detect radiation reactions. Confirmation that MRI can detect radiation pneumonitis at or before accepted pre-clinical (pathology) and clinical (CT) methods was a primary goal of this thesis.

### 5.4.2 Results

The most extensive example of RILT occurred at week 16 in a mouse in the IGRT plus BKM cohort. This mouse showed progressive weight loss, an increase in breathing rate to a maximum of 20% over baseline, followed by a rapid decline to less than 75% of its baseline breathing rate, and clear radiographic changes on CT and MRI. The time from peak respiratory rate increase (500 BPM) to maximum weight loss and severe respiratory decline was 10 days. Figure 5.25 shows CT, MRI and gross pathology images for this mouse at 16 weeks, immediately prior to (CT and MRI) or following (pathology) euthanasia.

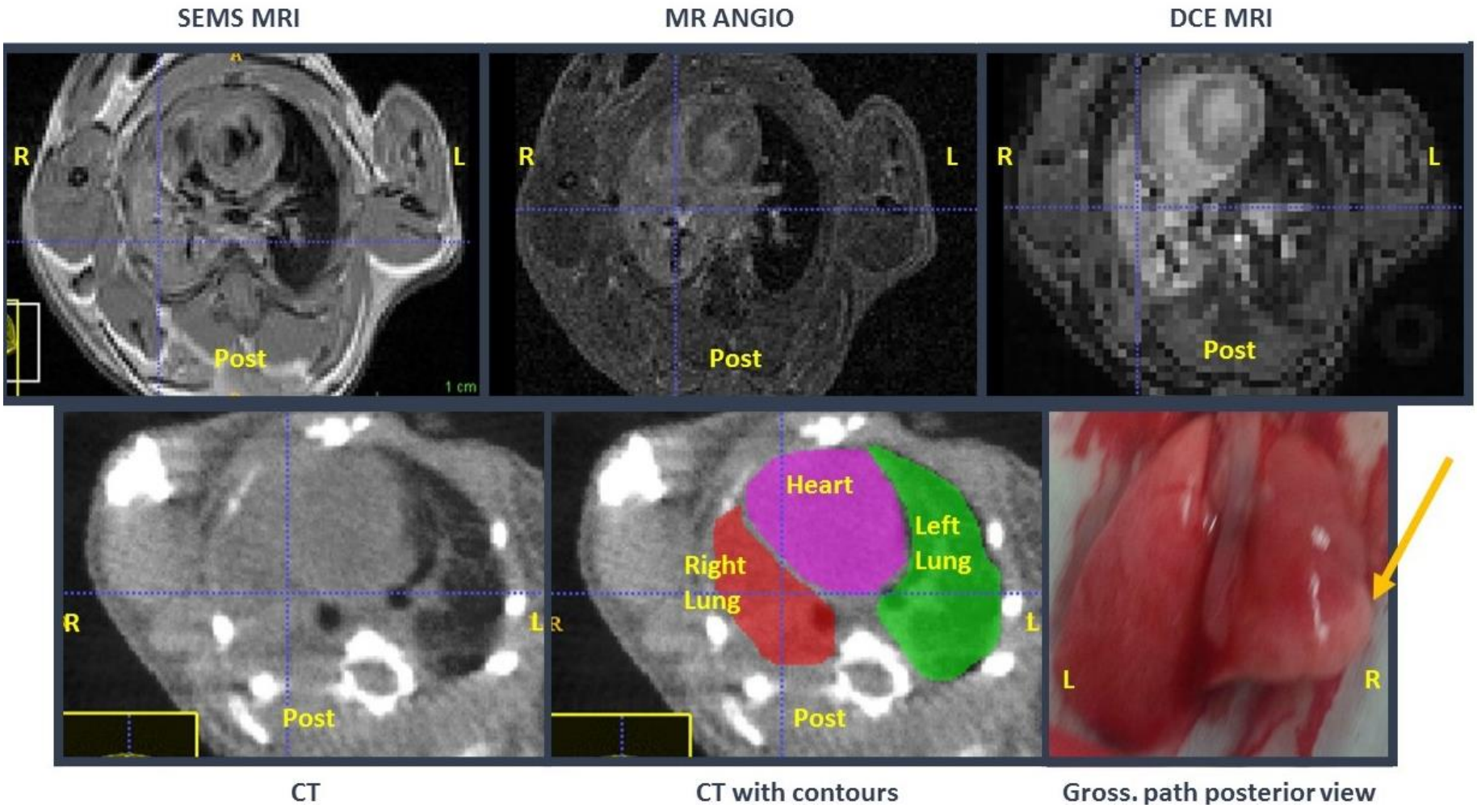



**Figure 5.25 Multi-modality RILT:** Comparison of RILT findings for a single mouse at 16 weeks following radiation on MRI, CT and gross pathological findings. The yellow arrow indicates changes in right lung texture and colour observed on extraction.

The majority of the animals imaged on the IGRT experiment underwent both CT and MRI at weeks 8, 14, 18 and 20 weeks. CT was unavailable at week 12. All 6 animals imaged at 8 weeks showed no radiation changes on either CT or MRI. Student paired t-tests confirmed there were no statistically significant differences in RILT scores assigned on CT and MRI with P-values of 0.1890, 0.0622, and 0.1778 at weeks 14, 18 and 20 respectively.

The incidence of RILT observed on CT and pathology was compared between all animals treated with RT + BKM or ≥ 20 Gy RT alone. Statistical analysis was limited by the limited numbers and lack of completeness of paired events at each time point. Therefore a simple comparison of the proportion of animals exhibiting RILT ≥ 1 over all times points was performed and is summarized in Table 5.2. Using RT only data from experiments NFV2, IGRT and IGRTfx and RT + BKM data from experiments NFV2, IGRT and IGRTfx, it is likely the radiation dose (i.e., 45 Gy) and method used to deliver it (i.e., IGRT) have a greater impact on the development of RILT in normal lung tissue than the administration of the PI3K inhibitor BKM.

**Table 5.2 Inter-study RT versus RT + BKM Comparisons:** Proportion of all animals exhibiting RILT over all time points for animals undergoing RT or RT + BKM

| | Cabinet Irradiator | | SARRP | | SARRP | |
|---|---|---|---|---|---|---|
| | 20 Gy | 20 Gy + BKM | 20 Gy | 20 Gy + BKM | 45 Gy | 45 Gy + BKM |
| CT | 1/7 (0.14) | 1/12 (0.08) | 11/20 (0.55) | 2/8 (0.25) | 13/15 (0.87) | 9/11 (0.82) |
| Pathology | 3/9 (0.33) | 4/10 (0.40) | 6/9 (0.67) | 6/9 (0.67) | 10/11 (0.91) | 11/14 (0.79) |

As a summary of the experiments undertaken in Chapter Five, Figure 5.25 plots the population mean RILT score of all animals sampled at each time point using CT, MRI, and

pathology for evaluation. Although in almost all instance the presence or absence of RILT is in agreement across the observational methods, the magnitude does show variability. The variability is likely due to the fact that not all animals underwent all three procedures at each time point.

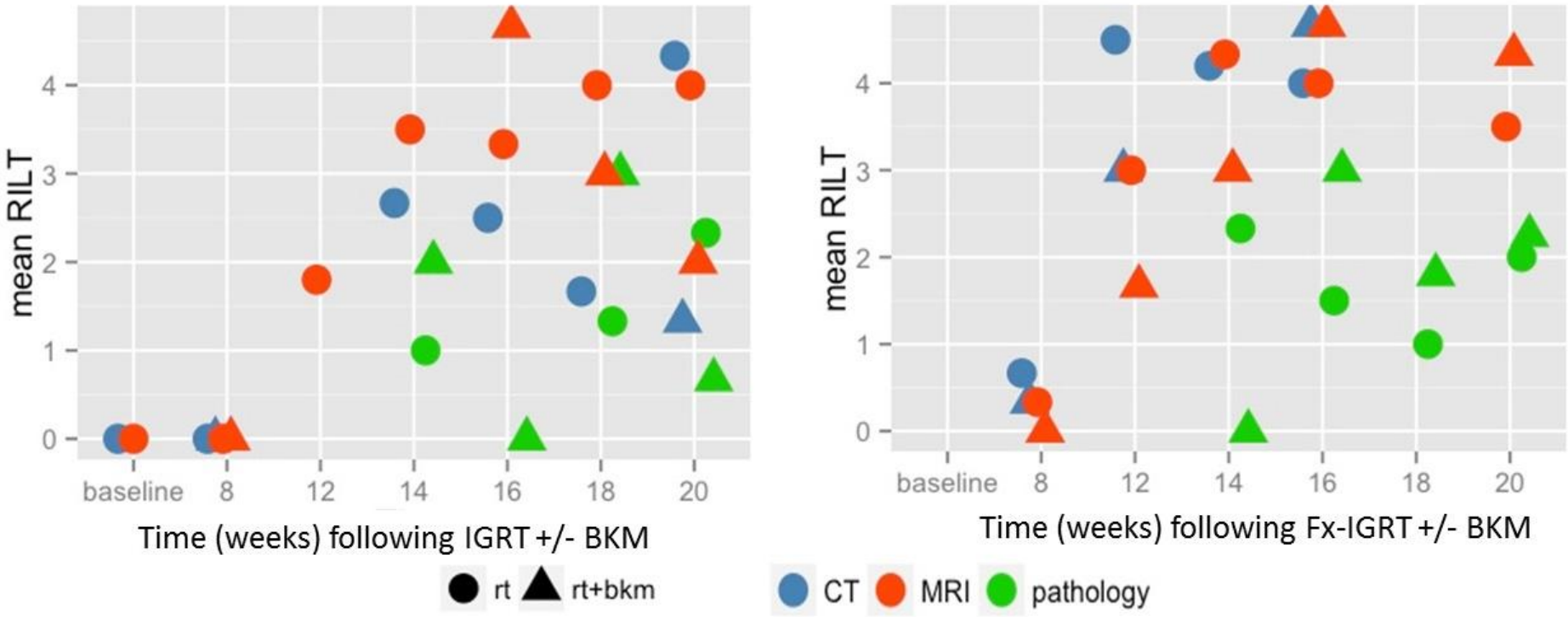



**Figure 5.26 Summary of RILT on CT, MRI and Histopathology**: Intermodality comparison of mean population RILT for studies IGRT (left) and IGRTfx (right) showing population mean RILT scores as assessed on each of CT, MRI and pathology at each time point.

### 5.4.3 **Discussion**

The pooled results shown in Figure 5.26, show a stronger correlation with between CT and MRI than either method with pathology when evaluating radiation changes in normal lung tissue. However, it must be noted that pathology analysis was based on a single lung section, whereas imaging was reported using the entire lung (or 'treated volume'), the use of multiple lung sections would be more representative of the pathology of each sampled lung.

A limitation of the RILT scoring and comparisons was that all RILT imaging scores were assigned by a single observer. To further validate this work, repeat observations should be undertaken by multiple observers. Repeat observations by the single observer were undertaken on CT and MRI data sets, to determine intra-observer variation of lung segmentation and was reported in section 2.7.

## 5.5 **Chapter Discussion**

The experiments reported in Chapters Three and Four informed the rationale, selection of treatment protocols and imaging techniques used in the studies reported in this Chapter. As a result of experimental refinements, the following achievements were made:

1. RILT was successfully induced in the majority of animals and at earlier time points than in previous chapters.
2. Imaging methods, in particular cardiorespiratory-gated MRI, proved to be a reliable, method of RILT detection and correlation was observed between imaging methods (as well as with pathology) in terms of RILT scores.
3. High throughput pre-clinical IGRT was successfully undertaken (52 mice received 102 fractions over the course of two weeks).

4. Missing events were significantly reduced, allowing for more robust statistical analysis.

Fifty-two mice underwent IGRT with both CBCT and portal imaging, delivered in 102 fractions over 3-weeks, using a mouse holder and custom collimator that were developed in-house and which were designed to irradiate one lung only. A review of the literature suggests this is the most extensive conformal RT project undertaken on an image guided micro irradiation platform to date (268, 272-277). The effect of these irradiations on development of RILT was evaluated using CT, MRI, plethysmography and pathology. In contrast to the results presented in Chapter Three and Four, evidence of RILT was clear using all evaluation metrics.

An increase in the breathing rate of 15% or more over baseline was seen from 8 weeks post irradiation in the IGRTfx group of animals, and from 14 weeks for all arms of both studies. Other researchers have reported an approximately 1.2-fold increase in breathing rate for irradiated animals over controls. However in most of these studies mice received whole thorax irradiation. Liao et al studied the effect of partial (40%) lung irradiation (14 Gy) in C3H mice and observed a 16% increase in the breathing rate at 20 weeks. When 70% of the lung was irradiated, the breathing rate increased by approximately 33% at the same time point (176).

Even without the fully quantified DCE-MRI sequence used in the previous chapter, a reliable DCE-MRI protocol was implemented that produced high quality images that could be correlated with RILT scores. The greatest difference in AUC and iAUC parameters between left (unirradiated) and right (irradiated) lungs was observed in mice with the highest RILT scores. SEMS image signal intensity was plotted against RILT scores, and increased signal in the irradiated lung was found to correlate with increasing RILT score at all time points evaluated. This suggests that mean (or regional) lung signal in a well gated SEMS

image can be used to detect RILT. However these results should be interpreted with caution given the lack of a pulse sequence dependent standardized intensity scale in MRI. This lack of standardized scaling affects the post processing of the acquired images as, in general, segmentation and registration methods depend on the observed image intensities.

One of the aims of this thesis was to evaluate the differences in RILT incidence and severity between animals receiving radiation alone or radiation plus PI3K/AKT/mTOR inhibitors. In this Chapter, because the data was almost complete and RILT induction was generally achieved successfully, it was possible to ascertain that there was no apparent increase in RILT incidence or severity in the mice receiving combined treatment in either the IGRT or IGRTfx studies. RILT did occur earlier, and with greater severity, in the IGRTfx study when compared to the single fraction IGRT study.

Although 45 Gy given in 3 fractions is a plausible clinical dose-fractionation, it would most likely be given as a SABR treatment (administered to a small portion of the lung), rather than to an entire lung. Now that the appropriate tools are available to better model small field, or SABR treatments in mice, and a mouse model of RILT has been established locally, it would be feasible to assess this dose-fractionation in a more realistic simulation of SABR with and without targeted agents. In fact a series of protocols have now been established that could be used as a platform for investigating PI3K/AKT/mTOR inhibitors or other targeted agents in combination with radiation.

The proportion of lung samples displaying a radiation response on pathology analysis (alveolitis or fibrosis) was lower than might have been expected based on the proportion of animals displaying radiation changes using CT or MRI. This may be accounted for in part by the fact that mice from a particular cohort were not necessarily imaged and euthanized for lung extraction at the same time point. Animals underwent MRI and CT imaging in a single anaesthetic session whenever possible. However, for logistical reasons,

plethysmography and lung extractions were usually undertaken the day before or after the imaging sessions and when performed prior to imaging prevented the euthanized animal from being imaged.

# Chapter 6

*Discussion, Conclusions, and Future Work*

# 6 DISCUSSION

Radiation-induced pneumonitis develops four to twelve weeks following radiotherapy for lung cancer with variable presentation, but generally consisting of mild to severe dyspnoea and non-productive cough or respiratory insufficiency (278). With a lethality rate as high as 10%, it is clear that strategies to improve the diagnosis, prevention and treatment of radiation pneumonitis in patients undergoing radiotherapy for lung cancers is required (279-281).

The work presented in this thesis demonstrates that radiation induced lung changes can be detected using cardio-respiratory MRI in a mouse model. Severe lung toxicity in the irradiated lung resulting in inflammation and/or consolidation, appears as a region of strong signal when compared to the surrounding tissue and unirradiated lung on SEMS imaging. In experiments where RILT was detected (NFV2, BEZ-BKM, IGRT and IGRTfx), the incidence of lung changes following radiation using SEMS MRI was not significantly different to that of CT when all matched time points were considered ($P = 0.882$, $r = 0.793$). Similarly the proportion of animals shown to have RILT on MRI was similar to the proportion of animals that experienced pneumonitis (defined primarily as alveolitis within this thesis but also including the accumulation of foamy macrophage aggregates or perivascular inflammation) on histopathology ($P = 0.787$, $r = 0.834$). In contrast, there was no correlation between the incidence of MRI changes following radiation compared to the incidence of fibrosis on histopathology (using Masson's trichrome staining) ($P = 0.049$). These results, which take into consideration the time-line over which the lung changes appeared (8 to 20 weeks following RT), provide strong evidence that the changes seen on MRI are associated with radiation pneumonitis.

To our knowledge this thesis represents the first report of a correlation between CT and MR imaging and pathology for the detection of radiation induced lung toxicity following irradiation in a mouse model. Glazer et al (282) used MRI to distinguish between recurrent tumour and fibrosis in patients following radiation using stable sequential CT findings (and not biopsy) for comparison. It was not possible to distinguish acute radiation pneumonitis, infection or hemorrhage from recurrent disease. Similarly Kono et al (283) used T2-weighted and Gd-DTPA MR images to distinguish between radiation pneumonitis and recurrent disease in patients who had received radiation or chemo-radiation. These authors suggested that MRI is superior to CT for distinguishing recurrent disease from pneumonitis, but, because this was a clinical study and invasive biopsies were avoided, there was no histopathological confirmation.

In a pre-clinical MRI study, Shioya et al tracked T1, T2, water content and histology of lung tissue for one year in Wistar rats following hemi-thoracic single fraction radiotherapy (20 Gy). It was found that T2 correlated with acute inflammatory changes in the lung (284). This work however was performed following euthanasia and there was no comparison to CT imaging. The results presented in Chapters Four and Five of this thesis show that there is an increase in signal intensity on SEMS imaging in irradiated lungs demonstrating RILT when compared to control unirradiated lungs and, when available, compared to preceding imaging time points including baseline. The increase in signal intensity is caused by the inflammatory response seen in radiation pneumonitis and was correlated to increased lung density (using HU) on CT imaging.

In this thesis, images were evaluated and severity scores of RILT events were assigned to CT and MRI independently. The benefit of using a simplified scale of 0-5 to determine the severity of an event, was that it facilitated comparisons within longitudinal studies with multiple animal cohorts between different imaging modalities and to other physiologic

endpoints (i.e., pathology). A limitation of the scoring system was that it only provided a crude evaluation of RILT progression by categorizing the event on a scale of none, mild, moderate or severe. In future experiments, using deformable image registration and frequent imaging, a more accurate analysis could be undertaken, for example to evaluate geometrically accurate regional details about RILT. Such an approach was described by Cavanaugh et al who used CT imaging and pathology in mice to quantify the lung toxicity caused by BLM (255, 285).

Only a limited number of accounts of the use of functional MRI (fMRI) to detect RILT clinically or pre-clinically have been published. Ireland et al and Thind et al have used $^{3}$He and hyper-polarised $^{13}$C-pyruvate MR-spectroscopy to detect early radiation toxicity in patients and rats respectively (151, 152, 286). In 2010, Ireland et al compared the pre- and post- radiotherapy MR images of five patients with NSCLC to CT scans. It was found that ventilation changes on MRI correlated with evidence of RILT on CT in three patients. In 2012 Thind et al used hyper-polarised $^{13}$C-pyruvate MR-spectroscopy to detect radiation pneumonitis following 14 Gy whole thorax irradiation in rats. This group then went on to demonstrate it was possible to map metabolic changes associated with radiation pneumonitis as early as five days following 18.5 Gy whole thorax irradiation in Sprague Dawley rats using MR-spectroscopy. These findings were confirmed by comparison with CT imaging, blood lactate concentration and arterial oxygen concentration.

These functional MR techniques require specialized equipment and expertise which may make them challenging to adopt widely. In contrast, DCE-MRI, is a well-established imaging modality that is used for a number of diagnostic indications in the lung. Since it is already widely available, and has been used extensively to detect and monitor other inflammatory lung diseases, it is an appealing option for the detection of radiation-induced lung toxicity. This work is the first report of its implementation for this indication.

The development of DCE-MRI with and without the availability of fully quantified T1 maps was successfully undertaken for the detection of radiation pneumonitis in this thesis. In animal studies investigating asthma, it has been suggested that the administration of gadolinium leads to increased parenchymal signal when compared to healthy lungs (247). In the work presented in this thesis, animals with moderate to severe toxicity (Grade 4 or 5) showed an obvious increase in peak signal intensity (or contrast uptake) and delayed wash-out in the irradiated lungs when compared to the unirradiated lungs, and baseline images. Animals with no reported RILT (based on CT or SEMS MRI) demonstrated signal intensity curves and AUCs similar to those of the unirradiated lungs. Although the sample size was small, animals exhibiting mild RILT (Grade 1, 2, 3), showed an intermediate response on DCE-MRI.

The DCE-MRI results presented in Chapter Five, suggest that there may be a threshold change in SI of the irradiated lungs that is indicative of early RILT, which is only detectable using signal intensity curves generated from MRI raw data, and that is not observable by simple visual inspection. This is similar to the threshold of early non-visible lung changes using CT density was proposed by van Dyk and Mah (118, 119). These investigators suggested that any changes in HU greater than 5-10% over baseline values following radiation was predictive of radiation pneumonitis. De Ruysscher et al (146) proposed that instead of a simple percentage change in HU, any change greater than 0.5 HU/Gy of absorbed radiation dose was predictive of RILT. In the experiments reported here, the number of animals with mild to moderate RILT was small and so it is not possible to state categorically that a statistically significant threshold exists. However, the SI curves plotted in Chapter Five are suggestive of a threshold change that is predictive of radiation pneumonitis. Future studies, with more frequent imaging, would help confirm or refute the utility of DCE-MRI for the early detection of radiation pneumonitis.

In addition to the development of new MRI sequences for the early detection of RILT, studies to test the effect of the targeted agents on normal tissue, were undertaken. It was found that treatment with BEZ and BKM lead to a decrease in pAKT in normal lung tissues when compared to a control treatment (vehicle). This finding suggests that normal tissues are less dependent on the PI3K pathway for DNA damage repair following RT compared to malignant tissue. Further investigations, including the analysis of the effect of different pAKT inhibitors, are needed to address this hypothesis.

From Chapter Four, RILT occurred more frequently in animals in the RT + BEZ arm than in the RT + BKM arm on imaging and pathology. However the difference was not statistically significantly, and because the overall frequency of RILT was low, this result should be interpreted with caution. The incidence and severity of RILT in animals undergoing 20 Gy radiation alone as reported in Chapter Three (experiment NFV2), showed no statistically significant difference when compared to the incidence and severity of RILT reported experiment BKM-BEZ. Regression analysis of the HU values for animals treated with 20 Gy alone from Chapter Three were compared to animals treated with 20 Gy + BKM and 20 Gy + BEZ from Chapter Four. There were no statistically significant differences in the lungs treated with RT plus BEZ or BKM versus RT only ($P = 0.2684$ and $0.6557$, respectively). This indicates that in the experiments reported in this thesis, AKT inhibition did not enhance the detrimental effect of radiation on normal lung tissue. The overall incidence and severity of RILT was greater in the experiments using the SARRP irradiator than those using the Cabinet Irradiator. The results from Chapter Five suggest however, that the overall radiation dose had a greater effect on RILT induction than the addition of BKM.

This thesis is the first report of the effects of BKM and BEZ plus radiation on normal lung tissue in vivo. Others have reported the pre-clinical synergistic effects of these AKT inhibitors with radiation, in lung tumours (214, 222, 224, 226, 228-230). Although pAKT

expression is affected in normal tissues following PI3-Kinase inhibitors, this change is not associated with radiosensitization of lung tissue. These observations support the conduct of clinical trials that test the ability of these drugs to enhance the anti-tumour effect of co-administered radiation.

In order to achieve the aims of this thesis, several methodological outcomes were required, specifically the development of new imaging methods for the detection of RILT, and a high throughput, multi-modality imaging programme for longitudinal investigation of normal tissue toxicity in a pre-clinical model.

MRI of the lung has traditionally been limited due the challenges of low signal to noise ratios and respiratory motion. MRI signal is directly proportional to available tissue proton density, but the lung has proton density approximately ten times less than the surrounding tissue. Consequently the signal generated in lung MRI is approximately 10 times less that of other tissues (155). Recently, however, advances in MRI pulse sequences, radiofrequency (RF) coils and the integration of cardio-respiratory gating into clinical and pre-clinical MRI systems, have led to the emergence of MRI as a useful tool for lung imaging.

In collaboration with Dr. Sean Smart and the Imaging Core at the CRUK/MRC Institute for Radiation Oncology, three MRI sequences were developed for imaging mouse lung. These were a) a SEMS sequence with CR-gating and bandwidth optimization to produce reliable anatomical images, b) a DCE-MRI sequence that could be acquired with and without full $T_1$ quantification and c) an ANGIO sequence that was initially developed as a $B_1$ calibration sequence for the DCE-MRI sequence and demonstrates exquisite anatomical and pathological detail. The development of these sequences was only possible because of the ability to develop specialised accessories (e.g., MRI sled with integrated heating coil) and modifications to existing equipment locally.

Future work is planned to further exploit DCE-MRI to a) determine how early in the evolution of radiation pneumonitis changes can be detected and b) if a model-based analysis is required for an informative analysis or if a non-model-based analysis will suffice. Deformable image registration will be required to further understand local-regional development of RILT when comparing multiple imaging modalities (CT, SEMS, and DCE-MRI) and histopathology sections that are related geometrically to the images.

Future work will include histopathology from multiple lung sections to provide a 3-D description of radiation pneumonitis that better matches the 3-D information of the imaging studies. A limitation of using single lung sections is that RILT is heterogeneous both within and between subjects, therefore, a single section may not be an accurate representation of the incidence or severity of radiation pneumonitis within an individual or cohort of subjects. In the clinical situation, several studies and systematic reviews have been undertaken to predict the risk of radiation pneumonitis. Many have been summarized in a review by Zhang (287), who described several risk factors for radiation pneumonitis including comorbidities, the combination of RT with other therapies (surgery or chemotherapy), tumour location, smoking status, dose-volume parameters, and the pre/post radiation TGF-β1 ratio. However, even when accounting for all of the aforementioned factors, variability in radiation toxicity continues to be observed. Kelsey et al (288) contend that although it is clear that inherited mutations in certain genes lead to radiosensitivity (e.g., ataxia telangiectasia), even for the majority of otherwise healthy subject, genetic factors may play a significant role in radiation response (289, 290). They suggest that in addition to the general assumption that DNA sequence alterations, changes in gene function may also play an important role in underlying susceptibility to radiation-induced normal tissue toxicities. It has generally been accepted in animal studies, that dosimetric factors and the location of the irradiated lung volumes are most likely to affect the development of radiation pneumonitis.

As early as 1965, Teates (291) described the differences in severity of reactions following irradiation to dog lungs. In part the differences described in these earliest studies can be explained by the use of simple radiation techniques resulting in higher doses delivered to the thinnest region of the lungs (apex) and lower doses to the thickest part of the lungs (base). Conversely, Travis et al (292) and Tucker et al (293) found that the base of the lung was more sensitive that apex. They proposed the heterogeneity in lung radiosensitivity is primarily due to the anatomy of the tracheobronchial tree, i.e., to the distribution of non-gas exchange-conducting airways in the irradiated volume. Therefore even in a uniformly irradiated single lung, a single section for histopathology may over- or under- represent the presence or absence of radiation pneumonitis, and this may limit correlative studies with 3-dimensional imaging.

A practical system for the high throughput evaluation of radiation-induced normal tissue toxicity (with or without targeted radiosensitizers) using longitudinal imaging studies in a pre-clinical model has been established. In the current study, this experimental setup was used to investigate PI3K/AKT/mTOR inhibitors plus radiation, but the same approach could be used to investigate other targeted agents in combination with radiation delivered using single- or multi-fractionated protocols. Key to the establishment of this platform was the development of robust cardiorespiratory-gated imaging methods for the detection of RILT that were compared to conventional assessment methods, namely histopathology, plethysmography and computed tomography imaging.

From the work in Chapter Five, 52 CBA mice underwent 102 IGRT fractions over the course of 19 days on the SARRP system using customized animals holders with integrated physiological monitoring systems. To our knowledge this is the largest single-centre experiment of its kind. The experiments in this thesis were designed such that animals were observed following intervention at pre-determined time points using plethysmography, CT,

MRI, and histopathology for up to 20 weeks. Longitudinal studies of this type reflect the protocols used to follow up lung cancer patients and so are a powerful tool for simulating the clinical scenario. The platform could be further refined so that individual animals undergo longitudinal imaging as opposed to representative members of an experimental cohort, as was the case in the experiments reported in this thesis.

The severity of radiation-induced lung damage is heterogeneous even within a single subject. The future development of sensitive imaging protocols capable of detecting the variation in RILT will be a major advance to understanding the pathophysiology of this condition. It is possible that mapping of regional differences in RILT could prove useful in the management of pneumonitis in patients. The determinants of radiation pneumonitis following small field, high-dose irradiation techniques such as SABR, which are increasingly used in practise, are poorly understood. The development of sensitive imaging techniques may prove useful in identifying the treatment and patient characteristics that predispose patients to RILT following fractionated radiotherapy regimens. Imaging studies of patients undergoing radiotherapy for lung cancer, in combination with the investigation of circulating markers such as IL-6, IL-1 or TGF-β1, which are thought to be predictive of RILT, may be of particular interest.

In clinical radiotherapy for patients with lung cancers, radiation-induced pneumonitis develops four to twelve weeks following radiation with variable presentation, but generally consisting of mild to severe dyspnoea and non-productive cough or respiratory insufficiencies (278). It often goes un-diagnosed and untreated because of its similarity to symptoms resulting from co-morbidities and disease progression. The implementation of observational clinical studies using MRI protocols (including DCE-MRI) could provide an ionizing-radiation-free imaging method to monitor and mitigate the development of radiation pneumonitis in patients identified as being at increased risk (e.g., smokers, patients

with co-morbidities, region of lung irradiated, or patients on dose-escalation protocols). Using longitudinal imaging studies it may be possible to identify a threshold of early radiation pneumonitis at which point the modification of radiotherapy plans or the introduction of steroid treatments could be introduced. A more thorough understanding of the development of RILT in patients undergoing radiotherapy for lung cancers may also be useful in the development of improved models predicting radiation pneumonitis and fibrosis, the clinical implementation of MRI protocols presented in this thesis could provide a non-invasive, radiation-free method by which to study the development of radiation pneumonitis.

The work presented in this thesis provides evidence of that the pure and combined PI3K inhibitors NFV, BKM and BEZ do not enhance radiosensitization in normal lung tissue in a mouse model, compared to radiation alone, and that it is feasible to detect RILT using MRI sequences (including DCE-MRI). Further pre-clinical and/or clinical observation studies are required to refine the identification of mild to moderate radiation pneumonitis following radiation. To achieve these aims, a high-through-put radiation and multi-modality longitudinal imaging study platform was developed with the cooperation of a highly skilled multi-disciplinary team.

# References

# 7 REFERENCES


1. UK CR. Lung cancer survival statistics: © Cancer Research UK 2014 Registered charity in England and Wales (1089464), Scotland (SC041666) and the Isle of Man (1103); 2013 [updated 4 July 2013; cited 2014 October 2014].
2. Bray FR, JS. Masuyer, E. Ferlay, J. Estimates of global cancer prevalance for 27 sites in the adult population in 2008. International journal of cancer Journal international du cancer. 2013;132(5):1133-45.
3. Ferlay JS, I. Ervik, M. Dikshit, R. Eser, S. Mather, C. Rebelo, M. Parking, DM. Froman, D. Bray, F. GLOBOCAN 2012 v1.9 Lyon, France: International Agencey for Research on Cancer; 2013 [13 01 2015]. Available from: http://globocan.iarc.fr.
4. Parkin DM, Bray F, Ferlay J, Pisani P. Global cancer statistics, 2002. CA: a cancer journal for clinicians. 2005;55(2):74-108.
5. Provencio M, Sanchez A, Garrido P, Valcarcel F. New molecular targeted therapies integrated with radiation therapy in lung cancer. Clinical lung cancer. 2010;11(2):91-7.
6. Cassidy A, Myles JP, van Tongeren M, Page RD, Liloglou T, Duffy SW, et al. The LLP risk model: an individual risk prediction model for lung cancer. British journal of cancer. 2008;98(2):270-6.
7. Raji OY, Duffy SW, Agbaje OF, Baker SG, Christiani DC, Cassidy A, et al. Predictive accuracy of the Liverpool Lung Project risk model for stratifying patients for computed tomography screening for lung cancer: a case-control and cohort validation study. Annals of internal medicine. 2012;157(4):242-50.
8. Kalemkerian GP, Akerley W, Downey RJ, Ettinger DS, Fossella F, Grecula JC, et al. Small cell lung cancer. Journal of the National Comprehensive Cancer Network : JNCCN. 2008;6(3):294-314.
9. Ettinger DS, Akerley W, Bepler G, Chang A, Cheney RT, Chirieac LR, et al. Non-small cell lung cancer. Journal of the National Comprehensive Cancer Network : JNCCN. 2008;6(3):228-69.
10. Hocking WG, Hu P, Oken MM, Winslow SD, Kvale PA, Prorok PC, et al. Lung cancer screening in the randomized Prostate, Lung, Colorectal, and Ovarian (PLCO) Cancer Screening Trial. Journal of the National Cancer Institute. 2010;102(10):722-31.
11. Kramer BS, Berg CD, Aberle DR, Prorok PC. Lung cancer screening with low-dose helical CT: results from the National Lung Screening Trial (NLST). Journal of medical screening. 2011;18(3):109-11.
12. National Lung Screening Trial Research T, Aberle DR, Berg CD, Black WC, Church TR, Fagerstrom RM, et al. The National Lung Screening Trial: overview and study design. Radiology. 2011;258(1):243-53.
13. Youlden DR, Cramb SM, Baade PD. The International Epidemiology of Lung Cancer: geographical distribution and secular trends. Journal of thoracic oncology : official publication of the International Association for the Study of Lung Cancer. 2008;3(8):819-31.
14. Health NCIatNIo. Small Cell Lung Cancer Treatment (PDQ).Cancer Topics.
15. [Committee of TNM classification of the UICC]. Acta Oncol (Madr). 1968;7(2):254-64.
16. [Classification of TNM of the International Union for Cancer Prevention]. Acta Oncol (Madr). 1970;9(1):56-84.

17. [TNM-classification of malignant tumors. General rules]. Archiv fur Geschwulstforschung. 1971;37(3):266-84.
18. [TNM-classification of malignant tumors of the breast, larynx, stomach, cervix and corpus uteri]. Archiv fur Geschwulstforschung. 1973;41(4):373-81.
19. TNM Classification of Malignant Tumours, 7th Edition. 7th ed: Wiley-Blackwell; 2009 2009.
20. Appere de Vecchi C, Brechot JM, Lebeau B. [The TNM classification. Critical review]. Revue des maladies respiratoires. 1998;15(3 Pt 2):323-32.
21. Bailey BJ. Beyond the 'new' TNM classification. Archives of otolaryngology--head & neck surgery. 1991;117(4):369-70; discussion 71.
22. Watanabe Y. TNM classification for lung cancer. Annals of thoracic and cardiovascular surgery : official journal of the Association of Thoracic and Cardiovascular Surgeons of Asia. 2003;9(6):343-50.
23. Higashino T, Ohno Y, Takenaka D, Watanabe H, Nogami M, Ohbayashi C, et al. Thin-section multiplanar reformats from multidetector-row CT data: utility for assessment of regional tumor extent in non-small cell lung cancer. European journal of radiology. 2005;56(1):48-55.
24. Lim E, Baldwin D, Beckles M, Duffy J, Entwisle J, Faivre-Finn C, et al. Guidelines on the radical management of patients with lung cancer. Thorax. 2010;65 Suppl 3:iii1-27.
25. Markos J, Mullan BP, Hillman DR, Musk AW, Antico VF, Lovegrove FT, et al. Preoperative assessment as a predictor of mortality and morbidity after lung resection. The American review of respiratory disease. 1989;139(4):902-10.
26. Kwa SL, Lebesque JV, Theuws JC, Marks LB, Munley MT, Bentel G, et al. Radiation pneumonitis as a function of mean lung dose: an analysis of pooled data of 540 patients. International journal of radiation oncology, biology, physics. 1998;42(1):1-9.
27. Graham MV, Purdy JA, Emami B, Harms W, Bosch W, Lockett MA, et al. Clinical dose-volume histogram analysis for pneumonitis after 3D treatment for non-small cell lung cancer (NSCLC). International journal of radiation oncology, biology, physics. 1999;45(2):323-9.
28. Roach M, 3rd, Gandara DR, Yuo HS, Swift PS, Kroll S, Shrieve DC, et al. Radiation pneumonitis following combined modality therapy for lung cancer: analysis of prognostic factors. Journal of clinical oncology : official journal of the American Society of Clinical Oncology. 1995;13(10):2606-12.
29. Gandara DR, Chansky K, Albain KS, Leigh BR, Gaspar LE, Lara PN, Jr., et al. Consolidation docetaxel after concurrent chemoradiotherapy in stage IIIB non-small-cell lung cancer: phase II Southwest Oncology Group Study S9504. Journal of clinical oncology : official journal of the American Society of Clinical Oncology. 2003;21(10):2004-10.
30. Abratt RP, Willcox PA, Smith JA. Lung cancer in patients with borderline lung functions--zonal lung perfusion scans at presentation and lung function after high dose irradiation. Radiotherapy and oncology : journal of the European Society for Therapeutic Radiology and Oncology. 1990;19(4):317-22.
31. Marks LB, Munley MT, Bentel GC, Zhou SM, Hollis D, Scarfone C, et al. Physical and biological predictors of changes in whole-lung function following thoracic irradiation. International journal of radiation oncology, biology, physics. 1997;39(3):563-70.
32. Marks LB, Munley MT, Spencer DP, Sherouse GW, Bentel GC, Hoppenworth J, et al. Quantification of radiation-induced regional lung injury with perfusion imaging. International journal of radiation oncology, biology, physics. 1997;38(2):399-409.
33. Tsujino K, Hirota S, Endo M, Obayashi K, Kotani Y, Satouchi M, et al. Predictive value of dose-volume histogram parameters for predicting radiation pneumonitis after

concurrent chemoradiation for lung cancer. International journal of radiation oncology, biology, physics. 2003;55(1):110-5.
34. Robnett TJ, Machtay M, Vines EF, McKenna MG, Algazy KM, McKenna WG. Factors predicting severe radiation pneumonitis in patients receiving definitive chemoradiation for lung cancer. International journal of radiation oncology, biology, physics. 2000;48(1):89-94.
35. Kocak Z, Borst GR, Zeng J, Zhou S, Hollis DR, Zhang J, et al. Prospective assessment of dosimetric/physiologic-based models for predicting radiation pneumonitis. International journal of radiation oncology, biology, physics. 2007;67(1):178-86.
36. Henderson M, McGarry R, Yiannoutsos C, Fakiris A, Hoopes D, Williams M, et al. Baseline pulmonary function as a predictor for survival and decline in pulmonary function over time in patients undergoing stereotactic body radiotherapy for the treatment of stage I non-small-cell lung cancer. International journal of radiation oncology, biology, physics. 2008;72(2):404-9.
37. Miller KL, Shafman TD, Marks LB. A practical approach to pulmonary risk assessment in the radiotherapy of lung cancer. Seminars in radiation oncology. 2004;14(4):298-307.
38. Wang D, Shi J, Liang S, Lu S, Qi X, Wang Q, et al. Dose-volume histogram parameters for predicting radiation pneumonitis using receiver operating characteristic curve. Clinical & translational oncology : official publication of the Federation of Spanish Oncology Societies and of the National Cancer Institute of Mexico. 2013;15(5):364-9.
39. Wang W, Xu Y, Schipper M, Matuszak MM, Ritter T, Cao Y, et al. Effect of normal lung definition on lung dosimetry and lung toxicity prediction in radiation therapy treatment planning. International journal of radiation oncology, biology, physics. 2013;86(5):956-63.
40. Giuliani ME, Lindsay PE, Kwan JY, Sun A, Bezjak A, Le LW, et al. Correlation of Dosimetric and Clinical Factors With the Development of Esophagitis and Radiation Pneumonitis in Patients With Limited-Stage Small-Cell Lung Carcinoma. Clinical lung cancer. 2014.
41. Stenmark MH, Cai XW, Shedden K, Hayman JA, Yuan S, Ritter T, et al. Combining physical and biologic parameters to predict radiation-induced lung toxicity in patients with non-small-cell lung cancer treated with definitive radiation therapy. International journal of radiation oncology, biology, physics. 2012;84(2):e217-22.
42. UK CR. Types of surgery for lung cancer: © Cancer Research UK 2014 Registered charity in England and Wales (1089464), Scotland (SC041666) and the Isle of Man (1103); [updated 28 March 2014October 2014]. Available from: http://www.cancerresearchuk.org/about-cancer/type/lung-cancer/treatment/surgery/types-of-surgery-for-lung-cancer.
43. Pignon JP, Tribodet H, Scagliotti GV, Douillard JY, Shepherd FA, Stephens RJ, et al. Lung adjuvant cisplatin evaluation: a pooled analysis by the LACE Collaborative Group. Journal of clinical oncology : official journal of the American Society of Clinical Oncology. 2008;26(21):3552-9.
44. Group N-SCLCC. Chemotherapy in non-small cell lung cancer: a meta-analysis using updated data on individual patients from 52 randomised clinical trials. Non-small Cell Lung Cancer Collaborative Group. Bmj. 1995;311(7010):899-909.
45. Sedrakyan A, Van Der Meulen J, O'Byrne K, Prendiville J, Hill J, Treasure T. Postoperative chemotherapy for non-small cell lung cancer: A systematic review and meta-analysis. The Journal of thoracic and cardiovascular surgery. 2004;128(3):414-9.
46. Hotta K, Matsuo K, Ueoka H, Kiura K, Tabata M, Tanimoto M. Role of adjuvant chemotherapy in patients with resected non-small-cell lung cancer: reappraisal with a meta-

analysis of randomized controlled trials. Journal of clinical oncology : official journal of the American Society of Clinical Oncology. 2004;22(19):3860-7.
47. Hamada C, Tanaka F, Ohta M, Fujimura S, Kodama K, Imaizumi M, et al. Meta-analysis of postoperative adjuvant chemotherapy with tegafur-uracil in non-small-cell lung cancer. Journal of clinical oncology : official journal of the American Society of Clinical Oncology. 2005;23(22):4999-5006.
48. Alam N, Darling G, Evans WK, Mackay JA, Shepherd FA, Lung Cancer Disease Site Group of Cancer Care Ontario's Program in Evidence-Based C. Adjuvant chemotherapy for completely resected non-small cell lung cancer: a systematic review. Critical reviews in oncology/hematology. 2006;58(2):146-55.
49. Buccheri G, Ferrigno D. Therapeutic options for regionally advanced non-small cell lung cancer. Lung cancer. 1996;14(2-3):281-300.
50. Machtay MB, K. Movsas, B. Paulus, R. Gore, EM. Komaki, R. Albain, K. Sause, WT. Curran, WJ. Higher biologically effective dose of radiotherapy is associated with improved outcomes for locally advanced non-small cell lung carcinoma treated with chemoradiation: and analysis of the Radiation Therapy Oncology Group. International journal of radiation biology and related studies in physics, chemistry, and medicine. 2012;82(1):425-34.
51. Marino P, Preatoni A, Cantoni A, Buccheri G. Single-agent chemotherapy versus combination chemotherapy in advanced non-small cell lung cancer: a quality and meta-analysis study. Lung cancer. 1995;13(1):1-12.
52. Curran WJ, Jr., Paulus R, Langer CJ, Komaki R, Lee JS, Hauser S, et al. Sequential vs. concurrent chemoradiation for stage III non-small cell lung cancer: randomized phase III trial RTOG 9410. Journal of the National Cancer Institute. 2011;103(19):1452-60.
53. Simon CJ, Dupuy DE, DiPetrillo TA, Safran HP, Grieco CA, Ng T, et al. Pulmonary radiofrequency ablation: long-term safety and efficacy in 153 patients. Radiology. 2007;243(1):268-75.
54. Fernando HC, De Hoyos A, Landreneau RJ, Gilbert S, Gooding WE, Buenaventura PO, et al. Radiofrequency ablation for the treatment of non-small cell lung cancer in marginal surgical candidates. The Journal of thoracic and cardiovascular surgery. 2005;129(3):639-44.
55. Pennathur A, Luketich JD, Abbas G, Chen M, Fernando HC, Gooding WE, et al. Radiofrequency ablation for the treatment of stage I non-small cell lung cancer in high-risk patients. The Journal of thoracic and cardiovascular surgery. 2007;134(4):857-64.
56. Hata M, Tokuuye K, Kagei K, Sugahara S, Nakayama H, Fukumitsu N, et al. Hypofractionated high-dose proton beam therapy for stage I non-small-cell lung cancer: preliminary results of a phase I/II clinical study. International journal of radiation oncology, biology, physics. 2007;68(3):786-93.
57. Abbas G, Schuchert MJ, Pennathur A, Gilbert S, Luketich JD. Ablative treatments for lung tumors: radiofrequency ablation, stereotactic radiosurgery, and microwave ablation. Thoracic surgery clinics. 2007;17(2):261-71.
58. Grieco CA, Simon CJ, Mayo-Smith WW, DiPetrillo TA, Ready NE, Dupuy DE. Percutaneous image-guided thermal ablation and radiation therapy: outcomes of combined treatment for 41 patients with inoperable stage I/II non-small-cell lung cancer. Journal of vascular and interventional radiology : JVIR. 2006;17(7):1117-24.
59. Le Pechoux C. Role of postoperative radiotherapy in resected non-small cell lung cancer: a reassessment based on new data. The oncologist. 2011;16(5):672-81.

60. Christodoulou M, Bayman N, McCloskey P, Rowbottom C, Faivre-Finn C. New radiotherapy approaches in locally advanced non-small cell lung cancer. European journal of cancer. 2014;50(3):525-34.
61. Chi A, Nguyen NP, Welsh JS, Tse W, Monga M, Oduntan O, et al. Strategies of dose escalation in the treatment of locally advanced non-small cell lung cancer: image guidance and beyond. Frontiers in oncology. 2014;4:156.
62. Saunders M, Dische S, Barrett A, Harvey A, Griffiths G, Palmar M. Continuous, hyperfractionated, accelerated radiotherapy (CHART) versus conventional radiotherapy in non-small cell lung cancer: mature data from the randomised multicentre trial. CHART Steering committee. Radiotherapy and oncology : journal of the European Society for Therapeutic Radiology and Oncology. 1999;52(2):137-48.
63. Baumann M, Herrmann T, Koch R, Matthiessen W, Appold S, Wahlers B, et al. Final results of the randomized phase III CHARTWEL-trial (ARO 97-1) comparing hyperfractionated-accelerated versus conventionally fractionated radiotherapy in non-small cell lung cancer (NSCLC). Radiotherapy and oncology : journal of the European Society for Therapeutic Radiology and Oncology. 2011;100(1):76-85.
64. Baumann M, Herrmann T, Matthiessen W, Koch R, Strelocke K, Paul U. [CHARTWEL-Bronchus (ARO 97-1): a randomized multicenter trial to compare conventional fractionated radiotherapy with CHARTWEL radiotherapy in inoperable non-small-call bronchial carcinoma]. Strahlentherapie und Onkologie : Organ der Deutschen Rontgengesellschaft [et al]. 1997;173(12):663-7.
65. Ball D, Withers HR. Stereotactic radiotherapy for stage I non-small-cell lung cancer--the triumph of technology over biology? Nature clinical practice Oncology. 2007;4(11):614-5.
66. Iyengar P, Timmerman RD. Stereotactic ablative radiotherapy for non-small cell lung cancer: rationale and outcomes. Journal of the National Comprehensive Cancer Network : JNCCN. 2012;10(12):1514-20.
67. De Ruysscher D, Wanders R, van Haren E, Hochstenbag M, Geraedts W, Pitz C, et al. HI-CHART: a phase I/II study on the feasibility of high-dose continuous hyperfractionated accelerated radiotherapy in patients with inoperable non-small-cell lung cancer. International journal of radiation oncology, biology, physics. 2008;71(1):132-8.
68. Oral EN. Long term results of CHART and weekly Paclitaxel in locally advanced non-small cell lung cancer. Lung cancer. 2005;49(3):421-2.
69. Hatton M, Stephens R. CHART in non-small-cell lung cancer: INCHing forward. Clinical oncology. 2005;17(4):207-9.
70. Lievens Y, Kesteloot K, Van den Bogaert W. CHART in lung cancer: economic evaluation and incentives for implementation. Radiotherapy and oncology : journal of the European Society for Therapeutic Radiology and Oncology. 2005;75(2):171-8.
71. Bentzen SM, Saunders MI, Dische S. From CHART to CHARTWEL in non-small cell lung cancer: clinical radiobiological modelling of the expected change in outcome. Clinical oncology. 2002;14(5):372-81.
72. Eakin RL, Saunders MI. Non-small cell lung cancer and CHART (continuous hyperfractionated accelerated radiotherapy)--where do we stand? The Ulster medical journal. 2000;69(2):128-36.
73. Vokes EE. CHART for non-small-cell lung cancer--promises and limitations. Lancet. 1997;350(9072):156-7.
74. Fowler JF. Hyperfractionated radiotherapy. Clinical oncology. 2015;27(1):65.
75. Haslett K, Pottgen C, Stuschke M, Faivre-Finn C. Hyperfractionated and accelerated radiotherapy in non-small cell lung cancer. Journal of thoracic disease. 2014;6(4):328-35.

76. Li Q, Swanick CW, Allen PK, Gomez DR, Welsh JW, Liao Z, et al. Stereotactic ablative radiotherapy (SABR) using 70Gy in 10 fractions for non-small cell lung cancer: Exploration of clinical indications. Radiotherapy and oncology : journal of the European Society for Therapeutic Radiology and Oncology. 2014;112(2):256-61.
77. Huang K, Dahele M, Senan S, Guckenburger M, Rodrigues G, Ward A, et al. Radiographic Changes After Lung Stereotactic Ablative Radiotherapy (SABR) -- Can We Distinguish Fibrosis From Recurrence? A Systematic Review of the Literature. Practical radiation oncology. 2013;3(2 Suppl 1):S11-2.
78. Iyengar P, Westover K, Timmerman RD. Stereotactic ablative radiotherapy (SABR) for non-small cell lung cancer. Seminars in respiratory and critical care medicine. 2013;34(6):845-54.
79. Solda F, Lodge M, Ashley S, Whitington A, Goldstraw P, Brada M. Stereotactic radiotherapy (SABR) for the treatment of primary non-small cell lung cancer; systematic review and comparison with a surgical cohort. Radiotherapy and oncology : journal of the European Society for Therapeutic Radiology and Oncology. 2013;109(1):1-7.
80. Kong C, Guo WJ, Zha WW, Zhu XZ, Huang SF, Zhang YW, et al. A new index comparable to BED for evaluating the biological efficacy of hypofractionated radiotherapy schemes on early stage non-small cell lung cancer: analysis of data from the literature. Lung cancer. 2014;84(1):7-12.
81. Beli I, Koukourakis G, Platoni K, Tolia M, Kelekis N, Kouvaris J, et al. Hypofractionated radiotherapy in non small cell lung cancer: a review of the current literature. Reviews on recent clinical trials. 2010;5(2):103-11.
82. Brock J, Ashley S, Bedford J, Nioutsikou E, Partridge M, Brada M. Review of hypofractionated small volume radiotherapy for early-stage non-small cell lung cancer. Clinical oncology. 2008;20(9):666-76.
83. Kong FM, Ten Haken RK, Schipper MJ, Sullivan MA, Chen M, Lopez C, et al. High-dose radiation improved local tumor control and overall survival in patients with inoperable/unresectable non-small-cell lung cancer: long-term results of a radiation dose escalation study. International journal of radiation oncology, biology, physics. 2005;63(2):324-33.
84. Rosenzweig KE, Fox JL, Yorke E, Amols H, Jackson A, Rusch V, et al. Results of a phase I dose-escalation study using three-dimensional conformal radiotherapy in the treatment of inoperable nonsmall cell lung carcinoma. Cancer. 2005;103(10):2118-27.
85. Willner J, Baier K, Caragiani E, Tschammler A, Flentje M. Dose, volume, and tumor control prediction in primary radiotherapy of non-small-cell lung cancer. International journal of radiation oncology, biology, physics. 2002;52(2):382-9.
86. Bradley J, Graham MV, Winter K, Purdy JA, Komaki R, Roa WH, et al. Toxicity and outcome results of RTOG 9311: a phase I-II dose-escalation study using three-dimensional conformal radiotherapy in patients with inoperable non-small-cell lung carcinoma. International journal of radiation oncology, biology, physics. 2005;61(2):318-28.
87. Chen M, Hayman JA, Ten Haken RK, Tatro D, Fernando S, Kong FM. Long-term results of high-dose conformal radiotherapy for patients with medically inoperable T1-3N0 non-small-cell lung cancer: is low incidence of regional failure due to incidental nodal irradiation? International journal of radiation oncology, biology, physics. 2006;64(1):120-6.
88. Baumann P, Nyman J, Lax I, Friesland S, Hoyer M, Rehn Ericsson S, et al. Factors important for efficacy of stereotactic body radiotherapy of medically inoperable stage I lung cancer. A retrospective analysis of patients treated in the Nordic countries. Acta oncologica. 2006;45(7):787-95.

89. Lagerwaard FJ, Haasbeek CJ, Smit EF, Slotman BJ, Senan S. Outcomes of risk-adapted fractionated stereotactic radiotherapy for stage I non-small-cell lung cancer. International journal of radiation oncology, biology, physics. 2008;70(3):685-92.
90. Nagata Y, Takayama K, Matsuo Y, Norihisa Y, Mizowaki T, Sakamoto T, et al. Clinical outcomes of a phase I/II study of 48 Gy of stereotactic body radiotherapy in 4 fractions for primary lung cancer using a stereotactic body frame. International journal of radiation oncology, biology, physics. 2005;63(5):1427-31.
91. Nyman J, Johansson KA, Hulten U. Stereotactic hypofractionated radiotherapy for stage I non-small cell lung cancer--mature results for medically inoperable patients. Lung cancer. 2006;51(1):97-103.
92. Onishi H, Shirato H, Nagata Y, Hiraoka M, Fujino M, Gomi K, et al. Hypofractionated stereotactic radiotherapy (HypoFXSRT) for stage I non-small cell lung cancer: updated results of 257 patients in a Japanese multi-institutional study. Journal of thoracic oncology : official publication of the International Association for the Study of Lung Cancer. 2007;2(7 Suppl 3):S94-100.
93. Salazar OM, Sandhu TS, Lattin PB, Chang JH, Lee CK, Groshko GA, et al. Once-weekly, high-dose stereotactic body radiotherapy for lung cancer: 6-year analysis of 60 early-stage, 42 locally advanced, and 7 metastatic lung cancers. International journal of radiation oncology, biology, physics. 2008;72(3):707-15.
94. Timmerman RD, Park C, Kavanagh BD. The North American experience with stereotactic body radiation therapy in non-small cell lung cancer. Journal of thoracic oncology : official publication of the International Association for the Study of Lung Cancer. 2007;2(7 Suppl 3):S101-12.
95. Uematsu M, Shioda A, Suda A, Fukui T, Ozeki Y, Hama Y, et al. Computed tomography-guided frameless stereotactic radiotherapy for stage I non-small cell lung cancer: a 5-year experience. International journal of radiation oncology, biology, physics. 2001;51(3):666-70.
96. Onishi H, Araki T, Shirato H, Nagata Y, Hiraoka M, Gomi K, et al. Stereotactic hypofractionated high-dose irradiation for stage I nonsmall cell lung carcinoma: clinical outcomes in 245 subjects in a Japanese multiinstitutional study. Cancer. 2004;101(7):1623-31.
97. Onishi H, Kuriyama K, Komiyama T, Tanaka S, Sano N, Marino K, et al. Clinical outcomes of stereotactic radiotherapy for stage I non-small cell lung cancer using a novel irradiation technique: patient self-controlled breath-hold and beam switching using a combination of linear accelerator and CT scanner. Lung cancer. 2004;45(1):45-55.
98. Lee S, Lim MJ, Kim MH, Yu CH, Yun YS, Ahn J, et al. An effective strategy for increasing the radiosensitivity of Human lung Cancer cells by blocking Nrf2-dependent antioxidant responses. Free radical biology & medicine. 2012;53(4):807-16.
99. Schuurbiers OC, Kaanders JH, van der Heijden HF, Dekhuijzen RP, Oyen WJ, Bussink J. The PI3-K/AKT-pathway and radiation resistance mechanisms in non-small cell lung cancer. Journal of thoracic oncology : official publication of the International Association for the Study of Lung Cancer. 2009;4(6):761-7.
100. Chang JY, Cox JD. Improving radiation conformality in the treatment of non-small cell lung cancer. Seminars in radiation oncology. 2010;20(3):171-7.
101. Ausborn NL, Le QT, Bradley JD, Choy H, Dicker AP, Saha D, et al. Molecular profiling to optimize treatment in non-small cell lung cancer: a review of potential molecular targets for radiation therapy by the translational research program of the radiation therapy oncology group. International journal of radiation oncology, biology, physics. 2012;83(4):e453-64.

102. Tsoutsou PG, Koukourakis MI. Radiation pneumonitis and fibrosis: mechanisms underlying its pathogenesis and implications for future research. International journal of radiation oncology, biology, physics. 2006;66(5):1281-93.
103. Gross NJ. Experimental radiation pneumonitis. IV. Leakage of circulatory proteins onto the alveolar surface. The Journal of laboratory and clinical medicine. 1980;95(1):19-31.
104. Ding NH, Li JJ, Sun LQ. Molecular mechanisms and treatment of radiation-induced lung fibrosis. Current drug targets. 2013;14(11):1347-56.
105. Sime PJ, O'Reilly KM. Fibrosis of the lung and other tissues: new concepts in pathogenesis and treatment. Clinical immunology. 2001;99(3):308-19.
106. Marks LB, Yu X, Vujaskovic Z, Small W, Jr., Folz R, Anscher MS. Radiation-induced lung injury. Seminars in radiation oncology. 2003;13(3):333-45.
107. McDonald S, Rubin P, Phillips TL, Marks LB. Injury to the lung from cancer therapy: clinical syndromes, measurable endpoints, and potential scoring systems. International journal of radiation oncology, biology, physics. 1995;31(5):1187-203.
108. Bentzen SM, Skoczylas JZ, Overgaard M, Overgaard J. Radiotherapy-related lung fibrosis enhanced by tamoxifen. Journal of the National Cancer Institute. 1996;88(13):918-22.
109. Levinson B, Marks LB, Munley MT, Poulson J, Hollis D, Jaszczak R, et al. Regional dose response to pulmonary irradiation using a manual method. Radiotherapy and oncology : journal of the European Society for Therapeutic Radiology and Oncology. 1998;48(1):53-60.
110. Marks LB. The pulmonary effects of thoracic irradiation. Oncology. 1994;8(6):89-106; discussion 0, 3-4.
111. Theuws JC, Kwa SL, Wagenaar AC, Boersma LJ, Damen EM, Muller SH, et al. Dose-effect relations for early local pulmonary injury after irradiation for malignant lymphoma and breast cancer. Radiotherapy and oncology : journal of the European Society for Therapeutic Radiology and Oncology. 1998;48(1):33-43.
112. Moreno M, Aristu J, Ramos LI, Arbea L, Lopez-Picazo JM, Cambeiro M, et al. Predictive factors for radiation-induced pulmonary toxicity after three-dimensional conformal chemoradiation in locally advanced non-small-cell lung cancer. Clinical & translational oncology : official publication of the Federation of Spanish Oncology Societies and of the National Cancer Institute of Mexico. 2007;9(9):596-602.
113. Fu XL, Huang H, Bentel G, Clough R, Jirtle RL, Kong FM, et al. Predicting the risk of symptomatic radiation-induced lung injury using both the physical and biologic parameters V(30) and transforming growth factor beta. International journal of radiation oncology, biology, physics. 2001;50(4):899-908.
114. Hayman JA, Martel MK, Ten Haken RK, Normolle DP, Todd RF, 3rd, Littles JF, et al. Dose escalation in non-small-cell lung cancer using three-dimensional conformal radiation therapy: update of a phase I trial. Journal of clinical oncology : official journal of the American Society of Clinical Oncology. 2001;19(1):127-36.
115. Yorke ED, Jackson A, Rosenzweig KE, Merrick SA, Gabrys D, Venkatraman ES, et al. Dose-volume factors contributing to the incidence of radiation pneumonitis in non-small-cell lung cancer patients treated with three-dimensional conformal radiation therapy. International journal of radiation oncology, biology, physics. 2002;54(2):329-39.
116. Kong FM, Hayman JA, Griffith KA, Kalemkerian GP, Arenberg D, Lyons S, et al. Final toxicity results of a radiation-dose escalation study in patients with non-small-cell lung cancer (NSCLC): predictors for radiation pneumonitis and fibrosis. International journal of radiation oncology, biology, physics. 2006;65(4):1075-86.

117. Seppenwoolde Y, De Jaeger K, Boersma LJ, Belderbos JS, Lebesque JV. Regional differences in lung radiosensitivity after radiotherapy for non-small-cell lung cancer. International journal of radiation oncology, biology, physics. 2004;60(3):748-58.
118. Van Dyk J, Hill RP. Post-irradiation lung density changes measured by computerized tomography. International journal of radiation oncology, biology, physics. 1983;9(6):847-52.
119. Mah K, Van Dyk J, Keane T, Poon PY. Acute radiation-induced pulmonary damage: a clinical study on the response to fractionated radiation therapy. International journal of radiation oncology, biology, physics. 1987;13(2):179-88.
120. Hernando ML, Marks LB, Bentel GC, Zhou SM, Hollis D, Das SK, et al. Radiation-induced pulmonary toxicity: a dose-volume histogram analysis in 201 patients with lung cancer. International journal of radiation oncology, biology, physics. 2001;51(3):650-9.
121. Kwa SL, Theuws JC, van Herk M, Damen EM, Boersma LJ, Baas P, et al. Automatic three-dimensional matching of CT-SPECT and CT-CT to localize lung damage after radiotherapy. Journal of nuclear medicine : official publication, Society of Nuclear Medicine. 1998;39(6):1074-80.
122. Martel MK, Ten Haken RK, Hazuka MB, Turrisi AT, Fraass BA, Lichter AS. Dose-volume histogram and 3-D treatment planning evaluation of patients with pneumonitis. International journal of radiation oncology, biology, physics. 1994;28(3):575-81.
123. Gross NJ, Narine KR, Wade R. Protective effect of corticosteroids on radiation pneumonitis in mice. Radiation research. 1988;113(1):112-9.
124. Gross NJ. Radiation pneumonitis in mice. Some effects of corticosteroids on mortality and pulmonary physiology. The Journal of clinical investigation. 1980;66(3):504-10.
125. Gross NJ. Pulmonary effects of radiation therapy. Annals of internal medicine. 1977;86(1):81-92.
126. Yamada M, Kudoh S, Hirata K, Nakajima T, Yoshikawa J. Risk factors of pneumonitis following chemoradiotherapy for lung cancer. European journal of cancer. 1998;34(1):71-5.
127. Oetzel D, Schraube P, Hensley F, Sroka-Perez G, Menke M, Flentje M. Estimation of pneumonitis risk in three-dimensional treatment planning using dose-volume histogram analysis. International journal of radiation oncology, biology, physics. 1995;33(2):455-60.
128. Moiseenko V, Craig T, Bezjak A, Van Dyk J. Dose-volume analysis of lung complications in the radiation treatment of malignant thymoma: a retrospective review. Radiotherapy and oncology : journal of the European Society for Therapeutic Radiology and Oncology. 2003;67(3):265-74.
129. Uitterhoeve AL, Belderbos JS, Koolen MG, van der Vaart PJ, Rodrigus PT, Benraadt J, et al. Toxicity of high-dose radiotherapy combined with daily cisplatin in non-small cell lung cancer: results of the EORTC 08912 phase I/II study. European Organization for Research and Treatment of Cancer. European journal of cancer. 2000;36(5):592-600.
130. Abid SH, Malhotra V, Perry MC. Radiation-induced and chemotherapy-induced pulmonary injury. Current opinion in oncology. 2001;13(4):242-8.
131. Parris TM, Knight JG, Hess CE, Constable WC. Severe radiation pneumonitis precipitated by withdrawal of corticosteroids: a diagnostic and therapeutic dilemma. AJR American journal of roentgenology. 1979;132(2):284-6.
132. Rengan R, Rosenzweig KE, Venkatraman E, Koutcher LA, Fox JL, Nayak R, et al. Improved local control with higher doses of radiation in large-volume stage III non-small-cell lung cancer. International journal of radiation oncology, biology, physics. 2004;60(3):741-7.

133. Tucker SL, Mohan R, Liengsawangwong R, Martel MK, Liao Z. Predicting pneumonitis risk: a dosimetric alternative to mean lung dose. International journal of radiation oncology, biology, physics. 2013;85(2):522-7.
134. Burman C, Kutcher GJ, Emami B, Goitein M. Fitting of normal tissue tolerance data to an analytic function. International journal of radiation oncology, biology, physics. 1991;21(1):123-35.
135. Nalbantov G, Kietselaer B, Vandecasteele K, Oberije C, Berbee M, Troost E, et al. Cardiac comorbidity is an independent risk factor for radiation-induced lung toxicity in lung cancer patients. Radiotherapy and oncology : journal of the European Society for Therapeutic Radiology and Oncology. 2013;109(1):100-6.
136. Provatopoulou X, Athanasiou E, Gounaris A. Predictive markers of radiation pneumonitis. Anticancer research. 2008;28(4C):2421-32.
137. Yamashita H, Kobayashi-Shibata S, Terahara A, Okuma K, Haga A, Wakui R, et al. Prescreening based on the presence of CT-scan abnormalities and biomarkers (KL-6 and SP-D) may reduce severe radiation pneumonitis after stereotactic radiotherapy. Radiation oncology. 2010;5:32.
138. Goto K, Kodama T, Sekine I, Kakinuma R, Kubota K, Hojo F, et al. Serum levels of KL-6 are useful biomarkers for severe radiation pneumonitis. Lung cancer. 2001;34(1):141-8.
139. Evans ES, Kocak Z, Zhou SM, Kahn DA, Huang H, Hollis DR, et al. Does transforming growth factor-beta1 predict for radiation-induced pneumonitis in patients treated for lung cancer? Cytokine. 2006;35(3-4):186-92.
140. Fu ZZ, Peng Y, Cao LY, Chen YS, Li K, Fu BH. Correlations Between Serum IL-6 Levels and Radiation Pneumonitis in Lung Cancer Patients: A Meta-Analysis. Journal of clinical laboratory analysis. 2014.
141. Chen Y, Hyrien O, Williams J, Okunieff P, Smudzin T, Rubin P. Interleukin (IL)-1A and IL-6: applications to the predictive diagnostic testing of radiation pneumonitis. International journal of radiation oncology, biology, physics. 2005;62(1):260-6.
142. Chen Y, Rubin P, Williams J, Hernady E, Smudzin T, Okunieff P. Circulating IL-6 as a predictor of radiation pneumonitis. International journal of radiation oncology, biology, physics. 2001;49(3):641-8.
143. Iwata H, Shibamoto Y, Baba F, Sugie C, Ogino H, Murata R, et al. Correlation between the serum KL-6 level and the grade of radiation pneumonitis after stereotactic body radiotherapy for stage I lung cancer or small lung metastasis. Radiotherapy and oncology : journal of the European Society for Therapeutic Radiology and Oncology. 2011;101(2):267-70.
144. Hara R, Itami J, Komiyama T, Katoh D, Kondo T. Serum levels of KL-6 for predicting the occurrence of radiation pneumonitis after stereotactic radiotherapy for lung tumors. Chest. 2004;125(1):340-4.
145. Robbins ME, Brunso-Bechtold JK, Peiffer AM, Tsien CI, Bailey JE, Marks LB. Imaging radiation-induced normal tissue injury. Radiation research. 2012;177(4):449-66.
146. De Ruysscher D, Sharifi H, Defraene G, Kerns SL, Christiaens M, De Ruyck K, et al. Quantification of radiation-induced lung damage with CT scans: the possible benefit for radiogenomics. Acta oncologica. 2013;52(7):1405-10.
147. Fox MS, Ouriadov A, Thind K, Hegarty E, Wong E, Hope A, et al. Detection of radiation induced lung injury in rats using dynamic hyperpolarized (129)Xe magnetic resonance spectroscopy. Medical physics. 2014;41(7):072302.
148. Uzal C, Durmus-Altun G, Caloglu M, Ergulen A, Altaner S, Yigitbasi NO. The protective effect of amifostine on radiation-induced acute pulmonary toxicity: detection by

(99m)Tc-DTPA transalveolar clearances. International journal of radiation oncology, biology, physics. 2004;60(2):564-9.
149. Dirlik A, Erinc R, Ozcan Z, Atasever A, Bacakoglu F, Nalbantgil S, et al. Technetium-99m-DTPA aerosol scintigraphy in amiodarone induced pulmonary toxicity in comparison with Ga-67 scintigraphy. Annals of nuclear medicine. 2002;16(7):477-81.
150. Thind K, Chen A, Friesen-Waldner L, Ouriadov A, Scholl TJ, Fox M, et al. Detection of radiation-induced lung injury using hyperpolarized (13) C magnetic resonance spectroscopy and imaging. Magnetic resonance in medicine : official journal of the Society of Magnetic Resonance in Medicine / Society of Magnetic Resonance in Medicine. 2012.
151. Thind K, Jensen MD, Hegarty E, Chen AP, Lim H, Martinez-Santiesteban F, et al. Mapping metabolic changes associated with early Radiation Induced Lung Injury post conformal radiotherapy using hyperpolarized (1)(3)C-pyruvate Magnetic Resonance Spectroscopic Imaging. Radiotherapy and oncology : journal of the European Society for Therapeutic Radiology and Oncology. 2014;110(2):317-22.
152. Ireland RH, Din OS, Swinscoe JA, Woodhouse N, van Beek EJ, Wild JM, et al. Detection of radiation-induced lung injury in non-small cell lung cancer patients using hyperpolarized helium-3 magnetic resonance imaging. Radiotherapy and oncology : journal of the European Society for Therapeutic Radiology and Oncology. 2010;97(2):244-8.
153. Wielputz M, Kauczor HU. MRI of the lung: state of the art. Diagnostic and interventional radiology. 2012;18(4):344-53.
154. Ley-Zaporozhan J, Puderbach M, Kauczor HU. MR for the evaluation of obstructive pulmonary disease. Magnetic resonance imaging clinics of North America. 2008;16(2):291-308, ix.
155. Wild JM, Marshall H, Bock M, Schad LR, Jakob PM, Puderbach M, et al. MRI of the lung (1/3): methods. Insights into imaging. 2012;3(4):345-53.
156. Biederer J, Mirsadraee S, Beer M, Molinari F, Hintze C, Bauman G, et al. MRI of the lung (3/3)-current applications and future perspectives. Insights into imaging. 2012;3(4):373-86.
157. Evelhoch JL, LoRusso PM, He Z, DelProposto Z, Polin L, Corbett TH, et al. Magnetic resonance imaging measurements of the response of murine and human tumors to the vascular-targeting agent ZD6126. Clinical cancer research : an official journal of the American Association for Cancer Research. 2004;10(11):3650-7.
158. Evelhoch JL, Gillies RJ, Karczmar GS, Koutcher JA, Maxwell RJ, Nalcioglu O, et al. Applications of magnetic resonance in model systems: cancer therapeutics. Neoplasia. 2000;2(1-2):152-65.
159. Rukat T, Walker-Samuel S, Reinsberg SA. Dynamic contrast-enhanced MRI in mice: an investigation of model parameter uncertainties. Magnetic resonance in medicine : official journal of the Society of Magnetic Resonance in Medicine / Society of Magnetic Resonance in Medicine. 2015;73(5):1979-87.
160. Walker-Samuel S, Leach MO, Collins DJ. Evaluation of response to treatment using DCE-MRI: the relationship between initial area under the gadolinium curve (IAUGC) and quantitative pharmacokinetic analysis. Physics in medicine and biology. 2006;51(14):3593-602.
161. Naish JH, Kershaw LE, Buckley DL, Jackson A, Waterton JC, Parker GJ. Modeling of contrast agent kinetics in the lung using T1-weighted dynamic contrast-enhanced MRI. Magnetic resonance in medicine : official journal of the Society of Magnetic Resonance in Medicine / Society of Magnetic Resonance in Medicine. 2009;61(6):1507-14.
162. Borisch I, Horn M, Butz B, Zorger N, Draganski B, Hoelscher T, et al. Preoperative evaluation of carotid artery stenosis: comparison of contrast-enhanced MR angiography and

duplex sonography with digital subtraction angiography. AJNR American journal of neuroradiology. 2003;24(6):1117-22.
163. De Cobelli F, Venturini M, Vanzulli A, Sironi S, Salvioni M, Angeli E, et al. Renal arterial stenosis: prospective comparison of color Doppler US and breath-hold, three-dimensional, dynamic, gadolinium-enhanced MR angiography. Radiology. 2000;214(2):373-80.
164. Randoux B, Marro B, Koskas F, Chiras J, Dormont D, Marsault C. Proximal great vessels of aortic arch: comparison of three-dimensional gadolinium-enhanced MR angiography and digital subtraction angiography. Radiology. 2003;229(3):697-702.
165. Stojadinovic S, Low DA, Hope AJ, Vicic M, Deasy JO, Cui J, et al. MicroRT-small animal conformal irradiator. Medical physics. 2007;34(12):4706-16.
166. Hill RP. Response of mouse lung to irradiation at different dose-rates. International journal of radiation oncology, biology, physics. 1983;9(7):1043-7.
167. Newcomb CH, Van Dyk J, Hill RP. Evaluation of isoeffect formulae for predicting radiation-induced lung damage. Radiotherapy and oncology : journal of the European Society for Therapeutic Radiology and Oncology. 1993;26(1):51-63.
168. Travis EL. Early indicators of radiation injury in the lung: are they useful predictors for late changes? International journal of radiation oncology, biology, physics. 1980;6(9):1267-9.
169. Travis EL, Vojnovic B, Davies EE, Hirst DG. A plethysmographic method for measuring function in locally irradiated mouse lung. The British journal of radiology. 1979;52(613):67-74.
170. Brunner TB, Geiger M, Grabenbauer GG, Lang-Welzenbach M, Mantoni TS, Cavallaro A, et al. Phase I trial of the human immunodeficiency virus protease inhibitor nelfinavir and chemoradiation for locally advanced pancreatic cancer. Journal of clinical oncology : official journal of the American Society of Clinical Oncology. 2008;26(16):2699-706.
171. Travis EL, Down JD, Holmes SJ, Hobson B. Radiation pneumonitis and fibrosis in mouse lung assayed by respiratory frequency and histology. Radiation research. 1980;84(1):133-43.
172. Down JDT, N.J. Warhol, M. Mauch, P. Dose-limiting complications from upper half body irradiation in C3H mice. International journal of radiation oncology, biology, physics. 1998;14:483-9.
173. Jackson IL, Vujaskovic Z, Down JD. Revisiting strain-related differences in radiation sensitivity of the mouse lung: recognizing and avoiding the confounding effects of pleural effusions. Radiation research. 2010;173(1):10-20.
174. Jackson IL, Vujaskovic Z, Down JD. A further comparison of pathologies after thoracic irradiation among different mouse strains: finding the best preclinical model for evaluating therapies directed against radiation-induced lung damage. Radiation research. 2011;175(4):510-18.
175. Down JD, Nicholas D, Steel GG. Lung damage after hemithoracic irradiation: dependence on mouse strain. Radiotherapy and oncology : journal of the European Society for Therapeutic Radiology and Oncology. 1986;6(1):43-50.
176. Liao ZX, Travis EL, Tucker SL. Damage and morbidity from pneumonitis after irradiation of partial volumes of mouse lung. International journal of radiation oncology, biology, physics. 1995;32(5):1359-70.
177. Eldh T, Heinzelmann F, Velalakan A, Budach W, Belka C, Jendrossek V. Radiation-induced changes in breathing frequency and lung histology of C57BL/6J mice are time- and

dose-dependent. Strahlentherapie und Onkologie : Organ der Deutschen Rontgengesellschaft [et al]. 2012;188(3):274-81.
178. Cappuccini F, Eldh T, Bruder D, Gereke M, Jastrow H, Schulze-Osthoff K, et al. New insights into the molecular pathology of radiation-induced pneumopathy. Radiotherapy and oncology : journal of the European Society for Therapeutic Radiology and Oncology. 2011;101(1):86-92.
179. Nicholas D, Down JD. The assessment of early and late radiation injury to the mouse lung using X-ray computerised tomography. Radiotherapy and oncology : journal of the European Society for Therapeutic Radiology and Oncology. 1985;4(3):253-63.
180. Travis EL, Down JD, Hall L, Vojnovic B, Holmes SJ. Factors affecting the breathing rate of mice as used for studies of radiation damage to lungs. The British journal of radiology. 1981;54(637):50-3.
181. Down JD. The nature and relevance of late lung pathology following localised irradiation of the thorax in mice and rats. The British journal of cancer Supplement. 1986;7:330-2.
182. Karvonen RL, Fernandez-Madrid F, Maughan RL, Palmer KC, Fernandez-Madrid I. An animal model of pulmonary radiation fibrosis with biochemical, physiologic, immunologic, and morphologic observations. Radiation research. 1987;111(1):68-80.
183. Saito S, Murase K. Detection and early phase assessment of radiation-induced lung injury in mice using micro-CT. PloS one. 2012;7(9):e45960.
184. Abdollahi A, Li M, Ping G, Plathow C, Domhan S, Kiessling F, et al. Inhibition of platelet-derived growth factor signaling attenuates pulmonary fibrosis. The Journal of experimental medicine. 2005;201(6):925-35.
185. Urtreger AJ, Diament MJ, Ranuncolo SM, Del CVM, Puricelli LI, Klein SM, et al. New murine cell line derived from a spontaneous lung tumor induces paraneoplastic syndromes. International journal of oncology. 2001;18(3):639-47.
186. Chakraborty AK, Sodi S, Rachkovsky M, Kolesnikova N, Platt JT, Bolognia JL, et al. A spontaneous murine melanoma lung metastasis comprised of host x tumor hybrids. Cancer research. 2000;60(9):2512-9.
187. Granton PV, Dubois L, van Elmpt W, van Hoof SJ, Lieuwes NG, De Ruysscher D, et al. A longitudinal evaluation of partial lung irradiation in mice by using a dedicated image-guided small animal irradiator. International journal of radiation oncology, biology, physics. 2014;90(3):696-704.
188. Cho J, Kodym R, Seliounine S, Richardson JA, Solberg TD, Story MD. High dose-per-fraction irradiation of limited lung volumes using an image-guided, highly focused irradiator: simulating stereotactic body radiotherapy regimens in a small-animal model. International journal of radiation oncology, biology, physics. 2010;77(3):895-902.
189. Stojadinovic S, Low DA, Hope AJ, Vicic M, Deasy JO, Cui J, et al. MicroRT-small animal conformal irradiator. Med Phys. 2007;34(12):4706-16.
190. Stojadinovic S, Low DA, Vicic M, Mutic S, Deasy JO, Hope AJ, et al. Progress toward a microradiation therapy small animal conformal irradiator. Med Phys. 2006;33(10):3834-45.
191. El-Khatib E, Sharplin J, Battista J. The density of mouse lung in vivo following X irradiation. International journal of radiation oncology, biology, physics. 1983;9(6):853-8.
192. Furlow B. Bringing radiotherapy into the personalized medicine revolution. Oncol Nurs Advis. 2012.
193. Diaz R, Nguewa PA, Diaz-Gonzalez JA, Hamel E, Gonzalez-Moreno O, Catena R, et al. The novel Akt inhibitor Palomid 529 (P529) enhances the effect of radiotherapy in prostate cancer. British journal of cancer. 2009;100(6):932-40.

194. Kleibeuker EA, Griffioen AW, Verheul HM, Slotman BJ, Thijssen VL. Combining angiogenesis inhibition and radiotherapy: a double-edged sword. Drug resistance updates : reviews and commentaries in antimicrobial and anticancer chemotherapy. 2012;15(3):173-82.
195. Liauw SL, Connell PP, Weichselbaum RR. New paradigms and future challenges in radiation oncology: an update of biological targets and technology. Science translational medicine. 2013;5(173):173sr2.
196. Palacios DA, Miyake M, Rosser CJ. Radiosensitization in prostate cancer: mechanisms and targets. BMC urology. 2013;13(1):4.
197. Herscher LL, Cook JA, Pacelli R, Pass HI, Russo A, Mitchell JB. Principles of chemoradiation: theoretical and practical considerations. Oncology. 1999;13(10 Suppl 5):11-22.
198. New Topics in Cancer Research: Nova Science Publishers INc: 1 edition; 1 Dec 2006.
199. Frytak S, Moertel, C, and Childs, D.S. . Neurologic toxicity associated with high-dose metronidazole therapy. Annals of internal medicine. 1978;88(3):361-2.
200. WAsserman T, Chapman, J., Coleman, C., Klingerman, M. Chemical modifiers of radiation. In: Brady CAPaW, editor. Principles and Practice of Radiation Oncology. 3rd ed. Philadelphia: Lippincott-Raven Publishers; 1997. p. 685-91.
201. Overgaard J, Hansen HS, Overgaard M, Bastholt L, Berthelsen A, Specht L, et al. A randomized double-blind phase III study of nimorazole as a hypoxic radiosensitizer of primary radiotherapy in supraglottic larynx and pharynx carcinoma. Results of the Danish Head and Neck Cancer Study (DAHANCA) Protocol 5-85. Radiotherapy and oncology : journal of the European Society for Therapeutic Radiology and Oncology. 1998;46(2):135-46.
202. Overgaard J, Hansen HS, Specht L, Overgaard M, Grau C, Andersen E, et al. Five compared with six fractions per week of conventional radiotherapy of squamous-cell carcinoma of head and neck: DAHANCA 6 and 7 randomised controlled trial. Lancet. 2003;362(9388):933-40.
203. Li F, Zhao C, Wang L. Molecular-targeted agents combination therapy for cancer: developments and potentials. International journal of cancer Journal international du cancer. 2014;134(6):1257-69.
204. Guix M, Mayer IA, Meszoely IM, Arteaga CL. Evaluation of biological agents targeted at early-stage disease. Breast cancer research : BCR. 2008;10 Suppl 4:S25.
205. Guix M, Granja Nde M, Meszoely I, Adkins TB, Wieman BM, Frierson KE, et al. Short preoperative treatment with erlotinib inhibits tumor cell proliferation in hormone receptor-positive breast cancers. Journal of clinical oncology : official journal of the American Society of Clinical Oncology. 2008;26(6):897-906.
206. Kaufman H L WS, Antman K, editor. Molecular Targeting in Oncology: Springer Science + Buisness Media LLC; 2008.
207. Doroshow JH, Kummar S. Translational research in oncology-10 years of progress and future prospects. Nature reviews Clinical oncology. 2014;11(11):649-62.
208. Sathe A, Guerth F, Cronauer MV, Heck MM, Thalgott M, Gschwend JE, et al. Mutant PIK3CA controls DUSP1-dependent ERK 1/2 activity to confer response to AKT target therapy. British journal of cancer. 2014;111(11):2103-13.
209. Cao P, Maira SM, Garcia-Echeverria C, Hedley DW. Activity of a novel, dual PI3-kinase/mTor inhibitor NVP-BEZ235 against primary human pancreatic cancers grown as orthotopic xenografts. British journal of cancer. 2009;100(8):1267-76.

210. Wojcik S. Crosstalk between autophagy and proteasome protein degradation systems: possible implications for cancer therapy. Folia histochemica et cytobiologica / Polish Academy of Sciences, Polish Histochemical and Cytochemical Society. 2013;51(4):249-64.
211. Fokas E, McKenna WG, Muschel RJ. The impact of tumor microenvironment on cancer treatment and its modulation by direct and indirect antivascular strategies. Cancer metastasis reviews. 2012;31(3-4):823-42.
212. Kuger S, Graus D, Brendtke R, Gunther N, Katzer A, Lutyj P, et al. Radiosensitization of Glioblastoma Cell Lines by the Dual PI3K and mTOR Inhibitor NVP-BEZ235 Depends on Drug-Irradiation Schedule. Translational oncology. 2013;6(2):169-79.
213. Liu Q, Xu C, Kirubakaran S, Zhang X, Hur W, Liu Y, et al. Characterization of Torin2, an ATP-competitive inhibitor of mTOR, ATM, and ATR. Cancer research. 2013;73(8):2574-86.
214. Zhu W, Fu W, Hu L. NVP-BEZ235, dual phosphatidylinositol 3-kinase/mammalian target of rapamycin inhibitor, prominently enhances radiosensitivity of prostate cancer cell line PC-3. Cancer biotherapy & radiopharmaceuticals. 2013;28(9):665-73.
215. Niehues T HG, Megahed M et al. Complete regression of AIDS-related Kaposi's sarcoma in a child treated with highly active antiretroviral therapy. Aids. 1999;13:1148-9.
216. Sgadari C, Monini P, Barillari G, Ensoli B. Use of HIV protease inhibitors to block Kaposi's sarcoma and tumour growth. The lancet oncology. 2003;4(9):537-47.
217. Pore N, Gupta AK, Cerniglia GJ, Jiang Z, Bernhard EJ, Evans SM, et al. Nelfinavir down-regulates hypoxia-inducible factor 1alpha and VEGF expression and increases tumor oxygenation: implications for radiotherapy. Cancer research. 2006;66(18):9252-9.
218. Pan J, Mott M, Xi B, Hepner E, Guan M, Fousek K, et al. Phase I study of nelfinavir in liposarcoma. Cancer chemotherapy and pharmacology. 2012;70(6):791-9.
219. Buijsen J, Lammering G, Jansen RL, Beets GL, Wals J, Sosef M, et al. Phase I trial of the combination of the Akt inhibitor nelfinavir and chemoradiation for locally advanced rectal cancer. Radiotherapy and oncology : journal of the European Society for Therapeutic Radiology and Oncology. 2013;107(2):184-8.
220. Alonso-Basanta M, Fang P, Maity A, Hahn SM, Lustig RA, Dorsey JF. A phase I study of nelfinavir concurrent with temozolomide and radiotherapy in patients with glioblastoma multiforme. Journal of neuro-oncology. 2014;116(2):365-72.
221. Chapman CH, Shen J, Filion EJ, Tran PT, Hara W, Asuncion A, et al. Marked tumor response and fatal hemoptysis during radiation for lung cancer in a human immunodeficiency virus-positive patient taking nelfinavir. Journal of thoracic oncology : official publication of the International Association for the Study of Lung Cancer. 2009;4(12):1587-9.
222. Liu WL, Gao M, Tzen KY, Tsai CL, Hsu FM, Cheng AL, et al. Targeting Phosphatidylinositide3-Kinase/Akt pathway by BKM120 for radiosensitization in hepatocellular carcinoma. Oncotarget. 2014;5(11):3662-72.
223. Rodon J, Brana I, Siu LL, De Jonge MJ, Homji N, Mills D, et al. Phase I dose-escalation and -expansion study of buparlisib (BKM120), an oral pan-Class I PI3K inhibitor, in patients with advanced solid tumors. Investigational new drugs. 2014;32(4):670-81.
224. Chang L, Graham PH, Hao J, Ni J, Bucci J, Cozzi PJ, et al. PI3K/Akt/mTOR pathway inhibitors enhance radiosensitivity in radioresistant prostate cancer cells through inducing apoptosis, reducing autophagy, suppressing NHEJ and HR repair pathways. Cell death & disease. 2014;5:e1437.
225. Fokas E, Yoshimura M, Prevo R, Higgins G, Hackl W, Maira SM, et al. NVP-BEZ235 and NVP-BGT226, dual phosphatidylinositol 3-kinase/mammalian target of

rapamycin inhibitors, enhance tumor and endothelial cell radiosensitivity. Radiation oncology. 2012;7:48.
226. Potiron VA, Abderrahmani R, Giang E, Chiavassa S, Di Tomaso E, Maira SM, et al. Radiosensitization of prostate cancer cells by the dual PI3K/mTOR inhibitor BEZ235 under normoxic and hypoxic conditions. Radiotherapy and oncology : journal of the European Society for Therapeutic Radiology and Oncology. 2013;106(1):138-46.
227. Chang L, Graham PH, Hao J, Ni J, Bucci J, Cozzi PJ, et al. Acquisition of epithelial-mesenchymal transition and cancer stem cell phenotypes is associated with activation of the PI3K/Akt/mTOR pathway in prostate cancer radioresistance. Cell death & disease. 2013;4:e875.
228. Wang WJ, Long LM, Yang N, Zhang QQ, Ji WJ, Zhao JH, et al. NVP-BEZ235, a novel dual PI3K/mTOR inhibitor, enhances the radiosensitivity of human glioma stem cells in vitro. Acta pharmacologica Sinica. 2013;34(5):681-90.
229. Gil del Alcazar CR, Hardebeck MC, Mukherjee B, Tomimatsu N, Gao X, Yan J, et al. Inhibition of DNA double-strand break repair by the dual PI3K/mTOR inhibitor NVP-BEZ235 as a strategy for radiosensitization of glioblastoma. Clinical cancer research : an official journal of the American Association for Cancer Research. 2014;20(5):1235-48.
230. Kim KW, Myers CJ, Jung DK, Lu B. NVP-BEZ-235 enhances radiosensitization via blockade of the PI3K/mTOR pathway in cisplatin-resistant non-small cell lung carcinoma. Genes & cancer. 2014;5(7-8):293-302.
231. Engelman JA, Chen L, Tan X, Crosby K, Guimaraes AR, Upadhyay R, et al. Effective use of PI3K and MEK inhibitors to treat mutant Kras G12D and PIK3CA H1047R murine lung cancers. Nature medicine. 2008;14(12):1351-6.
232. Konstantinidou G, Bey EA, Rabellino A, Schuster K, Maira MS, Gazdar AF, et al. Dual phosphoinositide 3-kinase/mammalian target of rapamycin blockade is an effective radiosensitizing strategy for the treatment of non-small cell lung cancer harboring K-RAS mutations. Cancer research. 2009;69(19):7644-52.
233. Mukherjee B, Tomimatsu N, Amancherla K, Camacho CV, Pichamoorthy N, Burma S. The dual PI3K/mTOR inhibitor NVP-BEZ235 is a potent inhibitor of ATM- and DNA-PKCs-mediated DNA damage responses. Neoplasia. 2012;14(1):34-43.
234. Wong J, Armour E, Kazanzides P, Iordachita I, Tryggestad E, Deng H, et al. High-resolution, small animal radiation research platform with x-ray tomographic guidance capabilities. International journal of radiation oncology, biology, physics. 2008;71(5):1591-9.
235. Tryggestad E, Armour M, Iordachita I, Verhaegen F, Wong JW. A comprehensive system for dosimetric commissioning and Monte Carlo validation for the small animal radiation research platform. Phys Med Biol. 2009;54(17):5341-57.
236. Fokas E, Prevo R, Hammond EM, Brunner TB, McKenna WG, Muschel RJ. Targeting ATR in DNA damage response and cancer therapeutics. Cancer treatment reviews. 2014;40(1):109-17.
237. Fokas E, Prevo R, Pollard JR, Reaper PM, Charlton PA, Cornelissen B, et al. Targeting ATR in vivo using the novel inhibitor VE-822 results in selective sensitization of pancreatic tumors to radiation. Cell death & disease. 2012;3:e441.
238. Prevo R, Fokas E, Reaper PM, Charlton PA, Pollard JR, McKenna WG, et al. The novel ATR inhibitor VE-821 increases sensitivity of pancreatic cancer cells to radiation and chemotherapy. Cancer biology & therapy. 2012;13(11):1072-81.
239. Mueller A, Bachmann E, Linnig M, Khillimberger K, Schimanski CC, Galle PR, et al. Selective PI3K inhibition by BKM120 and BEZ235 alone or in combination with

chemotherapy in wild-type and mutated human gastrointestinal cancer cell lines. Cancer chemotherapy and pharmacology. 2012;69(6):1601-15.
240. Ren H, Chen M, Yue P, Tao H, Owonikoko TK, Ramalingam SS, et al. The combination of RAD001 and NVP-BKM120 synergistically inhibits the growth of lung cancer in vitro and in vivo. Cancer letters. 2012;325(2):139-46.
241. Ford JG, Rennick D, Donaldson DD, Venkayya R, McArthur C, Hansell E, et al. Il-13 and IFN-gamma: interactions in lung inflammation. Journal of immunology. 2001;167(3):1769-77.
242. Ashcroft T, Simpson JM, Timbrell V. Simple method of estimating severity of pulmonary fibrosis on a numerical scale. Journal of clinical pathology. 1988;41(4):467-70.
243. Yushkevich PA, Piven J, Hazlett HC, Smith RG, Ho S, Gee JC, et al. User-guided 3D active contour segmentation of anatomical structures: significantly improved efficiency and reliability. NeuroImage. 2006;31(3):1116-28.
244. Lee HJ, Goo JM, Kim NR, Kim MA, Chung DH, Son KR, et al. Semiquantitative measurement of murine bleomycin-induced lung fibrosis in in vivo and postmortem conditions using microcomputed tomography: correlation with pathologic scores--initial results. Investigative radiology. 2008;43(6):453-60.
245. Team RC. R: A language and environment for statistical computing. . Vienna: R Foundation for Statistical Computing; 2013.
246. Lockhart SP. Inhaled thiol and phosphorothiol radioprotectors fail to protect the mouse lung. Radiotherapy and oncology : journal of the European Society for Therapeutic Radiology and Oncology. 1990;19(2):187-91.
247. Tigani B, Cannet C, Karmouty-Quintana H, Ble FX, Zurbruegg S, Schaeublin E, et al. Lung inflammation and vascular remodeling after repeated allergen challenge detected noninvasively by MRI. American journal of physiology Lung cellular and molecular physiology. 2007;292(3):L644-53.
248. Washko GR. Diagnostic imaging in COPD. Seminars in respiratory and critical care medicine. 2010;31(3):276-85.
249. Ohno Y, Hatabu H, Takenaka D, Van Cauteren M, Fujii M, Sugimura K. Dynamic oxygen-enhanced MRI reflects diffusing capacity of the lung. Magnetic resonance in medicine : official journal of the Society of Magnetic Resonance in Medicine / Society of Magnetic Resonance in Medicine. 2002;47(6):1139-44.
250. Maki DD, Gefter WB, Alavi A. Recent advances in pulmonary imaging. Chest. 1999;116(5):1388-402.
251. Meadors M, Floyd J, Perry MC. Pulmonary toxicity of chemotherapy. Seminars in oncology. 2006;33(1):98-105.
252. Jules-Elysee K, White DA. Bleomycin-induced pulmonary toxicity. Clinics in chest medicine. 1990;11(1):1-20.
253. Sleijfer S. Bleomycin-induced pneumonitis. Chest. 2001;120(2):617-24.
254. O'Sullivan JM, Huddart RA, Norman AR, Nicholls J, Dearnaley DP, Horwich A. Predicting the risk of bleomycin lung toxicity in patients with germ-cell tumours. Annals of oncology : official journal of the European Society for Medical Oncology / ESMO. 2003;14(1):91-6.
255. Cavanaugh D, Travis EL, Price RE, Gladish G, White RA, Wang M, et al. Quantification of bleomycin-induced murine lung damage in vivo with micro-computed tomography. Academic radiology. 2006;13(12):1505-12.
256. Collis CH, Down JD, Pearson AE, Steel GG. Bleomycin and radiation-induced lung damage in mice. The British journal of radiology. 1983;56(661):21-6.

257. Moore BB, Hogaboam CM. Murine models of pulmonary fibrosis. American journal of physiology Lung cellular and molecular physiology. 2008;294(2):L152-60.
258. Lissner J, Argenton H, Bock H, Breddin HK, Dippell J. [Animal experiment studies on radiation pneumonitis]. Strahlentherapie. 1966;131(4):577-94.
259. Marks LB, Bentzen SM, Deasy JO, Kong FM, Bradley JD, Vogelius IS, et al. Radiation dose-volume effects in the lung. International journal of radiation oncology, biology, physics. 2010;76(3 Suppl):S70-6.
260. Chiang CS, Liu WC, Jung SM, Chen FH, Wu CR, McBride WH, et al. Compartmental responses after thoracic irradiation of mice: strain differences. International journal of radiation oncology, biology, physics. 2005;62(3):862-71.
261. Rube CE, Wilfert F, Palm J, Konig J, Burdak-Rothkamm S, Liu L, et al. Irradiation induces a biphasic expression of pro-inflammatory cytokines in the lung. Strahlentherapie und Onkologie : Organ der Deutschen Rontgengesellschaft [et al]. 2004;180(7):442-8.
262. Schneider CA, Rasband WS, Eliceiri KW. NIH Image to ImageJ: 25 years of image analysis. Nature methods. 2012;9(7):671-5.
263. Yamamoto S. [Fundamental of medical image processing with personal computer system--Image processing of computed tomography with imageJ]. Nihon Hoshasen Gijutsu Gakkai zasshi. 2009;65(12):1680-2.
264. Rasband WS. ImageJ: National Institutes of Health, Bethesda, Maryland, USA; 1997-2014. Available from: http://imagej.nih.gov/ij.
265. Lockhart SP, Down JD, Steel GG. Mouse hemithoracic irradiation and its interaction with cytotoxic drugs. Radiotherapy and oncology : journal of the European Society for Therapeutic Radiology and Oncology. 1992;24(3):177-85.
266. Schnell CR, Stauffer F, Allegrini PR, O'Reilly T, McSheehy PM, Dartois C, et al. Effects of the dual phosphatidylinositol 3-kinase/mammalian target of rapamycin inhibitor NVP-BEZ235 on the tumor vasculature: implications for clinical imaging. Cancer research. 2008;68(16):6598-607.
267. Bazalova M, Nelson G, Noll JM, Graves EE. Modality comparison for small animal radiotherapy: a simulation study. Medical physics. 2014;41(1):011710.
268. Ngwa W, Korideck H, Chin LM, Makrigiorgos GM, Berbeco RI. MOSFET assessment of radiation dose delivered to mice using the Small Animal Radiation Research Platform (SARRP). Radiation research. 2011;176(6):816-20.
269. Simone CB, 2nd, Dorsey JF. Additional data in the debate on stage I non-small cell lung cancer: surgery versus stereotactic ablative radiotherapy. Annals of translational medicine. 2015;3(13):172.
270. Louie AV, Palma DA, Dahele M, Rodrigues GB, Senan S. Management of early-stage non-small cell lung cancer using stereotactic ablative radiotherapy: controversies, insights, and changing horizons. Radiotherapy and oncology : journal of the European Society for Therapeutic Radiology and Oncology. 2015;114(2):138-47.
271. Peguret N, Dahele M, Lagerwaard F, Senan S, Slotman BJ. A brief report of 10-year trends in the use of stereotactic lung radiotherapy at a dutch academic medical center. Journal of thoracic oncology : official publication of the International Association for the Study of Lung Cancer. 2014;9(1):114-7.
272. Sharabi AB, Nirschl CJ, Kochel CM, Nirschl TR, Francica BJ, Velarde E, et al. Stereotactic Radiation Therapy Augments Antigen-Specific PD-1 Mediated Anti-Tumor Immune Responses via Cross-Presentation of Tumor Antigen. Cancer immunology research. 2014.
273. Bolcaen J, Descamps B, Deblaere K, Boterberg T, Hallaert G, Van den Broecke C, et al. MRI-guided 3D conformal arc micro-irradiation of a F98 glioblastoma rat model using

the Small Animal Radiation Research Platform (SARRP). Journal of neuro-oncology. 2014;120(2):257-66.
274. Tuli R, Surmak A, Reyes J, Hacker-Prietz A, Armour M, Leubner A, et al. Development of a novel preclinical pancreatic cancer research model: bioluminescence image-guided focal irradiation and tumor monitoring of orthotopic xenografts. Translational oncology. 2012;5(2):77-84.
275. Armour M, Ford E, Iordachita I, Wong J. CT guidance is needed to achieve reproducible positioning of the mouse head for repeat precision cranial irradiation. Radiation research. 2010;173(1):119-23.
276. Lee SH, Kim JY, Lee KC, Nam JS, Choi J, Lee SH, et al. Establishment of linear accelerator-based image guided radiotherapy for orthotopic 4T1 mouse mammary tumor model. Laboratory animal research. 2014;30(2):64-72.
277. Kim H, Fabien J, Zheng Y, Yuan J, Brindle J, Sloan A, et al. Establishing a process of irradiating small animal brain using a CyberKnife and a microCT scanner. Medical physics. 2014;41(2):021715.
278. Graves PR, Siddiqui F, Anscher MS, Movsas B. Radiation pulmonary toxicity: from mechanisms to management. Seminars in radiation oncology. 2010;20(3):201-7.
279. Trott KR, Herrmann T, Kasper M. Target cells in radiation pneumopathy. International journal of radiation oncology, biology, physics. 2004;58(2):463-9.
280. Movsas B, Raffin TA, Epstein AH, Link CJ, Jr. Pulmonary radiation injury. Chest. 1997;111(4):1061-76.
281. Roeder F, Friedrich J, Timke C, Kappes J, Huber P, Krempien R, et al. Correlation of patient-related factors and dose-volume histogram parameters with the onset of radiation pneumonitis in patients with small cell lung cancer. Strahlentherapie und Onkologie : Organ der Deutschen Rontgengesellschaft [et al]. 2010;186(3):149-56.
282. Glazer HS, Lee JK, Levitt RG, Heiken JP, Ling D, Totty WG, et al. Radiation fibrosis: differentiation from recurrent tumor by MR imaging. Radiology. 1985;156(3):721-6.
283. Kono M, Sako M, Adachi S, Hirota S, Shimizu T, Tanaka K, et al. [MR imaging in the assessment of lung cancer patients: primary lung cancer staging, evaluation of therapeutic effect and diagnosis of recurrent tumor]. Nihon Igaku Hoshasen Gakkai zasshi Nippon acta radiologica. 1989;49(7):831-40.
284. Shioya S, Haida M, Ono Y, Fukuzaki M, Yamabayashi H. Lung cancer: differentiation of tumor, necrosis, and atelectasis by means of T1 and T2 values measured in vitro. Radiology. 1988;167(1):105-9.
285. Woo J, Stone M, Prince J. Multimodal Registration via Mutual Information Incorporating Geometric and Spatial Context. IEEE transactions on image processing : a publication of the IEEE Signal Processing Society. 2014.
286. Thind K, Chen A, Friesen-Waldner L, Ouriadov A, Scholl TJ, Fox M, et al. Detection of radiation-induced lung injury using hyperpolarized (13)C magnetic resonance spectroscopy and imaging. Magnetic resonance in medicine : official journal of the Society of Magnetic Resonance in Medicine / Society of Magnetic Resonance in Medicine. 2013;70(3):601-9.
287. Zhang XJ, Sun JG, Sun J, Ming H, Wang XX, Wu L, et al. Prediction of radiation pneumonitis in lung cancer patients: a systematic review. Journal of cancer research and clinical oncology. 2012;138(12):2103-16.
288. Kelsey CR, Rosenstein BS, Marks LB. Predicting toxicity from radiation therapy--it's genetic, right? Cancer. 2012;118(14):3450-4.

289. Pollard JM, Gatti RA. Clinical radiation sensitivity with DNA repair disorders: an overview. International journal of radiation oncology, biology, physics. 2009;74(5):1323-31.
290. Alsner J, Andreassen CN, Overgaard J. Genetic markers for prediction of normal tissue toxicity after radiotherapy. Seminars in radiation oncology. 2008;18(2):126-35.
291. Teates CD. Effects of unilateral thoracic irradiation on lung function. J Appl Physiol. 1965;20(4):628-36.
292. Travis EL, Liao ZX, Tucker SL. Spatial heterogeneity of the volume effect for radiation pneumonitis in mouse lung. International journal of radiation oncology, biology, physics. 1997;38(5):1045-54.
293. Tucker SL, Liao ZX, Travis EL. Estimation of the spatial distribution of target cells for radiation pneumonitis in mouse lung. International journal of radiation oncology, biology, physics. 1997;38(5):1055-66.
294. Gafchromic EBT2 Self-developing film for radiotherapy dosimetry. In: Corporation GM, editor. Revision 1 ed2009.
295. Aldelaijan S, Nobah A, Alsbeih G, Moftah B, Aldahlawi I, Alzahrany A, et al. Dosimetry of biological irradiations using radiochromic films. Phys Med Biol. 2013;58(10):3177-89.
296. Ma CM, Coffey CW, DeWerd LA, Liu C, Nath R, Seltzer SM, et al. AAPM protocol for 40-300 kV x-ray beam dosimetry in radiotherapy and radiobiology. Medical physics. 2001;28(6):868-93.
297. Yoo S, Grimm D, Zhu R, Jursinic P, Lopez F, Rownd J, et al. Clinical implementation of AAPM TG61 protocol for kilovoltage x-ray beam dosimetry. Medical physics. 2002;29(10):2269-73.

# Appendices

## *A Appendices*


**A.1 Appendix 1 – Dosimetric Characterisation of Irradiation Systems**

**A.2 Appendix 2 – Publications and Presentations**

**A.3 Appendix 3 –Plethysmography**

# Appendix 1

*Dosimetric Characterization of Radiation Delivery Systems (RT QA)*

# Dosimetric Characterisation of the Cabinet Irradiator

## Methods

Dosimetric characterisation of the treatment was performed with the support and Guidance of Dr. James Thompson, and Luke Bird of Professor Mark Hill's Group (Radiation Biophysics, Oxford Institute for Radiation Oncology and Biology), using Gafchromic EBT3 film (International Specialty Products, Wayne, NJ) positioned in the centre of a solid water (WT1) equivalent (produced by St Bartholomew's Hospital, London) phantom consisting of two identical rectangular section blocks 7.5 x 15 x 70 $mm^3$ stacked together (to represent a 15 mm thick mouse) placed in the Perspex mouse holder and irradiated with the middle of the phantom positioned along the central axis of the cabinet. Positions representing mice irradiated at the centre, far left or right of this axis within the 51 cm diameter treatment field were used for dosimetry measurements. Measurements were also performed with film on the incident and exit surfaces of the phantom.

Twenty-four hours following exposure the EBT3 film was scanned in transmission mode at 48 bit RGB (16 bits per colour) with 300 dpi resolution using a flatbed scanner (Epson Expression 10000XL). A template was used to position the film within the scanner and the scanning direction was kept constant with respect to the film orientation, as recommended in the manufacturer's guidelines. The dose was calculated using the optical density of the red channel and corrected using the optical density of the blue channel in order to compensate for small non-uniformities in the film which cause false apparent variations in dose (as described in the technical brief: *Gafchromic EBT2 Self-developing film for radiotherapy dosimetry* which is available at http://www.veritastk.co.jp/attached/2062/GAFCHROMICEBT2TechnicalBrief-Rev1.pdf) (294). The batch of EBT3 film was calibrated over a range of doses (0-5 Gy) against a

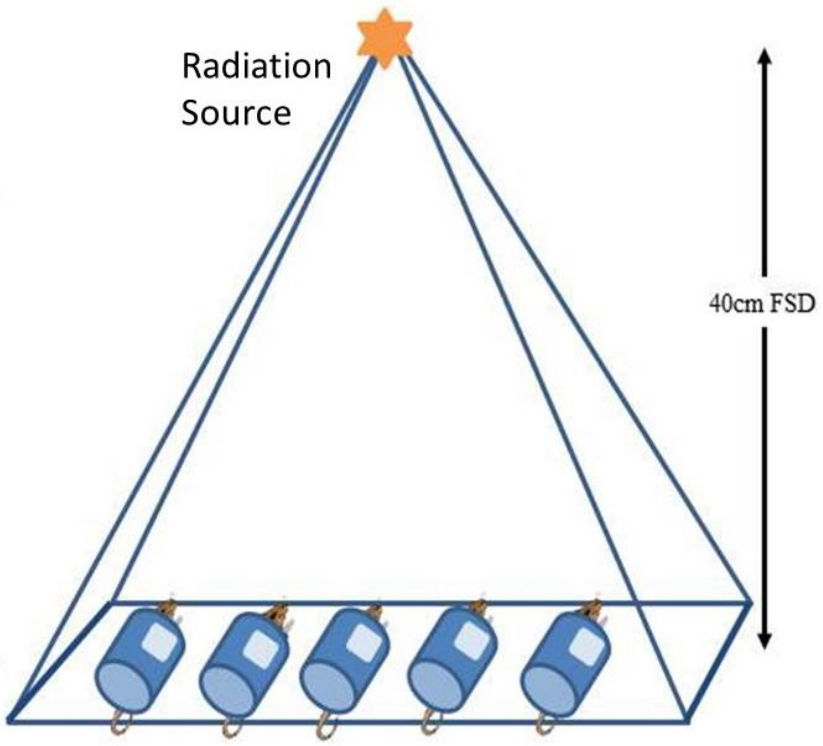



**Figure 1. Schematic of setup for cabinet irradiation** (adapted from S. Aldelaijan et al (295)): Mice are aligned on central axis on adjustable base plate in lead covered Perspex holders with right thorax exposed for treatment.

National Physical Laboratory (NPL) calibrated ionisation chamber (2581, Thermo) with absolute dosimetry performed following the recommendations of the report of AAPM Task Group 61 (296).

## Results

Dose rates were calculated using a weighted fit to the uncertainties in each dose point (calibration + film/scanner/image noise) - the quoted uncertainties in the *dose rates* and *dose offsets* were obtained from the standard error in the estimates of the fitting parameters (y = mx +c) to the weighted data.

With a zero-centred beam, the full-width at half maximum (FWHM) and penumbrae of the profiles were obtained from other fitting parameters and their quoted errors relate to their predicted 95% confidence bounds. The dosimetry results for films irradiated for 60 seconds at the edges and in the centre of the treatment field at the incident, and exit surfaces of the

phantom as well as the mid-plane are summarised in Table 1. Using this dose profile and those of films irradiated for 30, 45, 90 and 120 seconds (Figure 3), we can confirm the predicted dose given over longer durations beyond the sensitivity of the film. Table 2 summarizes these doses predictions for the doses delivered in 11 minutes (or 19.8 Gy), by extrapolating the data from these curves. It shows that the mice placed at the isocentre, received a mean dose of just over the prescribed 20 Gy at mid-plane. Mice placed at the far sides of the treatment fields received exactly or slightly under 20 Gy at mid-plane. Entrance (skin) doses were slightly higher and exit dose a little lower for the mice at the isocentre and field edge respectively.

**Table 1. Expected Entrance and Exit Doses**: Expected skin (entrance and exit) and mid-plane radiation doses (Gy) delivered in an 11 minute exposure using the Gulmay 320 cabinet irradiator (Xstrahl), extrapolated from a 60 second exposure.

| | Left | Middle | Right | Mean |
|---|---|---|---|---|
| **Entrance** | 22.0 | 26.2 | 24.0 | 24.0 |
| **Midplane** | 20.0 | 22.3 | 19.8 | 20.7 |
| **Exit** | 17.5 | 18.5 | 17.9 | 17.9 |

Although image guided radiation (IGRT) was not used in these experiments, confirmation of geometric accuracy was possible by direct visualization of fur-loss in the irradiated area (right thorax) where a well demarcated re-growth of white or grey fur. Figure 2 is an example of an animal irradiated with a single fraction of 18 Gy delivered as a single posterior field to the right thorax, demonstrating a loss of fur in the irradiated volume.

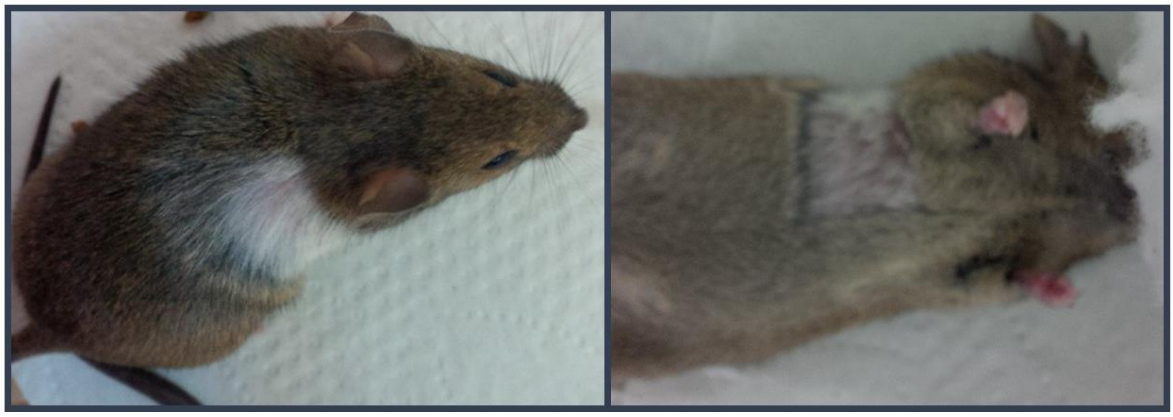


**Figure 2. Fur Loss in treated thorax.** Prone (left) and supine (right) animals showing change in fur demarcating irradiated volume on right thorax.

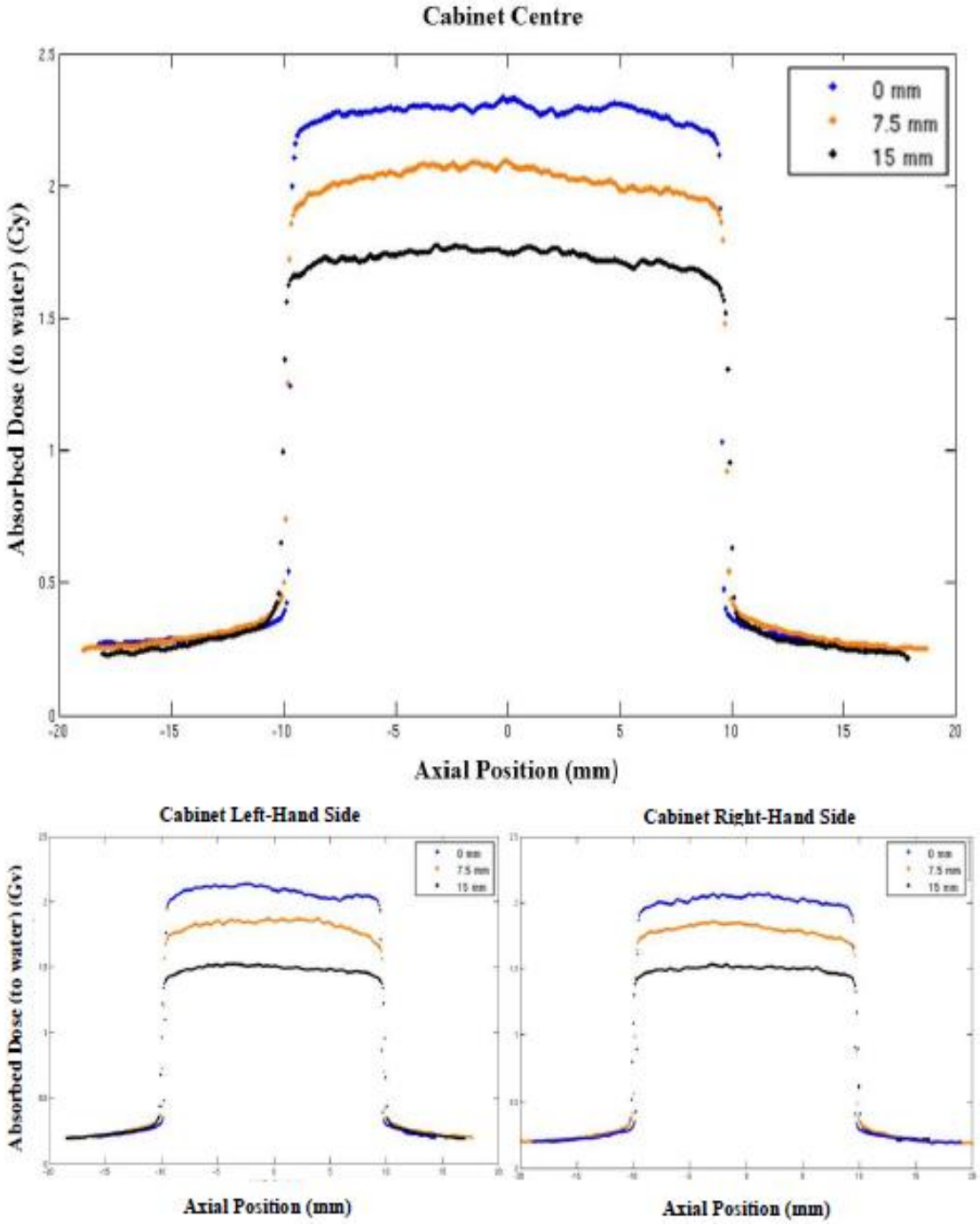



**Figure 3. Dose-rate profiles for Cabinet Irradiator:** Dose-rate profiles across treatment field defined by the collimator on the incident surface (0 mm), centre (7.5 mm) and exit surface (15 mm) of the phantom mouse measured at the centre (top), far left (bottom left), and far right (bottom right) of the treatment field.

## Small Animal Radiation Research Platform (SARRP) Characterization

### Dosimetry

Dose rate measurements and spatial characterization of the treatment field was performed in the same way as it was undertaken for the Cabinet Irradiator, using Gafchromic EBT3 film (International Specialty products, Wayne, NJ) positioned in the centre of a WT1 water equivalent phantom mouse (produced by St Bartholomew's Hospital, London) consisting of two identical rectangular section blocks 7.5 x 15 x 70 $mm^3$ stacked together (to represent a 15 mm thick mouse) placed in the mouse holder and irradiated with the middle of the mouse positioned at the isocentre with 220 kVp using the collimator. Measurements were also performed with additional film on the incident surface and rear of the phantom. Twenty-four hours following exposure the EBT3 film was scanned in transmission mode at 48 bit RGB (16 bits per colour) with 300 dpi resolution using a flatbed scanner (Epson Expression 10000XL). A template was used to position the film within the scanner and the scanning direction was kept constant with respect to the film orientation, as recommended in the manufacturer's guidelines.

The dose was calculated using the optical density of the red channel and corrected using the optical density of the blue channel in order to compensate for small non-uniformities in the film which cause false apparent variations in dose (as described in the technical brief: *Gafchromic EBT2 Self-developing film for radiotherapy dosimetry (294)*). The batch of EBT3 film was calibrated over a range of doses (0-5 Gy) with identical quality 220 kVp against a National Physical Laboratory (NPL) calibrated ionisation chamber (2581, Thermo) with absolute dosimetry performed following the recommendations of the report of AAPM

Task Group 61 (297) at a depth of 20 mm in a 300x300x40mm$^3$ CIRS Plastic Water® LR phantom (CIRS, Norfolk VA) irradiated with a 100 mm x 100 mm field.

To confirm dosimetry in a model simulating the mouse in its in-house developed, vertical holder, films were place at depths of 0, 7.5 and 15.0 mm representing the incident surface, the centre of the mouse and the exit dose respectively, the predicted doses determined based on film measurements and summarized in Tables 2 and 3. The system dosimetric and geometric characterization includes plots the dose rate profiles were generated for the treatment fields across both the short (7 mm) and long (14 mm) axes for a single incident beam as well as for a parallel opposing pair beam arrangement (Figure 4). Figure 5 plots the details of the penumbra region shown for the using incident beam in both axes.

The following parameters were used to fit the left and right side of the beam profiles (centred at zero), which were then evaluated at 0.5*(average dose), 0.8*(average dose) and 0.2*(average dose) to get the full-width-half-maximum (FWHM) and penumbrae, respectively. The fitting function was of the form:

$$F_{\mp} = \frac{a}{2} erf\left(\sqrt{\pi}\,\frac{\left(\frac{L}{2} \pm x\right)}{2s}\right) + c$$

**Table 2. Beam Profile Data**

| Short Axis | LHS of Beam Profile | | | | RHS of Beam Profile | | | |
|---|---|---|---|---|---|---|---|---|
| **Depth (mm)** | L | a | c | s | L | a | c | s |
| **0** | 38.85 | 2.371 | 1.308 | 1.263 | 39.66 | 2.35 | 1.291 | 1.2 |
| **7.5** | 39.97 | 2.004 | 1.154 | 1.466 | 40.56 | 1.984 | 1.139 | 1.365 |
| **15** | 40.44 | 1.619 | 0.9377 | 1.578 | 42 | 1.616 | 0.9252 | 1.489 |

| Long Axis | LHS of Beam Profile | | | | RHS of Beam Profile | | | |
|---|---|---|---|---|---|---|---|---|
| **Depth (mm)** | L | a | c | s | L | a | c | s |
| **0** | 78.37 | 2.451 | 1.292 | 1.7040 | 78.13 | 2.393 | 1.278 | 1.734 |
| **7.5** | 80.83 | 2.061 | 1.113 | 1.926 | 79.57 | 2.055 | 1.131 | 2.061 |
| **15** | 82.32 | 1.68 | 0.9089 | 2.218 | 81.93 | 1.648 | 0.9129 | 2.179 |

**Table 3. Dose rate and spatial profile of treatment field**

| | | Short axis | | Long axis | |
|---|---|---|---|---|---|
| Depth | Dose rate (Gy $min^{-1}$) | Beam width FWHM (mm) | Penumbra: 80% - 20% (mm) | Beam width FWHM (mm) | Penumbra: 80% - 20% (mm) |
| 0 mm | 2.446 | 39.4152 | 1.7441 | 78.4258 | 2.3489 |
| 7.5 mm | 2.126 | 40.5032 | 2.0933 | 80.4301 | 2.8083 |
| 15 mm | 1.712 | 41.5075 | 2.2530 | 82.4155 | 3.0857 |

**Figure 4. SARRP Dose Profiles:** SARRP Long and short axes dose profiles in a water phantom for single beam and parallel opposed pair (POP) beam arrangements

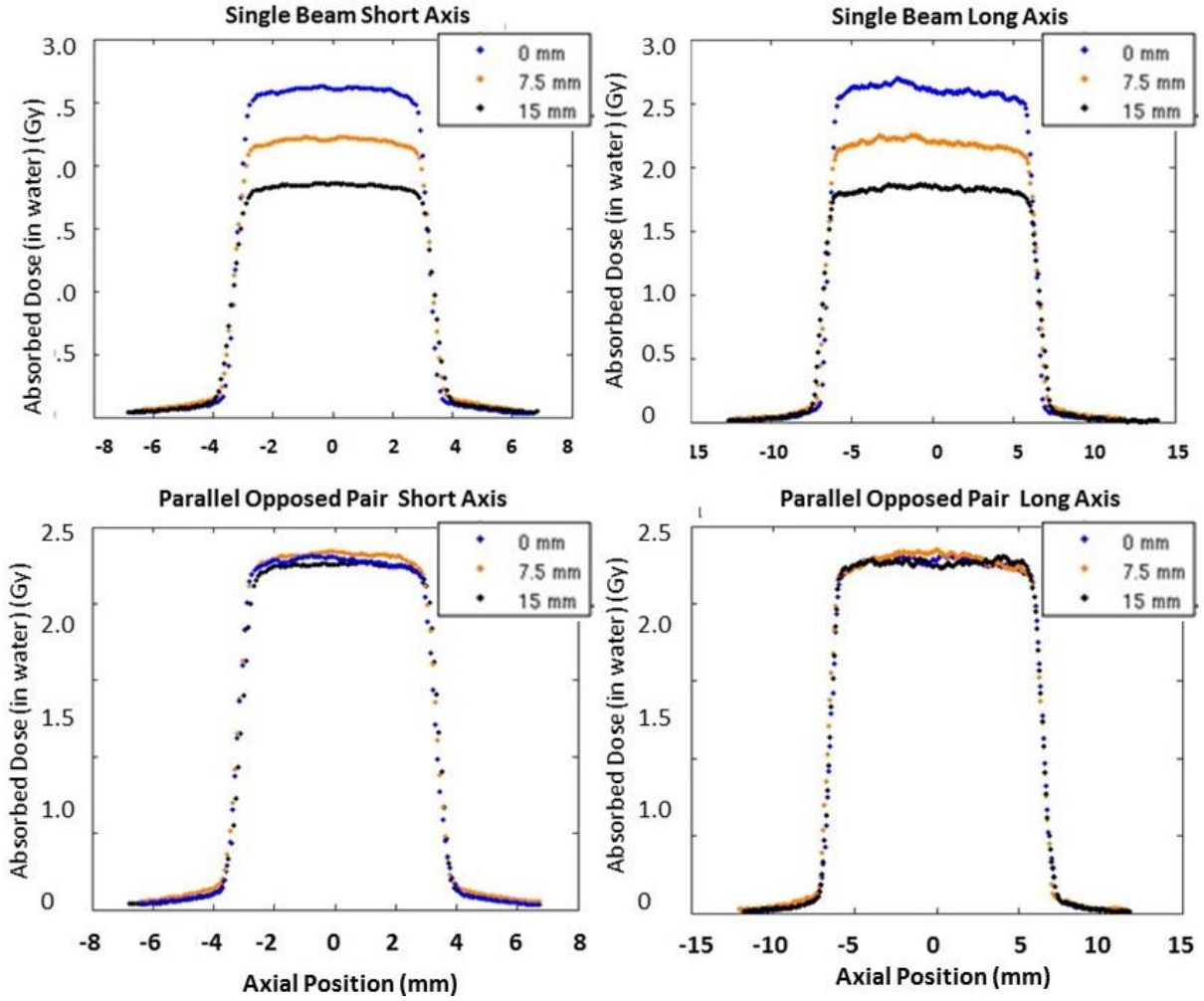
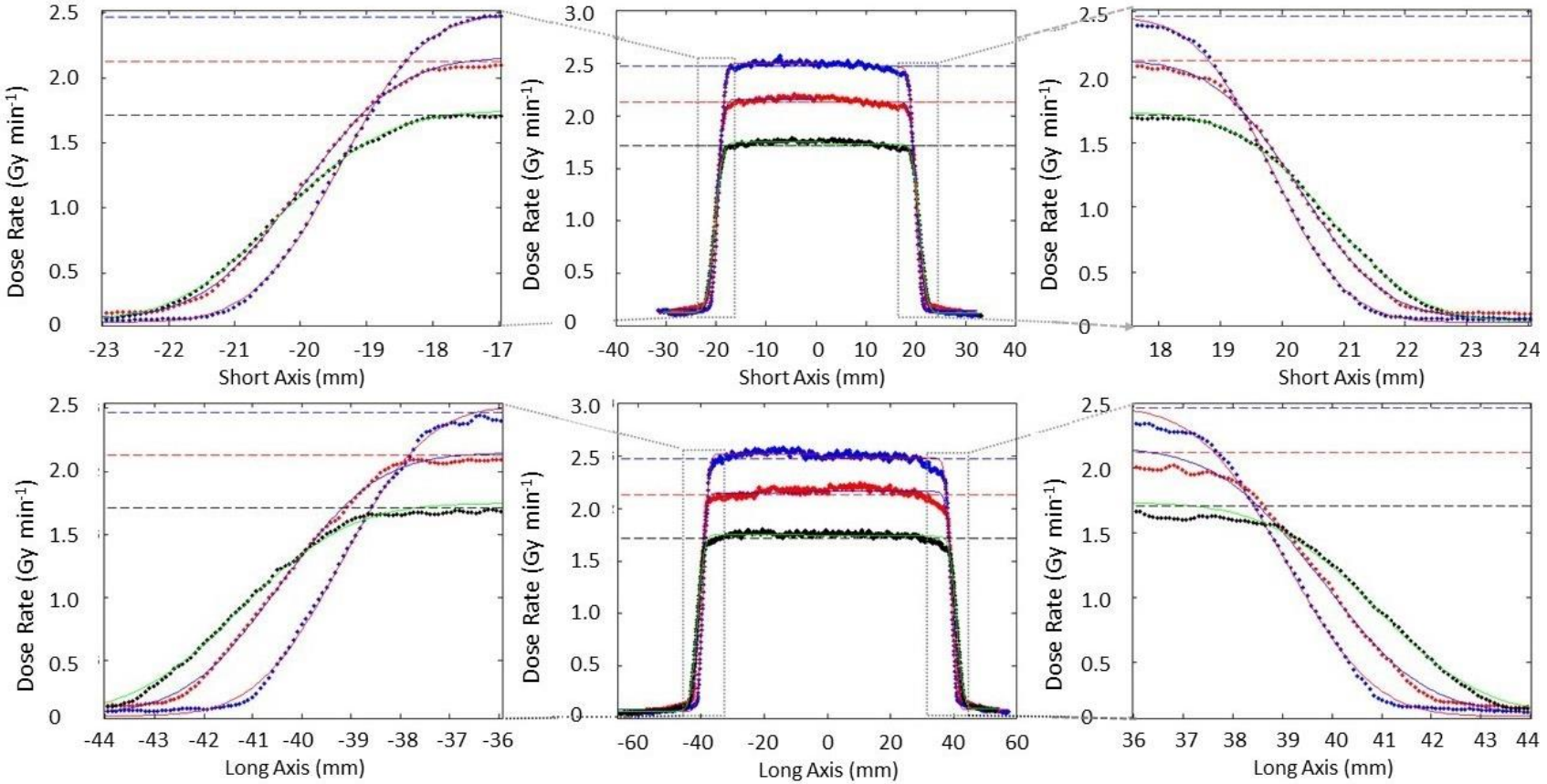


**Figure 5. Dose Rate Profiles for penumbra region for both the short and long axes of the beam**



### Timing

During the experiment further documentation was recorded in order to assess the speed and accuracy of the treatment. The time to deliver the radiation (starting from the start of anaesthetic induction to the removal of the mouse from the SARRP system) was recorded for 91 of 102 fractions. The time decreased considerably from the first to the last fraction, The mean treatment time on the first and last treatment days were 25.4 min (range 19-34) and the mean treatment time on the final treatment day being 21.6 min (range 17–28), respectively. Over all fractions delivered the mean treatment time was 21.8 min (range 17-34).

### Image Guidance

Portal images (radiographs) of the irradiated volumes taken immediately prior to the delivery of the posterior field (first bean delivered), and following the delivery of the anterior field (final beam delivered) show that minimal change in mouse positon from the start to the end of the irradiation procedure (Figure 6).

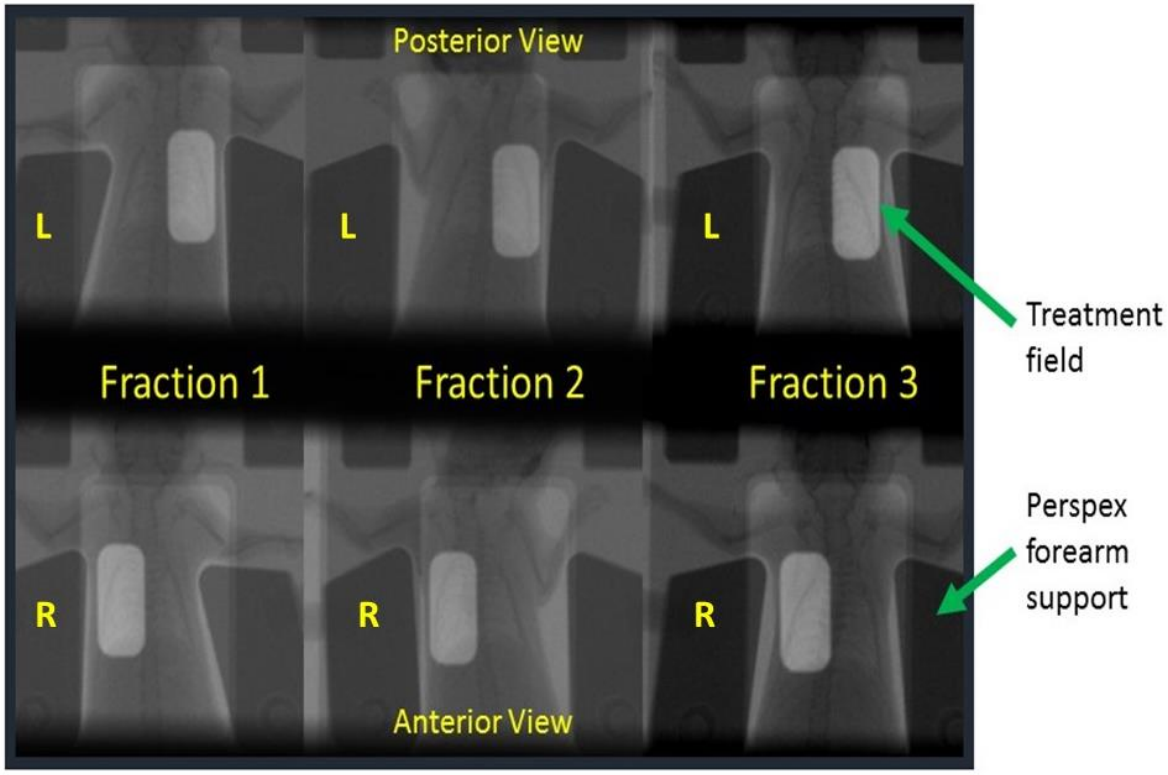



**Figure 6. Radiation Portal Images:** Representative double exposed portal images of the posterior (pre-treatment) and anterior (post-treatment) views for a single mouse irradiated on three days (Monday, Wednesday, Friday). Animal orientation indicated by R (right) and L (left).

# Appendix 2

*List of publications and presentations during studentship*

## Manuscripts

Radiotherapy and chemotherapy as therapeutic strategies on extrahepatic biliary duct carcinoma. Brunner TB, **Eccles CL**. Strahlenther Onkol. 2010 Dec; 186(12):672-80.

A treatment planning comparison of four target volume contouring guidelines for locally advanced pancreatic cancer radiotherapy. Fokas E**, Eccles C**, Patel N, Chu KY, Warren S, McKenna WG, Brunner TB. Radiother Oncol. 2013 May;107(2):200-6.

Comparison of four target volume definitions for pancreatic cancer. Guidelines for treatment of the lymphatics and primary tumour. Fokas E, **Eccles C**, Patel N, Chu KY, Warren S, Gilles McKenna, Brunner TB, Strahlenther Onkol. 2013 May;189(5):407-16.

Comparing dose-volume histogram and radiobiological endpoints for ranking intensity-modulated arc therapy and 3D-radiotherapy treatment-plans for locally-advanced pancreatic cancer. Warren S, Partridge M, Fokas E, **Eccles CL**, Bruner TB Acta Oncol. 2013 Oct; 52(7):1573-8.

Endobiliary Stent Position Changes during External-beam Radiotherapy. Chu KY, **Eccles CL**, Brunner TB. J Med Imaging Radiat Sci. 2015 Mar; 46(1):57-64.

## Conference Presentations

ASTRO 2015 Poster Presentation: Effect of AKT/PI3K inhibition on normal lung tissue following irradiation in normal lung tissue.

OIRO Symposium 2015 Poster Presentation: Feasibility of DCE-MRI to detect radiation-induced lung toxicity in a murine model.

ARR 2014 Poster and Oral Presentation: Comparison of physiological metrics in the assessment of radiation induced lung toxicities in a murine model (young scientist award winner)

RTi3 2014 Keynote Presentation: Inquire: A road-trip of RT questions though a research career

ASTRO 2013 IES Symposium Presentation: Role of Ancillary Services in Radiotherapy

Oxford Cancer Research Centre Symposium 2013 Poster Presentation: Comparison of physiological metrics in the assessment of radiation induced lung toxicity in a murine model

MIRO 2012 Poster and Oral Presentations: Radiotherapy target delineation methods for pancreatic cancers using $^{18}$FDG-PET-images

Management of locally advanced pancreatic cancer meeting 2012 Invited Talk: Radiotherapy for pancreatic cancer – the Oxford experience

CIRT 2011 Poster Presentation: Comparison of contrast enhanced CT and FDG-PET target volume delineation for locally advanced pancreatic cancer International Journal of Radiation Oncology • Biology • Physics, Vol. 81, Issue 2, S732 Published in issue: October 01, 2011

ESTRO 2011 Poster Presentation: Potential advantages and trade-offs of intensity modulated radiotherapy for locally advanced pancreas cancer (including elective nodal volumes) Radiotherapy and Oncology 99, S506 May 2011

NCRI 2010 Poster Presentation: Comparison of PERCIST to RECIST response assessment for patients receiving chemo-radiation plus Nelfinavir for unresectable pancreatic cancer

ASTRO 2010 Poster Presentation: Predicting respiratory motion for patients undergoing pancreatic chemo-radiation in the absence of volumetric motion imaging International Journal of Radiation Oncology • Biology • Physics, Vol. 78, Issue 3, S689–S690 November 01, 2010

# Appendix 3

*Plethysmography*

# Small rodent lung function plethysmograph

## 1. Introduction

Lung function in mice can be quantified with the aid of a whole body plethysmograph (derived from the Greek *plēthysm (ós)*, increase, multiplication): a chamber into which the animal is placed and in which pressure variations are monitored, resulting from air flow across the animal's airway resistance during breathing. The rate and depth of breathing can be determined from measurement of rate of pressure changes and amplitude of pressure changes. The device described here uses a sealed Perspex chamber (which can be vented) into which the animal is placed. When performing lung function testing, pressure changes within the chamber are monitored with a small electret-type microphone capsule which is used as a pressure sensor. These variations are processed and recorded on a computer with a chart recorder-like graphical user interface (GUI).

One end of the chamber has a user-movable assembly, while the other is sealed with a plug after the animal is inserted. Since $CO_2$ is continuously exhaled by the animal while $O_2$ is slowly depleted, the chamber must be periodically opened by the user-movable assembly. A small opening provides enough of an air gap to allow fresh air to enter the chamber, but the gap is small enough not to allow the animal to exit the chamber. The internal volume of the chamber is a compromise: the ability to sense small pressure changes requires a small chamber while a large chamber would allow longer periods of stress-free measurement. The chamber system is shown in Figure 1.




Figure 1: One of the plethysmograph chambers and the 4 channel interface



Lung function plethysmograph. © Gray Institute, Department of Oncology, University of Oxford, 2012. Included with Permission

The construction of the system is such that the pressure chamber 'tube' can be completely removed by loosening two clamps on vertical support members. This is to allow the chamber to be cleaned and to allow access for cleaning the user-movable assembly. This assembly also holds the sensor, which is held in the user-movable assembly with the aid of a small 'O' ring. This sensor 'plug' can also be removed for cleaning/replacement. This electret microphone sensor is of course not a calibrated sensor but has the advantage that its cost is very low, while being perfectly adequate for sensing *changes* in pressure. In any case an absolute pressure calibration is of minimal use since the pressure changes are related to the volume of air present in the chamber while the animal is in it and volumes taken up by animals very depending on strain, sex etc. Nevertheless, the sensor's peak-to-peak output signal is calibrated with the aid of a small loudspeaker which can replace the chamber 'plug'. This at least ensures consistency of sensitivity of pressure amplitude changes.

This calibration arrangement is shown in Figure 2. The loudspeaker is connected to a 50 Ω output impedance signal generator which delivers an open-circuit output voltage of ~5 V peak-peak at relevant frequencies comparable to the rodent breathing rate, i.e. in the range of 2 Hz - 9 Hz (120-450 bpm).

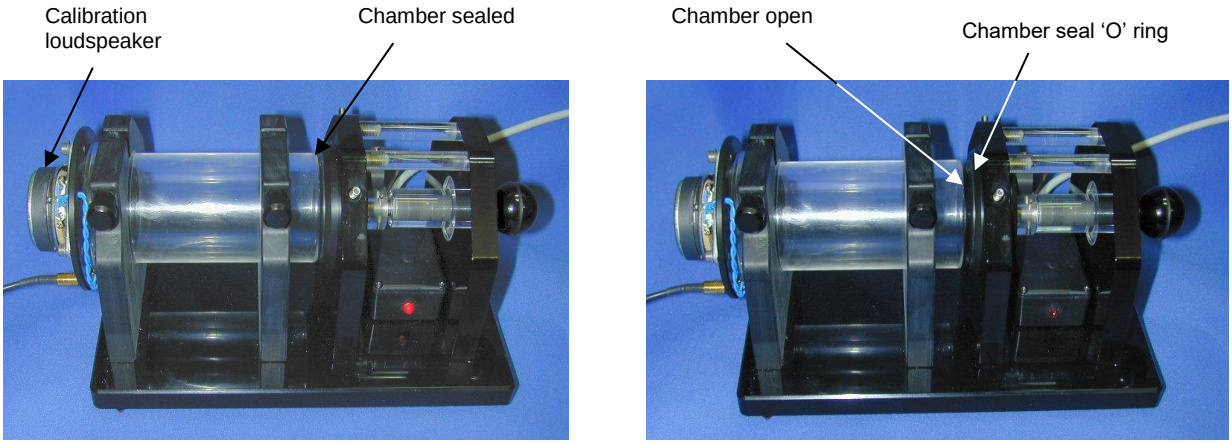



Figure 2: The plethysmograph fitted with a loudspeaker which replaces the chamber end-plug during calibration. The image on the left shows the chamber closed, while the image on the right shows the chamber open. This 'chamber closed status is indicated by the LED on the preamplifier unit.



Lung function plethysmograph. © Gray Institute, Department of Oncology, University of Oxford, 2012. Included with Permission

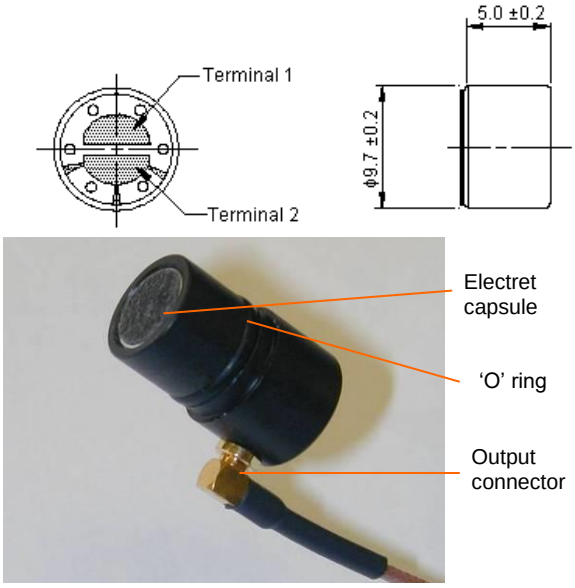



Figure 3: The electret microphone 'sensor'.

The electret microphone used in the system is a Pro Signal type ABM-712-RC (available from One Call/Farnell part # 1736569), shown in Figure 3. The bottom half of Figure 3 shows the microphone mounted in a plastic 'plug' which fits in the user-movable assembly described earlier. Although the microphone is internally protected against debris, it should be kept as clean as possible. It is mounted high up in the user-moveable assembly to avoid liquid entry….this is just a nice way to indicate that rodents pee and poo….

The electret microphone signal is boosted in a small preamplifier unit close to the chamber assembly (maximum gain ~x30). The output signal from this preamplifier is passed to a digitising unit which can accept analogue signals from up to 4 chamber preamplifiers.

## 2. Electronics

The complete electronic circuit is shown in Figure 4. The electrets are phantom-powered with a bias voltage of +2V and ac-coupled (1 sec low frequency time constant) to MAX495 single supply operational amplifiers, also biased to +2V dc nominal output, and powered by +5V derived from the USB connector. Since the output may have an additional gain-induced offset, their outputs are again AC coupled at the data acquisition system input. The preamplifier outputs are filtered with Butterworth 13 Hz 3-pole filters which remove unwanted signals due to animal movement etc. as well as ensuring that no aliasing frequency components are passed to subsequent analogue-to-digital converters.

Signals are digitised to 10 bit resolution with analogue-to digital converters in a PIC microcontroller. The converters are unipolar and arranged to have a full-scale sensitivity of +4.0 V; a DC offset signal of +2.0 V is therefore applied, ensuring that the digitiser outputs are such that 0-1023 counts correspond to +/- 2V chamber signal amplitudes.



Lung function plethysmograph. © Gray Institute, Department of Oncology, University of Oxford, 2012. Included with Permission

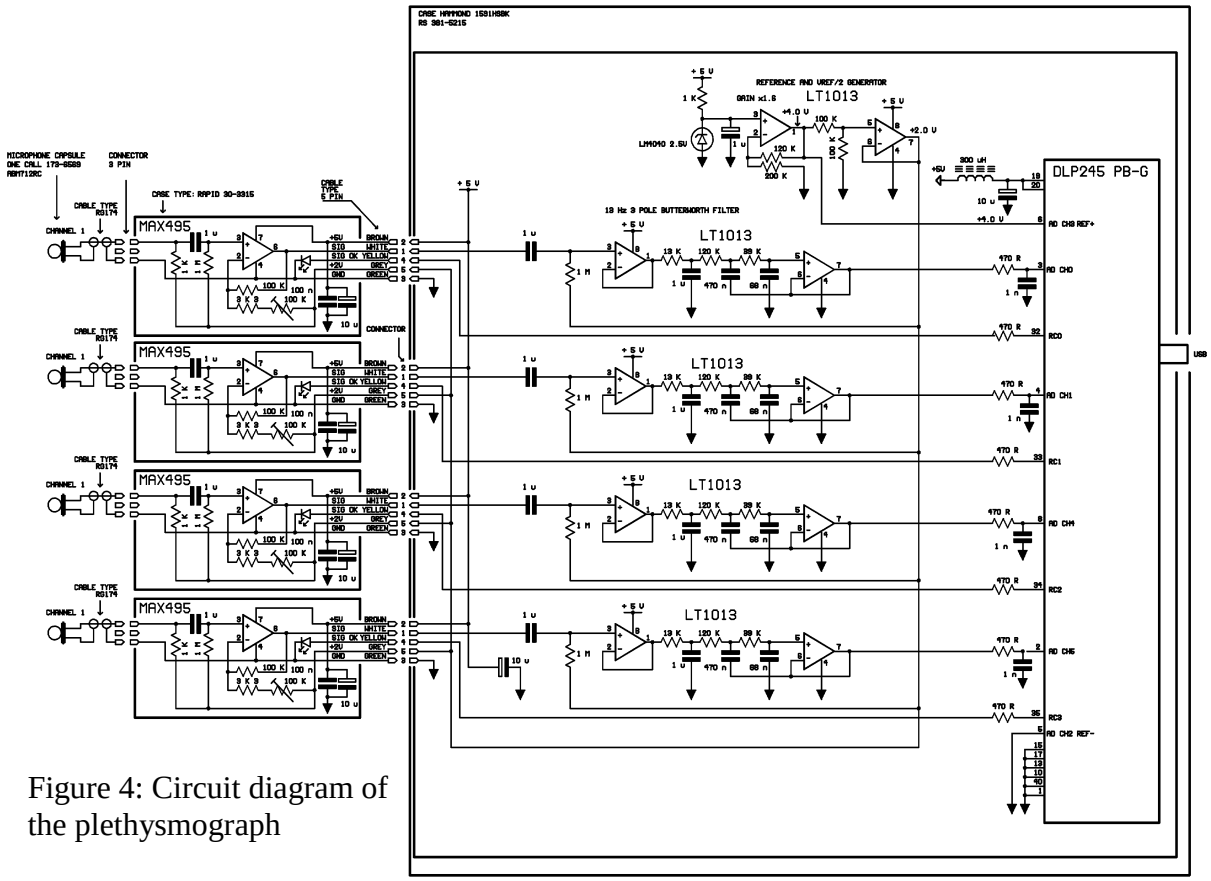



Figure 4: Circuit diagram of the plethysmograph

The PIC microntroller (Microchip 16F877) is contained in a USB module DLP245 PB-G (available from FTDI http://www.ftdichip.com/Products/Modules/DLPModules.htm or other suppliers) which is capable of transferring data to a host PC at rates of up to 2 megabit/sec.

All the electronics are powered from the USB connector; although the power consumption is very low, it is recommended that the host computer always mains powered, i.e. should a laptop be used, battery power should be avoided.

### 3. Mechanical construction

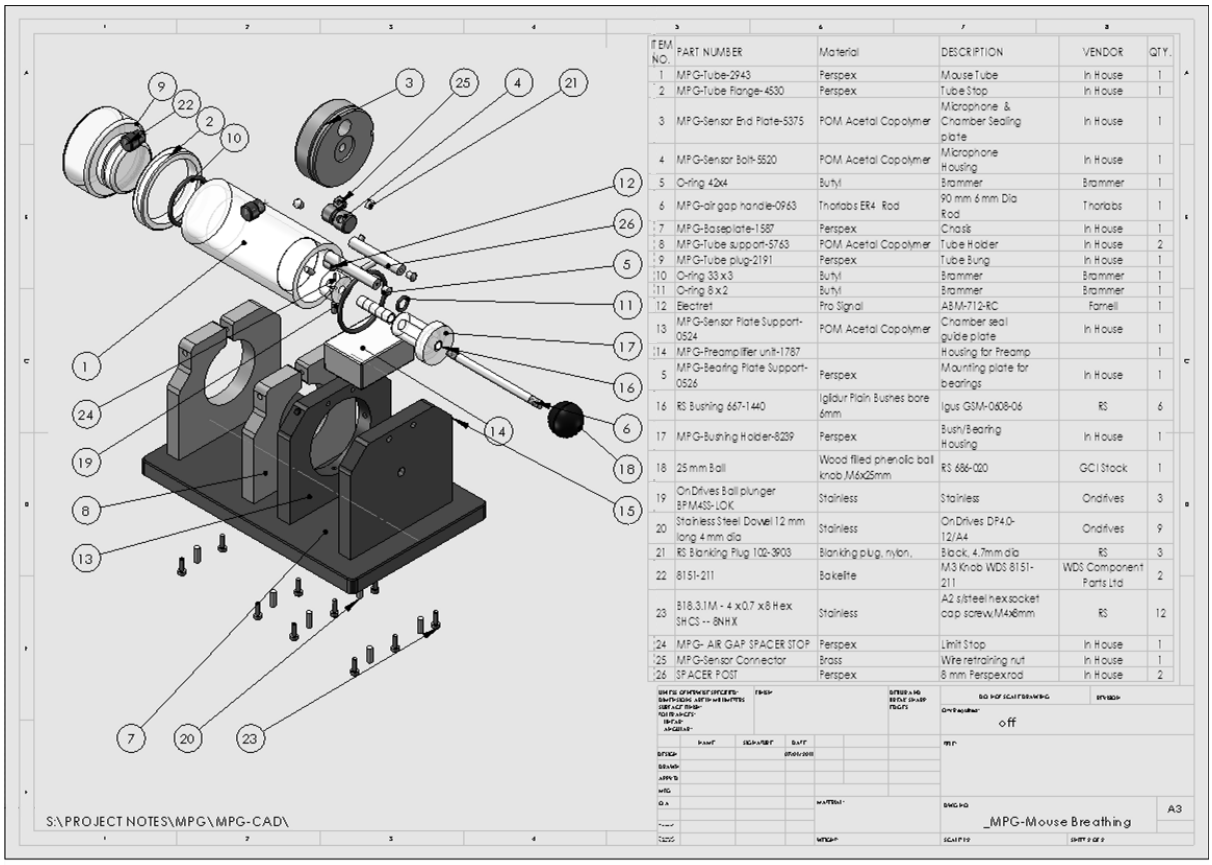
The mechanical arrangement of the plethysmograph chamber is shown in Figure 5. It consists of two vertical clamps made out of POM copolymer which hold a Perspex tube against a sensor end-plate. This plate is guided by a vertical support plate which two holds sprung ball-plungers, intended to ensure that the end-plate 'clicks' into position when closed. A guide bearing for a horizontal rod which moves the sensor plate is held in a fourth vertical plate, this time made out of Perspex for increased rigidity. The vertical plates are mounted on a Perspex baseplate



Lung function plethysmograph. © Gray Institute, Department of Oncology, University of Oxford, 2012. Included with Permission

The preamplifier electronics are mounted in a small plastic enclosure on the baseplate. A 5-way cable connects the preamplifier to the data acquisition electronics assembly; this is also constructed in a small plastic enclosure.

All the mechanics have been modelled in a SolidWorks (http://www.solidsolutions.co.uk) CAD package and are available as files _MPG Mouse Breathing.xx



| ITEM NO. | PART NUMBER | Material | DESCRIPTION | VENDOR | QTY. |
|---|---|---|---|---|---|
| 1 | MPG-Tube-2943 | Perspex | Mouse Tube | In House | 1 |
| 2 | MPG-Tube Flange-4530 | Perspex | Tube Stop | In House | 1 |
| 3 | MPG-Sensor End Plate-5375 | POM Acetal Copolymer | Microphone & Chamber Sealing plate | In House | 1 |
| 4 | MPG-Sensor Bolt-5520 | POM Acetal Copolymer | Microphone Housing | In House | 1 |
| 5 | O-ring 42x4 | Butyl | Brammer | Brammer | 1 |
| 6 | MPG-air gap handle-0963 | Thorlabs ER4 Rod | 90 mm 6 mm Dia Rod | Thorlabs | 1 |
| 7 | MPG-Baseplate-1587 | Perspex | Chassis | In House | 1 |
| 8 | MPG-Tube support-5763 | POM Acetal Copolymer | Tube Holder | In House | 2 |
| 9 | MPG-Tube plug-2191 | Perspex | Tube Bung | In House | 1 |
| 10 | O-ring 33 x 3 | Butyl | Brammer | Brammer | 1 |
| 11 | O-ring 8 x 2 | Butyl | Brammer | Brammer | 1 |
| 12 | Electret | Pro Signal | ABM-712-RC | Farnell | 1 |
| 13 | MPG-Sensor Plate Support-0524 | POM Acetal Copolymer | Chamber seal guide plate | In House | 1 |
| 14 | MPG-Preamplifier unit-1787 | | Housing for Preamp | | 1 |
| 5 | MPG-Bearing Plate Support-0526 | Perspex | Mounting plate for bearings | In House | 1 |
| 16 | RS Bushing 667-1440 | Igilidur Plain Bushes bore 6mm | Igus GSM-0608-06 | RS | 6 |
| 17 | MPG-Bushing Holder-8239 | Perspex | Bush/Bearing Housing | In House | 1 |
| 18 | 25 mm Ball | Wood filled phenolic ball knob M6x25mm | RS 686-020 | GCI Stock | 1 |
| 19 | On Drives Ball plunger BPM4SS-LOK | Stainless | Stainless | Ondrives | 3 |
| 20 | Stainless Steel Dowel 12 mm long 4 mm dia | Stainless | On Drives DP4.0-12/A4 | Ondrives | 9 |
| 21 | RS Blanking Plug 102-3903 | Blanking plug, nylon, | Black, 4.7mm dia | RS | 3 |
| 22 | 8151-211 | Bakelite | M3 Knob WDS 8151-211 | WDS Component Parts Ltd | 2 |
| 23 | B18.3.1M - 4 x 0.7 x 8 Hex SHCS -- 8NHX | Stainless | A2 s/steel hexsocket cap screw,M4x8mm | RS | 12 |
| 24 | MPG- AIR GAP SPACER STOP | Perspex | Limit Stop | In House | 1 |
| 25 | MPG-Sensor Connector | Brass | Wire retraining nut | In House | 1 |
| 26 | SPACER POST | Perspex | 8 mm Perspex rod | In House | 2 |

S:\PROJECT NOTES\MPG\MPG-CAD\

off

A3

_MPG-Mouse Breathing

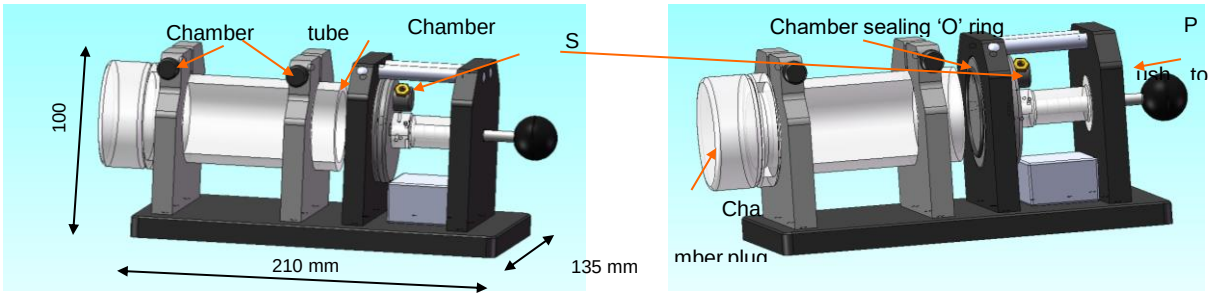



Figure 5: Mechanical construction of the chamber.



Lung function plethysmograph. © Gray Institute, Department of Oncology, University of Oxford, 2012. Included with Permission

## 4. System software and graphical user interfaces

The system requires two software programs: on runs on the PIC microcontroller which performs signal acquisition, while the host runs a data analysis, data storage and display program. A default 20 ms/point sampling rate is used, providing 100 data points over a 2 second long 'record' which is updated every 20 ms. Faster or slower sampling rates can be set to provide shorter or longer records (1 second and 4 seconds with 10 ms and 40 ms sample rates respectively).

Data transfer from the PIC and the host is performed as follows: a 10 ms interrupt is set on the PIC; this interrupt can be used directly, or every two or four interrupts can be used to determine the sampling rate. At the start of every interrupt (or every second or fourth interrupt, as set by a calibration file in the host PC) the program enters a routine which reads each of the four chamber channels (20 μs /channel = 80 μs) 8 times (taking a total of 640 μs) and averages the results. These sampling rates are more than fast enough to reproduce faithfully the 13 Hz band-limited signals. The default sampling rate is 20 ms; this rate (and the 40 ms sampling rate) minimises the consequences of any potential 50 Hz power line interference in the unlikely event that it is present.

After exiting the interrupt routine the measured value of each channel, which consists of 2 bytes per channel is written to a USB interface chip buffer, where it waits to be read by the host computer. The computer requests data every 100 ms and thus 5 readings per channel (20 values) are transferred when the default 20 ms sampling rate is used. A further counter in the PIC interrupt routine is used to store readings from each channel every 400 ms. This slower sampling rate is used to determine whether the chamber is closed or not. The last 4 channel readings are added together and if the result is less than a value set on the host PC, a 'no-signal' condition is assumed, resulting from an 'open' chamber. This condition turns on a logic level which is fed back to the appropriate chamber preamplifier, turning off the LED indicator on the relevant chamber assembly. This arrangement overcomes any potential reliability problems that would have been caused by fitting, for example, a microswitch to the user-movable assembly. Such arrangements, or detection with a reflective opto-sensor, had been tried in the past but were found to be unreliable in the longer term. The state of the 'chamber closed' signal is also used by the host to control a software LED. Furthermore, this signal is used to start a timer on the host software. A value for the maximum time allowed is preset on the calibration panel, shown in Figure 7. When this time has been reached, a warning message is displayed and an audible alarm sounded. At this point, the user must open the chamber for a certain time, again as defined on the calibration panel.



Lung function plethysmograph. © Gray Institute, Department of Oncology, University of Oxford, 2012. Included with Permission

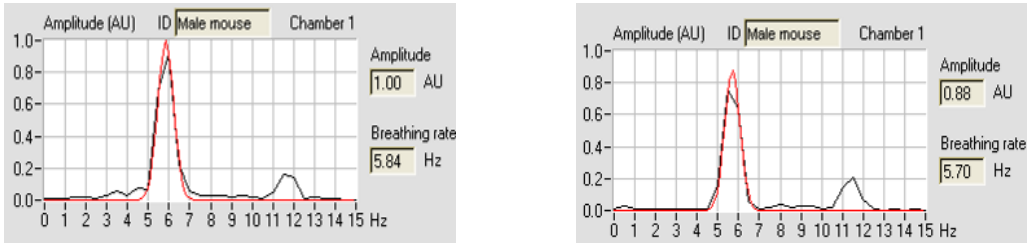



Figure 6: Representative 'coarse' FFT spectra (black) and Gaussian fits applied (red).

Once the time-varying pressure data are present in the host, two second portions of data are passed through a Hamming window and a Fast Fourier transform (FFT) is performed to determine the spectral content of the breathing rate signal. The FFTs are updated at every transfer and continuously averaged. The 20 ms sample rate thus results in a full scale FFT spectrum of 25 Hz occupying 50 points and thus a frequency resolution of 0.5 Hz/pt. The shorter and longer sampling rates provide a resolution of 1 and 0.25 Hz respectively.

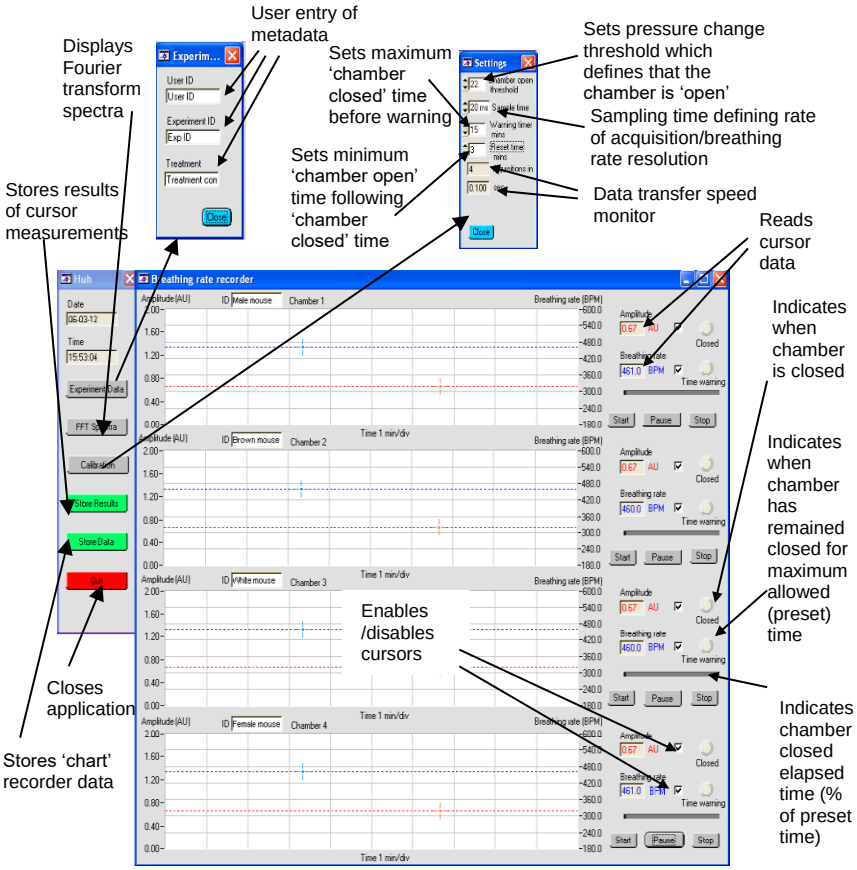



Figure 7: Part of the graphical user interface

Any of these resolutions is too coarse for our purposes, but the resolution can be enhanced through fitting of the FFT spectrum: the peaks of the FFT are identified and a Gaussian fit is applied to the highest peak, as shown in Figure 6. In this figure second harmonics are clearly visible and correctly ignored by the fitting code.

The position of the fit peak is identified with a resolution of 0.01 Hz (0.6 bpm) and the fitted peak amplitude recorded. The 'moving average' type of FFT does involve significant data redundancy but provides a convenient compromise between update rate and frequency resolution.



Lung function plethysmograph. © Gray Institute, Department of Oncology, University of Oxford, 2012. Included with Permission

These amplitude and breathing rate data streams are plotted on the GUI 'chart recorder' shown in Figure 7. Any of the chart recorder chamber channel can be started, paused or stopped at any time. The total displayed time is 10 minutes (timebase is 1 min/div). Pairs of cursors are provided to 'read' the relevant values at time of acquisition, and either the complete chart data or the cursor data can be stored. It is however pointed out that the 'cursor data' reading is a somewhat rough measurement since the cursor can only be moved in increments defined by the screen pixel resolution. The more accurate way involves the storage of all the chart data and readout in some other program, e.g. Excel, or any other setup which allows readout of .csv type variables.

User, experiment and chamber metadata can be entered on the GUI and stored alongside the breathing rate and breathing amplitude information. Figure 8 shows the extended GUI capabilities. The pressure waveforms can be observed as can the FFT spectra and associated fits.






Figure 8: The host GUIs showing the chamber pressure signals and the FFT spectra. In these examples 6.00 Hz (upper panels) and 9.00 Hz (lower panels) sinusoidal signals are fed to the calibration device shown in Figure 2. Although FFT abscissa is scaled in Hz, the chart recorder ordinates are scaled in the more 'convenient' units of breaths per minute, 'bpm'.

In addition to the breathing rate and breathing rate information, the experiment date and time of measurement are updated automatically. An example of the 'cursor data' stored is shown below:

Date: 07-03-12

Time: 08:22:22

User ID: User ID

Experiment ID: Exp ID

Treatment: Treatment comment

| Male mouse, | Brown mouse, | White mouse, | Female mouse |
|---|---|---|---|
| Breathing rate, Amplitude, | Breathing rate, Amplitude, | Breathing rate, Amplitude, | Breathing rate, Amplitude |
| 461.0,0.667, | 460.0, 0.667, | 358.7, 0.766, | 461.0, 0.667 |

The full data file contains three streams for each chamber: time, rate and amplitude, as shown below:

Date: 07-03-12

Time: 08:22:02

User ID: User ID

Experiment ID: Exp ID

Treatment: Treatment comment

Plot interval (secs) 1.000

| Male mouse | | Brown mouse | | | White mouse | | | Female mouse |
|---|---|---|---|---|---|---|---|---|
| Channel 1 | | Channel 2 | | | Channel 3 | | | Channel 4 |
| Time | Breathing rate | Amplitude | Breathing rate | Amplitude | Breathing rate | Amplitude | Breathing rate | Amplitude |
| 0.00 | 0.00 | 0.0000 | 0.00 | 0.0000 | 359.63 | 0.7627 | 0.00 | 0.0000 |
| 1.00 | 0.00 | 0.0000 | 0.00 | 0.0000 | 359.64 | 0.7629 | 0.00 | 0.0000 |
| 2.00 | 0.00 | 0.0000 | 0.00 | 0.0000 | 359.62 | 0.7617 | 0.00 | 0.0000 |
| 3.00 | 0.00 | 0.0000 | 0.00 | 0.0000 | 359.64 | 0.7616 | 0.00 | 0.0000 |

etc.

A representative recording is shown in Figure 9



Lung function plethysmograph, © Gray Institute, Department of Oncology, University of Oxford, 2012. Included with Permission

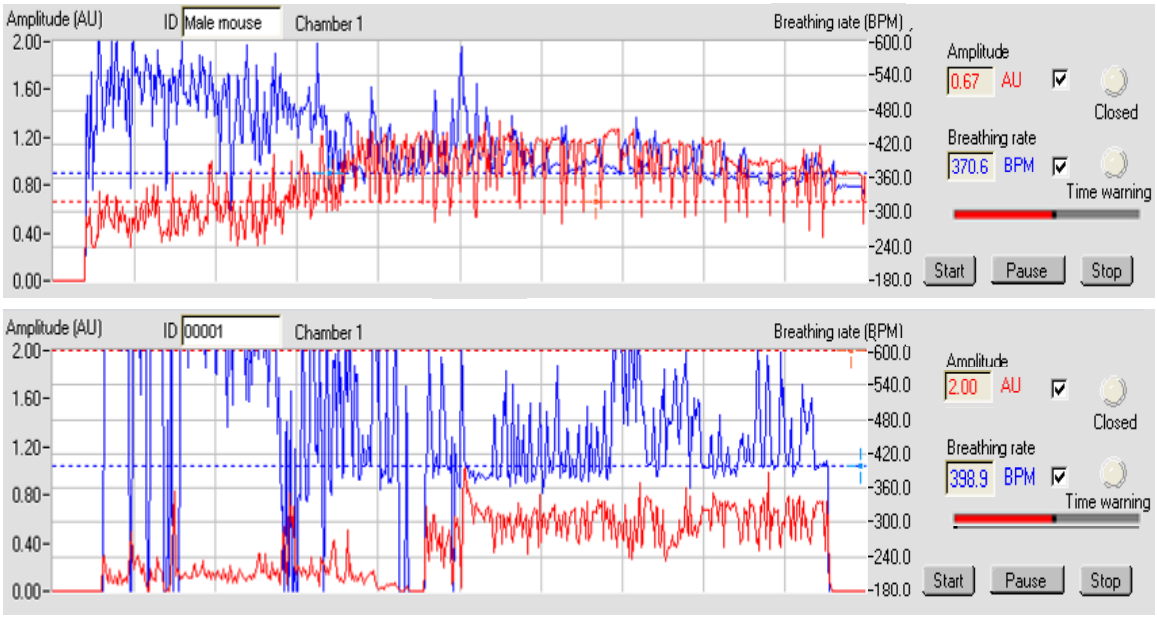



Figure 9: Representative traces from two animals 'new' to the chamber. The upper recording shows the readings from an 'agitated' mouse, who settles after about 3-4 minutes, having been sniffing at the start, resulting in a low-amplitude, high rate recording. When the animal has settled, the breathing rate too settles to around 370 bpm. The bottom trace shows similar behaviour from another mouse, this time the rate minima are at around 390 bpm. The jump in the amplitude trace is due to a leak in the chamber 'O' ring seal at the start of the recording; this was intentionally produced demonstrate the importance of sealing the chamber if amplitude data were to be used: the rate information is still recorded correctly, while the amplitude is not.



Lung function plethysmograph. © Gray Institute, Department of Oncology, University of Oxford, 2012. Included with

## 5. Understanding the measurement

Mice may spend a significant amount of time exploring their new surroundings (i.e. the chamber) by sniffing and moving around in it. The resulting fast pressure changes are *not* representative of their correct breathing rate. However, the lowest recorded rate, during periods when they are quiet, does represent a correct rate. An expanded portion of a recording from an 'inquisitive' mouse is shown in Figure 10. Even in such a recording, the resting rate periods can be identified. After mice have had several sessions in the chamber, they become accustomed to it and the resting periods become longer and easier to identify.

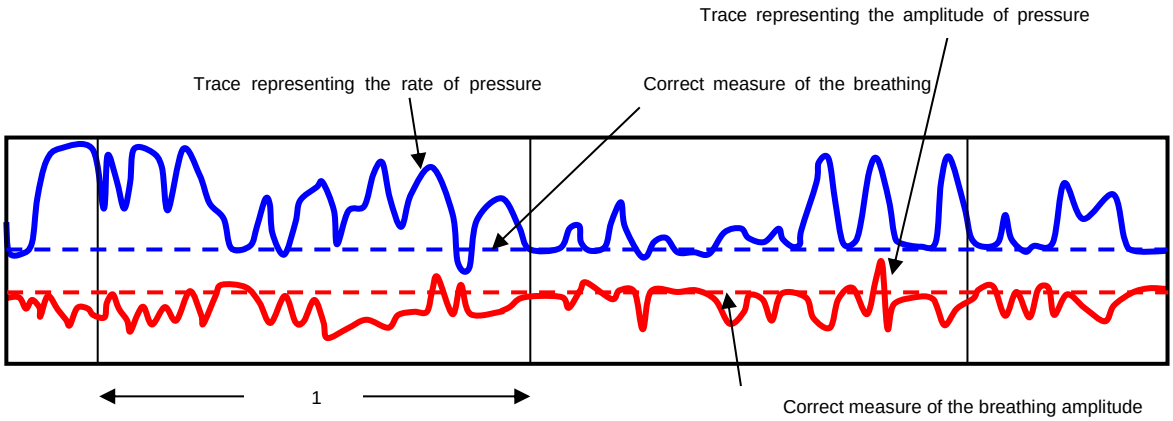



Figure 10: An expanded portion of the breathing traces recorded from an animal 'new' to the chamber, which spent a significant portion of time sniffing around, creating higher than normal breathing rate (blue trace). The appropriate measurement for the breathing rate is that when the mouse was still, for periods of a few seconds, as indicated by the blue cursor. Amplitude variations are shown by the red trace. Here it is harder to estimate the correct value, but in general, the amplitude peaks correlate with the stable periods of the breathing

With practice a rate measurement can be easily made with the cursors provided. A more accurate, though possibly unnecessary way would be to perform an analysis of the distribution of rates. In this instance, one would expect to find a defined peak corresponding to the lowest rate and multiple smaller peaks, or a continuum, at higher breathing rates. Such an analysis could readily be performed using Matlab or similar software tools. If required, it could be added to the existing code.

One way of ensuring that the animals are quiet is to cover the chamber with a dark cloth, and of course to avoid external noise as much as possible, particularly high frequency 'clicks' which cause mice to jump.

The breathing amplitude is an additional, relative indicator of lung function. This parameter however, is not an absolute one but depends on the volume of the mouse, or the volume of gas present in the chamber when the animal is inside: the lower that is, the greater the amplitude variations for a given animal tidal volume. The volume of the chamber has been made



Lung function plethysmograph. © Gray Institute, Department of Oncology, University of Oxford, 2012. Included with Permission

intentionally large (~120 $cm^3$) so that variations of recorded amplitude between mice of different volumes are minimised.

A more important consideration is to ensure that enough oxygen ($O_2$) is present in the chamber and that build up of carbon dioxide ($CO_2$) is minimised, by periodically venting (opening) the chamber. Breathing rates would be expected to increase once 4 to 5% of $CO_2$ has been accumulated. The percentage of $O_2$ available is also dependent on the animal volume and on the amount of time the animal has spent in the chamber, i.e. the number of breathing cycles. Indeed, induction of stress by $CO_2$ could also be used to provide additional lung function information. The available $O_2$ and the accumulation of $CO_2$ can be readily calculated if the tidal volume is known. This in turn can be derived from the weight of the animal. If different weight animals are used in this system, it may be useful to calculate the kinetics of oxygen depletion in the chamber and determine the appropriate length of time that the animals could be kept in the closed chamber, particularly if this time will be significantly more than ten minutes. This is one of the reasons why the chart recorder timebase has been set to 1 min/div, 10 divisions.

The following equations can be used to calculate $O_2$ depletion and $CO_2$ production in the chamber after various periods of respiration.

$$n_z(O_2) = n_o(O_2)\ \{1 - ((V_t/V_c)(1\text{-}f))\}^Z$$

where: $Z$ = number of breaths
$n_z(O_2)$ = amount of $O_2$ (or $CO_2$) in chamber after $Z$ breaths
$n_o(O_2)$ = amount of $O_2$ (or $CO_2$) in chamber at the start, i.e. at Z = 0
$V_t$ = tidal volume (volume of air exhaled) by the mouse
$V_c$ = volume of chamber less the volume occupied by the mouse
f = ratio of exhaled to inhaled $O_2$ (i.e. 16%/21% = 0.762)

The volume available for respiration, $V_c$, is ~100 $cm^3$ but the exact value of course depends on the volume taken up by the animal.

The tidal volume, $V_t$, can be calculated as follows:

$V_t$ = [Minute volume ($cm^3$ air/min)] / [Breathing rate (mean observed bpm value)]

The minute volume can be determined using a semi-empirical relation derived by Guyton (Guyton, AC (1947) Measurement of the respiratory volumes of laboratory animals. American Journal of Physiology, **150**, 10-11):

Minute volume = 2.10 x animal weight $(gm)^{0.75}$.

The minute volume, for a 30 gram mouse is ~ 27 $cm^3$/min. If the mean bpm is 390 bpm (6.5 Hz)
The tidal volume $V_t \approx$ 0.07 $cm^3$.



Lung function plethysmograph. © Gray Institute, Department of Oncology, University of Oxford, 2012. Included with Permission

This system was developed in early 2011 as part of a collaborative project with Ms C. Eccles and Prof. K. Vallis. Most of the construction was performed by R.G. Newman who also wrote the software. J. Prentice and B. Vojnovic designed the mechanics and electronics respectively while R.G. Newman was also involved in the project design. This note was prepared by B Vojnovic and R.G. Newman in March 2012, shortly after preliminary animal testing, once Home Office approval had been obtained.

We acknowledge the financial support of Cancer Research UK.

© Gray Institute, Department of Oncology, University of Oxford, 2012.

*This work is licensed under the Creative Commons Attribution-NonCommercial-NoDerivs 3.0 Unported License. To view a copy of this license, visit http://creativecommons.org/licenses/by-nc-nd/3.0/ or send a letter to Creative Commons, 444 Castro Street, Suite 900, Mountain View, California, 94041, USA.*

# END